



Christian Josef Paar, MSc.

Thermal Design of Electric Traction Machines Integrated in Hybrid Electric Vehicles

DOCTORAL THESIS

to obtain the university degree of
Doktor der technischen Wissenschaften
submitted to

Graz University of Technology

Supervisor and First Assessor

Univ.-Prof. Dr.-Ing. Annette Mütze
Electric Drives and Machines Institute, Graz University of Technology, Austria

Second Assessor

Prof. Dr. Ali Emadi
McMaster Institute for Automotive Research and Technology, Canada

AFFIDAVIT

I declare that I have authored this thesis independently, that I have not used other than the declared sources/resources, and that I have explicitly indicated all material which has been quoted either literally or by content from the sources used. The text document uploaded to TUGRAZonline is identical to the present doctoral thesis.

Date

Signature

Contents

Table of contents	I
Abstract	V
Zusammenfassung (in German)	VII
Acknowledgements	IX
Motivation	XI
1 Introduction	1
1.1 Electric Machines for HEV and EV Applications	1
1.2 Review of Electric Machine Design Fundamentals	4
1.3 Thermal Modeling and Monitoring of Electric Machines	6
1.4 The Challenge: Thermal Design Review of HEV Integrated EMs	7
1.5 Example Case Machine Designs	8
1.5.1 Overview: Example Case Applications	8
1.5.2 Windings	10
1.5.3 Magnetic Circuit Modeling	12
1.6 Outline	14
2 Loss Modeling	17
2.1 Winding Copper Losses	17
2.2 Core Losses	19
2.3 Losses in Permanent Magnets	20
2.4 Bearing Losses	21
2.5 Seal Ring Losses	22
2.6 Clutch Losses	22
2.7 Windage Losses	22
2.8 Gearbox Losses	23
2.8.1 Loss Generation in Geared Transmissions	23
2.8.2 Tooth Friction Losses	24
2.8.3 (Oil) Churning Losses	26

3	Thermal Modeling	29
3.1	Thermal Analysis and Design of Electric Machines	29
3.2	Lumped Parameter Thermal Network Models	30
3.2.1	Overview	30
3.2.2	Approach	31
3.2.3	Implementation	32
3.3	The Finite Element Method	33
3.4	Computational Fluid Dynamics	35
3.5	Determination of Thermal Parameters	37
3.5.1	Introduction into Thermal Transport Mechanisms	37
3.5.2	Convection	38
3.5.3	Conductance	41
3.5.4	Radiation	45
4	Application Study I: Electric Rear Axle Drive	49
4.1	System Description	49
4.2	Model	51
4.2.1	Loss Model	51
4.2.2	Lumped Parameter Thermal Network Model	53
4.2.3	Numerical Thermal Model	57
4.2.4	Thermal Parameters	60
4.3	Model Validation	65
4.3.1	Losses	65
4.3.2	Analytic Thermal Model Steady-State Validation	68
4.3.3	Analytic Thermal Model Transient Validation	70
4.3.4	Numerical Thermal Model Steady-State Validation	72
4.3.5	Numerical Thermal Model Transient Validation	74
4.4	Thermal Real Time Monitoring of Critical Machine Components	79
4.4.1	Sensitivity Analysis	79
4.4.2	Real Time Model	86
4.4.3	Comparison of Real Time Model Performances	87
4.4.4	Discussion of Real Time Model Inverter Implementation Aspects	88
4.5	Analysis of Baseline Thermal Packaging Situation	90
4.5.1	Simulation Approach	90
4.5.2	Scenario I - Boost Cycle	91
4.5.3	Scenario II - FTP-75	92
4.5.4	Scenario III - Variation of Gearbox Heat Flow	92
4.5.5	Numerical Thermal Analysis of the Gearbox-Machine Interface	93

4.6	Design Optimization Study: Alternative Cooling Approach	94
4.6.1	Review of Possible Approaches and Simulation Study	94
4.6.2	Prove of Concept: Oil Cooling of End Windings	95
4.6.3	Computation of Convection Coefficients for EM Operation Range . . .	102
5	Application Study II: Integrated Starter Generator	105
5.1	System Description	105
5.2	Model	107
5.2.1	Loss Model	107
5.2.2	Numerical Thermal Model	109
5.2.3	Thermal Parameters	112
5.3	Model Validation	114
5.3.1	Losses	114
5.3.2	Numerical Thermal Model Steady-State Validation	115
5.3.3	Numerical Thermal Model Transient Validation	116
5.4	Dry Friction Clutch and Actuation System Integration	119
5.5	Vehicle Integration Study: ICE and Transmission	122
5.6	Vehicle Integration Study: Steady-State System Simulation	123
5.6.1	Combined Influence of External Heat Sources	123
5.6.2	Parameter Correlation Analysis	124
5.7	Real World Simulation: Driving Cycle	125
6	Application Thermal Performance Comparison	127
6.1	Approach	127
6.2	Thermal Utilization	129
6.2.1	eRAD	129
6.2.2	ISG	134
6.3	Discussion of the Air Gap Shear Stress	136
6.3.1	eRAD	136
6.3.2	ISG	137
6.4	Correlation of Mechanical, Thermal and Electric Loading	138
6.4.1	eRAD	138
6.4.2	ISG	140
7	Conclusion	143
	Bibliography	147
	List of Publications	163

List of Figures	165
List of Tables	171
Acronyms	173
Symbols	177
A Vehicle Model	183
B eRAD Numerical Thermal Model Steady-State Validation	185
C eRAD Numerical Thermal Model Transient Validation	189
D eRAD Lumped Parameter Thermal Model Implementation	193
D.1 MATLAB/Simulink Implementation	193
D.1.1 Model Structure Overview	193
D.1.2 Loss Model	195
D.2 Thermal Model Parameters	196

Abstract

State-of-the-art design methods for electric machines (EMs) have been established for decades. They are usually based on published correlations between either power or torque and electromagnetic (flux density) and current loading (current density or current sheet loading), which are available for different cooling approaches and applications. The applicability of these correlations for EMs used within hybrid electric vehicles (HEVs), with their different degrees of integration into the overall system (e.g., axle drive, transmission integration, starter/generator), is limited if external heat sources thermally influence the machine during operation.

The influence of the thermal environment within the HEV application is studied, i.e., heat sinks and sources external to the machine, on the thermal design of the machines. An integrated starter generator (ISG) and an electric Rear Axle Drive (eRAD) are used as example case applications. These influences are quantified by: (i) scaling factors for the air gap shear stress and (ii) discussion of the operating points using established driving cycles.

To expand on established design techniques for conventional machines, the influence of the thermal environment by scaling factors of the so-called air gap shear stress, a commonly used design parameter, is quantified. These scaling factors are derived from extensive discussions and analysis of the different operating points of the machines as they occur within established driving cycles.

The example cases comprise the heat sinks and sources that are typical for the rough thermal environment of an electric machine within the HEV context and hence its thermal integration. The latter includes a gearbox, a transmission, a clutch and an internal combustion engine (ICE).

The thermal models include analytic, numerical and computational-fluid-dynamic models all of which have been validated experimentally. These are used selectively to analyze the aforementioned aspects of the electric machine's thermal integration: The lumped-parameter thermal-network (LPTN) model is proposed as a tool for fast parameter studies and thermal monitoring of critical machine components in control algorithms. The numerical approach

allows a more detailed view of the different aspects such as heat flow path analysis and fluid (oil) flow computation and the study of design criteria that take into account the external heat sources and sinks. The models also allow the study of alternative cooling methods such as direct cooling of a machine's end windings, which are not included in established modeling approaches.

Considering the eRAD for an HEV: The interior-mounted permanent-magnet synchronous-machine (IPMSM) with v-shaped buried magnets supports the diesel fuel powered ICE to reduce the CO₂ emissions in a given driving cycle. By means of this application, the influence of gearbox integration on the thermal model for different load scenarios is discussed including the influence of the gearbox losses on the end winding and magnet center temperatures. A further step was the application of an alternative cooling method which cools down the end windings to increase the thermal situation and dynamic capabilities of the EM. Real time monitoring aspects are discussed using this application.

Due to the transmission (TM) integration located close to the ICE, the ISG EM is integrated in a rough thermal environment. The influence of additional heat sources such as the (dry) friction clutch and the electromagnetic actuator on the ISG machine are presented.

Through parameter correlation analysis the influence of each external heat source on the critical temperatures of the different machine components and their interaction is quantified. Such analysis may help to eventually determine to which extent the different heat sources must be considered in the design of an electric machine for use within HEV applications.

Chapters 1 to 3 are the introductory part of the thesis, explaining the methods, approaches and tools used for the research work. Chapters 4 and 5 present the modeling and thermal discussion of the example cases. In Chapter 6 driving cycles are used for quantification of the scaling factors of the design parameters.

Zusammenfassung

Stand-der-Technik Berechnungsmethoden für elektrische Maschinen haben sich über Jahrzehnte etabliert. Der Design-Ingenieur nutzt dabei publizierte Korrelationen entweder von Leistung oder Drehmoment mit der elektromagnetischen Last oder Strombelastung. Die Anwendbarkeit dieser Methoden für elektrische Traktionsantriebe in Hybrid- und/oder Elektrofahrzeugen ist limitiert. Die verschiedenen Integrationsarten oder Integrationstiefen wie beispielsweise Achsantriebe, Getriebeintegration oder Starter/Generator-Anwendungen erfordern eine neue Betrachtungsweise dieser Zusammenhänge.

In dieser Arbeit werden ein integrierter Starter/Generator und ein elektrischer Achsantrieb als Beispielanwendungen herangezogen. Der Einfluss der thermischen Umgebung auf das thermische Design wird analysiert. Die thermischen Einflussfaktoren und der Zusammenhang mit Designparametern, wie zum Beispiel Drehschub, werden mittels verschiedenen Fahrzyklen quantifiziert.

Um diese Einflussfaktoren zu quantifizieren, behandelt diese Arbeit Aspekte der thermischen Integration mit dem Fokus auf integrierte elektrische Maschinen in Hybridfahrzeugen. Ziel ist es, einen neuen Blickwinkel auf den Entwurfsprozess elektrischer Antriebe durch Betrachtung zusätzlicher Wärmequellen wie Kupplungen, Verbrennungskraftmaschinen, elektrische Aktuatoren und Getriebe von fahrzeugintegrierten elektrischen Maschinen zu geben. Zur Quantifizierung wird der Drehschub verwendet.

In der Arbeit werden analytische und numerische Modelle verwendet, um die thermische Auswirkung der Systemintegration auf die Maschinenperformance zu analysieren. Analytische Modelle eignen sich für schnelle Parameterstudien und thermisches Monitoring kritischer Bauteile in Regler-Algorithmen. Numerische Modelle geben einen detaillierteren Blick auf spezielle Probleme, wie zum Beispiel die Verlustentstehung und Aufteilung innerhalb der Maschine. Alle Resultate basieren auf, mittels Messdaten, validierten Simulationen.

Die erste Applikation ist ein elektrischer Achsantrieb (electric rear axle drive, eRAD) eines Hybridfahrzeuges. Die permanenterrregte Synchronmaschine mit v-förmig vergrabenen Magneten unterstützt den Dieselmotor um CO₂ Emissionen zu reduzieren. Anhand dieser

Applikation wird die Problematik der Getriebeintegration diskutiert. Der zweite Schritt ist die Darstellung einer alternativen Kühlung zur Reduktion der Wickelkopf­temperatur, um so die Überlastfähigkeit der Maschine zu steigern.

Die zweite Anwendung, die in dieser Arbeit diskutiert wird, ist ein koaxial-integrierter Starter Generator (ISG). Dieser Antrieb ist zwischen Getriebe und Verbrennungskraftmaschine positioniert und daher einer besonders rauen thermischen Umgebung ausgesetzt. Am Beispiel dieser Anwendung wird der Einfluss von zusätzlichen Wärmequellen wie Kupplung und elektrischen Aktuatoren diskutiert.

Eine Parameter-Korrelationsanalyse zeigt den Einfluss von externen Wärmequellen auf kritische Bauteiltemperaturen, weiters wird deren Interaktion quantifiziert. Die Ergebnisse zeigen die notwendige Betrachtung der thermischen Umgebung fahrzeugintegrierter elektrischer Maschinen während der Designphase und auch in den Regler-Algorithmen, um den Kompromiss zwischen Leistungsdichte und (thermischer) Performance zu erfüllen.

Kapitel 1 und 3 beinhalten die Einführung in die verwendeten Methoden und Modelle dieser Arbeit. Kapitel 4 und 5 präsentieren die Modellierung und thermische Diskussion der Beispielanwendungen. Kapitel 6 diskutiert, mittels Fahrzyklen, die Quantifizierung der Skalierung der Design Parameter.

Acknowledgements

The author would like to thank the Austrian Government and Province of Styria, proprietary of the Austrian Research Promotion Agency (FFG) and the Styrian Business Promotion Agency (SFG). Further gratitude is to conveyed to MAGNA Powertrain GmbH & Co KG, enabling the financial and technical support of this research work.

Many thanks to my MAGNA colleagues Dr. Wolfgang Schweiger and Dominik Schober for their support and discussions in questions of mechanical loss modeling and CAD related problems. I also thank Dr. Markus Schermann, Dipl.-Ing. Robert Kremsl and Dipl.-Ing. Hermann Frühwirth for their support.

I want to express my cordial thanks to Univ.-Prof. Dr.-Ing. Annette Mütze for her supervision of the thesis. She gave me the opportunity to carry out the research work at the Electric Drives and Machines Institute. Her steadfast commitment, guidance and encouragement during the research was an important contribution to the thesis.

I thank Prof. Dr. Ali Emadi who was the second assessor of this thesis.

My heartfelt appreciation goes to my girlfriend Angelika. She gave me the strength and patience to finish this work.

Finally, I thank my friends and family for their support and patience during the last years.

Motivation

The development of electric machines (EMs) for hybrid electric vehicles (HEVs) requires thermal computation and analysis for the investigation of the various trade-offs between power density, peak torque performance, thermal limits of the complex material combinations and costs. Possible approaches to meet customer requirements such as small packaging areas [1], demanding drive cycles [1], weight, performance and costs, are: (i) Oversizing of the machine (reduced current and magnetic loading) [2] to exploit the thermal inertia. (ii) Use of high-performance materials like Fe-Co sheets [3] or dysprosium [4]. (iii) Optimization/enhancement of the cooling concept such as water/oil combinations or direct winding cooling. (iv) An alternative approach is application-specific thermal optimization using thermal and electromagnetic models in combination with selected realizations of prototypes: high thermal utilization of the EM for a specific application can be reached if the EM is tailored to its thermal environment within the vehicle and to its operating profiles.

Regarding the electric Rear Axle Drive (eRAD) application with gearbox attached, the gearbox losses may heat up the rotor (and magnets). Another example is the internal combustion engine (ICE), which in the case of the integrated starter generator (ISG) is a significant heat source and may be problematic if the EM is located nearby, and if the thermal paths between the loss sources and the thermally critical parts of the machine (winding insulation, magnets) have a low thermal resistance. Another additional heat source is for instance the dry-friction clutch in combination with the electric actuator: both components act as an additional heat source if they are located near or maybe within the EM. Without taking into account these additional heat sources, the machine designer may tend to an overly conservative estimation of (thermal) design parameters such as the air gap shear stress σ , the utilization factor C or the effective electric loading A .

An additional aspect is the safety requirements and the desire for a thermal utilization of the EM during operation in the vehicle: it is necessary to monitor critical temperatures in the different machine elements. If critical temperatures seem to be exceeded, derating of the machine's current in the inverter software is a possible way to ensure thermal protection of, e.g., the magnets and/or the winding insulation. Furthermore, these additional heat sources (which are usually not considered in the inverter software) have an influence on the thermal model's accuracy used to monitor the critical machine components.

To review these design parameters, which have been used for decades, consideration of the loss generation, heat paths and cooling approaches of HEV integrated EMs is mandatory. For computation of the thermal influence of additional components, e.g., the gearbox, also the loss generation and computation are required with certain model depth necessary to discuss two case studies: an ISG and an eRAD. These two applications are an example for typical additional heat sources, such as gearboxes/transmissions, ICEs and actuators.

The aspects of gearbox integration and an alternative cooling approach are studied for the eRAD application. The second application is the ISG focalizing on ICE and friction clutch related topics.

Thermal analysis results of both applications are necessary to review the design parameters which have been commonly used for decades and to quantify the influence of the external heat sources on the machine design.

The research work presented delivers approaches for quantifying a scaling for machine design parameters.

Chapter 1

Introduction

This chapter introduces the topic: the effect of adjacent heat sources on the thermal design of electric machines in hybrid electric vehicle applications. As part of this, it reviews aspects of electric machine design as they have been established. Approaches of how to calculate the main machine dimensions for given power, cooling and/or packaging situations are shown. Furthermore, it introduces the machine designs of the example case applications discussed in this thesis, their winding designs and magnetic circuit modeling, which is required for equivalent parameter and loss computation. Finally, an outline of the thesis is given.

1.1 Electric Machines for HEV and EV Applications

The design and computation of electric machines (EMs) for hybrid electric vehicles (HEVs) and electric vehicles (EVs) is a trade-off between manifold requirements such as cost, efficiency, performance (torque and speed), dimensions/volume and weight. For some applications (e.g., electric wheel-hub drives) special safety requirements might also have an influence on the design process. However, the major requirement in the automotive industry with impact on all design decisions is the cost factor.

Driven by the requirements, which are derived from the defined vehicle (or application) performance and costs characteristics, the first step in the design process (Fig. 1.1) is the selection of the cooling technology (air, liquid, etc.) which, in turn, significantly determines the size/volume of the machine.

Basic decisions concerning, for example, the machine technology: e.g., interior-mounted permanent-magnet synchronous-machine (IPMSM) or induction machine (IM); or the materials: e.g., rare-earth vs. ferrite magnets, are commonly based on the design engineer's experience supported by rough computations using (often in-house) analytic software tools with respect to the requirements.

Based on those basic decisions, the machine's dimensions (active length, rotor inner and outer diameter, etc.) are determined followed by a more detailed computation of the magnetic circuit which is usually supported by finite element method (FEM) software tools.

FEM tools enable the machine’s designer to define the lamination (magnetic circuit) and compute both the machine performance and efficiency data (maps) in the operating point area required. Thermal simulations are useful to verify that the critical machine component temperatures are within their absolute maximum ratings. Test-rig measurements are typically used to optimize the machine design so as to obtain an application tailored machine sizing.

This design process, which typically might be adapted depending on the design-toolchain and company-internal processes, uses design parameters which have been established for decades. The EM’s manifold torque and speed requirements are met by changing the design parameters, for example reduction of air gap shear stress σ (or utilization factor C) and effective electric loading A (or current density J) [2, 5, 6].

Considering the torque-speed curve characteristics, the definition of a nominal point (circular mark 1 in Fig. 1.2) is appropriate if the EM is used as a conventional industry machine, operated using the power grid with a small speed and torque range. Application tailored optimization in one operating point is recommended. In this case, the design

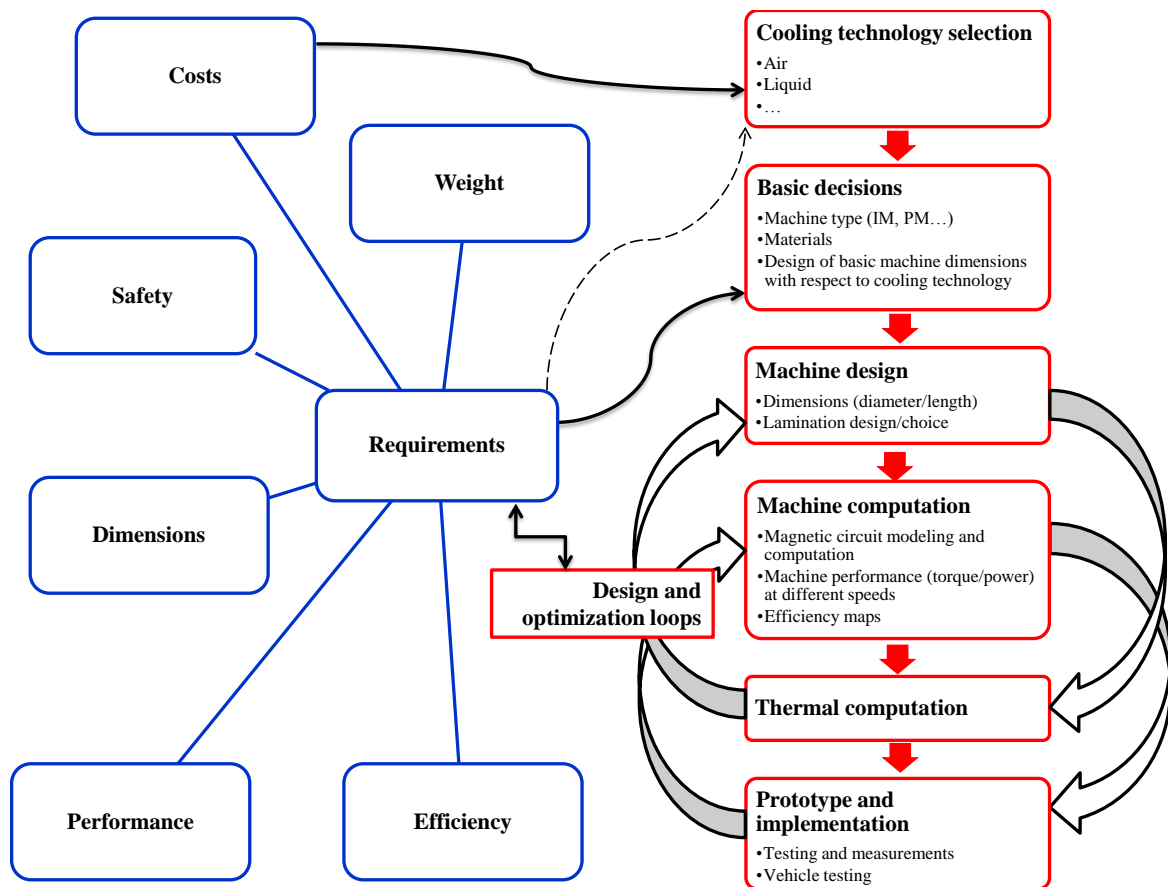


Figure 1.1: Design process of electric drives/EMs for automotive applications.

parameters (σ/C and A/J) are defined by the cooling method, the nominal point is identified as the thermal design point.

If variable speed or torque control is required, variable frequency drives (VFDs) or inverter driven machines with control software are necessary. In this case, the shaft speed and maximum torque (circular marks 2 and 3 in Fig. 1.2) have additional design degrees of freedom, but the nominal point may be further denoted as the thermal design point. However, the maximum shaft speed is also limited by mechanical restrictions, sometimes a gearbox needs to be used to obtain the speed required on the output shaft. Oversizing the machine leads to an exploitation of the thermal inertia (circular mark 3 in Fig. 1.2) of the EM to allow short term overload operation. Other approaches try to use high performance materials such as dysprosium [4] for the magnets (better high-temperature performance) and Fe-Co sheets [3] (higher magnetic loading possible) to increase the performance [5, 6].

In this thesis, focus is placed upon highly integrated EMs/electric drives. The design parameters (i.e., σ or C and A or J) of two example cases are reviewed and compared with existing machines and literature. Existing automotive traction drives are realized using highly integrated and application tailored machines as installation space (packaging) and costs are mandatory factors while designing the machine. Referring to Fig. 1.2, the question arises: Where is the nominal (thermal) design point? To this aim, the two example case applications are thermally analyzed using FEM and lumped-parameter thermal-network

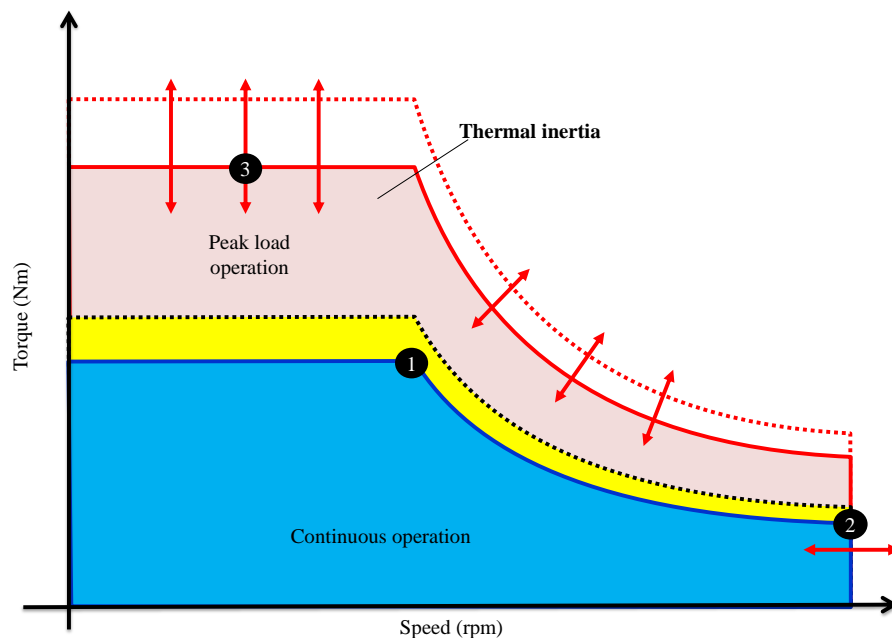


Figure 1.2: Traditional design points of electric drives/EMs.

(LPTN) approaches to discuss the influence of additional heat sources, i.e., gearbox, dry-friction clutch, electromagnetic actuator, internal combustion engine (ICE) and transmission (TM) on the machine's operation.

Using numerical and analytic thermal models, the influence of the gearbox attached (gearbox losses) on the design parameters of an electric Rear Axle Drive (eRAD) application is studied. A post-design approach to manage thermally limited areas of operation (real-time monitoring) and the influence of additional heat sources on the analytic real-time models using this case example is shown. As the gearbox attached is oil lubricated, an alternative cooling approach using the lubricant to cool down the end windings is used as additional input in the thermal design studies.

The second case study (integrated starter generator [ISG] example) discusses the influence of ICE and TM integration on these design parameters. Furthermore, the integrated starter generator (ISG) is equipped with a dry-friction clutch which is integrated into the rotor carrier, acting as an additional heat source if the clutch is actuated.

1.2 Review of Electric Machine Design Fundamentals

Without considering a specific machine type and related mandatory design issues, the torque T_r or force F_r available at the shaft of an EM may be described with [7]:

$$T_r = \frac{F_r d_{r,o}}{2} = 0.5 \pi \alpha A \hat{B} d_{r,o}^2 l_a, \quad (1.1)$$

with the pole coverage ratio α , the effective electric loading A , the peak flux density \hat{B} , the active length l_a and the rotor outer diameter $d_{r,o}$. The effective electric loading is the total number of current-carrying conductors, referring to the air gap circumference [8–10], rotor circumference [7] or inner stator circumference:

$$A = \frac{2 m_{ph} N_{ph} I}{d_{s,i} \pi}, \quad (1.2)$$

with number of phases m_{ph} , number of turns per phase N_{ph} and effective current I . If $2\delta \ll d_{r,o}$, then the simplification $d_{r,o} \approx d_\delta \approx d_{s,i}$ is permissible [11], therefore the air gap δ is usually neglected for these considerations in literature [8].

A common sizing factor or coefficient of performance is the nominal air gap shear stress σ_n [8–10], which is defined as tangential torque-producing force F_r divided by the rotor surface area:

$$\sigma_n = \frac{F_r}{d_{r,o} \pi l} = \alpha A \hat{B}. \quad (1.3)$$

Considering the fundamental waves only eq. (1.3) changes to:

$$\sigma_n = \frac{\hat{A}_1 \hat{B}_1}{2}, \quad (1.4)$$

with the fundamental wave electric loading peak value $\hat{A}_1 = \sqrt{2}k_{w,1}A$ and the winding factor $k_{w,1}$.

Another factor which describes the electromagnetic utilization is the utilization factor C [7], also denoted as Esson number [11]:

$$C = \pi^2 \sigma_n. \quad (1.5)$$

The power production for zero phase angle ($\cos \phi = 1$),

$$P = \frac{\pi d_\delta^2 l}{4} \hat{A}_1 \hat{B}_1 \omega, \quad (1.6)$$

is now defined by the current sheet and the flux density as well as the shaft speed and air gap diameter. Summarizing eqs. (1.1) to (1.6), the torque production is caused by the product of the densities of current and flux, and the power is significantly defined by the shaft speed. As the current and flux densities are limited by thermal and material restrictions [12], the torque is defined by the air gap diameter. Therefore, assuming a fixed nominal air gap shear stress σ_n : if more torque is required, the (air gap) volume increases and if the speed range is expanded, the power increases.

The magnetic loading or the peak flux density \hat{B} is limited by the saturation of the magnetic material (iron sheet) and the available magnetomotive force (MMF) of the excitation source (e.g., permanent magnets) [8]. For example, considering a slotted stator, the teeth flux densities are approximately twice the air gap flux density [8]. The maximum air gap flux densities are given in literature with 0.5 T to 1.1 T [9, 10] or 0.9 T [8]. Because of the nonlinear material behavior, typical maximum flux densities for electrical steels are 1.7 T for SiFe materials and 2.2 T for CoFe sheets [3]. Higher flux densities would lead to very high magnetic field strengths and hence MMFs which would lead to an uneconomically high excitation demand [8].

As the flux density is restricted by the used material, the shear stress (or available torque) is limited by the current density. The current density is limited by the thermal environment (or cooling design) of the EM.

The following equation relates the electric loading and the current density in the slots [8, 9]:

$$A = \frac{J k_{f,sl} h_{sl} w_{sl}}{\tau_{sp}}, \quad (1.7)$$

with the current density J , the slot pitch τ_{sp} and the slot fill factor $k_{f,sl}$. The slot height and the slot width are denoted by h_{sl} and w_{sl} , respectively.

The nominal design restrictions (e.g., current) might be exceeded shortly during overload operation. Regardless of long-term operation or short-term overload operation, the thermal state of the machine is of interest.

1.3 Thermal Modeling and Monitoring of Electric Machines

To protect critical machine components such as the magnets and end windings from thermal damage, the knowledge of critical machine temperatures (hot-spots) during operation is mandatory. Furthermore, it is necessary to predict hot-spot temperatures in the design phase for selected (critical) operating points. Additionally, the magnet temperature is an important control and safety aspect (e.g., [13, 14]). As a matter of fact, the influence on the torque production and energy conversion efficiency has been characterized long ago, e.g., in [15] or [16].

Additionally, limited to IPMs: cross-coupling effects, high levels of magnetic saturation and strong armature reaction result in a complex conjunction of the thermal and, consequently, the electromagnetic behavior [17].

Measuring the temperature of non-rotating machine components, such as the windings, is more or less a matter of technical effort (signal conditioning), manufacturing effort and costs. Using thermistors or thermocouples to measure critical machine components, such as the end winding temperature, during operation is state-of-the-art. The situation is different for the rotating parts (rotor), i.e., the rotor as a whole and the magnets, as the elements commonly of highest interest.

Possible approaches for measuring the rotor temperature are, e.g.:

1. *Non-contact, direct measurement* of the magnet/rotor temperature, e.g., via battery powered Bluetooth [18], battery powered optical links [19] or thermography [20]. These are too costly for automotive applications and also bring along accuracy, installation and robustness issues [21].
2. *Direct measurement using slip rings* for rotational decoupling of the (thermal) sensor wires. Drawback: abrasive wear and costs.
3. *Observation techniques* which are similar to sensorless control approaches (e.g., [22, 23]), as presented in [13, 21, 24, 25], use voltage or current signal injection. The drawback to these methods is a higher torque ripple or instability of the control system [25]. Furthermore, that parameter changes depending on temperature, for example, which must be taken into consideration. A method as proposed in [25] also needs temperature sensors for estimation of the rotor flux. As several parameters change with temperature, the robustness and accuracy also depends on the modeling depth/effort.

The method proposed in [13] follows the idea that the degree of saturation and therefore flux linkage is reflected by the current in the direct axis and measures the current response slope of a d -axis voltage pulse, using a permanent-magnet synchronous-machine (PMSM).

However, these injection methods require interruption of, e.g., the torque or speed control of the inverter software for at least one pulse-width modulation (PWM) period. The behavior during field weakening mode needs further consideration.

1.4 The Challenge: Thermal Design Review of HEV Integrated EMs

Miller [8], gives 1.5 to 5 A/mm² for totally-enclosed (TE), 5 to 10 A/mm² for air-over fan-cooled and 10 up to 30 A/mm² or more, for liquid cooled EMs as typical values for the current density J . This emphasizes the dependency of the current density on the cooling method.

The nominal air gap shear stress σ_n is only constant for a small power range; If the power changes, also the shear stress or the electromagnetic utilization (factor of Esson) changes. Miller, [8] gives a range from 3.4 to 6.9 kN/m² for small TE ferrite, 6.9 to 20.7 kN/m² for rare-earth, and 69 to 103 kN/m² for large liquid cooled machines. Especially European (particularly German) publications give some indications/suggestions on how to describe the increase of the machine diameter with increasing power (e.g., [26]) or give some mathematical suggestions to calculate the diameter directly using empirical equations (e.g., [10]).

Tab. 1.1 summarizes typical values for the nominal and peak air gap shear stress for air cooled TE, liquid cooled and direct winding cooled electric EMs compared with realized examples.

	TYPICAL	REALIZED EXAMPLES				
TYPE	σ_n (kN/m ²)	VEHICLE/DRIVE	σ_n (kN/m ²)	$\hat{\sigma}$ (kN/m ²)	\hat{T} (Nm)	\hat{P} (kW)
IM, TE	13 [9]	Magna, eHub [9]	13	≈ 30	35	11
		Renault Twizy	13	21	57	13
IPM, liquid cooling	30 [9]	Volvo V60 (2012)	32	71	200	50
		Magna, IPM ¹	37		150	45
IPM, liquid, oil combination	30 - 50	Toyota Prius III ²	25	106	205	60
		Toyota Camry ²	20	113	270	70
		Lexus LS600h ²	14	88	300	110
Direct winding	50 [9]					

Table 1.1: Typical and realized shear stress values of EMs.

Table 1.1: The data of the Renault Twizy electric drive is calculated based on name plate information data available in the literature (see [29]). The air gap shear stress values of

¹EM was under small series production for a minivan/utility van and a similarly version for a compact car.

² $\hat{\sigma}$ and σ_n are computed/estimated on measurements reported in [27] and [28].

Toyota Prius III, Camry and Lexus LS600h are calculated based on the test results of the Oak Ridge National Laboratory ([28]). Referring to [28]:

Continuous duration varies significantly with motor speed and specified stator temperature limit for each power level. . . . There is no standard for establishing continuous or peak power rating specifications for motors designed for HEV applications such as the LS 600h, Camry, and Prius motors. [28, p. 76]

The tests in [28] showed: The Prius EM sustains the power level of 25 kW at 50 °C coolant temperature and 5000 rpm shaft speed for 25 minutes, as they stayed below a stator temperature limit of 150 °C. Similar results are reported for the Lexus LS 600h EM, with the same boundary conditions. The Camry's EM also has a continuous power of 25 kW at 65 °C and 5000 rpm shaft speed. Therefore, the nominal air gap shear stress σ_n seems to be very low under these test conditions, but these EMs are highly utilized. Therefore, the peak air gap shear stress $\hat{\sigma}$ values are also shown in Table 1.1. This emphasizes also the importance of the proportions \hat{P}/P and \hat{T}/T for the design.

To meet the torque-speed requirements defined by the application, one approach is to oversize the EM [2] by increasing the active length l_a , thereby reducing the nominal air gap shear stress σ_n (torque density) or effective electric loading A [9], to exploit the thermal inertia for short-term overload operations and/or use costly high temperature performance materials like dysprosium [4–6]. Another approach to achieving packaging targets is the use of high performance sheets (Fe-Co) to increase the possible peak flux density \hat{B} [3], which also comes at the disadvantage of a higher price [6].

As presented in [6], a further challenge is given by the driving profiles that can hardly be described by the definition of a rated torque and speed. For HEV, integrated EMs, a definition of the EM's absolute maximum power may be derived using the hybridization factor [30] which differs depending on the HEV categories, i.e., parallel, series and parallel/series [31]:

$$HF = \frac{P_{EM}}{P_{EM} + P_{ICE}}, \quad (1.8)$$

where P_{EM} and P_{ICE} are the maximum powers of the EM and the ICE, respectively. As stated in [6], besides the drive train topology, another influencing factor which must be taken into account is the operating strategy of the vehicle [32].

1.5 Example Case Machine Designs

1.5.1 Overview: Example Case Applications

Both applications presented in this research work are integrated into an HEV. The example case applications presented are both liquid cooled (water/glycol) IPMSMs. Both applications

enable the vehicle to be driven purely electrically and support the ICE during the acceleration phase of the vehicle.

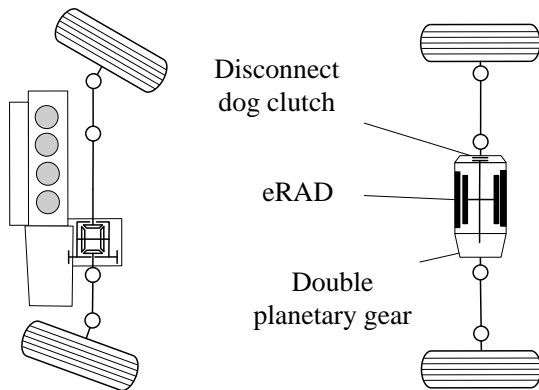


Figure 1.3: eRAD placement in drive train.

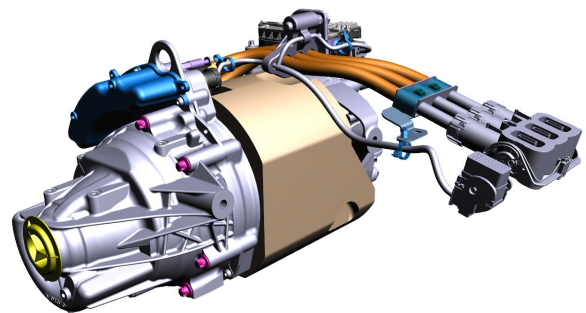


Figure 1.4: eRAD CAD view.¹

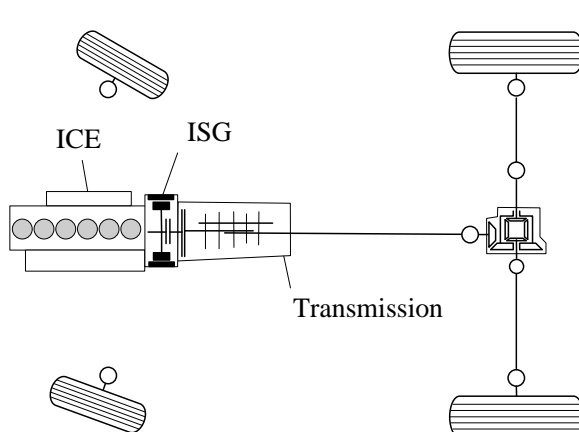


Figure 1.5: ISG placement in the drive train.

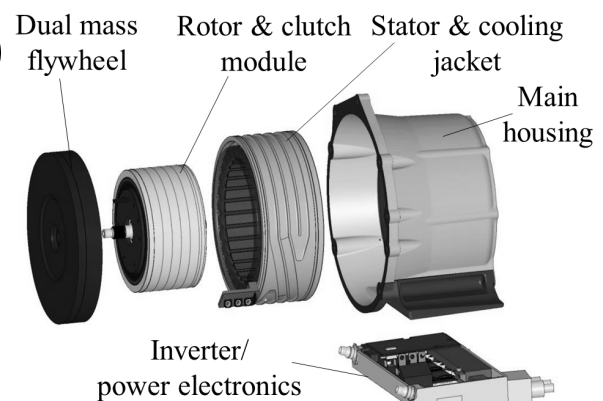


Figure 1.6: ISG exploded view.²

The eRAD application has 50 kW peak power at 200 Nm with a maximum speed of 12000 rpm. The eRAD is mounted on the rear axle of a D-segment (mid-size) car. The placement of the EM in the plug-in HEV is shown in Fig. 1.3, a CAD-model view in Fig. 1.4. A detailed description of the eRAD system description including dimensions and performance ratings is given in Section 4.1, p. 49.

The ISG application (Fig. 1.6) has 80 kW peak power at 325 Nm with a maximum speed of 6800 rpm and is located between the ICE and TM of a sport utility vehicle (SUV). The ISG system description is presented in Section 5.1, p. 105.

The challenge is the comparison of both applications, as the eRAD is thermally influenced

¹Source: Magna Powertrain GmbH & Co KG.

²Source: Magna Powertrain GmbH & Co KG.

by the gearbox attached. The eRAD has also a disconnect system (DCS) integrated, which allows for disconnecting the EM at higher vehicle speeds. The ISG application is thermally influenced by the ICE at one side and also by the TM at the other side. Furthermore, it has a dry-friction clutch integrated, which also generates heat during actuation. The inverter is attached to the ISG housing in Fig. 5.1, but is not within the scope of this research work. To ensure that there was no thermal influence during the measurements, the inverter was not mounted during the test-rig measurements.

1.5.2 Windings

During the design phase of EM development and for the computation of the losses (copper and core losses), it is necessary to consider the design of the stator windings. The eRAD analyzed in Chapter 4 is equipped with distributed windings (Fig. 1.7). The ISG in Chapter 5 has concentrated windings (Fig. 1.8). The ISG's tooth coil windings are interconnected with a toroidal bus bar.

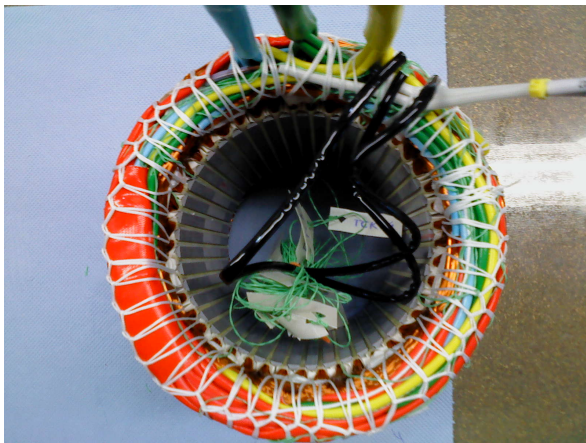


Figure 1.7: eRAD distributed winding.

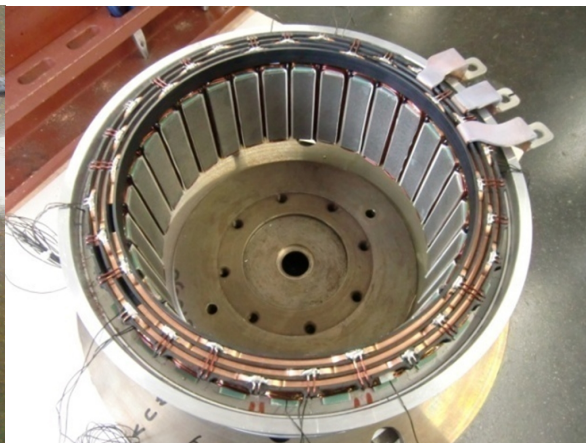


Figure 1.8: ISG concentrated winding.

Distributed Windings

The distributed type of winding usually has several slots per pole and several conductors per phase-belt [33]. A further distinction, but with the same total voltage and different end windings, is lap-wound or concentric coils [7, 33]. Concentric coils have advantages if using automated manufacturing machines [7]. This type of winding is designed to minimize both electromotive force (EMF) and MMF harmonics [33] and therefore “... have been the winding of choice for high performance speed drives due to the ability of producing a unity winding factor and close to sinusoidal magnetomotive force (MMF) waveform.” [34, p. 1]

Relevant for the eRAD application: according to [35], if the number of slots per pole and

phase is,

$$q = g \pm \frac{1}{n}, \quad (1.9)$$

with g and n as integers (whole number), then the winding factor $k_{w,1}$ for the fundamental wave is defined by,

$$|k_{w,1}| = \left| \sin \frac{\pi}{2} \frac{y}{m_{ph}q} \frac{\sin \frac{\pi}{2m_{ph}}}{nq \sin \frac{\pi}{2nm_{ph}q}} \right|, \quad (1.10)$$

with the coil span (number of slots) y and the number of phases m_{ph} .

Concentrated Windings

Concentrated winding designs have the advantages of,

- shorter end windings: reduction in end winding length due to shorter non-overlapping end turns [36, 37] and therefore lower copper losses (or higher energy efficiency [7, 36]);
- being easily manufacturable [34] (lower manufacturing cost [36], especially if the slots are open [7]);
- having a better heat transport to the (stator) lamination [7];
- having very compact coils with higher slot fill factor [7, 36];
- and having a better flux-weakening capability [36].

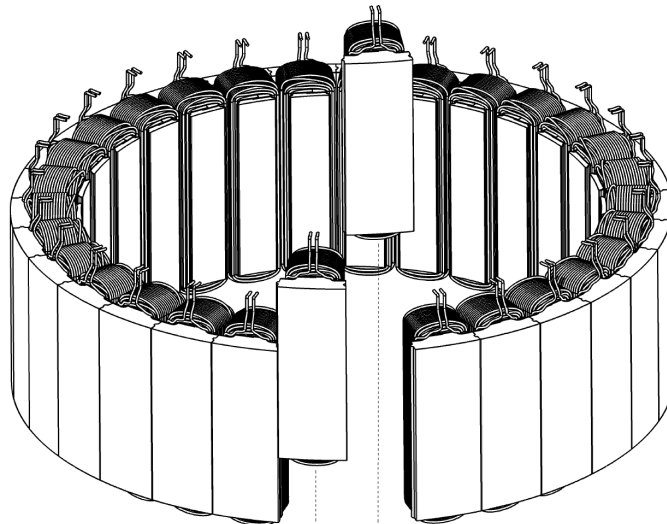


Figure 1.9: ISG stator design.

This type of winding is a special type of fractional slot-per-pole winding [7]. Each (partial) coil is wound around a tooth. If the stator yoke is segmented between the particular teeth,

each tooth can be manufactured separately (see Fig. 1.9). Because of the typically high harmonic content of fractional slot windings, the practical use of this winding may be restricted to permanent-magnet synchronous-machines (PMSMs) [7]. Note that the higher amount of harmonics in the air gap flux density also increases the rotor losses and the noise emission.

Both applications discussed in this thesis are realized using fractional slot-per-pole designs. Requirements for the realization of such winding types are discussed in [35]. The winding design of the ISG application is discussed in detail in [38].

1.5.3 Magnetic Circuit Modeling

Analytic Magnetic Circuit Modeling

The computation of the core losses and parameters such as the d -axis inductance L_d , the q -axis inductance L_q and the permanent magnet flux ψ_{PM} requires the flux density B in different parts of the machine (e.g., teeth, stator yoke, rotor yoke). Different analytic approaches are presented in, e.g., [33, 39–41]. In [39], an equivalent magnetic circuit with 144 elements is presented and compared with FEM results: the equivalent magnetic circuit is faster but less accurate if compared with FEM. The approach presented in [40] uses a simplified magnetic circuit (if compared to [39]) with reluctance elements also considering saturation. The magnetic circuit of the machine presented in [40] is comparable to the eRAD application due to the v-shaped buried magnets. During the research work, an analytic magnetic circuit model, which considers the magnetic d -axis, q -axis coupling in a simplified manner, was developed for the eRAD application and is mainly based on [40] and [33]. However, the approach as implemented has the drawback that the estimation of the stray flux reluctances beside the magnets is very rough.

If a complex model such as presented in [39] is used, the air gap flux density variation (in time and space) is one output of the model, assuming enough spatial sampling points exist. The implemented model uses an empiric approach (see [33] and [37]). The analytic magnetic circuit approach as developed for the eRAD application was adapted for the ISG application in [38]. The drawback of using equivalent magnetic circuits (or magnetic reluctances) and the empiric approaches mentioned is that harmonics are not modeled sufficiently enough. This might lead to a high inaccuracy of the results, especially as the ISG application uses concentrated windings. Therefore, in [38] the approach presented in [41] is used to extend the capabilities of the equivalent magnetic circuit model. The approach presented in [41] and used in [38] for the ISG application delivers accurate results if current in quadrature axis direction is injected into the EM magnetic circuit model. This might be useful if surface mounted magnets are used, but the control software of the applications discussed here uses maximum torque per ampere (MTPA) control and automotive traction applications usually

require field weakening capability.

Numerical Computation

To summarize, analytic approaches are the appropriate tool if fast parameter studies are required. To ensure computational accuracy of the parameters L_d , L_q and permanent magnet flux ψ_{PM} and the core losses, FEM was used during this research work, using a commercially available software³.

³ANSYS® Maxwell®, Release 15.0, see [42] for details.

1.6 Outline

Chapters 1 to 3 are the introductory part of the thesis that supplement the methods, approaches and tools used in Chapters 4 to 6 which are the main part of the research work.

A short introduction to loss modeling of the various heat sources required for the thermal analysis of the example case study machines and their additional loss sources, such as the eRAD's gearbox and the ISG's clutch, is given in Chapter 2.

Chapter 3 shows the thermal modeling approaches used during the research work. Based on the literature study, the LPTN and FEM thermal modeling approaches are introduced briefly. Computational fluid dynamics (CFD) simulations were required for the thermal computation of the alternative cooling approach and to derive mean heat transfer coefficients for the LPTN and the FEM simulation models.

The first example case application, the eRAD, is presented in Chapter 4. Using this example case application, the generated losses are discussed and an LPTN and an FEM thermal model are introduced and validated using test-rig measurement results. These models are used as simulation tools to discuss additional heat sources and their influence on the thermal behavior. The eRAD application has a gearbox attached on the drive end (DE). Section 4.4 discusses thermal real time monitoring of critical machine components. Furthermore, the thermal baseline packaging situation is shown and an alternative cooling method are introduced. The analysis results in this chapter are the basis for the discussion of the thermal design and comparison with the ISG application in Chapter 6.

Chapter 5 shows the ISG as the second example case application. As with the eRAD application, the losses and an FEM thermal model is introduced and validated experimentally using the previously introduced simulation tools. The thermal analysis of critical machine components in this chapter focuses on the influence of the ICE, TM and dry-friction clutch. Again, the computed thermal analysis results are used for a discussion of the (thermal) EM design and comparison in Chapter 6.

A comparison of both case studies with their additional external heat sources on state-of-the-art design parameters is given in Chapter 6. Real world driving cycles, heat sinks and sources external to the machine on the thermal design of the machines are considered, expanding the limitations of the conventional design approach. The thermal effect is quantified for both applications using the conventional design criteria introduced in Chapter 1.

Note that selected results of this thesis have also been published in [5, 6, 43–46]. Reference to the individual publications is made in the relevant Chapters.

Chapter 2

Loss Modeling

In this chapter, loss modeling and computation approaches are reviewed and relevant literature is presented. The loss computation approaches presented are based on available literature, e.g., [7, 10, 33, 37, 47–62] for the electric machine losses and, e.g., [63–71] for determination of the gearbox losses. The loss computation approaches are further used as an input for the thermal models developed. Therefore, an important aspect was the practical implementation in the simulation tools used, with appropriate accuracy.

2.1 Winding Copper Losses

Winding losses or (winding) copper losses P_{cu} are caused by ohmic (also denoted as resistive or Joule) heating and are proportional to the electrical resistance R and the square of the effective current I . If only DC losses are considered, R is defined as

$$R = \frac{\rho(T)l_c}{A}, \quad (2.1)$$

with the conductor length l_c and the conductor area A . The temperature dependency of the electrical resistivities ρ , of the materials considered in this thesis, are considered linear for practical purposes [10]:

$$\rho(T) = \rho_{\text{ref}}(1 + \alpha(T - T_{\text{ref}})), \quad (2.2)$$

with the linear temperature coefficient (of resistivity) α , the reference temperature T_{ref} and the electrical resistivity at reference temperature ρ_{ref} . With $\alpha = 0.004041$ 1/K at 20 °C for copper conductors [47] (0.00392 1/K in [10]). The computation of R also requires the conductor length l_c : “[a]n accurate definition of the winding length in an electrical machine is a fairly difficult task.” [62, p. 255]. Approaches for estimation or computation of the winding length are presented e.g., in [10, 48] and [62].

Skin and proximity eddy-current effects, increase the winding copper losses [47, 49], as they influence the current density distribution inside the conductor(s):

1. DC winding losses: $P_{\text{cu,DC}} = I_{\text{RMS}}^2 R$, with the RMS current I_{RMS} and the (DC) electrical resistance R .

2. AC winding losses: $P_{\text{cu,AC}} = P_{\text{cu,DC}} + P_{\text{cu,add}}$, with the additional losses $P_{\text{cu,add}}$ caused by skin and proximity effects.

The proximity (eddy-current) effect is caused by circulating AC currents which are generated by magnetic fields. Localised current loops or concentrated distributions are formed due to nearby conductors [50], such as the parallel conductors of coil turns in a slot [51].

The skin effect is caused by a nonuniform current density in the conductors [49]. If the skin effect occurs, (high-frequency) current tends to flow on the surface of the conductors [47, 50]. High-frequency currents might be caused by the eddy current introduced by e.g., high frequency harmonics due to pulse-width modulation (PWM) current chopping.

The largest eddy-currents are induced close to the tooth openings [52]. However, [72] shows (using an analytic model) that the slot-opening to slot-pitch ratio influences the AC copper losses: the AC copper losses reduce as more magnetic field is shielded by the tooth-tips. A further mitigation could be achieved [52]: (i) if multi-stranded Litz wires are used, but with the drawback of poor thermal performance, reduction of packaging factor and increased costs (reduction due to twisted geometry [47]); (ii) if selected wire profiles are used; (iii) and if selected winding techniques are used. Flux density variation reduction in the slot (or conductor region) reduces the proximity eddy-current losses [49].

Regarding the proximity effect, an analytic estimation for one strand, neglecting the eddy-current redistribution effect on the field distribution, is [49, 53]:

$$P_{\text{cu,e}} = \frac{\pi d^4 \omega^2 \hat{B}^2}{128 \rho}, \quad (2.3)$$

with the conductor (wire) diameter d , the conductor electrical resistivity ρ , the peak value of flux density harmonic \hat{B} and the angular velocity ω . This equation shows that the additional losses due to the proximity effect can be reduced by reducing d (stranded wires or Litz wire, [49]).

Iwasaki et al. [49] further show the ratio of the AC to the DC copper loss for an increasing conductor diameter or increasing number of strands in one conductor: for a single conductor in an air core at 20 kHz sine-wave current the additional amount of losses ($P_{\text{cu,add}}$) for wire diameters up to 1 mm is neglectable; the AC to DC ratio approaches asymptotically one with increasing the number of strands in one conductor. Gieras [48], referring to [73] defines a skin-effect coefficient e.g., for a double-layer winding ($w_c = \tau_p$), and a three-phase winding ($\phi = 60^\circ$). In the case of chorded windings with $w_c < \tau_p$ and $\phi = 60^\circ$, the skin-effect coefficient is:

$$k_{\text{cu}} \approx \xi \frac{\sinh 2\xi + \sin 2\xi}{\cosh 2\xi - \cos 2\xi} + \left(\frac{m_{\text{sl}}^2 - 1}{3} - \frac{m_{\text{sl}}^2}{16} \right) \left(2\xi \frac{\sinh \xi - \sin \xi}{\cosh \xi + \cos \xi} \right), \quad (2.4)$$

with the number of conductors per slot m_{sl} and the relative conductor height ξ .

Summarizing,

$$P_{\text{cu}} = m_{\text{ph}} I_{\text{ph}}^2 R(T) k_{\text{cu}}, \quad (2.5)$$

is relevant for the practical computation of the losses. With the number of phases m_{ph} , the phase current I_{ph} and the temperature depending phase resistance $R(T)$. Note that eq. (2.4) only considers the skin effect. However, the correction factor k_{cu} may also include the proximity losses (see [10]). [48] further discusses the coefficient k_{cu} and gives an additional coefficient, which is multiplied with k_{cu} , considering that there are differences between slot and end winding (proximity effect).

2.2 Core Losses

Ferromagnetic materials consist of domains with 100 % aligned magnetic dipoles, which are distributed randomly if no external magnetic field is applied [47]. If an external magnetic field is applied, the domains align (themselves) depending on the strength of the external magnetic field. The core losses (also denoted as iron losses or iron core losses) in ferromagnetic materials are caused by change of the magnetic state, these hysteresis losses are friction losses of the elementary magnets (see [10]). If the external magnetic field alternates, the magnetic material is exposed to periodic magnetization [47], and heat is generated. Additionally, eddy current losses are caused by the electrical conductivity of the material and induction effects [10]. The eddy current losses are reduced by using electrically insulated (very thin) stacked lamination sheets with silicon (increases electric resistivity). Precise computation of the (iron) core losses is still a wide field of research with a large number of publications: [7] and [47] give an overview; [10], [54] and [62] give some more details with an explanation of computation approaches; different approaches including a five parameter equation are presented, e.g., in [55]. The five parameter equation presented in [55] overcomes the underestimation of losses at high magnetic flux densities and frequencies by adding an additional loss term with higher order flux densities (higher than B^2).

A practical and established approach for fast computation of the (iron) core losses in different parts of the machine (core backs and teeth) is based on the Steinmetz equation [56], e.g., Fischer [7] proposes:

$$P_{\text{fe}} = m p_{\text{core}} \left(\frac{B}{B_{\text{ref}}} \right)^2 \left(\frac{f}{f_{\text{ref}}} \right)^{1.6} k_{\text{p}}, \quad (2.6)$$

with the mass m , the specific losses p_{core} based on a reference flux density B_{ref} and reference frequency f_{ref} and the processing factor k_{p} to take the degradation of the magnetic properties of the lamination material due to the manufacturing process into consideration. This approach was used for the analytic computations of the used iron core losses during this research work. For the computation of the flux densities, an equivalent circuit model similar to the one presented in [33] which describes the magnetic circuit by stator back iron, teeth,

air gap, rotor yoke, and permanent magnet equivalent reluctance was used. However, the modeling accuracy depth of the magnetic circuit for the calculation of the flux densities is determined by the geometric complexity of the flux paths.

Regarding the finite element method (FEM) computations, the approaches implemented in the proprietary software tools were used. For the electric Rear Axle Drive (eRAD) application, the different approaches which are coming with the FEM software are compared in Tab. 4.2 (p. 52).

2.3 Losses in Permanent Magnets

Losses in permanent magnets (PMs) are (mainly) caused by eddy currents [47]: assuming a (ideal) sinusoidal flux distribution, no eddy currents are generated when the rotor rotates with the same speed as the field, as there is no change in time of the flux density in the rotor. Harmonics are generated by [47]: (i) the non-sinusoidal ampere-conductor distribution of the windings, (ii) in the case of PWM supply: time harmonics in stator current, (iii) and slot harmonics (change of air gap permeance due to the slots). The losses which are generated further are influenced by the electric conductivity, which ranges from $0.6 \cdot 10^6$ to $0.81 \cdot 10^6$ S/m for (rare-earth) neodymium, iron and boron (NdFeB) magnets [48]. Ferrites have a higher resistivity and therefore lower losses [47]. The machines used in the application studies, are both use NdFeB magnets.

The computation of the eddy currents (and in consequence losses) in the magnets, requires knowledge of the air gap flux distribution in every operating point. [37] uses both, an analytic approach and an FEM model with the conclusion that eddy current loss computation of magnets using FEM requires 3D transient simulation. Gieras [48] proposes analytic equations to estimate such magnet losses. The theoretical solution of the eddy-current losses is,

$$P_{\text{mag}} = \frac{1}{\sigma} \int_{\text{vol}} \mathbf{J}^2 dV, \quad (2.7)$$

with the current density vector \mathbf{J} and the electrical conductivity σ . This equation is used in [57] and adapted for a thin conductor leading to the following approximation for $\delta \ll x$ and $\delta \ll y$,

$$P_{\text{mag}} \approx \frac{2yz}{\sigma\delta} |H|^2 \frac{x+y}{y}, \quad (2.8)$$

with x, y and z half of the magnet width, length and height respectively; the skin depth δ ; and the magnetic field strength H . A further comparison between an analytic approach and 3D FEM is presented in [58]. [39] computes the magnet losses using a complex magnetic equivalent circuit which approximates the flux density distribution (in time and space) in the air gap resulting in lower iron and magnet losses if compared to FEM. [59] presents

an experimental verification of a core and magnet loss computation based on FEM (2D and 3D) for a 1 kW interior-mounted permanent-magnet synchronous-machine (IPMSM) with concentrated windings. The conclusion is, that magnet and core losses might be minimized if thin core laminations and v-shaped buried magnets are used. In [59], the magnet and core losses were in the range of some percent of the total output power. [60] compared five topologies of IPMSM for hybrid electric vehicle (HEV) applications concerning the performance characteristics (e.g., magnet mass, iron loss, torque ripple): the v-shaped topology was found to have the lowest magnet mass. In [74] rotor configurations and their influence on the magnet losses using fractional-slot IPMSM machines are studied: the v-shape IPMSM was found to have the lowest loss generation as each magnet pole is formed by two pieces of magnets. Furthermore, [74] mentioned that the magnet segmentation further significantly reduces the magnet losses.

In the case of the application study eRAD (Chapter 4), the eRAD machine has v-shaped buried magnets which are axially segmented to reduce the magnet losses to a minimum (see [59, 60, 74]). 2D FEM simulations of the realized machine showed that the losses within the magnets are at approximately 1 % of the total losses: these losses are not exact but accurate enough for the thermal models. Also the analytic approach presented in [57] was used for the analytic loss computations.

Referring to the integrated starter generator (ISG) application 3D FEM computations were carried out, showing that the 2D FEM computation underestimates the magnet losses up to 100 % at higher speeds. As with the eRAD, the amount of the magnet losses compared to the total losses is low.

2.4 Bearing Losses

Losses in the bearings are generated due to friction. The losses may vary with: the load, the lubricant properties, the (shaft) speed, the bearing type and temperature. [47] and [48] show that the bearing losses increase linearly with speed, simplified expressed by [37, 62],

$$P_{\text{bear}} = T \omega = \mu_{t,r} F r_{\text{bear},i} \omega, \quad (2.9)$$

with the rolling friction coefficient $\mu_{t,r}$, and the bearing inner radius $r_{\text{bear},i}$, whereas F is the Pythagorean sum of axial and radial forces (see [37]). More details are given e.g., in [61].

The bearing manufacturers/suppliers give guidelines how to estimate the bearing losses for a given temperature and (axial and radial) load condition (see also [62]). During the research work loss-strip-down measurements results and computed results¹ were used to compute the generated mechanical losses for different temperatures and shaft speeds for each bearing.

¹Software: BEARINX, Schaeffler Technologies AG & Co. KG, www.ina.de

2.5 Seal Ring Losses

As with the bearing losses, the measured losses are implemented as look-up tables in the model and show a non-linear dependence on speed and temperature. The look-up tables are based on loss-strip-down measurements which allow splitting up windage, bearing and seal ring losses to a certain extent. Using these measurement results, supported by bearing supplier data and computations, the seal ring losses were determined.

2.6 Clutch Losses

The thermal energy input into the friction plates of the dry clutch can be simplified as

$$E_{\text{clutch}} = \int T(t)\Delta\omega(t) dt, \quad (2.10)$$

with the transmitted torque $T(t)$, the speed difference $\Delta\omega(t)$, and the time t . Eq. (2.10) shows that losses in the friction plates are only generated if a speed difference occurs.

The clutch losses are relevant for the thermal simulation of the ISG application. As with the bearing, seal ring and windage losses, measurement results have been used to determine these losses: both, the speed difference $\Delta\omega(t)$ between the clutch module input and output shaft together with the transmitted torque T were measured at the clutch test-rig.

2.7 Windage Losses

A possible approach for the mechanical losses caused by air friction (windage losses) is [10]:

$$P_{\text{air}} = C_{\text{air}}v^2d_{r,o}(l_a + 0.8^30.6\tau_p), \quad (2.11)$$

where v is the surface speed, $d_{r,o}$ the rotor diameter, l_a the stack length (assuming that the rotor length equals the stack length) and the pole pitch τ_p . The empirical value C_{air} is assumed at $8 - 10 \text{Ws}^2/\text{m}^4$ for open-circuit ventilated and up to $15 \text{Ws}^2/\text{m}^4$ for surface ventilated [10] machines. These values are not applicable to all machines [10]. [48] and [62] both give an equation for estimating the air friction which is proportional to the shaft speed with ω^3 .

The windage losses were determined using measurement results: a dummy rotor was used to avoid cogging torque.

2.8 Gearbox Losses

2.8.1 Loss Generation in Geared Transmissions

Traditionally power losses in gearboxes are separated into load dependent and load independent losses [6, 63–66]: The losses caused by friction in the teeth and in the rolling-element bearings are load dependent and therefore change with the transmitted power. Losses independent of the load are mainly caused by oil churning of the rotating parts (e.g., splashing of planets in oil), and depend on the speed. Further load independent losses are generated by oil shearing in synchronizer cones, journal bearings rotary joints as well as seal rings and clutches. These load independent losses are traditionally termed as drag losses, but [63] points out that also load dependent losses may occur, using the example of a multistage gearbox.

The efficiency η of a gearbox is defined by [63]

$$\eta = \frac{P_{\text{in,mech}} - P_{\text{gbx}}}{P_{\text{in,mech}}}, \quad (2.12)$$

with the mechanical input power $P_{\text{in,mech}}$ and the total gearbox losses P_{gbx} . The efficiency is constant if the gearbox has reached thermal equilibrium [65]. Then, the operating temperature is constant and the power dissipated inside the gearbox equals the cooling power (or heat evacuated) [75].

The total loss power of the gearbox is the sum of

$$P_{\text{gbx}} = P_{\text{gbx,tf}} + P_{\text{gbx,oc}} + P_{\text{gbx,bear}} + P_{\text{gbx,seal}}, \quad (2.13)$$

with the tooth friction losses $P_{\text{gbx,tf}}$, the seal ring losses $P_{\text{gbx,seal}}$, the oil churning losses $P_{\text{gbx,oc}}$ and the bearing losses $P_{\text{gbx,bear}}$. Also the bearing losses might be further divided into a load dependent and load independent part [76].

A correlation between the load dependent losses $P_{\text{gbx,tf}}$ and the load independent losses $P_{\text{gbx,oc}}$ is given by [69, 77], with the total gear mesh losses

$$P_{\text{gbx,tg}} = \frac{P_{\text{gbx,tf}}}{1 - \frac{P_{\text{gbx,oc}}}{P_{\text{gbx,tg}}}}, \quad (2.14)$$

and the no-load losses

$$P_{\text{gbx,oc}} = P_{\text{gbx,tf}} \frac{\frac{P_{\text{gbx,oc}}}{P_{\text{gbx,tg}}}}{1 - \frac{P_{\text{gbx,oc}}}{P_{\text{gbx,tg}}}}. \quad (2.15)$$

2.8.2 Tooth Friction Losses

The main loss source within gears are the load dependent losses caused by tooth friction for the majority of applications [63, 65]. These losses are generated during the gear meshing under load [64], particularly by sliding and rolling friction [63] on the surface of the tooth flanks and increase with [67]: (i) oil viscosity (minor increase if oil viscosity decreases), (ii) load (proportionally), (iii) circumferential speed (less than proportionally).

According to Coulomb's law of friction the loss (friction) power is the product of the normal force F_N , sliding speed difference v_s and coefficient of friction $\mu_f(x)$ between two surfaces [67]. The friction losses are defined for one point x on the path of contact as [63]:

$$P_{\text{gbx,tf}}(x) = \mu_f(x) F_N(x) |v_s(x)|. \quad (2.16)$$

For the sake of simplification the coefficient of friction $\mu_f(x)$ may be assumed constant along the path of contact for the calculation of the loss power of transmission [63, 67]. Defining a mean coefficient of friction $\mu_{f,m}$, integrating the losses over the path of contact and dividing by the base pitch (geometrical factor) leads to the simplified description

$$P_{\text{gbx,tf}} = \mu_{f,m} H_v P_{\text{in}}, \quad (2.17)$$

as proposed in [63–65, 67, 71], with the gear loss factor H_v describing geometrical influences and the input power P_{in} .

The mean coefficient of friction $\mu_{f,m}$ unifies a potpourri of influencing factors, parameters and boundary conditions such as the properties of the lubricant (e.g., viscosity), the operating conditions (load and number of revolutions), the temperature and the roughness of the material especially the finish of the tooth flanks, which depends on the manufacturing process [63, 71]. Furthermore the friction state such as dry friction or mixed/boundary friction respective the regime of lubrication, e.g., elastohydrodynamic (EHD) lubrication is also an important factor if computing $\mu_{f,m}$. These influencing factors can be evaluated using test-rig measurement results. The drawback of non-experimental approaches as e.g., discussed in [63] is the high modeling effort. Some parameters of the lubricant (limit shear stress) may only be determined with sufficient accuracy using measurements, a mandatory step during the design phase [63], as the required tests and measurements are valid only for one lubricant.

Durand de Gevigney et al. [64] refers to Winter and Michaelis [77] for the computation of $\mu_{f,m}$. Geiger [63] summarizes the current state of knowledge and refers to Michaelis [78] for a practical approach for computing $\mu_{f,m}$, which refers to the equation published by Leimann [65] who cites Winter and Michaelis [69]:

$$\mu_{f,m} = 0.045 \left(\frac{F_{n,pc}}{w_t} \frac{1}{v_{\Sigma m} \rho_{\text{redC}}} \right)^{0.2} \eta_{\text{mo}}^{-0.05} X_R, \quad (2.18)$$

with the tooth normal force at the pitch circle $F_{n,pc}$, the tooth width w_t in millimeters, the relative mean glide speed at the pitch point $v_{\Sigma m}$, the mean radius of curvature in the pitch point ρ_{redC} in millimeters, the dynamic (operating) viscosity η_{mo} in the meshing point and the surface roughness factor X_R . Heizenroether [68] states that this empirical approach of eq. (2.18) is only valid for spur gears. If using bevel gears he refers to [67] for the calculation of equivalent spur gear data. A further summary of different approaches is given by [70]. Chaugenet et al. clarifies:

The prediction of the friction coefficient is still a challenging task and its value depends on the lubrication regime, on the lubricant, on the surface texture of the mating parts, and on kinematics, etc. . . . In what follows, the Benedict and Kelley formula '[16]' [see [79] in this document - A/N] has been employed in order to be able to deal with multicomponent systems. [71, p. 619]

The following equation of Benedict and Kelley “. . . is recognized as an interesting compromise between accuracy and simplicity . . .” [71, p. 619]:

$$\mu_{f,m} = \log_{10} \left[\frac{291205.8 \cdot 10^{-6}}{\rho v v_{sl} v_{sr}^2 F_{nu}} \right], \quad (2.19)$$

with the sliding velocity v_{sl} , the sum of rolling velocities v_{sr} and the normal tooth load per unit length F_{nu} in decanewtons per meter (daN/m). Eq. (2.19) results in an alternating $\mu_{f,m}$, therefore [71] recommends to average $\mu_{f,m}$ over a mesh period.

Following the discussions of [75] or [63, 65], the gear loss factor might be computed by means of,

$$H_v = \frac{\pi}{\cos(\beta_b)} \left(\frac{1}{z_1} + \frac{1}{z_2} \right) (1 - \varepsilon_\alpha + \varepsilon_1^2 + \varepsilon_2^2), \quad (2.20)$$

with the base circle helix angle β_b , the number of the teeth z , the profile overlap ε_α and the head overlap of pinion ε_1 respective gear ε_2 .

The electric machine (EM) of the eRAD application study, presented in Chapter 4, is connected to a (double) planetary gear. A standard for the calculation for load-dependent gear losses is [61] but without giving details on planetary gears. According to the investigations of Gevigney et al. ([80]), the tooth friction losses can be estimated from the individual (internal and external) gear mesh losses of sun-gear, planet carrier or ring-gear. [80] extends an analytic approach for external gears to internal gears. Internal gear mesh losses are smaller than external gear losses and differences of different tooth forms for common use are small [81].

These analytic expressions, such as discussed in this section, for determination of tooth mesh losses and “. . . the relationships involved are rather complex and not always reliable. They appear to be best suited for comparative evaluation of different gear-tooth forms rather than for calculation absolute values of gear losses.” [81, p. 102]

Concluding this section, reference is made to [82], who gives an overview of the loss generation of planetary gears and the additional (loss generating) sliding interfaces or bearings such as thrust bearings and planet needle bearings, increasing the complexity of loss distribution in the models proposed in this thesis.

2.8.3 (Oil) Churning Losses

If focusing on splash lubrication, the load independent (hydraulic) losses are caused by oil churning and oil trapping. Ventilation is neglected for low speed applications [63]. Oil churning losses are caused as the gears plunge in an oil sump, the lubricant molecules near the gears are accelerated and losses occur [63]. Oil trapping happens during meshing of at least two gears: oil is squeezed out of the gear teeth [63]. These losses are influenced by the lubricant's properties, tooth and housing geometry and operating conditions such as the amount of oil, temperature and rotational speed [63, 75].

Geiger [63] discusses state-of-the-art approaches and corresponding literature such as: (i) exact modeling based on physical equations (fluid mechanics), which is too sophisticated; (ii) CFD simulations for prediction of oil flow and churning losses; and (iii) empirical approaches. The latter come with the drawback of simplification e.g., interaction between multiple gear stages like reduction of the oil level is not considered. "Some models . . . can be found in the literature but they are mostly related to one particular test-rig and can hardly be extrapolated to other gear arrangements." [71, p. 620]

A simple approach is given by [75],

$$P_{\text{gbx,oc}} = \omega \left(\frac{1}{2} \rho \omega^2 A_i r_p^3 \right) \left(\left(\frac{h}{r_p} \right)^{0.45} \left(\frac{V_{\text{oil}}}{d_p} \right)^{0.1} F_r Re^{-0.21} \right). \quad (2.21)$$

with the immersed (or submerged) area A_i , the pitch diameter $d_p = 2r_p$, the oil volume V_{oil} and the Fraude number F_r . This equation shows clearly the dependency of $P_{\text{gbx,oc}}$ on the geometry parameters and the lubricant's properties. A similar approach is presented in [64]:

$$P_{\text{gbx,oc}} = \frac{\rho \omega^3 A_i r_p^3 C_m}{2} \quad (2.22)$$

The dimensionless parameter (dimensionless torque) C_m used in eq. (2.22) depends on the fluid flow around rotating gears [64]. C_m is based on the three fundamental parameters d_p , ρ and ω [71].

[71] discusses the calculation of C_m based on the Pi theorem using six groups of parameters with seven constant coefficients which are adjusted from experimental results and obtains the following equation for lower rotational speeds:

$$C_m = 1.366 \left(\frac{h}{r_p} \right)^{0.45} \left(\frac{V_{\text{oil}}}{d_p^3} \right)^{0.1} F_r^{-0.6} Re^{-0.21}. \quad (2.23)$$

For higher rotational speeds the equation is extended by the influence of the ratio tooth face width w_{tf} and pitch diameter d_p and Re is discarded:

$$C_m = 3.644 \left(\frac{h}{r_p} \right)^{0.1} \left(\frac{V_{oil}}{d_p^3} \right)^{-0.35} F_r^{-0.88} \left(\frac{w_{tf}}{d_p} \right)^{0.85} \quad (2.24)$$

Eqs. (2.22) to (2.24) show the context with eq. (2.21) and the dependency of $P_{gbx,oc}$ on the gear geometry, immersion depth, rotating speed, gear immersed area as well lubricant parameters. The standard ISO/TR 14179-2:2001 ([61]) determines the total hydraulic loss torque of a gear stage as:

$$T_H = C_{sp} C_1 e^{C_2 \left(\frac{v_t}{v_{t0}} \right)}, \quad (2.25)$$

with the factors C_{sp} , C_1 and C_2 taking into account the splash oil, tooth width and immersion depth. v_t is the peripheral speed at the pitch circle and v_{t0} is the reference speed (specified with 10 m/s). The factor C_{sp} is influenced by the immersion depth at stationary oil level, the height of point of contact above the lowest point of the immersing gear and the hydraulic length. Using multi-stage gears the total no-load power loss is the sum of each stage and the power losses are calculated by multiplication of the torque with the angular velocity of each gear wheel ω_i :

$$P_{gbx,oc} = \sum_{i=1}^{stages} T_H \omega_i. \quad (2.26)$$

The equations presented here are used for determining the different losses to identify an appropriate loss distribution inside the gearbox for the eRAD application based on test-rig measurement results. Especially eqs. (2.14) and (2.15) are important ones to split up the different amount of losses. The other equations mentioned here, are used to verify the measured results by proving basic coherences, e.g., the ω^3 proportionality of $P_{gbx,oc}$ in eq. (2.22). The measured speed and torque dependent gearbox losses are implemented as a look-up table.

Regarding the lumped-parameter thermal-network (LPTN) for the eRAD application: As the main focus in this research work is on implementing a thermal model, and whereas the temperature distribution within the adjacent components is not of primary interest, the model of the EM is amended by the losses introduced into the system by the gearbox. Thermal behavior of the gearbox itself is neglected for the LPTN and focus on the losses it introduces into the machine via the thermal paths.

In the FEM thermal model of the eRAD application the computed amount of losses is applied as heat source in the different components of the gearbox.

Chapter 3

Thermal Modeling

This chapter reviews the thermal modeling approaches and computation methods used for this research, i.e., lumped-parameter thermal-network modeling, finite element method computation and computational fluid dynamics. The ideas behind these approaches are shortly summarized. Additionally, the literature relevant for thermal parameter computation in the field of electric machine thermal modeling is reviewed and interpreted with respect to its practicality in the presented context.¹

3.1 Thermal Analysis and Design of Electric Machines

Different thermal modeling approaches, including numerical and analytic lumped-parameter models [83], have been proposed for different applications. [84] proposes computational fluid dynamics (CFD) for detailed analysis of specific heat transport problems related to electric machine (EM) thermal modeling, like e.g., the air gap or optimization of the air flow to improve the cooling [85] of the EM. Finite element method (FEM) and lumped-parameter approaches require the definition of the thermal parameters, which is an elaborate task because of the complex materials and material combinations such as the laminated steel, impregnated wires or wires with dual coating. Approaches for EM thermal analysis in the context of the research work presented are:

1. FEM thermal models are used to compute the temperature distribution within solids (e.g., presented in [86] for magnets and windings). FEM modeling may also be used as a tool for model order reduction, which could be further used as input for real-time thermal observers [87]. FEM loss models are also an input for e.g., lumped-parameter thermal-network (LPTN) approaches (see [88]).
2. CFD is mainly used to compute, e.g., the fluid flow to derive convection coefficients used in FEM or LPTN models.
3. Analytic, e.g., LPTN approaches [86, 89–95], have the advantage to model the temperatures with a resolution depending on the designer's choice and modeling depth

¹Selected results of this chapter have also been published in [6] and [46].

required by the application. For example: the winding temperature may be modeled using one node representing a mean winding temperature, or three (or more) nodes to represent both end winding temperatures and the temperature of the winding in the nodes. Accuracy and computation speed are changing with modeling depth. For the sake of completeness, other analytic approaches are: transfer function based methods (which require identification of parameters, e.g., [96]).

An overview of the thermal analysis methods enumerated here has been given by Boglietti et al. [83]. All of these approaches require the definition of parameters such as contact resistances, material properties, fluid parameters. This is a complex task because of the diversified materials and material combinations, e.g., impregnated wires, laminated steel, press fits with different materials and unknown surface roughness. Furthermore, not only thermal conduction occurs within an EM, but also free and forced convection, as well as radiation and in addition, different types of cooling may be required to be investigated and compared [6]. Therefore FEM and/or CFD in combination with measurement data are typically used to determine selected heat transfer parameters for the thermal models presented.

In the case of LPTNs, compared to numerical methods, the thermal paths need definition, which might be time demanding, but these models come with the advantage of higher computational speed [83].

The thermal parameters of LPTNs are determined by: dimensional information, simulations or empirical correlations [83, 91, 97–99]. Other publications that have been presented discuss the determination of thermal resistance of the air gap [100], the winding [101] or the bearings thermal resistance [99, 102, 103].

3.2 Lumped Parameter Thermal Network Models

3.2.1 Overview

LPTNs, differing in terms of accuracy, parameter determination, and complexity are presented in e.g., [89–94]. Major challenges are: (i) the definition of the model and nodes to take all relevant thermal paths into account; (ii) the computation of parameters (e.g., discussed in [99]), especially with respect to uncertainties caused, e.g., by manufacturing tolerances such as press-fits and the related thermal contact resistance; (iii) the long-term stability and (iv) the modeling accuracy.

Particularly with regard to the topic of *thermal integration*, an LPTN model can easily be extended by additional nodes. This is also beneficial if different cooling approaches are compared. The advantage of lumped parameter approaches is their fast computation speed [104], but their challenge is the definition and computation of parameters of the network [83].

The LPTN model allows determining the temperatures at selected points like: the coolant temperature at the outer perimeter of the machine or the temperature in the center point of the magnets. The exact temperature distributions within certain parts of the machine, such as the magnets, cannot be computed with this approach, which is sometimes acceptable depending on the focus of the model developed.

3.2.2 Approach

Fig. 3.1 shows the example of a solid block with three nodes. [105] emphasizes the overestimation of the LPTN node temperatures using the example of such a solid block. Dajaku [105] computed the temperature profile using an FEM software with constant temperature at the front-end faces (cf. Fig. 3.1, node locations T_1 and T_2). Comparing the LPTN temperature result at the mid-point of the solid block T_m with the FEM results, the temperature is overestimated by 33 % if using the boundary conditions presented in [105]. This is caused by the loss distribution inside the solid block: starting from the center of the solid block, the heat flow through the block increases through the volume. The thermal resistances in Fig. 3.1 are calculated using the block length l_b and the block (end-face) area A_b ,

$$R_{th,1} = R_{th,2} = \frac{l_b}{2k_b A_b}, \quad (3.1)$$

with the thermal conductivity of the solid block k_b .

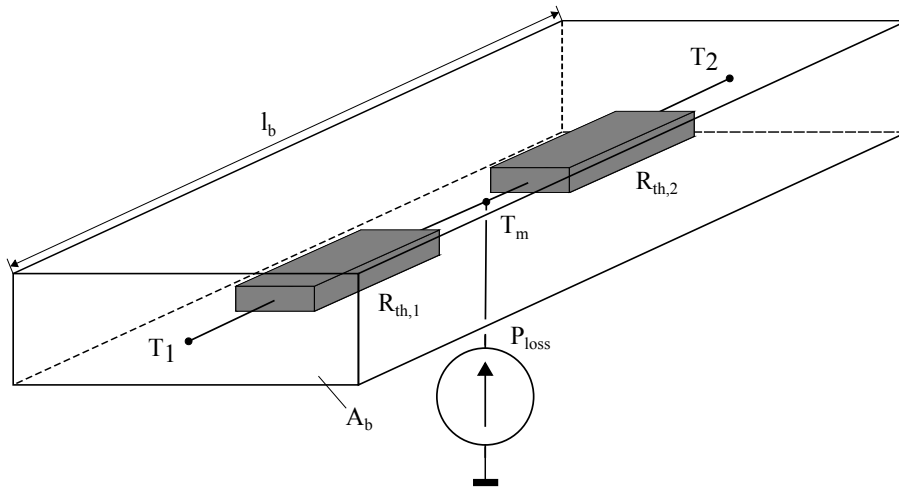


Figure 3.1: LPTN modeling example, solid block.

Mellor, Roberts and Turner [97], give an overview for the computation of typical thermal parameters related to EM geometries. The parameters relevant for the application studies presented are discussed in Section 3.5. As the (general) solid components of an EM are cylindrically shaped (and following the approach presented in [97]), the LPTN models

developed during this work assume that the heat transfers in the radial and axial directions can be treated independently from each other, and hence the associated flow paths can be considered as problems related to one-dimensional heat transfer [6]. Strictly speaking, no circumferential heat flow exists. The temperature at the midpoint of a solid is represented at the nodes, and the losses generated inside the solid body are injected into the corresponding nodes. Furthermore, the thermal capacitances and the loss generation within the different paths are assumed to be uniformly distributed:

This is generally true for stator windings and induction motor rotor bars, where Joulean heat generation occurs due to current flow. In the case of eddy current loss in the PM of a PMSM due to switching harmonics, this is NOT true. The penetration depth of the magnetic field causing the eddy currents can cause the currents to only flow in part of the PM. [106, p. 38]

Holman [107] describes the discretization of a solid: An energy transfer (or change in energy) ΔE into a node of a volume ΔV (or node of an LPTN) results in an increase in internal energy of each node (or element) [107]. As the internal energy of a node no. i may be expressed by the specific heat c and the temperature T , the rate of change with time maybe approximated by [107],

$$\frac{\Delta E}{\Delta \tau} = \rho c \Delta V \frac{T_i^{p+1} - T_i^p}{\Delta \tau}. \quad (3.2)$$

Defining the nodal thermal capacity/capacitance of a volume element ΔV [107],

$$C_i = \rho_i c_i \Delta V_i, \quad (3.3)$$

and with a (supposed) constant thermal capacitance in every node, a linear differential equation can be defined for an LPTN according to [94],

$$C_i \frac{dT_i}{dt} = \frac{1}{R_{thij}} (T_j - T_i) + q_i, \quad (3.4)$$

where q_i is the heat generation and i and j are node numbers.

3.2.3 Implementation

Rewriting these equations as matrices and vectors for the implementation of the model in MATLAB/Simulink², results in [93, 94]:

$$\mathbf{C} \frac{d\mathbf{T}(t)}{dt} = \mathbf{P} - \mathbf{GT}(t), \quad (3.5)$$

²MATLAB Release 2013b, The MathWorks, Inc., Natick, Massachusetts, United States.

with the thermal capacitance vector/matrix \mathbf{C} , the thermal conductivity matrix \mathbf{G} , the vector of loss injections \mathbf{P} and the temperature vector \mathbf{T} :

$$\mathbf{T}(t) = \begin{pmatrix} T_1(t) \\ T_2(t) \\ T_3(t) \\ \vdots \\ T_i(t) \end{pmatrix} \quad (3.6)$$

The thermal conductivities in the matrix \mathbf{G} are series and parallel resistances of equivalent thermal resistances defined by contact resistance, convection and radiation. The contact and/or convection conductance is defined as

$$G_{\text{th}} = 1/R_{\text{th}} = h_{\text{th}} A, \quad (3.7)$$

with surface area A and the effective contact or convection heat transfer coefficient h_{th} .

3.3 The Finite Element Method

FEM as a numerical computational technique for solving physical problems is established and is considered as a state-of-the-art tool in this work. Therefore, a short overview with respect to the FEM software used during the research work is given here.

FEM modeling discretizes a continuous physical problem of an arbitrary continuum. To put it another way: FEM computation finds an approximately solution for a system of partial differential equations with boundary values (boundary value problems). Starting with the first law of thermodynamics, which states the thermal energy conservation, applied to a differential control volume [108],

$$\rho c \left(\frac{\partial T}{\partial t} + \mathbf{v} \nabla T \right) + \nabla \cdot \mathbf{q} = q''', \quad (3.8)$$

with the velocity vector \mathbf{v} for mass transport of heat, the heat flux vector \mathbf{q} , the heat generation rate per unit volume q''' and the differential operator³ ∇ .

The term $\mathbf{v} \nabla T$ considers advection (convection) and is described by the material derivative or material derivative operator [110, 111],

$$\frac{dT}{dt} = \frac{\partial T}{\partial t} + \mathbf{v} \cdot \nabla T \quad (3.9)$$

which is also denoted as advective, convective, substantial or Lagrangian derivative and whereas T may vary with time and position: $T(\mathbf{x}, t)$. To link the heat flux vector with the thermal gradients Fourier's law of heat conduction [107, 108, 112],

$$\mathbf{q} = -\mathbf{k} \nabla T, \quad (3.10)$$

³Note: $\Delta = \nabla^2 = \nabla \cdot \nabla$; e.g., for two dimensions: $\Delta = \frac{\partial^2}{\partial x^2} + \frac{\partial^2}{\partial y^2}$ (see [109]).

is used. The thermal conductivity matrix \mathbf{k} describes the thermal conductivities in the x , y , and z directions respectively [108]:

$$\mathbf{k} = \begin{Bmatrix} k_{xx} & 0 & 0 \\ 0 & k_{yy} & 0 \\ 0 & 0 & k_{zz} \end{Bmatrix}. \quad (3.11)$$

Combining eqs. (3.8) and (3.10) yields

$$\rho c \left(\frac{\partial T}{\partial t} + \mathbf{v} \nabla T \right) = \mathbf{k} \nabla^2 T + q'''. \quad (3.12)$$

For solving the partial differential equation (3.12), three types of boundary conditions are introduced [108, 113]:

- **Dirichlet boundary-condition:** This first-type boundary-condition describes the isothermal case at e.g., a surface with a set temperature,

$$T(\mathbf{x}) = T^0(\mathbf{x}), \quad (3.13)$$

on a boundary of the continuum under consideration (e.g., temperature at a defined surface area of a solid body), where $T^0(\mathbf{x})$ is a temperature function or constant temperature.

- **Neumann boundary-condition,** the second-type of boundary-conditions, defines the heat flux perpendicular to e.g., the surface of a solid body:

$$q(\mathbf{x}) = q^0(\mathbf{x}). \quad (3.14)$$

For example, using Fourier's law and assuming perfect insulation [113], $q^0(\mathbf{x}) = 0$, then the Neumann boundary conditions may be simplified to

$$\frac{\partial T}{\partial \mathbf{n}}(\mathbf{x}, t) = 0, \quad (3.15)$$

with the normal vector \mathbf{n} .

- **Cauchy boundary-condition:** This third boundary condition which is also defined as "[s]pecified convection surfaces acting over surface ..." [108, p. 229], especially in the context of thermal computation may be considered as Newton's law of cooling. Expressed in simplified terms [108]:

$$\mathbf{q} \cdot \mathbf{n} = h_{\text{th,conv}}(T_S - T_B), \quad (3.16)$$

with the temperature of the continuum computed (solid) T_S , the fluid (bulk) temperature T_B and the convective heat transfer coefficient $h_{\text{th,conv}}$. The heat transfer by radiation may also be included using Cauchy boundary-conditions: Pentenrieder [113] suggests including an additional transport coefficient, Nikishkov [114] enumerates the radiation as additional boundary condition using the Stefan-Boltzmann constant σ .

The transition to a weak ([113]) formulation of eq. (3.12) is discussed in e.g., [108, 113, 114]. In summary, it can be stated that: if eqs. (3.10) to (3.16) are combined; a weight function is applied to eq. (3.12), [109] and integrating over the volume of the continuum, solid or element to be computed [108, 109], yields to the weak formulation [109, 113]. The weight function δT is the virtual change in temperature. Again, as the derivation and implementation of the FEM for thermal (transient) problems is topic of specific literature such as, [108, 113, 114]. The already discretized mathematical FEM form is:

$$C\dot{T} + KT = Q, \quad (3.17)$$

Additional topics and approaches in the field of FEM computation such as the mesh generation, application of boundary conditions and the solution process (numerical integration) are discussed in detail in the literature mentioned and might vary with the (commercial) FEM software used for a given problem.

3.4 Computational Fluid Dynamics

CFD is a tool which “... is a widely adopted methodology for solving complex problems in engineering fields[,]” [115, p. 1] such as aerospace, automotive, biological and mechanical engineering. CFD uses a numerical approach to solve or predict mathematical problems in the field of fluid mechanics, e.g., fluid flow behavior, heat transfer or chemical reactions [115]: discretized partial differential equations are solved. In this work, a commercial CFD software tool (*ANSYS® CFX®, Release 15.0*) is used. Already developed (commercial or freeware) CFD software tools coming at the advantage that users “... can initially treat these codes as black boxes and operate them with the main intentions of just practicing ...” [115, p. 1] and for solving the problem of interest.

As in the case of FEM, the CFD computation work flow can be split up into three (main) elements [115]: pre-processing, solving and post-processing. The engineer’s experience is mainly challenged during the pre-processing. Existing CAD models usually require adaption of the geometry to ensure an adequate mesh quality, as with FEM simulation: bolts, screws, holes and unnecessary fillets need to be simplified or removed. Furthermore, exploitation of symmetry or periodicity, which can be considered using boundary conditions, allows to reduce the number of elements required. Pre-processing furthermore includes the meshing process, definition of material properties and boundary conditions. Strictly speaking, pre-processing is the process of transitioning a computational problem from the physical domain into a computational domain.

The so called governing equations [115] of CFD or fluid dynamics are a mathematic formulation of the conservation laws of physics [111, 115]: (i) Newton’s second law (ii), mass conservation, and (iii) energy conservation respectively the first law of thermodynamics. In

the case of CFD, the set of equations describing these laws are denoted as Navier-Stokes equations [111, 115–118]:

$$\frac{\partial}{\partial t}(\rho \mathbf{v}) + \nabla \cdot (\rho \mathbf{v} \otimes \mathbf{v}) = -\nabla p + \nabla \cdot \boldsymbol{\tau} + \rho \mathbf{g}, \quad (3.18)$$

with the (shear) stress tensor $\boldsymbol{\tau}$ and the gravity or acceleration vector \mathbf{g} , is the momentum equation. $\rho \mathbf{g}$ is also denoted as \mathbf{S}_M in [116]. The momentum equation is supplemented by the continuity equation

$$\frac{\rho}{\partial t} + \nabla \cdot (\rho \mathbf{v}) = 0, \quad (3.19)$$

with the velocity vector \mathbf{v} , and describes the mass conservation in a control volume (or continuum). The total energy equation according to [116] is

$$\frac{\partial(\rho h_{\text{tot}})}{\partial t} - \frac{\partial p}{\partial t} + \nabla \cdot (\rho \mathbf{v} h_{\text{tot}}) = \nabla \cdot (k \nabla T) + \nabla \cdot (\mathbf{v} \cdot \boldsymbol{\tau}) + \mathbf{v} \cdot \mathbf{S}_M + S_E, \quad (3.20)$$

with the specific total enthalpy h_{tot} ⁴ and the energy source S_E . Whereas, $\nabla \cdot (\mathbf{v} \cdot \boldsymbol{\tau})$ is the viscous work term (the internal heating by the fluid viscosity) and $\mathbf{v} \cdot \mathbf{S}_M$ is the work caused by external momentum sources [116].

A further important aspect to consider is turbulence, which either more or less always occurs in nature. Turbulence is caused by (small) disturbances, such as surface roughness of a cooling jacket, in the fluid streamlines of a laminar flow and can lead to a randomized (chaotic) motion of the fluid flow [115]. “Turbulent flow is a complicated example of a chaotic dynamical system.” [118, p. 37] The occurrence of the turbulent flow is influenced by the Reynolds number Re , which describes the ratio of the inertia force to the viscous force [115]. Therefore, a low Reynolds number results in a flow which remains laminar as the naturally occurring disturbances are dissipated away [115]. Several models exist and some are implemented in (commercial) CFD software products. Referring to the theory reference guide [116] of the CFD software used in this thesis, most turbulence models are statistical ones. The origin governing equations are amended by averaged and fluctuating quantities resulting in the Reynolds-averaged Navier-Stokes (RANS) equations [116]. The different approaches may further be divided into:

- RANS eddy-viscosity models such as the $k-\epsilon$ model or $k-\omega$ model. These most widely used also called two equation models are a good compromise between numerical effort and computational accuracy [115, 116]. [115] mentions the assumption of isotropic eddy viscosity as a major weakness.
- RANS Reynolds-stress models use the Reynolds stress tensor and the dissipation rate to solve an equation for the transport of Reynolds stresses in the fluid. According to [116], two equation models are often superior to these models.

⁴Note: the formulation of eq. (3.20) in [116] defines h_{tot} as the specific enthalpy ($[h_{\text{tot}}] = \text{J/kg}$).

- Eddy simulation-model approaches such as the large-eddy simulation or detached-eddy simulation are non statistical approaches.

The advantages and disadvantages of the turbulence computation approaches mentioned and some more are discussed e.g., in [116, 119] and [118].

Summarized, the governing equations for CFD are: (i) the law of mass conservation, (ii) the momentum equation, (iii) the energy equations and (iv) the turbulence equations. In CFD these equations are discretized for a given problem. Different discretization methods such as the finite difference method, the FEM, spectral methods, and finite-volume methods are mentioned in literature (e.g., [117, 120]). The CFD software used during the research work, is based on an element-based finite-volume method: the spatial domain computed is discretized using a three dimensional mesh (finite volumes) [116], which is based on the integral form of eq. (3.19) to (3.20) (control volumes [117]). However, as with FEM computation, CFD might be a very complex topic depending on the physical problem to be solved, for details see e.g., [111] and [115–118, 120] as additional literature.

3.5 Determination of Thermal Parameters

3.5.1 Introduction into Thermal Transport Mechanisms

[112] defines the difference between thermodynamics and heat transfer: thermodynamics may be used for determining the amount of energy (heat) required to change the state of a system (first and second law); heat transfer quantifies the rate of heat exchange. Strictly speaking, heat transfer occurs if thermodynamic nonequilibrium occurs.

In practical applications of heat transfer and heat distribution four basic transport modes are relevant [112, 121]:

- *Heat conduction* is diffusion of heat through a stationary medium (solid or stationary fluid) caused by a temperature gradient.
- *Heat convection* is heat transfer from a (wetted) surface of a solid to a fluid even caused by a temperature difference.
- *Thermal radiation* is heat transfer between two surfaces by emission of electromagnetic waves.
- *A phase-change heat transfer* is caused if a liquid-solid or liquid-vapor state transformation of a fluid occurs (boiling or condensation).

For the thermal modeling approaches discussed in this thesis the phase-change heat transfer is not relevant. The following subsections discuss relevant parameters and modeling approaches for the calculation of the thermal resistances of the different bodies, caused by heat convection, heat conduction and thermal radiation, which are necessary for the thermal

computation of EMs. The heat transfer rate q can be written as [112]:

$$q = \frac{\Delta T}{R_{th}}, \quad (3.21)$$

where ΔT is the temperature difference and R_{th} the thermal resistance. The definition of R_{th} might differ depending on the underlying heat transport mode.

3.5.2 Convection

Overview

The characteristic thermal convection resistance R_{th} from a surface area or A to a fluid is defined as [105, 107]:

$$R_{th,conv} = \frac{1}{h_{th,conv}A'}, \quad (3.22)$$

with the mean or characteristic convection heat transfer coefficient $h_{th,conv}$. In EMs both, forced and natural convection occur. However, eq. (3.22) is a simplification describing the heat and mass transfer between a flowing fluid (motion of gas or liquid) and a surface. Detailed description considering, e.g., convection boundary layers, local and average convection coefficients, laminar and turbulent flow to illustrate the underlying physical effects are illustrated by Incropera et al. [112]. Further literature examples are: Holman [107]; the VDI Heat Atlas [122] which is a standard reference book in German-speaking Europe (English version: [123]); and [121].

Housing to Ambient Air or Liquid Cooling Medium

MATERIAL	FLUID PARAMETERS	HEAT TRANSFER COEFFICIENT	SOURCE
Aluminum	Water/glycol (50 %), 6 L/min	5000 W/m ² K	CFD ⁵
Aluminum	Water, 0.6 L/min Wall roughness 0.001 mm	1886 W/m ² K (axial ducts) 1019 W/m ² K (tangential ducts)	[124]
n/s	Water, 0.5 – 3 m/s	2000 – 12000 W/m ² K	[125]

Table 3.1: Computed examples of fluid to housing heat transfer coefficients for different material and fluid parameter combinations.

Combining natural convection and radiation a mean heat transfer of 10 to 14 W/m²K between a surface (area) and ambient air is specified by [126]. [122] gives 2 to 25 W/m²K for natural convection and 25 to 250 W/m²K for forced convection in gases. A more detailed

⁵Source: Magna Powertrain GmbH & Co KG.

description on free convection, which is generated if a body force acts on a fluid/gas and density gradients occur (buoyancy force), is given in [112].

If a liquid cooled housing is used the heat transfer to the coolant depends on parameters such as the fluid velocity, the surface of the channels, the fluid properties and the design of the channels. To avoid hot spots, cooling fluid shortage (still water zones) and fluid local turbulence [124], CFD computations are a possible tool: they may give an accurate estimation of the mean heat transfer coefficient from the surface area to the cooling fluid during the design and development phase of an electric drive system.

The convection coefficient for natural (or free) convection in fluids ranges from 10 to 1000 W/m²K, for forced convection from 50 to 20000 W/m²K [122]. Table 3.1 shows values of computed examples for the mean heat transfer coefficient from a housing to a fluid for different material and fluid conditions.

Air Gap

Depending on the machine type the air gap thermal resistance is more or less complex, e.g., [91] compared induction motors (four poles) from 4 kW up to 55 kW rated power and states that the Reynolds number Re in the air gap is below the critical one, for that power range. This topic is e.g., discussed in [91, 97, 100, 106, 127, 128]. However, most of the literature discussing a mathematical formulation of the air gap thermal resistance is based on the investigations of Taylor [128]. An alternative approach is CFD computation. The following formulation for the computation of the air gap thermal resistance was used:

The thermal resistance in the air gap is defined by a speed dependent forced convection formulation. A common modeling approach to distinguish laminar, vortex and turbulent air flow between two rotating cylinders, such as the air gap in an EM is considered, is the formulation using the Taylor number Ta [128]:

$$Ta = Re \sqrt{\frac{\delta}{r_{r,o}}}, \quad (3.23)$$

as defined in [106] with air gap length δ and rotor outer radius $r_{r,o}$.

$$Re = \frac{\omega \delta r_{r,o}}{\nu(T)} \quad (3.24)$$

An air gap length formulation of the Reynolds number Re [100] is used to calculate Ta for different shaft speeds ω in eq. (3.24). The kinematic viscosity ν has a temperature dependency. Eq. (3.23) is furthermore used to calculate the Nusselt number Nu using the

Prandtl number Pr :

$$Nu = 2 \quad \text{when } Ta < 41, \quad (3.25)$$

$$Nu = 0.212Ta^{0.63}Pr^{0.27} \quad \text{when } 41 < Ta < 100, \quad (3.26)$$

$$Nu = 0.386Ta^{0.5}Pr^{0.27} \quad \text{when } Ta > 100. \quad (3.27)$$

Eq. (3.25) which is used for laminar flow calculation, (3.26) for vortex flow and (3.27) is used for the turbulent case [106], have to be considered for each operating point. The thermal convection coefficient for the air gap is calculated as [100]:

$$h_{th,conv,airgap} = \frac{Nu k_{air}}{2\delta}, \quad (3.28)$$

with thermal conductivity of air k_{air} . The divisor in (3.28) is also denoted as the hydraulic diameter $D_h = 2\delta$ [100].

(Rotating) Surfaces to Air

Inside the EM, forced convection occurs if the machine is rotating, especially in the end cap region, hence all surfaces near the end caps of the rotor such as the end winding surfaces are from interest. It is hard to define a mathematical expression which is valid for most (or most common) machine types and also a wide speed range.

In the [end cap] region, a single film coefficient is used to model the heat transfer to and from all the surfaces in contact with the circulating [end cap] air. Clearly this is a simplification, as separate film coefficients would apply to each of the different surfaces in the path of the cooling air. However, the complex analysis that is required to evaluate a film coefficient for each case cannot be justified, especially when considering the accuracy to which they could be obtained. [97, p. 208]

Following this statement of Mellor, Roberts and Turner in [97], a mean convection coefficient $h_{th,r,a}$ for the forced convection of the surface areas inside the EM in the end cap region was defined, with respect to [129] and [130].

$$h_{th,r,a} = k_2 + k_1v, \quad (3.29)$$

with v as cooling air velocity and the coefficients k_1 and k_2 . Additionally, [130] shows a comparison plot for different (forced) convection heat transfer coefficients approaches depending on the inner air speed between the end windings and end caps. [97] gives $k_1 = 4.495 \text{ Ws/m}^3\text{K}$ and $k_2 = 15.5 \text{ W/m}^2\text{K}$ for small cooling air velocities. [130] gives $k_1 = 6.22 \text{ Ws/m}^3\text{K}$ and $k_2 = 41.4 \text{ W/m}^2\text{K}$. Comparing these values illustrate well how these

factors may differ from machine to machine. [97] uses the mean radius of the end ring fins and the rotor angular velocity to estimate the air speed inside the EM and introduces an additional factor including the fan efficiency. [89] presents (nonlinear) expressions for the end winding, rotor and internal air surfaces to the internal air.

With respect to the two machines used in this research work, no fans or other parts are attached to the rotor which may artificially increase the air speed. For both machine types and thermal modeling approaches used in this thesis, eq. (3.29) was used: the parameters k_1 and k_2 are roughly estimated and fitted with the measurement results.

3.5.3 Conductance

Homogeneous Solid Body Conductance

The thermal conductance is isotropic for homogeneous materials used in EMs. Variation of density, thermal conductance or specific heat capacity due to manufacturing process related differences are excluded here. Examples are: the housing, the cooling jacket, holders/brackets/mountings.

Referring to data sheets and material information available on the Internet⁶ or [131, 132] and specialised literature, e.g., [122, 123], the thermal conductivity and specific heat capacity is in the region of: (i) 160 W/mK and 880 J/kgK for aluminum cast alloys; (ii) 50 W/mK and 450 J/kgK for casted iron; (iii) 50 W/mK and 450 J/kgK for steel; (iv) 160 W/mK and 880 J/kgK for austenitic-ferritic steel. The exact values depends on the casting process used for manufacturing (sand casting, die casting or chill casting), to give an example, AlSi10Mg (EN AC-43000, EN AC-AlSi10Mg(a), DIN: 3.2381) is given with 140 – 170 W/mK thermal conductance in [131].

The thermal conductance of plastic and rubber materials is usually very low, in the region of 0.1 to 0.5 W/mK, e.g., [122] gives: 0.2 W/mK for polycarbonates, 0.25 W/mK for polyurethane and 0.25 W/mK for ethylene propylene diene M-class rubber (EPDM rubber). Compared to iron or aluminum alloys the specific heat capacity is higher, in the range of 900 to 2200 J/kgK.

Core Material

The laminated core material and the windings cannot be regarded as an isotropic material in thermal models, due to the lamination insulation it is regarded as orthotropic thermal material. Depending on the type of steel (e.g., Vacoflux 50, M270-35A) the thermal conductivity is in the region of 25 to 35 W/mK [133, 134]. A further example is given in a presentation of Mellor [135] for a silicon iron lamination stack, with ≈ 22 W/mK in the radial direction

⁶E.g., raffmetal.eu, robertlaminage.ch and dew-stahl.com.

of the core material and 4.9 W/mK in the axial (orthogonal to the surface) direction. [136] presents the (nonlinear) change in thermal conductivity from ≈ 48 to $\approx 25 \text{ W/mK}$, if the amount of silicon and aluminum (Si+Al) is changed for M400-50A from ≈ 0.4 to 3.75% at different temperatures.

The thermal conductivity depends on various parameters such as the amount of materials used (e.g., silicon, aluminum) for the core material, the insulation of the laminations and the pressure of the lamination stack. Reliable data for the thermal conductivity in the radial direction might come from the supplier of the used core material. Considering the already mentioned literature, a good approximation of the thermal conductivity in the axial direction might be 20 to 25 % of the conductivity in the radial direction.

Winding

Compared with the core material, the computation of the orthotropic winding thermal conductivity is more complex and depends on the insulation materials such as the coating of the strands, the insulation between the winding and the stator (slot insulation) and potting materials (e.g., epoxy resin). Also different windings types (concentrated, distributed) and manufacturing technologies have an influence. The computation of an equivalent thermal conductivity to avoid detailed modeling of each strand is topic of various publications and one main issue in thermal modeling. Summarized, in the axial (winding/slot) direction the solid (cylindrical) conductors are dominate the heat transfer process, in the radial direction also the insulation layers needs consideration. [97] assumes that the winding acts as a homogeneous solid with a conductivity of 2.5 times the insulation's conductivity.

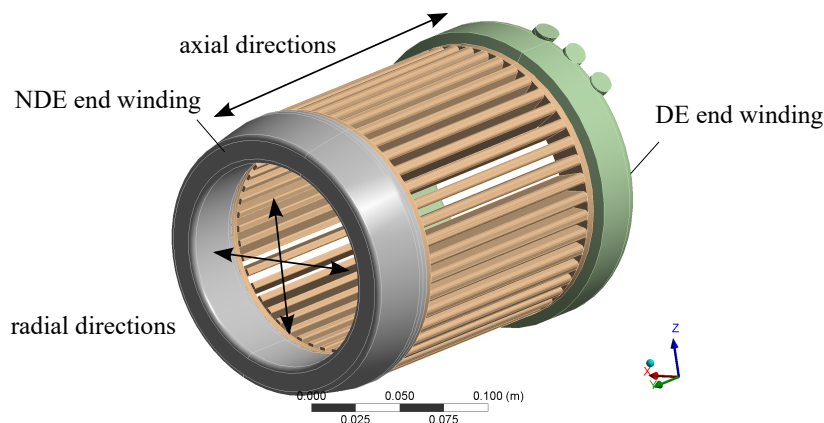


Figure 3.2: electric Rear Axle Drive (eRAD), FEM model, windings.

In this research work the computation of the equivalent thermal conductivity for both applications is mainly based on Simpson, Wrobel and Mellor [101], using the relevant material data sheets. Additionally publications specialized to this topic such as [83, 92, 97, 98, 137–

139], together with general literature (e.g., [107, 112, 122, 123]) was taken into account for crosschecking purposes.

In the FEM software the windings are modeled sectionally to consider the orthogonal thermal conductivity for the slots and end windings at the non-drive end (NDE) and drive end (DE) side respectively. Considering the eRAD application windings in Fig. 3.2: the slots are modeled orthotropic, the end windings are approximated isotropic.

Contact Resistance

An important contact resistance is the stator core to cooling jacket thermal interface resistance, as it is on the main heat flow path within the EM, it needs special consideration [97]. The thermal contact resistance may be simplified using a single thermal contact coefficient $h_{th,contact}$, which is a function of the pressure $p_{contact}$ and the contact surface area [97]. With respect to the example of the stator core to the cooling jacket (or housing/frame) contact, the pressure is defined by press fit dimensions and the roughness of the surface, which depends on the manufacturing process [97].

A representative figure which shows the stator core to frame thermal resistance is published in [97] (Fig. 3.3), which corresponds to [140] who states a range of approximately 500 up to 1000 W/m^2K .

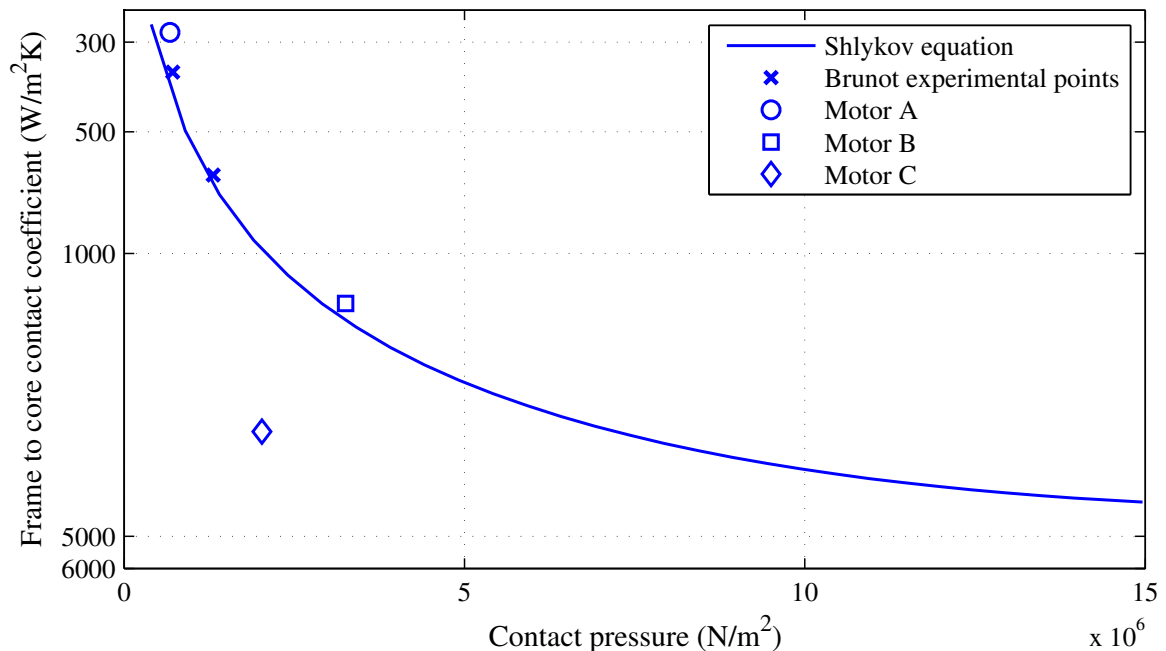


Figure 3.3: Stator core to frame coefficient [97].

An estimation for the pressure between two interference fits gives [141]:

$$p_{\text{contact}} = \frac{\zeta_W E_o}{K}, \quad (3.30)$$

with Youngs's modulus for the outer part E_o , the press fit length ratio ζ_W , and the the press fit calculation factor K . As the combined materials have different temperature depending coefficients of expansion, a coupled FEM simulation is recommended to give a more detailed view on the thermal stress.

Bearings

The computation of a bearing's thermal resistance is from interest for many different engineering fields and applications. Basically, the analytic computation is a complex task as the bearings are a mechanical complex component (from the thermal point of view, [92]): the balls, inner and outer races are in contact only at a few points. A thermal model with reasonable modeling effort which is valid with a defined accuracy over a wide torque and speed range and furthermore lifetime would be desirable. However, considering the scope of the research work, approaches from literature have been used.

Boglietti, Cavagnino and Staton [92] state that a reasonable model is using a thermal interface gap. In [92] also the calibration approach is summarized using test results of induction machines (IMs): a DC supply is used for calibration of the motor thermal model (especially the critical parameters needs consideration), a locked rotor test generates stator and rotor losses and the inner and outer bearing race temperature is measured. The computed equivalent interface gaps are in a range of 0.23 to 0.40 mm.

Knopik [142] splits up the heat transport through the bearings: (i) the shaft to bearing thermal resistance is compared with the stator core to cooling jacket contact resistance; (ii) the thermal resistance of the bearing's outer race to the ambient is also regarded; (iii) the thermal resistance of the bearing is explained as complex as the lubrication and wear condition are from significance. However, a simplified approach is shown which is based on measurements for different hours of operation. The heat transfer coefficients are in a range of $0.2 \cdot 10^{-6}$ to $1 \cdot 10^{-6}$ W/m²K.

Summarizing the results of the EM applications presented in [142], the thermal resistances range from 0.89 to 1.91 K/W.

[143] discusses grease-lubricated ball bearings: the maximum bearing temperature is used for choosing an appropriate grease. Kylander [143] allocates 50 % of the generated bearing losses to the inner and outer race (25 % respectively, regards also the shaft and end shield), and 50 % to the balls (and the cage), whereas the sealing losses are added to the outer race losses. Neglecting the thermal resistance due to the grease filled gap, leads to underestimation of the bearing temperature. Example values in [143] are 0.48 K/W and 0.88 K/W for a 15 kW

and 4 kW EM. Furthermore an equation considering the speed dependency is used in [143], stating that this is an approximation which is valid for bearing dimensions close to the presented ones.

In [103], dry and oil lubricated bearings are compared. The dependency of the conductance on the axial load condition, temperature and speed is shown. To depict one example shown in [103], of a 101-size steel bearing at constant temperature, the thermal resistance ranges from approx. 25 to 33 K/W without lubrication and is ≈ 9 K/W with lubrication but static, and ranges from 6.5 to 11 K/W with lubrication and at a dynamic condition and different axial loads. A further example is given by Isert [102] with 6 to 11 K/W, who compared an analytic expression with measurements.

A standardization for the thermal speed rating for oil bath lubricated rolling bearings including calculation principles is defined in [144].

Summarizing the literature mentioned: determining the bearing's thermal resistance is complex due to the often unknown or changing with manufacturing tolerances influencing conditions such as the axial load condition or thermal data of the grease/oil used for lubrication. For totally-enclosed fan-cooled (TEFC) EMs grease lubricated ball bearings are the most common ones [143]: the integrated starter generator (ISG) application uses grease lubricated bearings, the eRAD application has oil lubricated bearings.

3.5.4 Radiation

Radiation is emission of energy by transport of electromagnetic waves (or photons) [112]. "While the transfer of energy by conduction or convection requires the presence of a material medium, radiation does not. In fact, radiation transfer occurs most efficiently in a vacuum." [112, p. 38]

The upper limit of the power (power per surface area) which might be emitted is defined as [112]

$$E_{\text{rad}} = \sigma T^4, \quad (3.31)$$

with the Stefan-Boltzmann constant σ and the absolute surface temperature (K) T . Eq. (3.31) describes an ideal (black) body, if the emissivity is regarded, the heat flux emitted is reduced by emissivity ε :

$$E_{\text{rad}} = \varepsilon \sigma T^4, \quad (3.32)$$

Relevant for EM thermal simulation is furthermore the heat exchange between two surfaces. If the heat exchange between two (or more) surfaces is regarded also the surface geometries and their orientations need consideration. A detailed explanation introducing a view factor is given for example in [112]. [109] presents a simple example for computation of the energy transfer rate Q shown in Fig. 3.4 which is described by

$$\dot{Q}_{12} = q_{12} = A_1 F_{12} \sigma (T_1^4 - T_2^4), \quad (3.33)$$

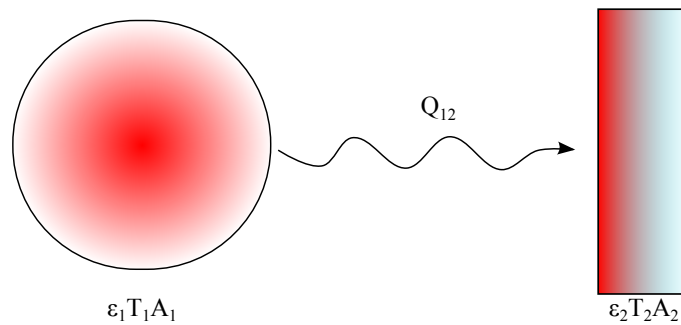


Figure 3.4: Radiation between two surface areas [109].

with the surface temperatures of the two bodies T_1 and T_2 and the surface area A_1 . The transfer factor F_{12} describes the emissivity and geometry of both bodies and is also denoted as view factor, the computation might only be a simple task if only smooth housings (or surface areas) are regarded [92]. If $A_1 \ll A_2$ or $\varepsilon_2 \approx 1$, then eq. (3.33) simplifies to $q_{12} = A_1 \varepsilon_1 \sigma (T_1^4 - T_2^4)$, [109].

Typical emissivities are [145]: 0.09 for commercial sheet aluminum, 0.03 to 0.1 for non-oxidized aluminum, 0.79 to 0.95 for carbon, 0.03 for polished copper, 0.78 for black oxidized copper and 0.74 to 0.89 for oxidized iron.

Summarizing the statements made in the literature with respect to radiation heat transfer and EM thermal modeling: [97] presented an LPTN neglecting the radiation of the internal surfaces. [146] states that heat transfer is mainly caused by conduction as well free and forced convection, radiation from every surface is from lesser extent. [135] remarks that the radiation often is negligible. [147] confirms that radiation has major role to play in EM thermal modeling. [148] showed that radiation is not negligible for low speed TEFC applications, for fan cooled applications the (lower) convection resistance dominates, as both are parallel. An equivalent natural convection resistance between the EM frame and ambient which incorporates both, radiation and convection, is shown in [92]

[149] uses two different thermal models (one incorporates radiation, the other one neglects radiation) which leads to the same statement considering the investigations of [148]: cooling by radiation is significant at zero fan speed, if forced convection occurs the radiation has a minor effect. [148] shows the measurement of housing thermal resistances and argues that the heat exchange by radiation needs consideration of the surrounding environment (emissivity and temperature).

Summarizing: radiation might be negligible, but needs consideration; the thermal models presented are developed without radiation in a first step. Considering a possible hot-spot, which are the windings for both applications: The windings are impregnated, which implies that thermal conduction dominates the thermal path from heat generation to the heat sink

(coolant). The preceding eqs. (3.31) to (3.33) are used to roughly check for eventually occurring thermal radiation, e.g., the end winding to housing radiation might be from interest. Furthermore, as measurement results are used to verify the thermal models experimentally, minor errors caused by neglecting the thermal radiation are corrected by adapting the thermal convection coefficients.

Chapter 4

Application Study I: Electric Rear Axle Drive

In this chapter, the electric rear axle drive application is discussed using a numerical and lumped-parameter thermal-network. Starting with a 21-node network, the development of a real-time (simplified) 4-node model of a gearbox-integrated interior-mounted permanent-magnet synchronous-machine for hybrid electric vehicles is presented. Sensitivity and heat flow path analyses are carried out to identify the most relevant thermal paths, with respect to the gearbox integration. The numerical model developed allows a more detailed analysis of the thermal paths between the gearbox and the electric machine. The change of temperatures caused by the vehicle integration within the electric machine and its consideration in the modeling are investigated. Furthermore, possible approaches to improve the thermal packaging situation are discussed. One solution is introduced and the model implementation of the cooling approach is discussed using measurement results and computational fluid dynamics results.¹

4.1 System Description

For the studies presented in this chapter, an interior-mounted permanent-magnet synchronous-machine (IPMSM) for an electric Rear Axle Drive (eRAD) application is used. The IPMSM with water-jacket cooling and 50 kW peak power, is able to accelerate the vehicle up to vehicle speeds of approx. 120 km/h (\approx 75 mph). Depending on the driver's choice and the operating strategy, the IPMSM: (i) supports the diesel powered vehicle, (ii) propels the vehicle without using the internal combustion engine (ICE) (pure electrically), or (iii) enables all-wheel driving. The IPMSM has a gearbox attached on its drive end (DE), and is mounted on the rear axle of a plug-in hybrid electric vehicle (HEV). The peak torque is 200 Nm during overload operation, up to a shaft speed of 2380 rpm, the maximum speed is 12500 rpm. The inverter controlled IPMSM has v-shaped buried neodymium, iron and boron (NdFeB) magnets². An overview of the IPMSM ratings and data is shown in Tab. 4.1.

¹Selected results of this chapter have also been published in [5, 6, 44] and [46].

²N39UH; material data sheet download available on: www.shinetsu.co.jp; accessed on 2015-02-03.

Operational shaft speed	± 12500 rpm
Maximum shaft speed	± 15000 rpm, (burst speed)
Shaft torque peak	± 200 Nm at ± 0 -2.380 rpm for 20 s at nominal cooling condition
Shaft torque continuous	± 90 Nm von 0-2.150 rpm at nominal cooling condition
Shaft power peak	± 50 kW at 2.380-8.000 rpm for 20 s at nominal cooling condition and min. 270 V (DC); ± 50 kW at 2.380-12.000 rpm for 20 s at nominal cooling condition and min. 300 V (DC)
Shaft power continuous	± 20 kW von 2.150-12.000 rpm at nominal cooling condition
Number of poles	10
Phase current peak	370 A (RMS)
Winding connection	Y (no external center star connection)
Fundamental electrical frequency	0-1.042 kHz
Voltage nominal	257 V (RMS, line-to-line)
Voltage range	176-297 V (RMS, line-to-line), 250-420 V (DC)
Temperature sensor	2xPT100, mounted in the DE end winding
Position sensor	Resolver
Cooling	Water jacket cooling, water:glycol = 50:50 (BASF G48G); coolant inlet temperature nominal 65 °C, coolant flow rate nominal 6 L/min

Table 4.1: eRAD, IPMSM characteristics.

The inverter software disconnects the IPMSM at 15000 rpm (burst speed) to allow for higher vehicle speeds (e.g., at autobahn/highway driving). The disconnect system (DCS), which uses a dog-clutch, is located at the machine's non-drive end (NDE) and is used for disconnecting the electric machine (EM) from one wheel. Because of the double-planetary gear-set (PGS) on the DE, if the clutch is opened then torque transmission is not possible and the EM can be stopped during vehicle propulsion (Fig. 4.1).

The main components in Fig. 4.1 are: the PGS, the resolver, the high-voltage (HV) and low-voltage (LV) wiring for the machine's power supply and measurement system respectively, and the DCS with the actuator and the dog-clutch. Both the PGS and DCS are oil-lubricated, with CASTROL BOT350 M3.

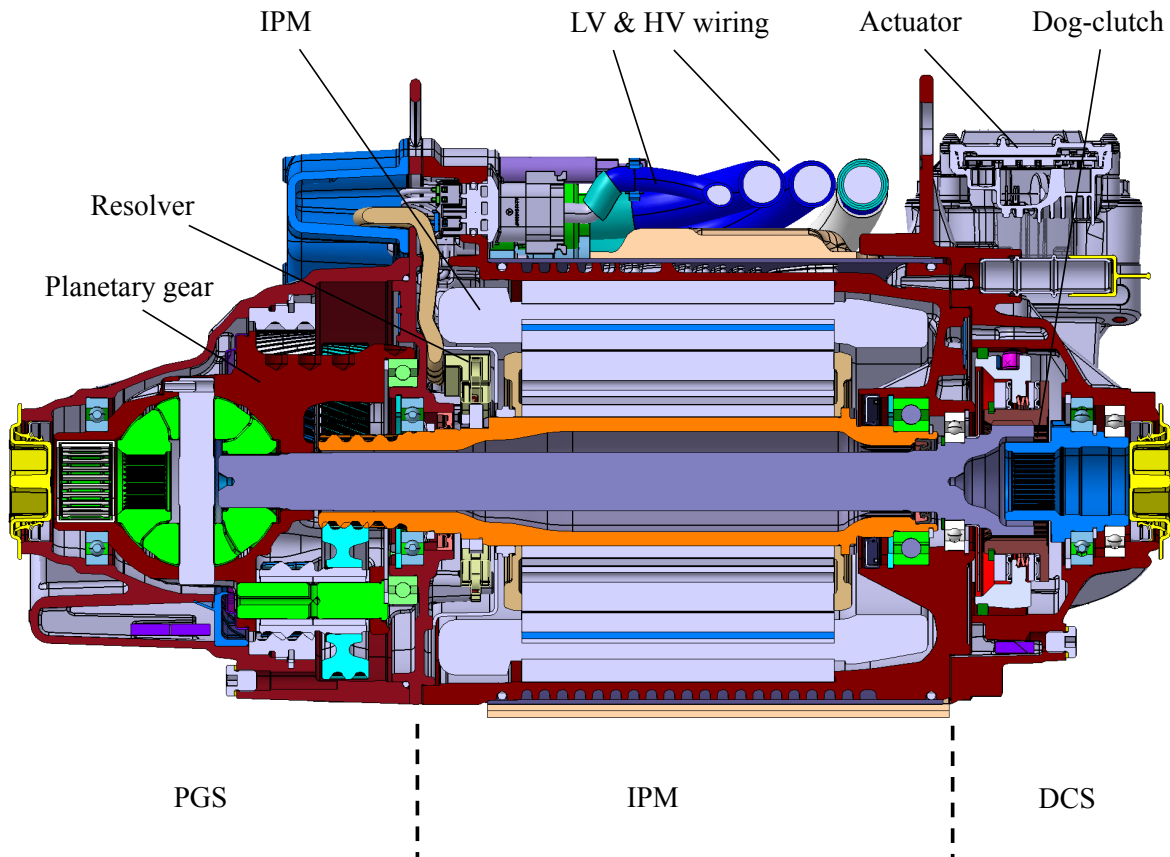


Figure 4.1: Cross-sectional view of the eRAD.

4.2 Model

4.2.1 Loss Model

Fig. 4.2 shows the finite element method (FEM) model for the computation of the core losses. To ensure adequate calculation of the core losses, different (state-of-the-art) computation approaches have been compared to ensure computational quality: an analytic approach (for fast parameters studies) and different FEM approaches were investigated to counter-check the core loss computation results. The FEM computation was also used for the definition of the core loss distribution in the lumped-parameter thermal-network (LPTN) model.

*ANSYS® Maxwell®, Release 15.0*³ was used for the FEM simulations and calculation of the machine parameters L_d , L_q and ψ_{PM} . The different core loss computation approaches of the FEM software are compared in Table 4.2.

Table. 4.2: the computation in the frequency domain leads to high losses, at higher frequencies. However, the computation of iron losses relies on material data, usually measured by

³See [42] for details.

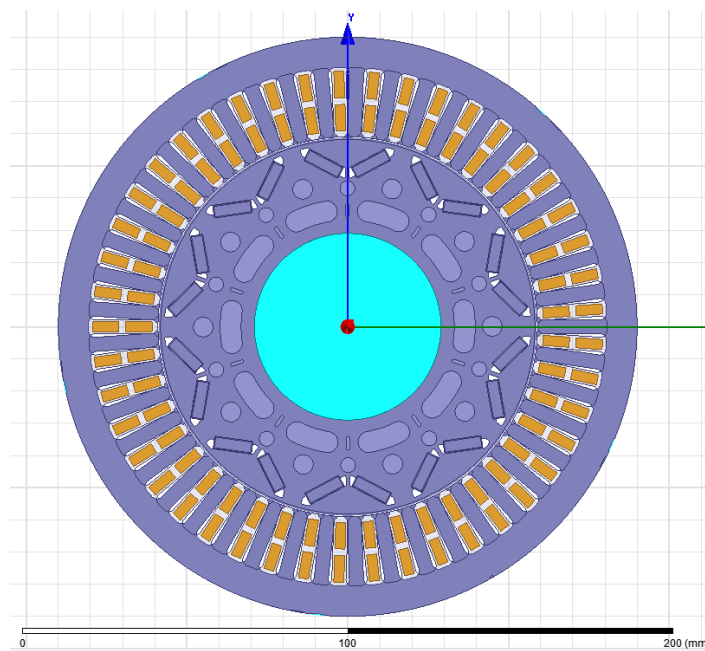


Figure 4.2: eRAD, FEM loss model.

OPERATING POINTS	LOSSES	DOMAIN		
		TIME	FREQUENCY, CONSTANT COEFFICIENTS	FREQUENCY, VARIABLE COEFFICIENTS
250 rpm, 200 Nm	Total (W)	31.7	37.0	22.4
	Hysteresis (W)	29.9	35.2	18.5
	Eddy (W)	1.8	1.8	3.9
2000 rpm, 200 Nm	Total(W)	350.4	397.1	344.3
	Hysteresis(W)	235.9	282.4	148.1
	Eddy (W)	114.4	114.7	196.2
4000 rpm, 60 Nm	Total (W)	428.5	432.6	578.1
	Hysteresis (W)	255.6	250.5	131.0
	Eddy (W)	172.8	182.1	447.2
7000 rpm, 60 Nm	Total (W)	748.9	43.6	578.1
	Hysteresis (W)	255.6	250.5	131.0
	Eddy (W)	172.8	182.1	447.2
11000 rpm, 40 Nm	Total (W)	428.5	432.6	578.1
	Hysteresis (W)	255.6	250.4	131.0
	Eddy (W)	172.8	182.1	447.2
11000 rpm, 0 Nm	Total (W)	428.5	432.6	578.1
	Hysteresis (W)	255.6	250.5	131.0
	Eddy (W)	172.8	182.1	447.2

Table 4.2: Core losses computed for selected operating points, comparison of FEM calculation methods.

the lamination sheet material supplier (specific losses at different flux densities and frequencies). As the frequency domain approach uses coefficients computed from such (measured) data sets, extrapolation at higher frequencies is necessary, which could lead to deviations in the results if compared to the time domain or frequency domain approach with constant coefficients.

4.2.2 Lumped Parameter Thermal Network Model

To meet the model requirements: (i) real-time capability: it is necessary to monitor the critical temperatures and the (magnet) temperature in the inverter software without essentially increasing the processor's computational load; (ii) flexibility: the model should be easily adaptable for different eRAD systems (with and/or without or other: PGS, DCS); (iii) simultaneous thermal monitoring of the relevant EM's components. Regarding these requirements, the choice was an LPTN approach.

As with other contexts in which LPTNs are used, the accuracy depends on the discretization level: e.g., [130] shows a sophisticated and a simple LPTN for an induction machine (IM) and states that the accuracy for both models depends upon several parameters for which reliable data is only available to a limited extent. An analytic LPTN with 21 nodes (Fig. 4.3), was defined during the research work, aiming to reflect all thermal paths of the IPMSM itself, following the approach presented in [97]. The temperature at the midpoint of a solid is represented at the nodes, and the losses generated inside the solid body are injected into the corresponding nodes. Following the approaches for LPTN modeling discussed in the literature review (Section 3.2) the following nodes are defined in the model:

- Stator and housing
 - 0: coolant temperature.
 - 1: cooling jacket node.
 - 2: stator yoke.
 - 3: teeth.
 - 4: boundary between stator teeth and air gap.
 - 13: node within frame between equivalent axial and radial section at NDE.
 - 14: node within frame between equivalent axial and radial section at DE.
- Winding
 - 9: winding (in stator slots).
 - 10: end winding at NDE.
 - 11: end winding at DE.

- 19: surface of end winding at NDE.
- 20: surface of end winding at DE.
- Rotor
 - 6: rotor.
 - 7: bearing at NDE.
 - 8: bearing at DE.
 - 12: shaft surface.
 - 17: side surface of rotor at NDE.
 - 18: side surface of rotor at DE.
- Air
 - 5: boundary between air gap and rotor surface.
 - 15: air volume in end winding region at NDE.
 - 16: air volume in end winding region at DE.

A thermal capacitance is assigned to nodes which are representing a thermal mass i.e., C_1 - frame (and mounted parts), C_2 - stator yoke, C_3 - stator teeth, C_6 - rotor, C_7/C_8 - bearings, C_9 - slots, C_{10} - end winding at NDE, C_{11} - end winding at DE, C_{12} - shaft, C_{15} inner air at NDE, C_{16} - inner air at DE. Nodes in the model which are representing e.g., surface temperature have no thermal capacitance as no thermal mass can be assigned to them.

The following loss sources are modeled: P_{sy} - core losses in stator yoke, P_{st} - core losses in stator teeth, $P_{w,sl}$ - winding copper losses in slots, $P_{w,DE}$ - winding copper losses in end winding DE, $P_{w,NDE}$ - winding copper losses in end winding NDE, P_v - ventilation losses, P_r - rotor losses, $P_{f,NDE}$ - losses injected in frame at NDE (seal ring losses), $P_{b,NDE}$ - bearing losses at NDE, $P_{b,DE}$ - bearing losses at DE, $P_{f,DE}$ - losses injected in frame at DE (seal ring losses), $P_{rs,NDE}$ - losses injected in rotor shaft (surface) at NDE, $P_{rs,DE}$ - losses injected in rotor shaft (surface) at DE.

Fig. 4.3 shows the LPTN model developed including the capacitances and the heat sources. Node 0 with the coolant temperature defines the thermal potential; the model is grounded using the coolant temperature information.

The model which is implemented in MATLAB/Simulink⁴, may be summarised mathematically following eqs. (3.5) and (3.6), (see p. 32).

Again, using LPTNs some simplifications, depending on the modeling depth are necessary. For example, in the case presented here the rotor and magnet temperature are concentrated

⁴MATLAB Release 2013b, The MathWorks, Inc., Natick, Massachusetts, United States.

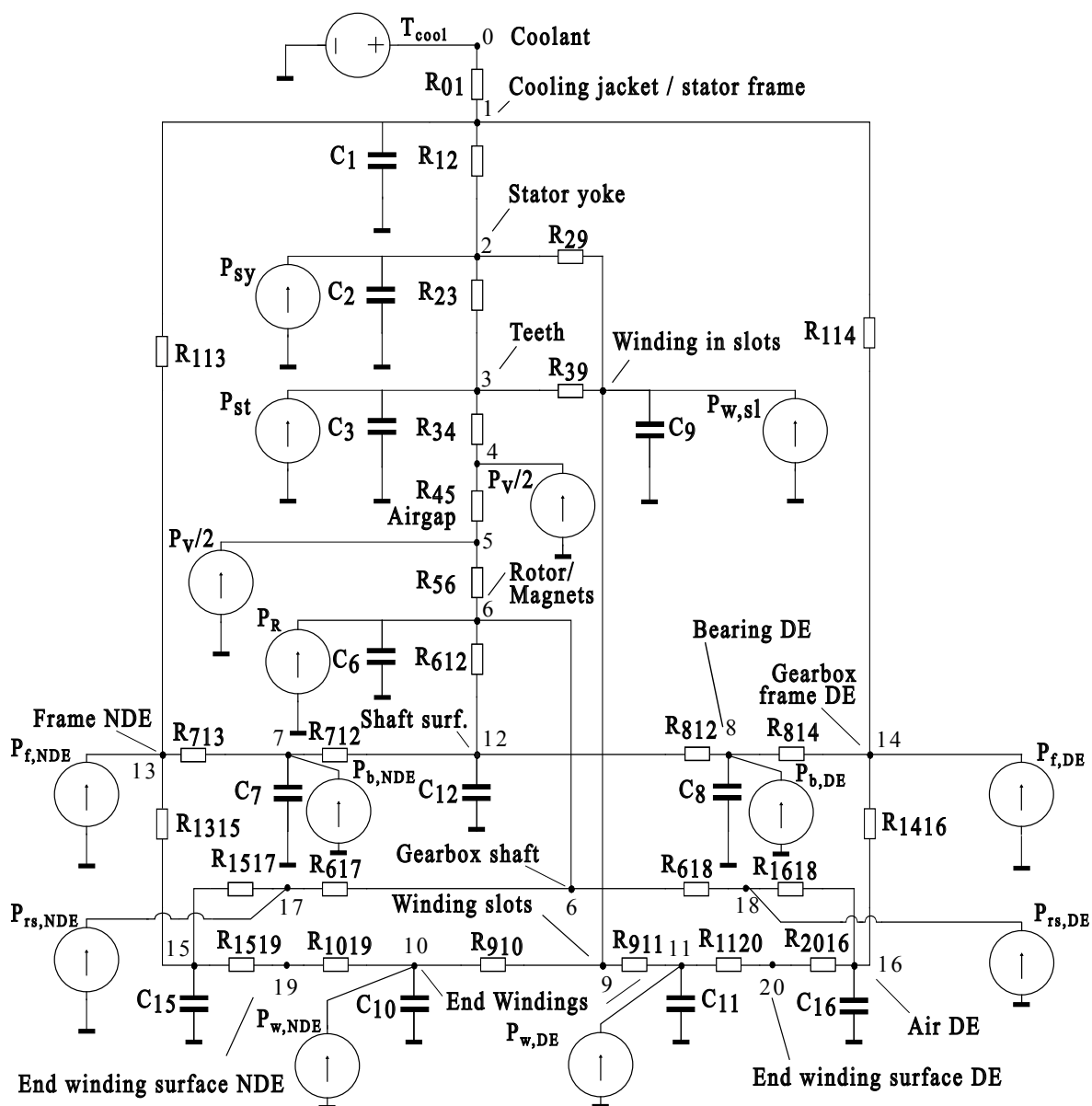


Figure 4.3: LPTN with capacitances and heat sources.

in the same node (no. 6 in Fig. 4.3), but the thermal resistance of the magnets is considered in the relevant thermal resistances in the radial (R_{56}) and axial (R_{618} and R_{617}) directions.

This approach requires the definition of thermal parameters and of thermal paths. This is a complex task because of the diversified materials and material combinations, e.g., impregnated wires, laminated steel, press fits with different materials and unknown surface roughnesses.

The discussion of each thermal path shown in Fig. 4.3 would be off the subject of this thesis. However, to illustrate the approach for the thermal path definition, the stator thermal

resistances from node 0 to 3 are discussed (see also Appendix D.2):

- R_{01} : The heat transfer from the stator jacket (node no. 1) to the coolant (node no. 0) is described by the convective heat transfer coefficient $h_{th,c,j}$:

$$R_{01} = \frac{1}{h_{th,c,j} A_c}, \quad (4.1)$$

with the coolant (fluid) to jacket area A_c . The coefficient $h_{th,c,j}$ is a simplified description comprising a potpourri of parameters such as the coolant (fluid) flow rate, the surface roughness and the shapes of cooling channels, which all influence the fluid flow.

- R_{12} is the thermal resistance between the cooling jacket (node no. 1) and the stator yoke (node no. 2) and comprises: (i) the cooling jacket resistance, which is the cylindrical wall conductive path from the (fluid) surface of the jacket at the cooling channel bottom diameter $d_{j,c,b}$ towards the inner diameter of the jacket (which equals the stator outer diameter $d_{s,o}$), see Fig. 4.4;

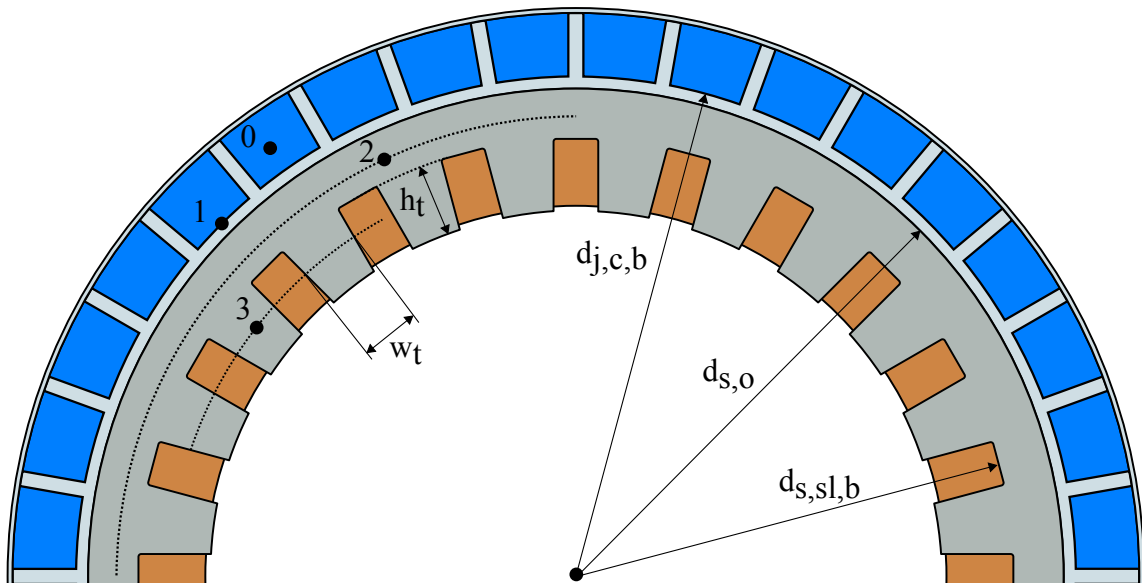


Figure 4.4: eRAD, schematic representation of cross-sectional view with relevant dimensions for computation of R_{12} and R_{23} , and nodes nos. 0-3.

- (ii) the contact resistance between the cooling jacket and the stator stack, which is defined by the contact area and the contact heat transfer coefficient from jacket to stator stack $h_{th,j,s}$; (iii) the yoke conductive resistance is the thermal path from the stator outer diameter $d_{s,o}$ to the stator slot (bottom) diameter $d_{s,sl,b}$. For the computation of R_{12} approximately half of the yoke conductive resistance is relevant (see Fig. 4.4).

$$R_{12} = \frac{\ln \frac{d_{j,c,b}}{d_{s,o}}}{2\pi k_j l_a} + \frac{1}{h_{th,j,s} \pi d_{s,o} l_a} + \frac{1}{2} \cdot \frac{\ln \frac{d_{s,o}}{d_{s,sl,b}}}{2\pi k_{Fe} l_a}, \quad (4.2)$$

with the thermal conductivity of the core material k_{Fe} , the thermal conductivity of the cooling jacket/frame k_j , and the active length l_a .

- R_{23} : Comprises the thermal path from the yoke node to the teeth node, mathematically defined as:

$$R_{23} = \frac{1}{2} \cdot \frac{\ln \frac{d_{s,o}}{d_{s,sl,b}}}{2\pi k_{Fe} l_a} + \frac{1}{2} \cdot \frac{h_t}{N_{sl} k_{Fe} l_a w_t}, \quad (4.3)$$

with the tooth height h_t , the tooth width w_t and the number of slots N_{sl} . As with R_{12} , the half of the yoke and teeth resistance is defined.

4.2.3 Numerical Thermal Model

Electric Machine

The eRAD numerical thermal model was implemented in ANSYS® Academic Research Mechanical and CFD, Release 16.2 (Fig. 4.5).

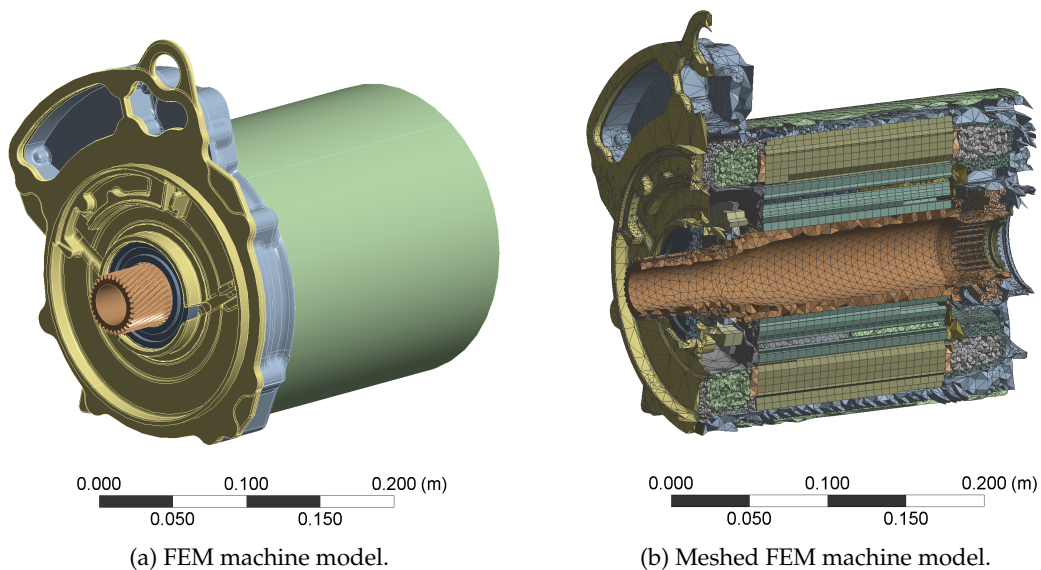


Figure 4.5: eRAD machine model; FEM model screenshots.

FEM meshing requires pre-processing of the model's geometry to ensure an adequate mesh quality with homogeneously distributed elements (to avoid deformation/small angles of the elements): To this aim, very small parts have been removed; surface geometries have been smoothed; very small holes, such as ventilation/degassing drill holes have been removed some screws have been removed or combined with the surrounding material. Adequate boundary conditions were defined with respect and as replacement of such simplifications.

For the validation of the simulation model, the boundary conditions have been adapted to reflect the test-rig conditions for comparison with the measurement results. The ambient temperature and flange boundary conditions have been applied. The flange at the machine's DE was insulated with a 5 mm polyurethane (or similar) material to avoid unknown heat flow during the measurement in the model. Without gearbox the lubrication was ensured using two lubrication tubes, this was also considered in the FEM model using the boundary conditions setup. Fig. 4.6 shows a more detailed model view: the bearings are simplified with I-beam shaped geometry replacements, the end windings and surrounding air are modeled as solid body.

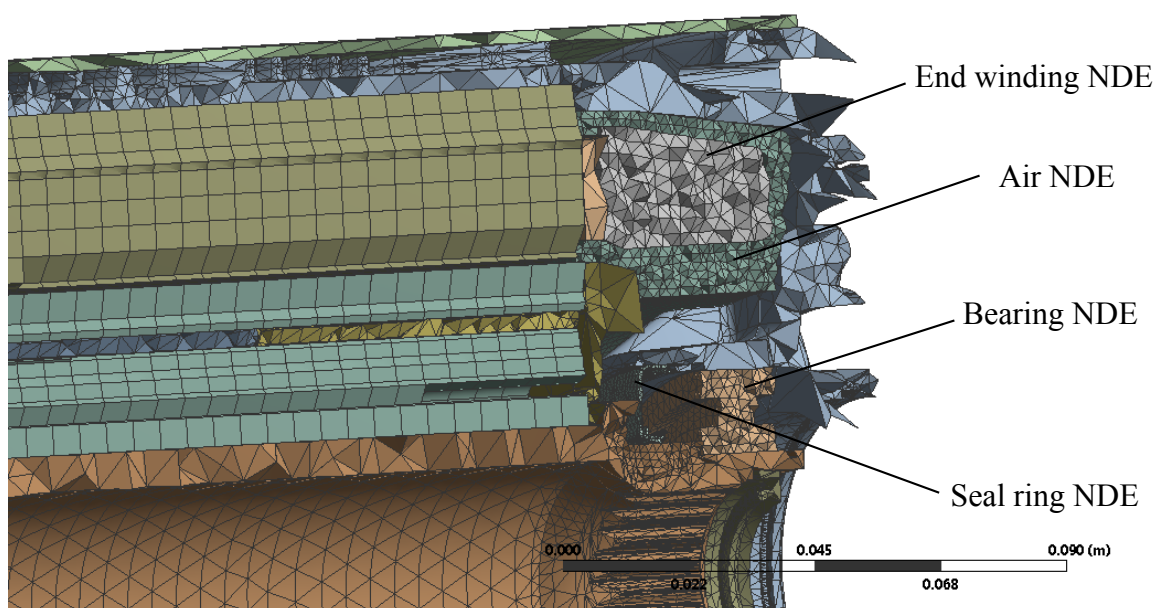


Figure 4.6: eRAD, FEM machine model details at NDE.

Gearbox

Fig. 4.7 shows the geometry of the gearbox FEM model including the housing of the PGS and the inner shaft between the DCS and PGS.

The PGS is a double planetary gear set with a gear ratio of 9.1375. The DCS disconnects one gearbox output, then there is no torque (power) transmission from the EM to the wheels. The oil fill amount is 426 ml for the PGS and 205 ml for the DCS. The oil flow inside the gearbox wasn't modeled. A possible approach for computation of the oil flow which occurs at different speeds may be computational fluid dynamics (CFD), but the prediction of (thermal) multiphase flows is complex due to the multi-scale nature of the involved physical phenomena [150]. One goal of the research work presented, is studying the thermal interaction of

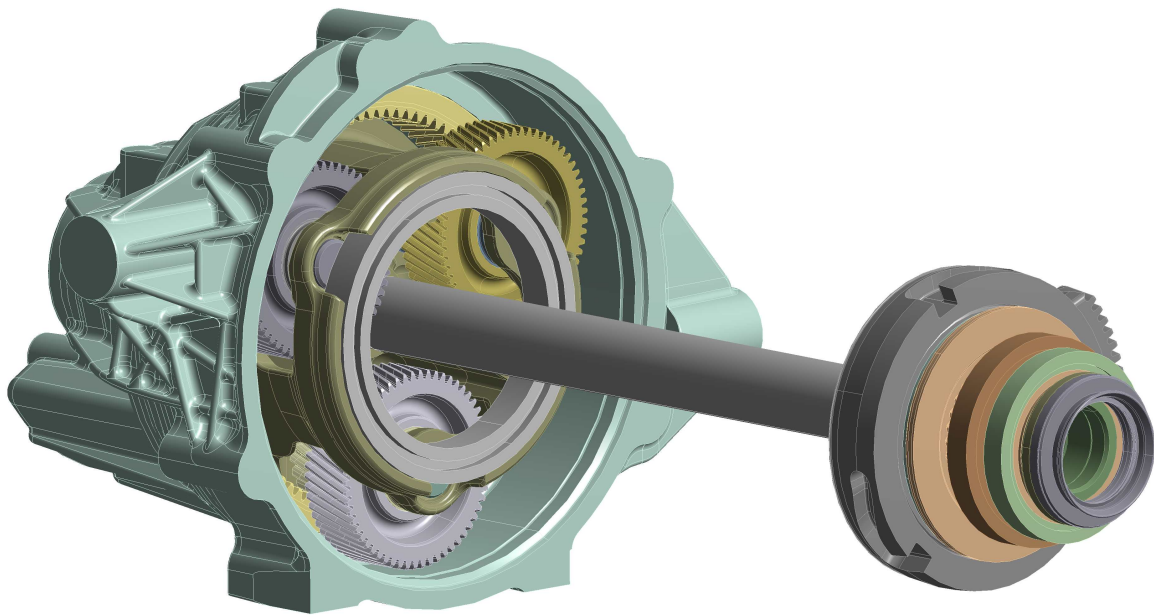


Figure 4.7: eRAD, planetary gear-set and disconnect system, geometry of FEM model.

the gearbox and the EM, therefore a simplified approach was used. A secondary aspect was to limit the computation time. CFD modeling of oil flows inside gearboxes is presented in literature, e.g., [82, 151], but in this work an FEM system simulation is presented: the detailed behavior of lubrication effects, cooling and loss generation inside the gearbox is from minor interest if the focus of the research work is regarded.

If the gear wheels are rotating, the oil is swirled up and small droplets get in contact with gearbox components which are not plunge in the oil sump. This air/oil mixture was simplified to a solid body in the FEM model (see Fig. 4.8), the material parameters are calculated to represent a replacement.

Due to the complex geometry, some simplifications are necessary to gain an appropriate mesh, strictly speaking the entire air/oil volume inside the gearbox housing was not modeled completely. Again, the modeled air/oil volume in the FEM thermal model doesn't represent a physical body: it's an approximation to simulate the air/oil heat transport from the heat generating components, i.e., gears, bearing and sealing rings to the housing and flanges. The physical air and oil volume are scaled to the FEM model's air/oil volume to compute an estimation for the density and specific heat capacity (linear material/liquid mixture). The heat conduction was adapted to fit to the measurements. Furthermore all thermal contacts within the gearbox are assumed to be ideal, which is a further simplification. The thermal parameters implemented in the FEM model are summarized in Section 4.2.4.

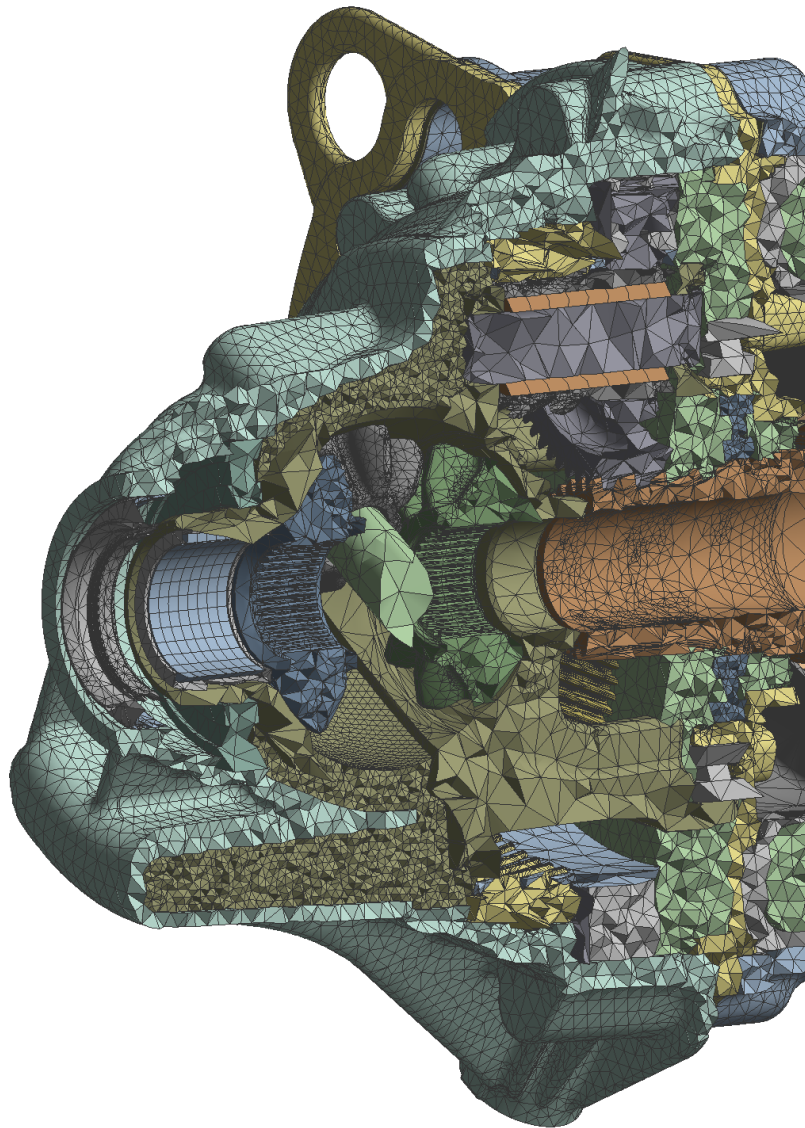


Figure 4.8: Meshed eRAD PGS FEM model.

4.2.4 Thermal Parameters

Approach for Computation and Validation of Thermal Parameters

The thermal parameters are calculated according to approaches reviewed in Section 3.5. The majority of the thermal parameters, especially the thermal conductivities, are defined by the materials used. Many of the thermal conductivities used in the model are based on data from the corresponding suppliers via data sheets, publications or measurement results available. Furthermore some parameters cannot be described directly using data from literature or analytic equations. For these, the parameter setting followed a mixed approach: using the information from the literature review (e.g., [94, 97, 100, 101, 129, 152]) the possible

ranges for these parameters were pre-calculated; the final parameter-set was determined from the test-rig measurement results. Some parameters (e.g., coolant fluid to cooling jacket convection coefficient) are (pre-) calculated using CFD simulation. Without prejudice to the sensitivity analysis discussion later in this chapter, parameters with a high sensitivity to the temperatures are considered. These parameters are difficult to determine and are of critical importance for both approaches, the FEM and the LPTN thermal model. Therefore, modeling related accuracy issues/parameters are shortly listed in this section. Furthermore, all parameters of both, the FEM and LPTN model, for the eRAD application are listed in Appendix D.2.

Winding Equivalent Thermal Conductivity

The winding equivalent thermal conductivity was determined using the approach of Simpson et al. [101]. The equations proposed in [101], which are discussed in Section 3.5.3, result in an equivalent thermal conductivity of the insulation k_a of 0.22 W/mK and a thermal conductivity of the winding replacement material k_{wr} of 0.75 W/mK in this case. In the FEM model the winding is defined using an orthotropic thermal conductivity with 401 W/mK in the winding direction and 0.75 W/mK in the orthogonal directions.

Cooling Jacket to Coolant Heat Transfer

The cooling jacket to coolant heat transfer coefficient was computed using CFD computation results. Fig. 4.9 shows such CFD computation results for 65 °C inlet temperature and 6 L/min coolant fluid flow rate. The heat transfer coefficient was derived by the CFD software's post-processor provided. In the CFD simulation model a heat load corresponding to the losses generated in the EM in the nominal operating point was applied at the inner surface of the cooling jacket.

Cooling Jacket to Stator Stack Contact Resistance

For the cooling jacket to stator stack contact resistance a possible range of 400 to 1200 W/m²K was identified, based on the discussion in Section 3.5.3. This is one of the parameters which can be seen as an adjusting screw for the fine-tuning of the model.

This contact resistance is hard to determine: caused by the manufacturing tolerances this parameter could differ within the range computed here. In fact, this fact could be problematic with regard to series production and the implementation of such an LPTN in an inverter software ready for series production. Furthermore, it is economically not suitable to request a parameter adaption during an end of line (EOL) test in the production. A controlled heat up and cool-down sequence using thermal measurement equipment to fit such critical parameters would be necessary.

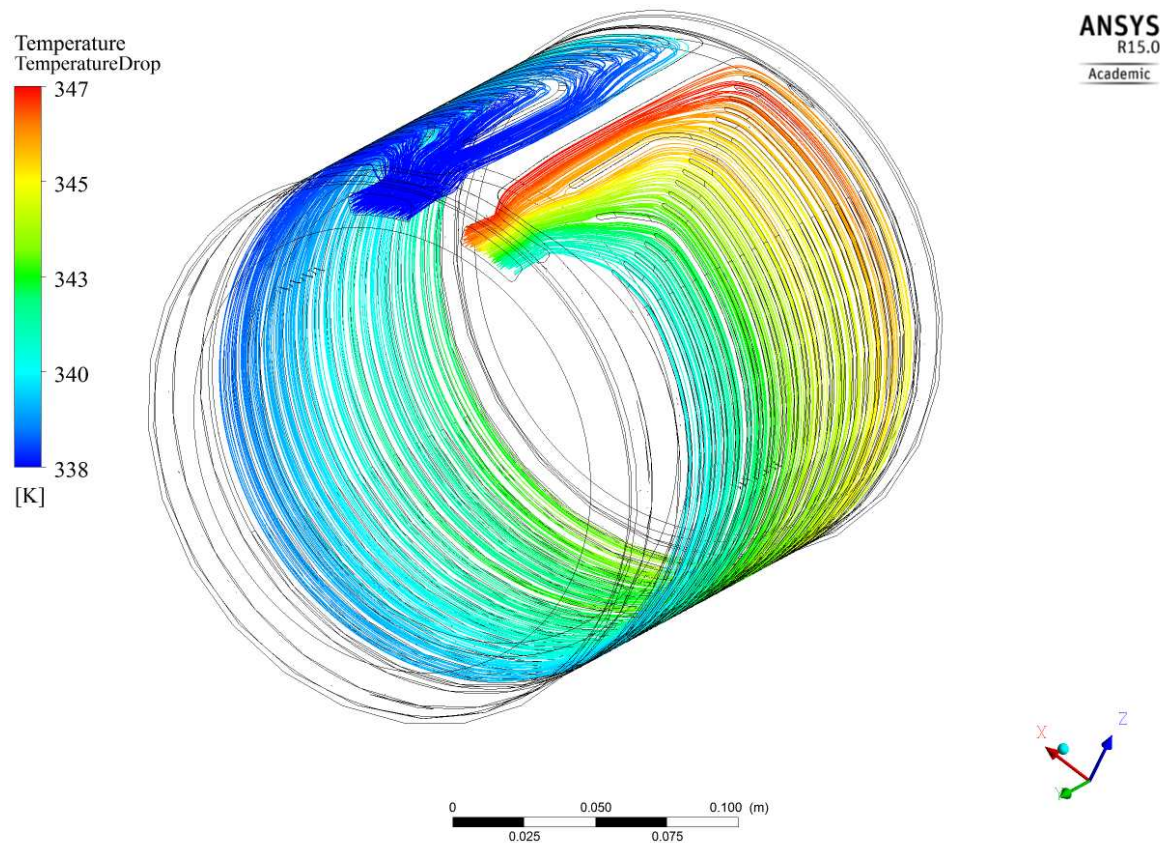


Figure 4.9: eRAD, CFD simulation results; computation of cooling jacket to coolant heat transfer coefficient.

Air Gap

The air gap resistance was calculated using eqs. (3.23) to (3.28) resulting in a speed and temperature dependent look-up table which is implemented in the MATLAB/Simulink model. Comparing the results shown in Fig. 4.10 with a worked example published in [100] for a machine with alike dimensions, the parameter range is plausible. This approach was used for both, the FEM and the LPTN model.

Bearings

The thermal conductance of the ball bearings can hardly be described and differs depending on the axial load and lubrication. According to measurements by [103] the thermal conductance for dry bearings ranges from 0.02 to 0.06 W/K. For oil lubricated bearings: a range of 0.09 to 0.13 W/K was determined in [103], depending on axial load, lubrication temperature and speed. A detailed modeling of the effects in the bearing would go beyond the scope of this research work. Therefore, values from the literature presented, have been used. In

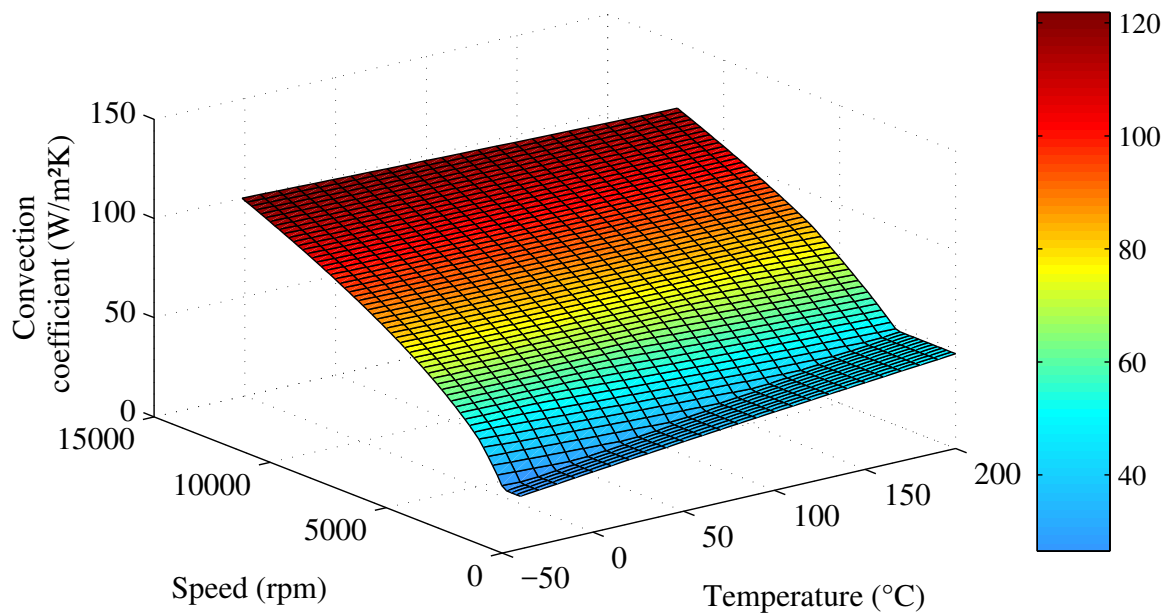


Figure 4.10: eRAD, air gap thermal conductance.

advance of the sensitivity analysis, the influence of the ball bearing thermal resistance on the magnet temperature is limited.

Another influencing factor is the cooling effect of the lubrication. Lubrication of the bearings and the wetting of the surrounding surfaces (shaft surface, seal rings) is a complex interaction of oil flow, material- and heat transport. In the model these effects are simplified using a single factor in the LPTN, see Fig. 4.11. Dirichlet boundary conditions are applied to the corresponding surfaces (shaft, seal ring) in the FEM model.

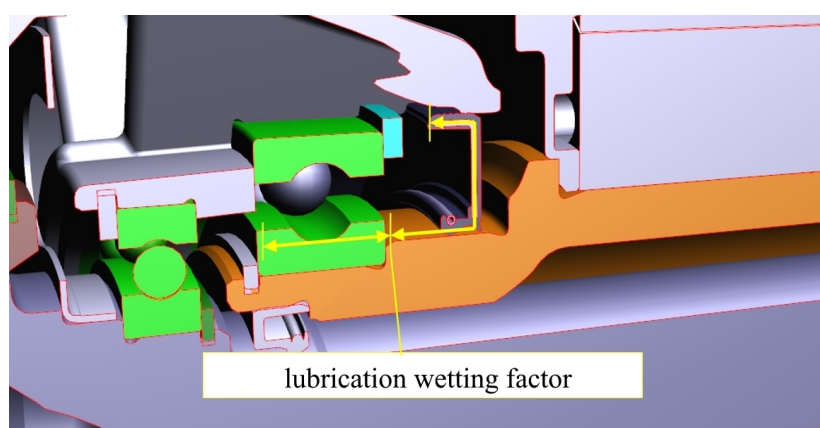


Figure 4.11: eRAD, factor for adapting the cooling effect of the bearing lubricant flow in the LPTN.

Gearbox

The air/oil mixture contact heat transfer coefficient to the housing is given with $200 \text{ W/m}^2\text{K}$ in [61]. Geiger [63] refers to Funck [153] giving a range of $150 - 300 \text{ W/m}^2\text{K}$, and [65] presents an equation with dependency on the circumferential speed of the fastest gear wheel. The function presented in [65] gives heat transfer coefficients up to $100 \text{ W/m}^2\text{K}$, for circumferential speeds of $\approx 22 \text{ m/s}$.

The air/oil mixture to housing heat transfer coefficient was defined with $300 \text{ W/m}^2\text{K}$ in the thermal model. For the gear wheels to the oil/air mixture heat transfer coefficient also $300 \text{ W/m}^2\text{K}$ was assumed as a starting value, and was adjusted for the validation.

The thermal conductivity of the oil/air mixture was computed with 5 W/mK . This is purely based on the thermal measurement results of the gearbox without any further physical interpretation.

Parameters for Model Adjustment and Fine-Tuning

Parameters for adjusting the model, which have a significant influence on fine-tuning of the LPTN temperatures are:

- The ratio of heat flow from the slots (or windings) to the yoke or teeth, defined by the slot wall length. Approximately 70 % of heat flow from the winding in the slots goes into the teeth, 30 % into yoke.
- The effect of the oil cooling, which is based on the lubrication flow. The lubrication flow was defined at the test-rig with 39 mL/s (Castrol BOT 350 M3) for each bearing using oil ducts. If the gearbox is attached the lubrication flow is speed dependent.
- The (wetting) factor for adjusting the amount of oil which cools the side surface of the shaft (Fig. 4.11).
- The loss distribution of winding copper losses, between end windings at DE and NDE side, and the slots.

4.3 Model Validation

4.3.1 Losses

Machine Total and Core Losses

For the validation of the loss calculation, measured results are compared with the computed ones. On the machine test bench several signals such as torque, speed, temperatures (e.g., winding, ambient) and phase currents are monitored in different operating points. The test bench and analysis approaches used, allow a separation of the losses only to a certain extend, the measurements are used to verify the overall model accuracy.

Tab. 4.3 shows the results for selected operating points to illustrate the overall model accuracy in a wide torque and speed range. The proposed analytic approach shows a sufficient agreement with measured data and FEM model results. The differences are caused by the proposed analytic calculation approach of the core losses. Note, also that the difference between the measurement results and the FEM simulation results is smaller. To ensure the accurate computation of the temperatures at the different locations (nodes) considered in the EM thermal model, the loss distribution in the IPMSM must also be considered. The relative distribution of the iron (core) losses within the machine is not discussed in detail at this point, because their accurate consideration is also reflected by the computed temperatures and was cross-checked using the FEM loss model.

POINT OF OPERATION	FEM	MEAS.	ANALYTIC	DIFFERENCE ANALYTIC & MEAS.
250 rpm, 200 Nm	5741 W	5933 W	5706 W	-3.83 %
2000 rpm, 200 Nm	6245 W	6327 W	6073 W	-4.00 %
4000 rpm, 60 Nm	1130 W	1138 W	1167 W	-2.55 %
7000 rpm, 20 Nm	917 W	918 W	906 W	-1.27 %
11000 rpm, 20 Nm	2107 W	2073 W	1916 W	-8.20 %

Table 4.3: Comparison of total losses: data obtained from FEM, loss model and measurement results.

Electric Machine Mechanical Losses

The losses from mechanical loss sources within the machine (i.e., sealing rings, bearings and ventilation/windage) need special consideration as they occur on distributed locations within the machine and affect the loss distribution in both the LPTN and FEM thermal model. These losses are taken from (loss-strip-down) measurements using the test bench (e.g., Fig. 4.12).

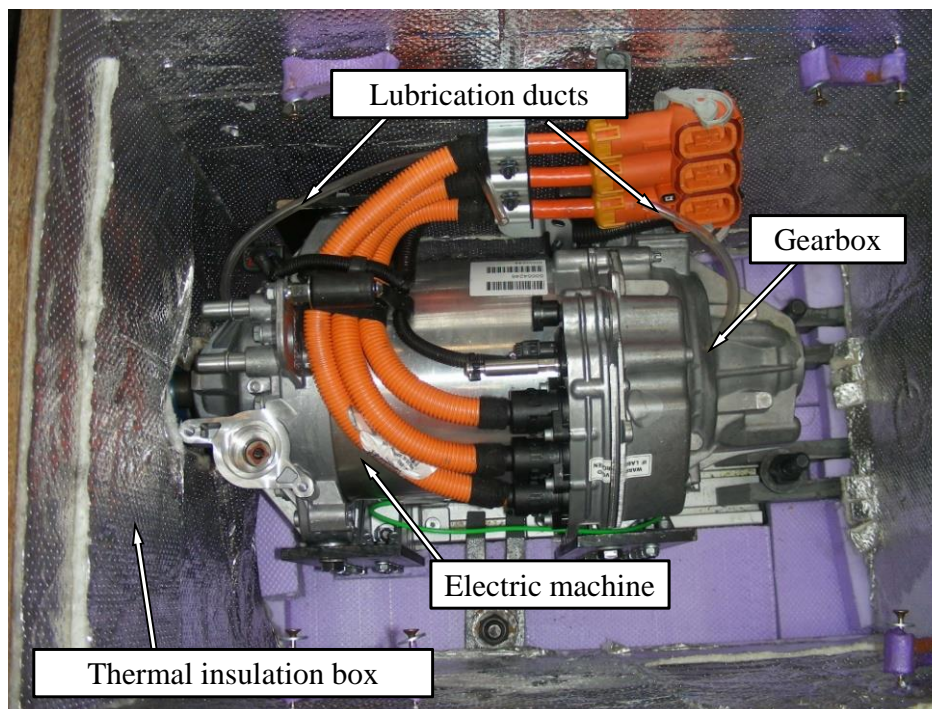


Figure 4.12: eRAD, test-rig with thermal insulation box and lubrication tubes.

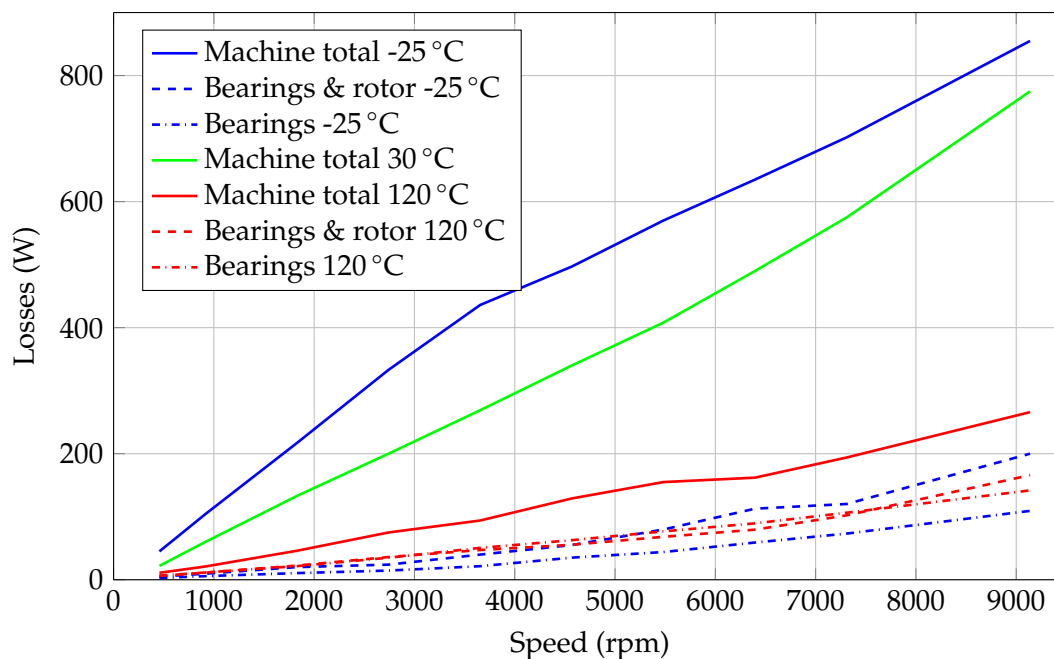


Figure 4.13: Measured EM spin losses as a function of speed and temperature.

The losses are measured with a dummy rotor (to avoid cogging torque) at different temperatures (from $-25\text{ }^{\circ}\text{C}$ up to $120\text{ }^{\circ}\text{C}$). The test program is repeated with the seal rings

removed and with the seal rings and the rotor removed. These results allow a separation of the gearbox, seal rings, windage and bearing losses at the DE and NDE.

The results (Fig. 4.13) clarify the significant influence of the temperature and the contribution of the sealing rings to the machine losses: For example, at -25°C and $48 \frac{\text{km}}{\text{h}}$ vehicle speed (4000 rpm), the sealing rings cause 91 % of the mechanical losses. For higher temperatures the sealing ring losses decrease but the contribution of the bearing losses increases up to 53 %.

Gearbox Losses

The gearbox losses are implemented using measurement results. The loss distribution inside the gearbox is determined using the theoretical background discussed in Section 2.8 and loss-strip-down measurements. Fig. 4.14 shows measured gearbox losses at different speeds and oil-sump temperatures at zero torque transmitted (spin-losses) including: bearing and seal ring losses of PGS and DCS, the tooth meshing of the PGS, the needle bearings of the planets and the oil churning (splash) losses. The figure clarifies the significance of the oil churning

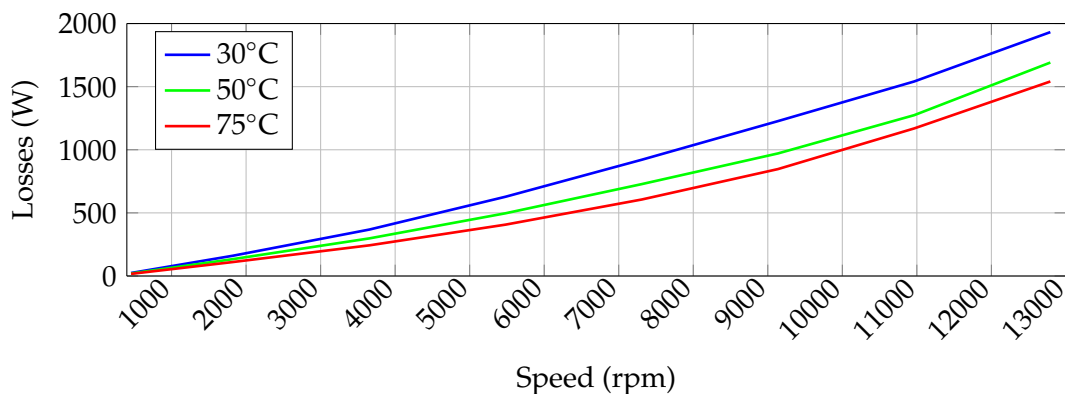


Figure 4.14: Measured gearbox losses for different oil sump temperatures at zero torque.

losses: Comparing the measured values with eqs. (2.21) and (2.22): the dependency on ω^3 is obvious for shaft speeds above 6000 rpm. In fact, the oil churning losses seem to prevail at higher speeds. At lower speeds the losses increase proportional with ω^2 , which equals the formulation of eq. (2.17). To validate this statement, Fig. 4.15 shows the gearbox loss distribution (or proportion of the different losses generated) for different vehicle speeds at 50°C oil sump temperature.

Fig. 4.15 shows clearly that the EM mechanical losses are the relevant ones. However, the sealing rings which separate PGS, DCS and EM are numbered to the EM mechanical losses.

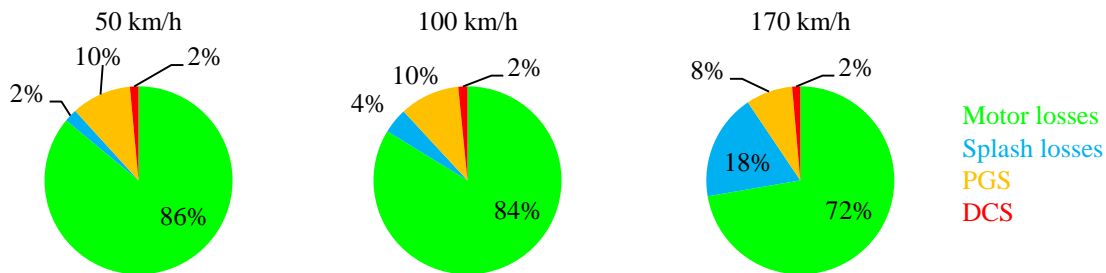


Figure 4.15: eRAD, EM, DCS and PGS spin losses (zero torque) strip-down measurement results at 50 °C oil sump temperature.

4.3.2 Analytic Thermal Model Steady-State Validation

Table 4.4 compares the measured data and the analytic simulation results for four different operating points (steady-state). Relevant points are the DE (node no. 11) and NDE end winding (node no. 10) , the winding temperature in the slots (node no. 9), and the rotor (respectively magnet) temperature (node no. 6). Note that these results already indicate the important role of the end windings both at the NDE and at the DE of the machine; these are the machine hot spots.

	LPTN NODE NO.	1000 rpm, 90 Nm		2150 rpm, 90 Nm	
		MEAS.	MODEL	MEAS.	MODEL
Winding, slot	9	113.9 °C	112.8 °C	117.6 °C	117.7 °C
Winding, NDE	10	118.0 °C	119.6 °C	123.5 °C	124.4 °C
Winding, DE	11	126.6 °C	127.9 °C	132.5 °C	132.9 °C
Coolant outlet		69.7 °C	70.1 °C	70.5 °C	70.2 °C
Rotor	6	71.4 °C	76.1 °C	77.9 °C	79.2 °C
	LPTN NODE NO.	6000 rpm, 32 Nm		12000 rpm, 17 Nm	
		MEAS.	MODEL	MEAS.	MODEL
Winding, slot	9	85.5 °C	84.6 °C	103.7 °C	106.0 °C
Winding, NDE	10	88.6 °C	85.6 °C	111.6 °C	108.5 °C
Winding, DE	11	89.3 °C	87.1 °C	112.4 °C	112.17 °C
Coolant outlet		67.0 °C	66.6 °C	69.6 °C	69.1 °C
Rotor	6	74.8 °C	82.5 °C	88.4 °C	99.8 °C

Table 4.4: eRAD EM LPTN model; steady-state; comparison of measured and computed temperatures at different operating points.

The modeled rotor temperature is higher than the measured one, but within acceptable tolerances, except for 12000 rpm/17 Nm and 6000 rpm/32 Nm in Tab. 4.4: As the bearings

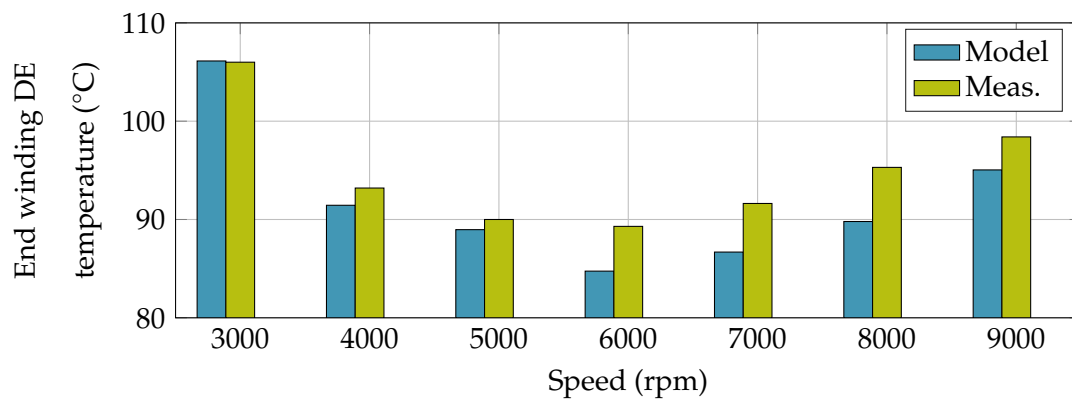


Figure 4.16: eRAD EM LPTN model; steady-state; comparison of measured and computed end winding DE (node no. 11) temperatures at 20 kW.

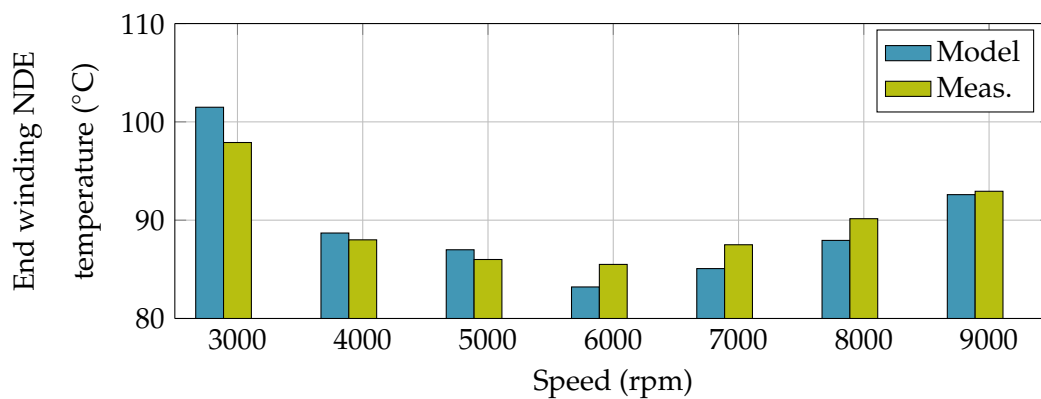


Figure 4.17: eRAD EM LPTN model; steady-state; comparison of measured and computed end winding NDE (node no. 10) temperatures at 20 kW.

are lubricated by the attached gearbox through special oil ducts, the test-rig was set up to ensure a defined lubrication of the bearings with 39 mL/s lube supply for each bearing using lubrication tubes (Fig. 4.12). The temperature of the oil sump was measured. From the change of temperature of oil flowing out of the bearings, a negative heat flow was determined (nodes no. 7 and no. 8 in Fig. 4.3). However, this defined lubrication flow does not correspond to the lubrication situation with the gearbox attached, therefore, this difference between measured and modeled rotor temperature is considered acceptable.

A further test series at 20 kW shaft power and different speeds proved, that the model is within the desired accuracy of ± 5 K with an insignificant overestimation of the rotor temperature, see Figs. 4.16 to 4.19. Here again, the rotor temperature is slightly overestimated but within acceptable tolerances.

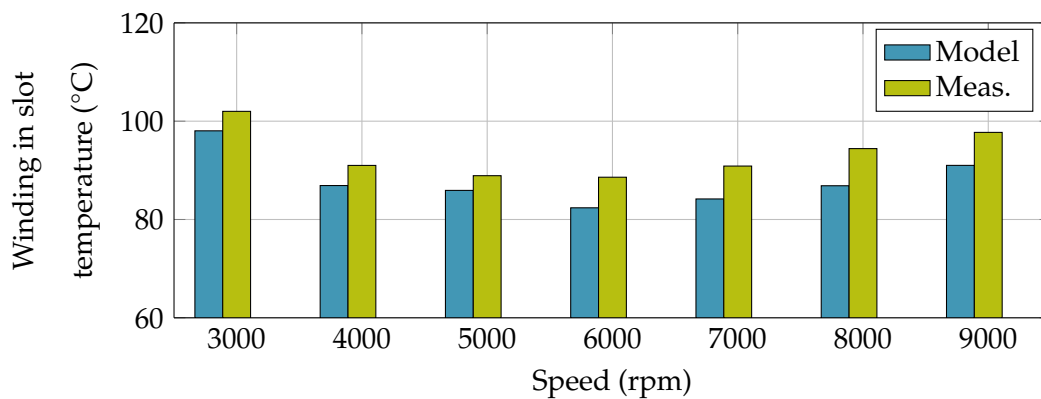


Figure 4.18: eRAD EM LPTN model; steady-state; comparison of measured and computed winding in slot (node no. 9) temperatures at 20 kW.

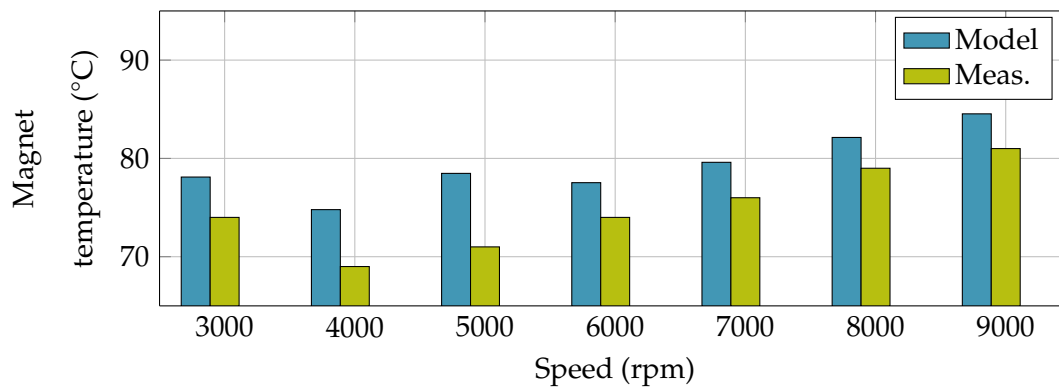


Figure 4.19: eRAD EM LPTN model; steady-state; comparison of measured and computed rotor (node no. 6) temperatures at 20 kW.

4.3.3 Analytic Thermal Model Transient Validation

Figs. 4.20 and 4.21 show the behavior under dynamic operating conditions, to represent the transient validation. The IPMSM was warmed up at 90 Nm and 1000 rpm until the end winding temperatures had reached a steady-state temperature of 120 °C. Then, a 200 Nm peak torque step at 250 rpm (Fig. 4.20) and 2380 rpm (Fig. 4.21) and was applied for 30 s.

Fig. 4.20 compares the temperature computed for the winding in the slots with those two measured by thermocouples (TC). The difference is considered acceptable because of the different measurement locations within the slots: the lumped parameter model only represents a mean temperature for the slot winding temperature.

Fig. 4.21 compares the temperature computed for the end winding at the DE with the one measured with a thermocouple (TC) and two PT100 sensors at different locations within the end winding.

Both step responses indicate a sufficient accuracy of the modeled thermal time constants

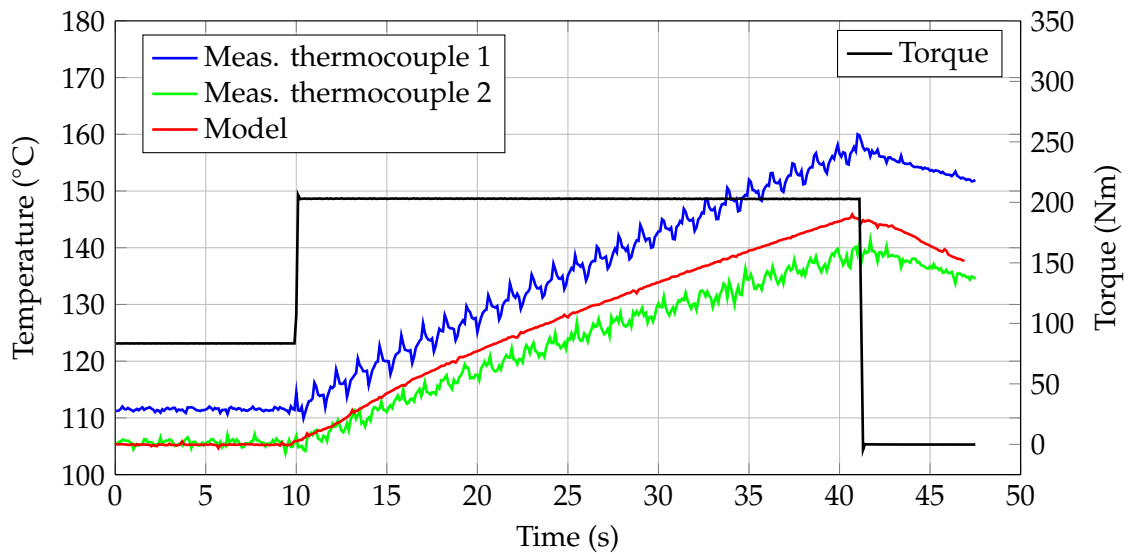


Figure 4.20: eRAD EM LPTN model; thermal transient; winding in slot (node no. 9) temperature, 30 s peak torque step response at 250 rpm.

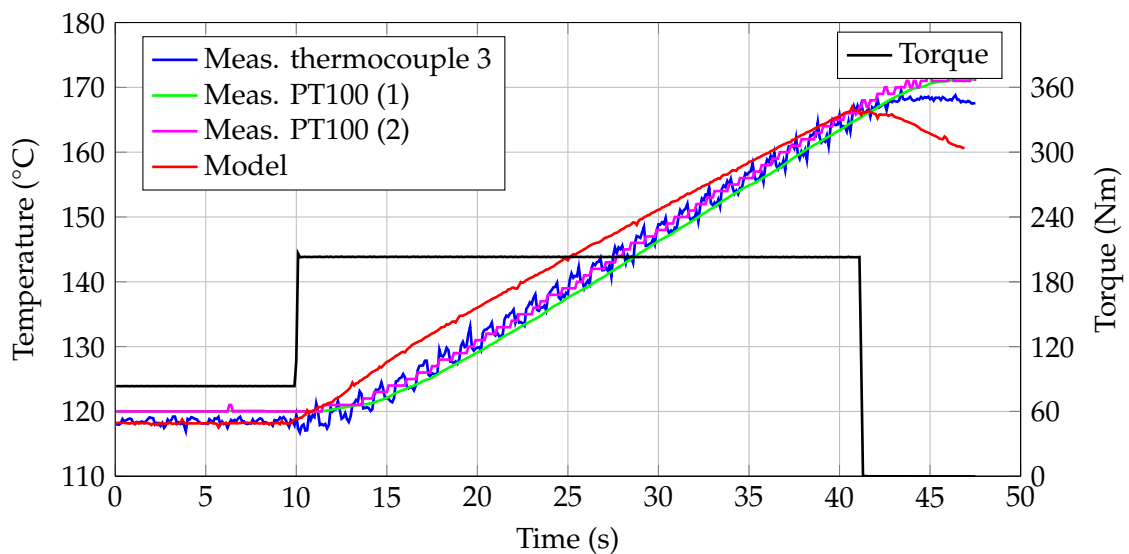


Figure 4.21: eRAD EM LPTN model; thermal transient; end winding DE (node no. 11) side, 30 s peak torque step response at 2380 rpm.

as well as thermal capacitances, as the transient simulations show a satisfying correlation between the computed and the measured values: the simulated values are always in between the measured ones.

To verify the thermal model's long term behavior, a transient run with varying load over an hour was carried out: Fig. 4.22 confirms the model's long-term thermal stability.

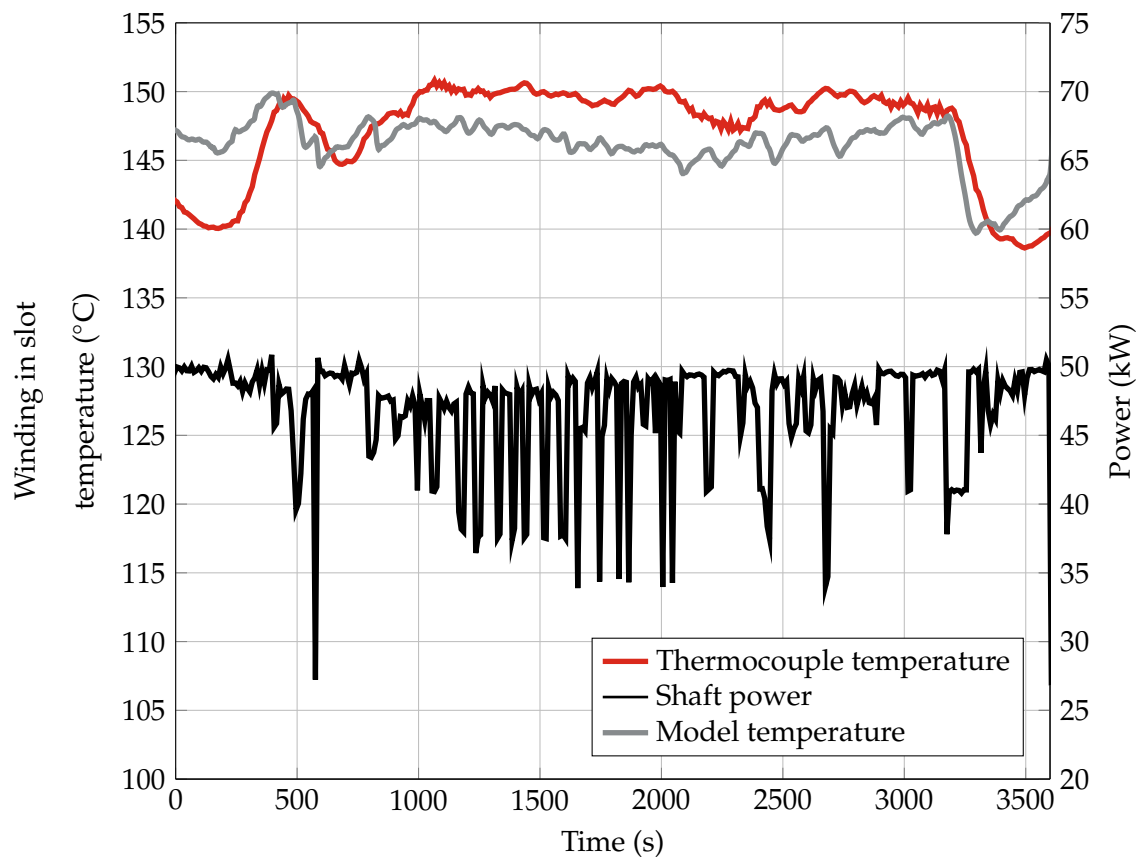


Figure 4.22: eRAD EM LPTN model; long term transient validation of full model.

4.3.4 Numerical Thermal Model Steady-State Validation

To validate the numerical thermal model, the simulation results are compared with measured ones. The test-rig conditions such as ambient temperature, coolant temperature and bearing lubrication, are applied as boundary conditions in the numerical model. Additional parts (e.g., actuator) are removed in the FEM model for the thermal validation.

The ± 5 K computation accuracy goal was reached for all relevant operating points in Tab. 4.5, except for maximum speed operation. The end winding at the non-drive end (EW-NDE) temperature and the winding in slot temperature at the stator stack centre position are underestimated at 12000 rpm. However, the error is within acceptable boundaries for the subsequent studies in this work. The difference between the mean value of the measured rotor temperatures and the mean value of all corresponding computed temperatures is 0.5 K. The same calculation for the winding temperatures results in a deviation of 1.1 K, which is an underestimation of the modeled ones, compared to the measured values.

Fig. 4.23 represents the comparison of the measured TC located between the rotor center and the NDE end and the computed magnet temperatures. The figure indicates the

		SHAFT SPEED (RPM)									
		3k	4k	5k	6k	7k	8k	9k	10k	11k	12k
TEMP. DIFFERENCE (K)	Magnet, DE-central		3.8	0.0	0.6	1.1	1.5	3.1	4.5	5.0	4.4
	Magnet, NDE-central	2.8	-3.3	-5.0	-3.6	-2.7	-2.2	-0.5	-0.1	1.0	0.8
	Magnet, NDE	2.2	-2.4	-3.7	-2.4	-0.8	-0.1	2.1	1.5	3.1	4.6
	Winding slot (center)	-1.4	0.3	1.7	4.8	3.7	4.9	3.9	3.1	4.0	6.0
	EW-DE, TC1	-3.0	-0.7	0.8		3.1	4.8	1.2	1.8	3.1	2.2
	EW-DE, TC2	0.8	0.9	1.1		2.2	3.7	1.4			-0.1
	EW-NDE	-5.0	-2.9			-0.9	-0.4	-2.4	-4.6	-4.3	-6.5
	EW-NDE, PT100	2.5	2.3	2.7	4.8	3.1	3.0	1.7	0.1	1.3	0.0

Table 4.5: eRAD EM numerical thermal model; steady-state validation; computed and measured temperature differences (meas.-sim.) at 20 kW shaft power for different shaft speeds, at various locations in the end winding at the drive end (EW-DE), the end winding at the non-drive end (EW-NDE), the magnets and winding in the slots.

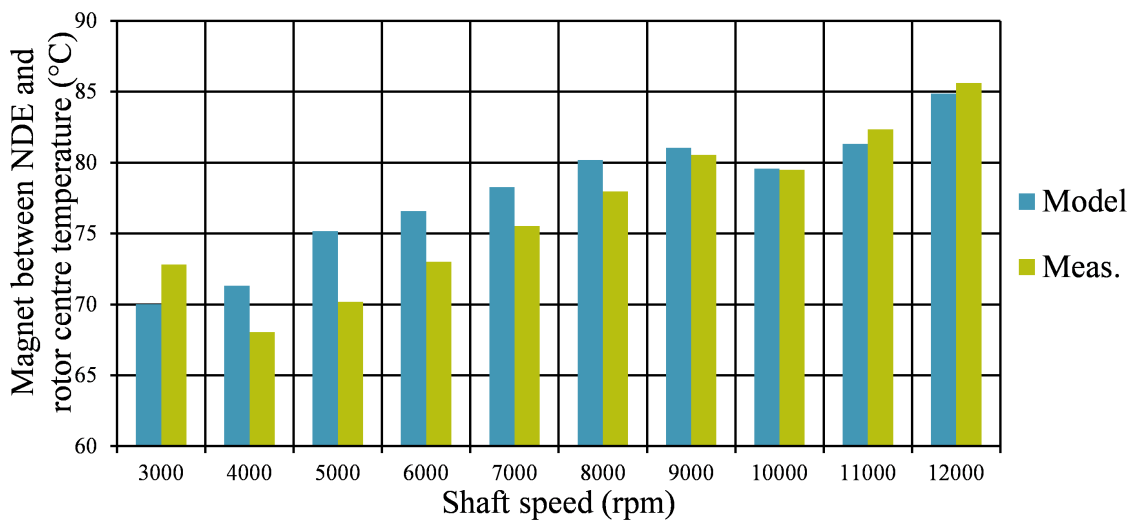


Figure 4.23: eRAD EM numerical thermal model; steady-state validation; computed vs. measured magnet temperatures, between NDE and center position, at 20 kW shaft power for different shaft speeds.

underestimation of the magnet temperatures by the FEM model (but within acceptable tolerances).

Fig. 4.24 shows the comparison of the simulated results with the computed ones for the winding in slot temperature for the same operating points. The sensor was placed in the slot approximately at the stator stack centre position. For the sake of completeness, other figures comparing the corresponding temperature sensor locations presented in Tab. 4.5 are shown in Appendix B.

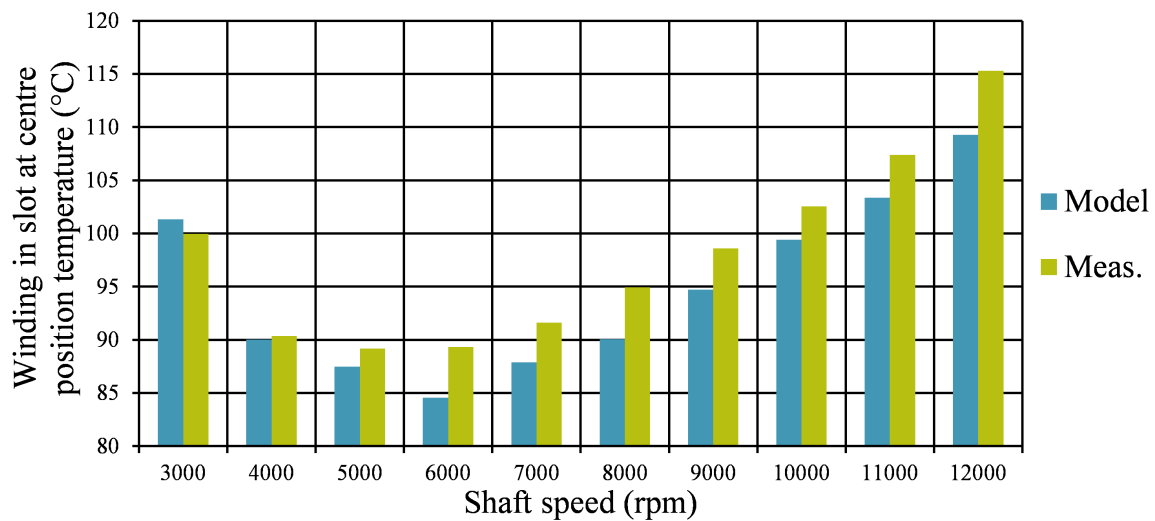


Figure 4.24: eRADEM numerical thermal model; steady-state validation; computed vs. measured winding in slot temperatures at stator stack centre, at 20 kW shaft power for different shaft speeds.

The validation showed that the magnet and rotor temperatures are very sensitive to the thermal resistance between the end plates and the ambient air. Furthermore also the lubricant temperature is an important boundary condition. The air gap resistance has a low significance. To obtain sufficient accuracy for the winding temperatures, only the winding to stator stack thermal resistance was adapted.

4.3.5 Numerical Thermal Model Transient Validation

Electric Machine

The numerical thermal model is validated using the same dynamic operating conditions as used for validation of the transient LPTN model (Section 4.3.3) in Figs. 4.25 to 4.28. Again, the IPMSM was warmed up at 90 Nm and 1000 rpm until 120 °C end winding temperature was reached, then a 200 Nm peak torque step at 250 rpm, 1000 rpm and 2380 rpm was applied. As with the LPTN model, the comparison of the measured temperatures with the computed ones shows sufficient agreement in respect of the goal of this research work.

The thermocouples are mounted (glued) at the components/locations which are measured, e.g., some TC are enveloped by the windings. Due to this mounting of the thermocouples and PT100 temperature sensors an additional thermal resistance was regarded in the FEM simulations.

Additional figures representing transient temperature curves are shown in Appendix C. A cross section view of the FEM thermal model at 2380 rpm and 83 Nm is shown in Fig. 4.29.

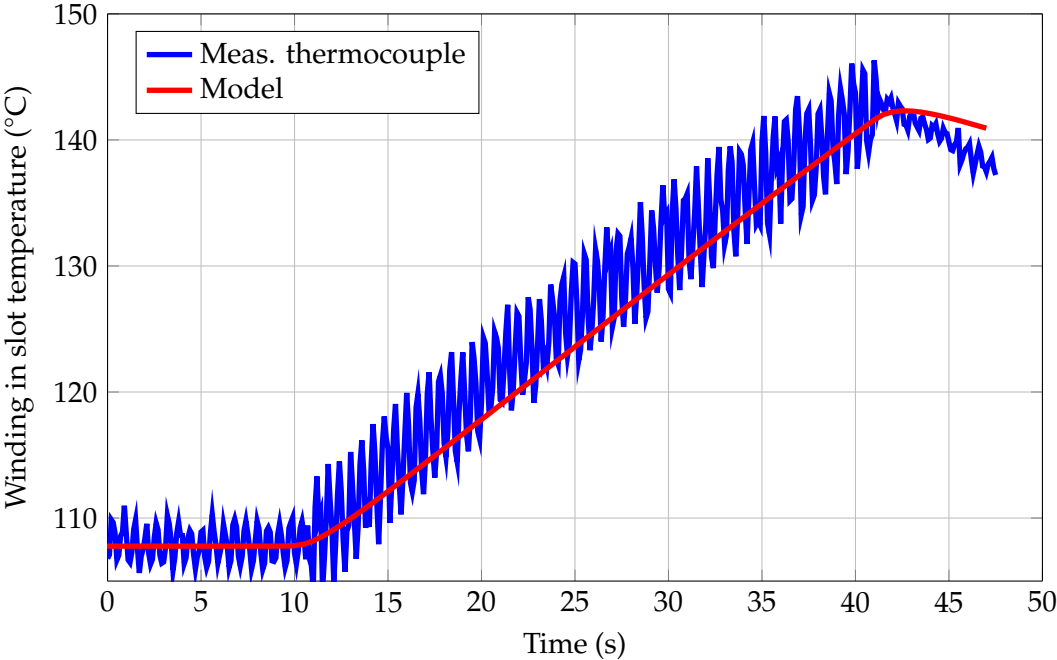


Figure 4.25: eRAD EM FEM model; thermal transient; winding in slot temperature, 30 s peak torque step response at 250 rpm.

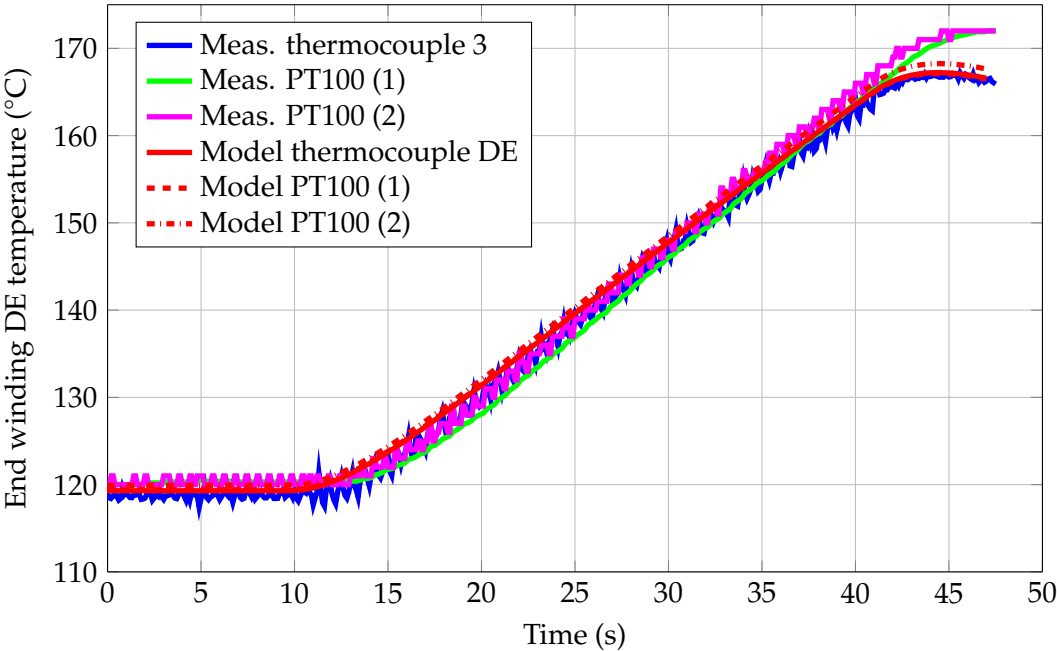


Figure 4.26: eRAD EM FEM model; thermal transient; end winding DE locations, 30 s peak torque step response at 250 rpm.

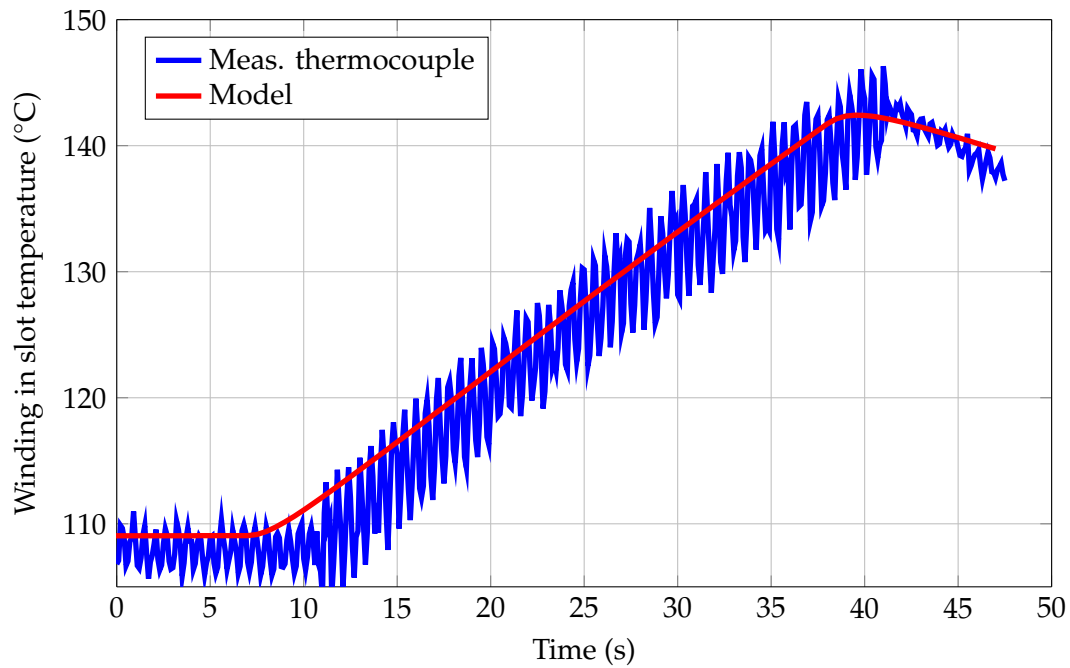


Figure 4.27: eRAD EM FEM model; thermal transient; winding in slot temperature, 30 s peak torque step response at 2380 rpm.

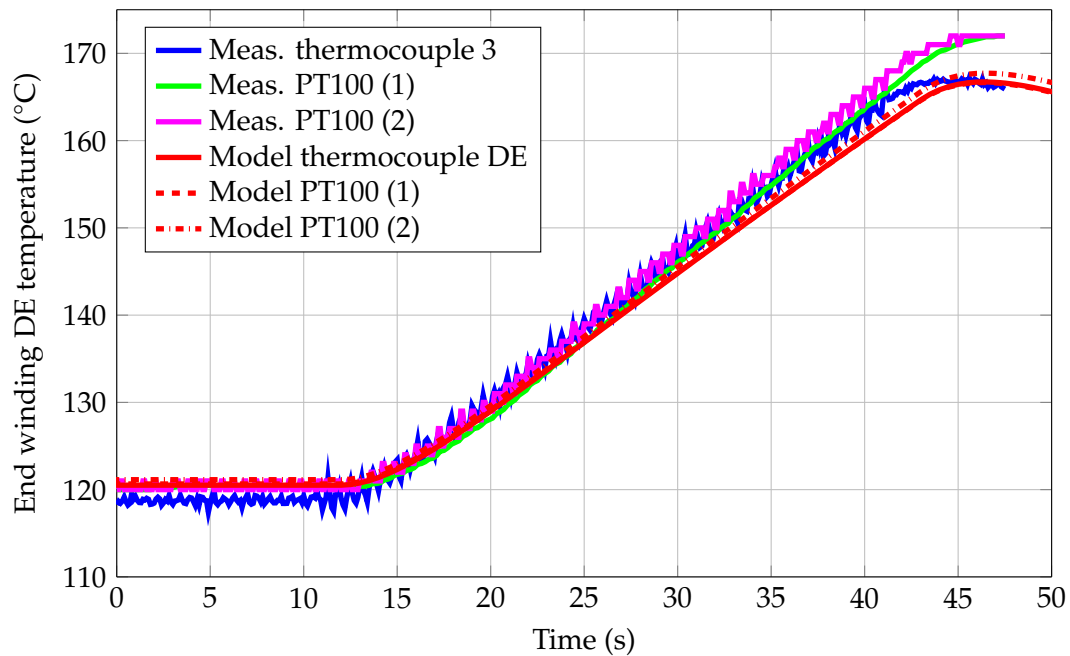


Figure 4.28: eRAD EM FEM model; thermal transient; end winding DE locations, 30 s peak torque step response at 2380 rpm.

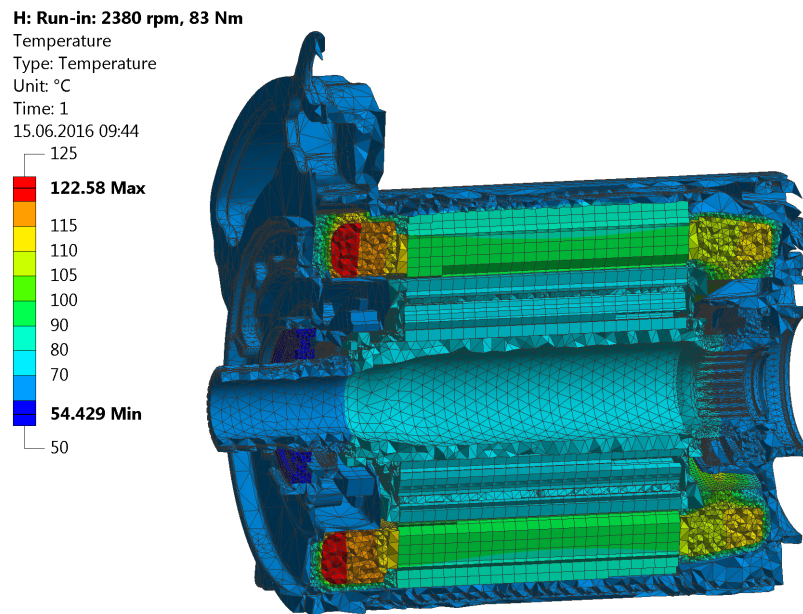


Figure 4.29: eRAD EM numerical thermal model; transient validation, run in at 2380 rpm, 83 Nm; FEM temperature plot.

Gearbox

Fig. 4.30 represents a transient warm-up condition at 12000 rpm. The complete system was measured on the test-rig (PGS, DCS and EM/IPMSM), the liquid cooling circuit was connected but no pump was activated during this measurement, aiming to reach higher temperatures. As the duration of the transient measurements was long enough to reach thermal equilibrium, the transient validation also represents the steady-state validation. The replacement thermal conductivity was defined with 5 W/mK, based on the measurement results.

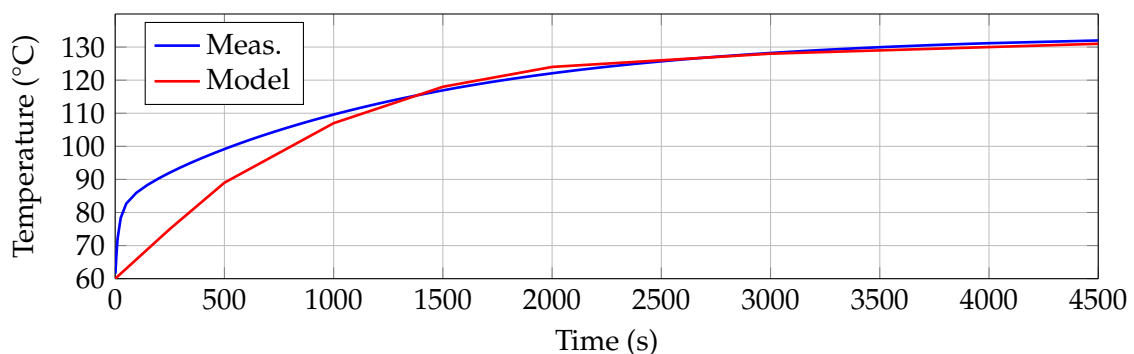


Figure 4.30: eRAD PGS FEM model; transient; comparison of measured and computed oil sump temperature at 12000 rpm and w/o cooling.

The validation of the gearbox shows sufficient accuracy. A possible improvement of the FEM thermal model might be reached if additional measurement locations are used to measure the oil temperature distribution inside the PGS and DCS units. However, for the validation of the simplified FEM approach, which regards the oil/air mixture as a solid body, the measurement results available are satisfactorily to estimate the thermal parameters.

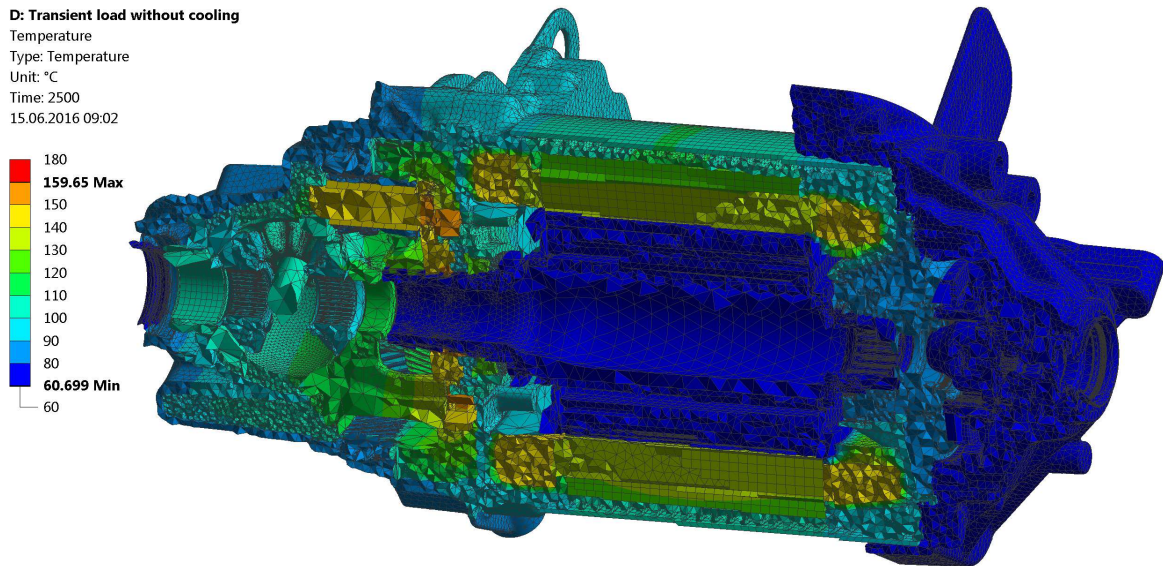


Figure 4.31: eRAD numerical thermal model; gearbox transient validation; temperature at 12000 rpm after 2500 s.

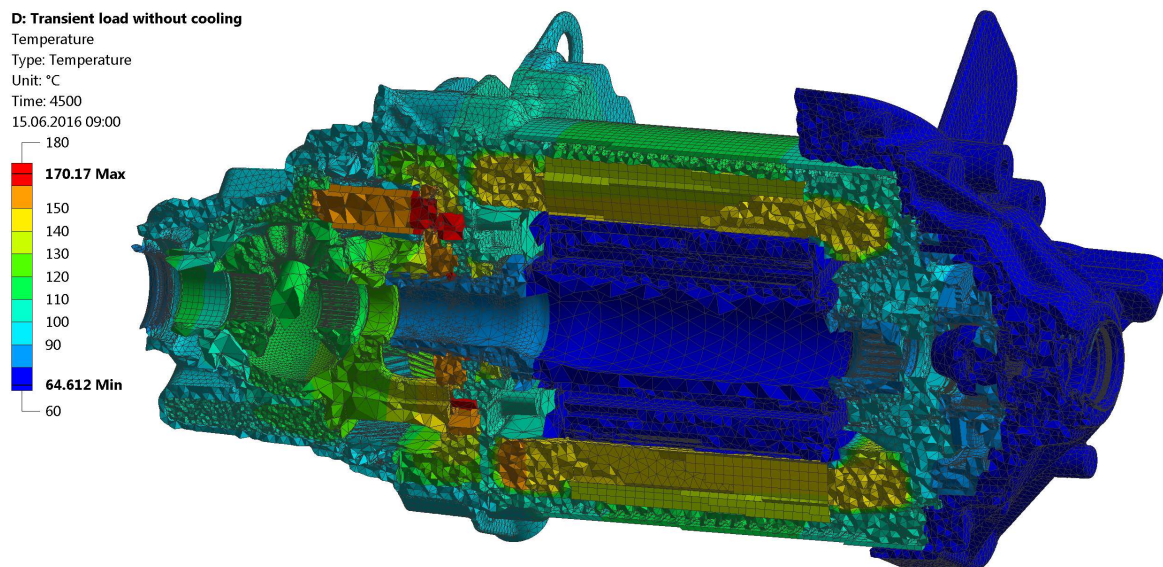


Figure 4.32: eRAD numerical thermal model; gearbox transient validation; temperature at 12000 rpm after 4500 s.

4.4 Thermal Real Time Monitoring of Critical Machine Components

4.4.1 Sensitivity Analysis

Overview and Approach

Practice showed, that it is difficult to integrate a rather complex LPTN model, such as this 21-node model of Fig. 4.3 (p. 55), into a real-time environment, because of the relatively high computation time [154], and as speed dependent parameters are also taken into account. Furthermore, especially in the inverter software, only the hot-spot temperatures of the machine (usually the center region of each slot and the PMs) or the nodal temperatures of the measurement locations are relevant [87]. A possible approach to predict critical temperatures, (as discussed in [92]) for e.g., the stator winding (thermal overload relays, [96]) are first order models. They are too simple, as they would also not compute the magnet temperature.

Instead of directly defining a reduced model (and as opposed to [155]), a simplified model with three nodes using a sensitivity analysis (similar to [149]) including an analysis of the influence of the gearbox to identify critical parameters and heat flow paths interior and exterior to the machine is presented here.

Regarding the gearbox attached: as with EMs, the thermal behavior of a gearbox is a complex combination of heat generation and transfer, as heat is generated in different locations within the gearbox, caused by friction (gear mesh, bearings, seals) and splashing losses (oil) [66]. Analytic [64, 66, 71, 156] or numerical approaches [151] allow computation of the temperature distribution within the gearbox. Prior work on thermal management and modeling of HEV components, such as gearboxes, has been published, aiming, e.g., to optimize exhaust emissions or to predict fuel economy including different thermal ambient conditions [157, 158]. Numerical simulations to compute thermal paths between transmission cases and EMs are presented e.g., in [157]. As the main focus in this section is on the development of a real-time LPTN of the IPMSM and whereas the temperature distribution within the adjacent components is not of primary interest, the model of the EM is amended by the losses introduced into the system by the gearbox neglecting the thermal behavior of the gearbox itself, as a first step. Aiming to discuss the gearbox influence, the focus in this section is placed on the power loss distribution from the gearbox to the shaft of the rotor and from the gearbox to the housing/frame (nodes no. 6 and no. 14 in Fig. 4.3), see Fig. 4.33.

Based on detailed discussions of the loss generation and distribution within the gearbox using CFD models compared with experimental results, which are e.g., given in [150, 159]: the temperature of the teeth is approximately 60-70 % higher than that of the shaft; the oil temperature is in the same range as the teeth temperature. The loss distribution, applied to

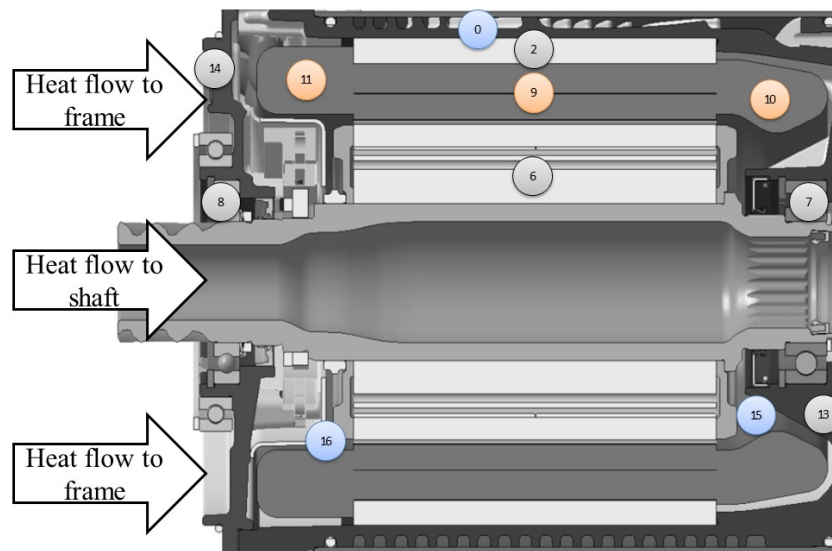


Figure 4.33: IPMSM cross section view, with location of gearbox loss injection and location of some LPTN nodes.

the model, is based on these results and using loss-strip-down measurements for the gearbox which showed that, depending on the vehicle speed, the losses caused by tooth friction vary within a range of 45-55% of the total gearbox losses. Based on these facts: for the baseline case of the sensitivity analysis, a fixed distribution of the heat flow of 70% over the frame (node 14), and 30% of the shaft (node 6) in Figs. 4.34 to 4.37 was defined. The analysis of the interface between gearbox and EM for the baseline case, using the eRAD FEM thermal model, in Section 4.5.5 proved that this assumption was accurate. The loss distribution is also varied and shown for the magnet temperature in Figs. 4.38 and 4.39.

Comparison of Sensitivity Analysis with and without Gearbox

The baseline temperature of the magnets was 69 °C at 80 Nm shaft torque, 1000 rpm shaft speed, 65 °C cooling fluid temperature and 35 °C oil (sump) reservoir temperature. At this operating point, the gearbox losses are 478 W and the total machine losses are 874 W. This is an operating point at the low speed and load region which reflects the mean power demand in a typical driving cycle. Strictly speaking, the results are only valid for this operating point. Especially overload operation always needs further consideration: We investigated this aspect further, concluding that the main results of the sensitivity analysis (main heat flow paths and parameters) do not change significantly during high torque (e.g., 2300 rpm/150 Nm) or high speed operation (e.g., 12000 rpm and zero torque).

1. *End windings without gearbox*: The analysis showed that the thermal resistances R_{12} , R_{23} , R_{29} , R_{39} and R_{910} are relevant for the end winding temperatures if the gearbox is

not attached (Fig. 4.34). Fig. 4.34 only shows resistances which lead to a relative change of temperature of at least 2.5%: R_{12} : stator housing to cooling jacket, R_{23} : yoke to teeth, R_{29} : yoke to winding in slot, R_{39} : teeth to winding in slot, and R_{910} : winding in slot to end winding at NDE thermal resistance. These resistances describe the thermal path from cooling jacket over stator iron (which agrees with the results published in [160]), the winding in the slots to the NDE and the DE end windings. Based on these results, the convection from the end winding surface to the air region inside the machine and the thermal path over the air gap to the rotor has a minor influence on the cooling of the winding and end windings. These findings differ from those presented in [149], in which a low sensitivity on the interface gap thermal resistance (R_{12}) for totally-enclosed fan-cooled (TEFC) induction motors was reported.

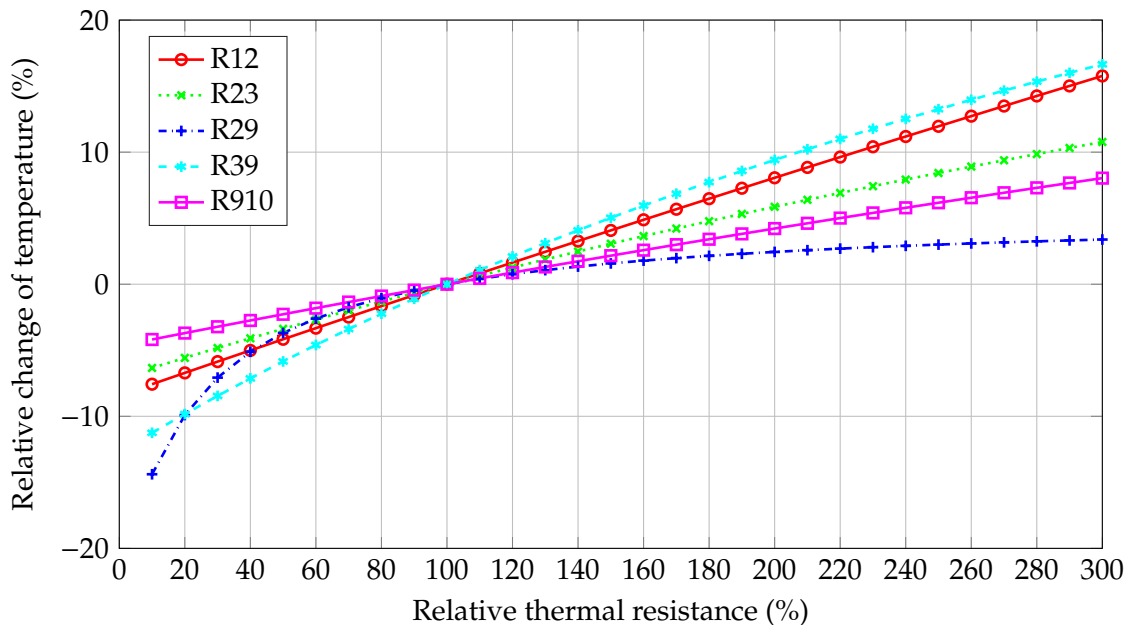


Figure 4.34: End winding sensitivity analysis without gearbox.

2. *End winding temperature with gearbox*: With a gearbox (Fig. 4.35), the main thermal paths are not affected. Fig. 4.35, again, shows only resistances which lead to a relative change of temperature of at least 2.5%: R_{01} : cooling jacket to coolant, R_{12} : stator housing to cooling jacket, R_{23} : yoke to teeth, R_{29} : yoke to winding in slot, R_{39} : teeth to winding in slot, and R_{910} : winding in slot to end winding at NDE thermal resistance.
3. *Magnet temperature without gearbox*: In this case, the thermal path from the housing over the air gap to the rotor has a higher influence on the magnet and rotor temperatures than that from the rotor over the bearings. Hence, the thermal resistances R_{01} , R_{12} , R_{23} , R_{29} , R_{45} , R_{1315} , R_{1517} and R_{1620} are the most important if the gearbox is not considered;

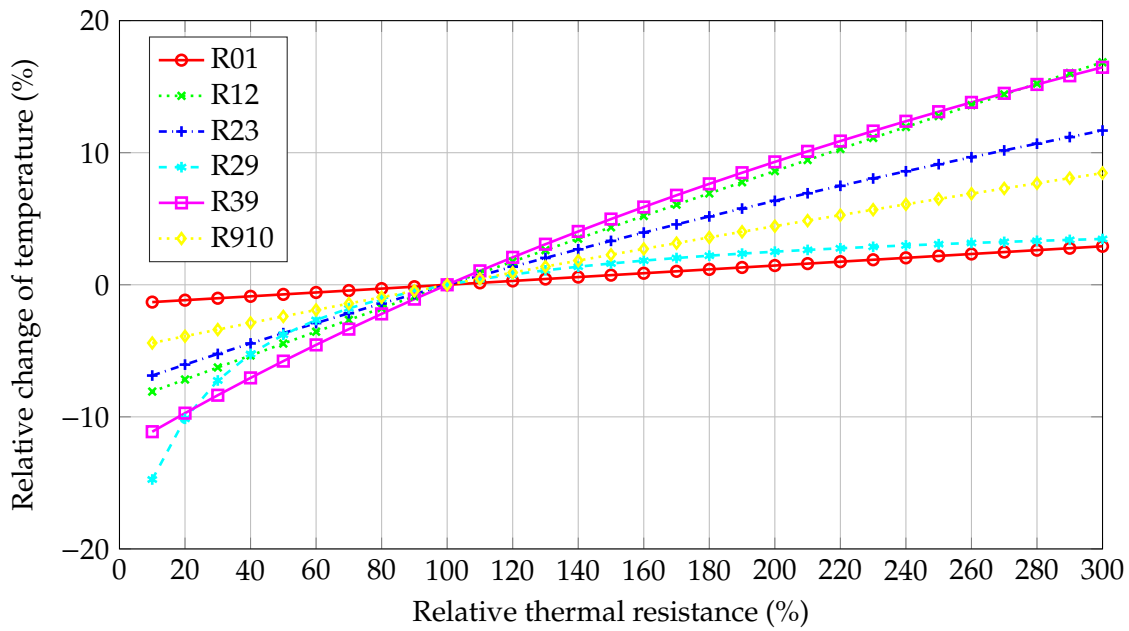


Figure 4.35: End winding temperature sensitivity analysis with gearbox.

as with the end winding sensitivity analysis, only resistances which lead to a relative change of temperature of at least 2.5% are shown in Fig. 4.36: R_{01} : cooling jacket to coolant, R_{12} : stator housing to cooling jacket, R_{23} : yoke to teeth, R_{29} : yoke to winding in slot, R_{45} : air gap, R_{1315} : frame to air volume at NDE, R_{1517} : (side) surface of rotor to air volume NDE, and R_{1620} : end winding surface to air volume DE thermal resistance.

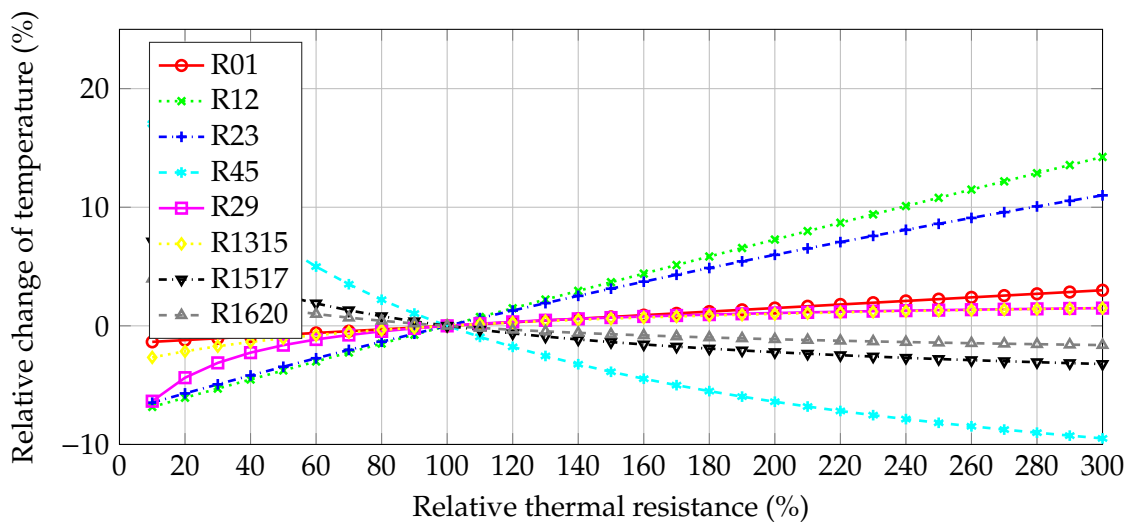


Figure 4.36: Magnet/rotor temperature sensitivity analysis without gearbox.

4. *Magnet temperature with gearbox*: In this case, the thermal path over the bearings (R_{712}) has a greater influence if compared to the simulation without the gearbox. As anticipated, with respect to the heat flow analysis in Fig. 4.40, the main heat flow paths remain unaffected. Resistances which lead to a relative change of temperature of at least 2.5 % are: R_{01} : cooling jacket to coolant, R_{12} : stator housing to cooling jacket, R_{23} : yoke to teeth, R_{29} : yoke to winding in slot, R_{45} : air gap, R_{712} : shaft to bearing NDE, and R_{114} : frame DE to cooling jacket thermal resistance.

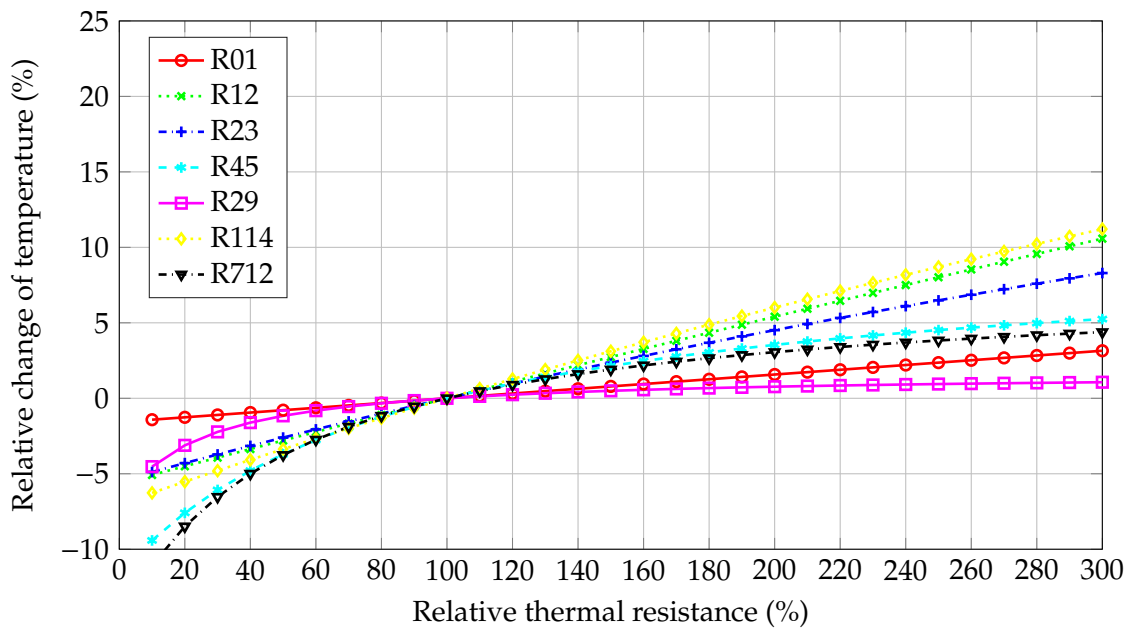


Figure 4.37: Magnet temperature sensitivity analysis with gearbox.

Influence of Gearbox Loss Distribution on Sensitivity Analysis Results

To analyze the influence of the gearbox loss distribution, the influence on the sensitivity investigations is analyzed in Fig. 4.38 for the stator to housing thermal resistance (contact resistance) R_{12} , as this resistance is critical in all cases. The loss distribution between the rotor (6) and the frame node (14) is varied from 0 to 100 %.

In Fig. 4.39 the influence of the gearbox loss distribution on the air gap thermal resistance R_{45} sensitivity is shown: the sensitivity increases with the losses injected into the rotor.

Regarding the end winding temperatures, the change in sensitivity is negligible (only 0.6 % if 30 % of gearbox losses are injected in rotor). Therefore, the influence of the loss distribution on the end winding sensitivity analysis is not significant, and hence not shown here.

The sensitivity analysis only provides information on the relative influence of a given

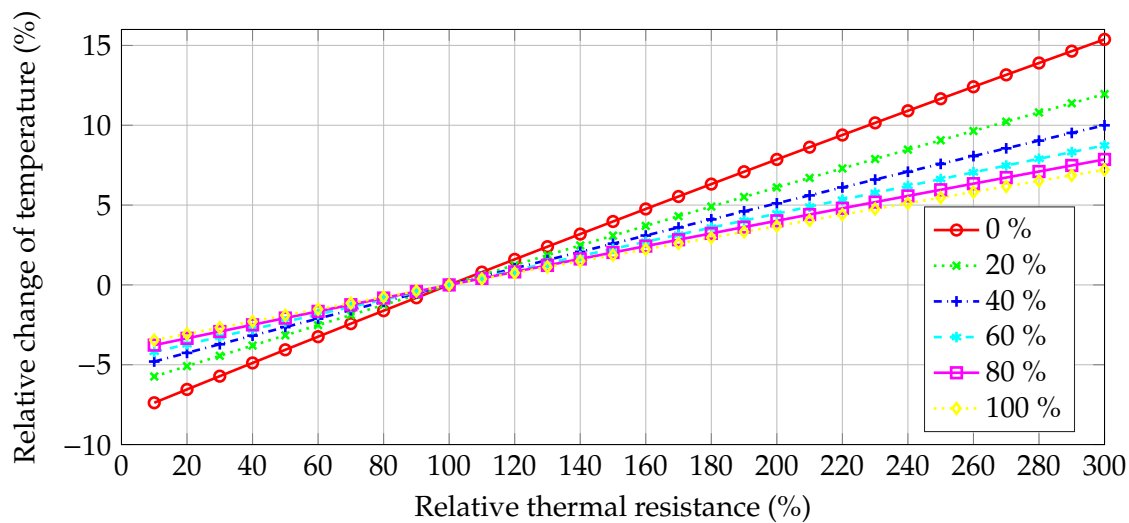


Figure 4.38: Sensitivity analysis: influence of relative change of stator to housing interface gap thermal resistance (R_{12}) on the magnet temperature.

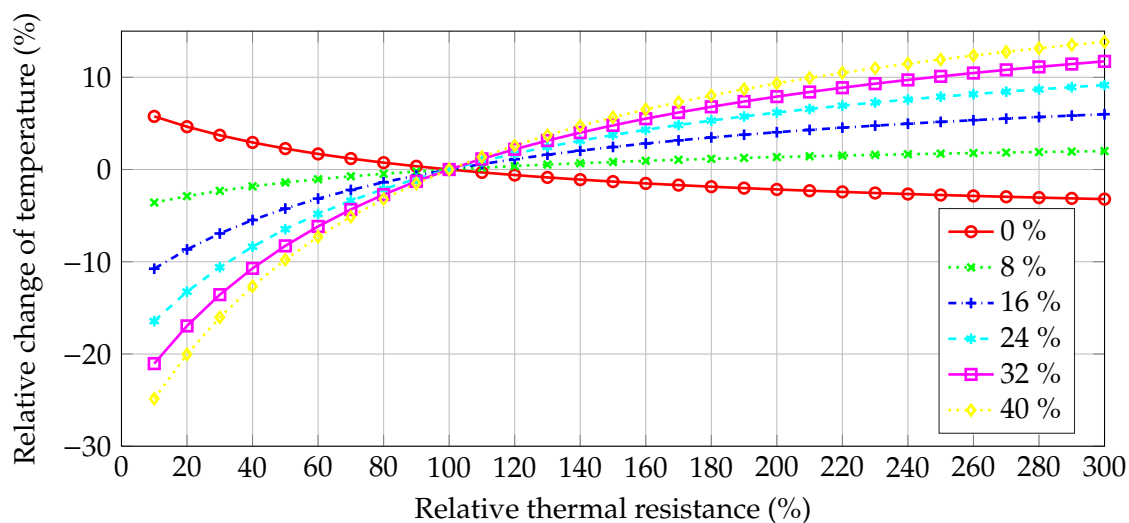


Figure 4.39: Sensitivity analysis: influence of relative change of air gap thermal resistance (R_{45}) on the magnet temperature.

thermal resistance on the temperature of interest. Therefore, the paths of the heat flow need additional consideration: Fig. 4.40 shows the main thermal paths as identified by the sensitivity analysis. Further analysis showed that only a major change in thermal resistance (factor > 2) would change the heat flow situation significantly. The attached gearbox does change the heat flow situation, but the overall thermal behavior remains unaffected.

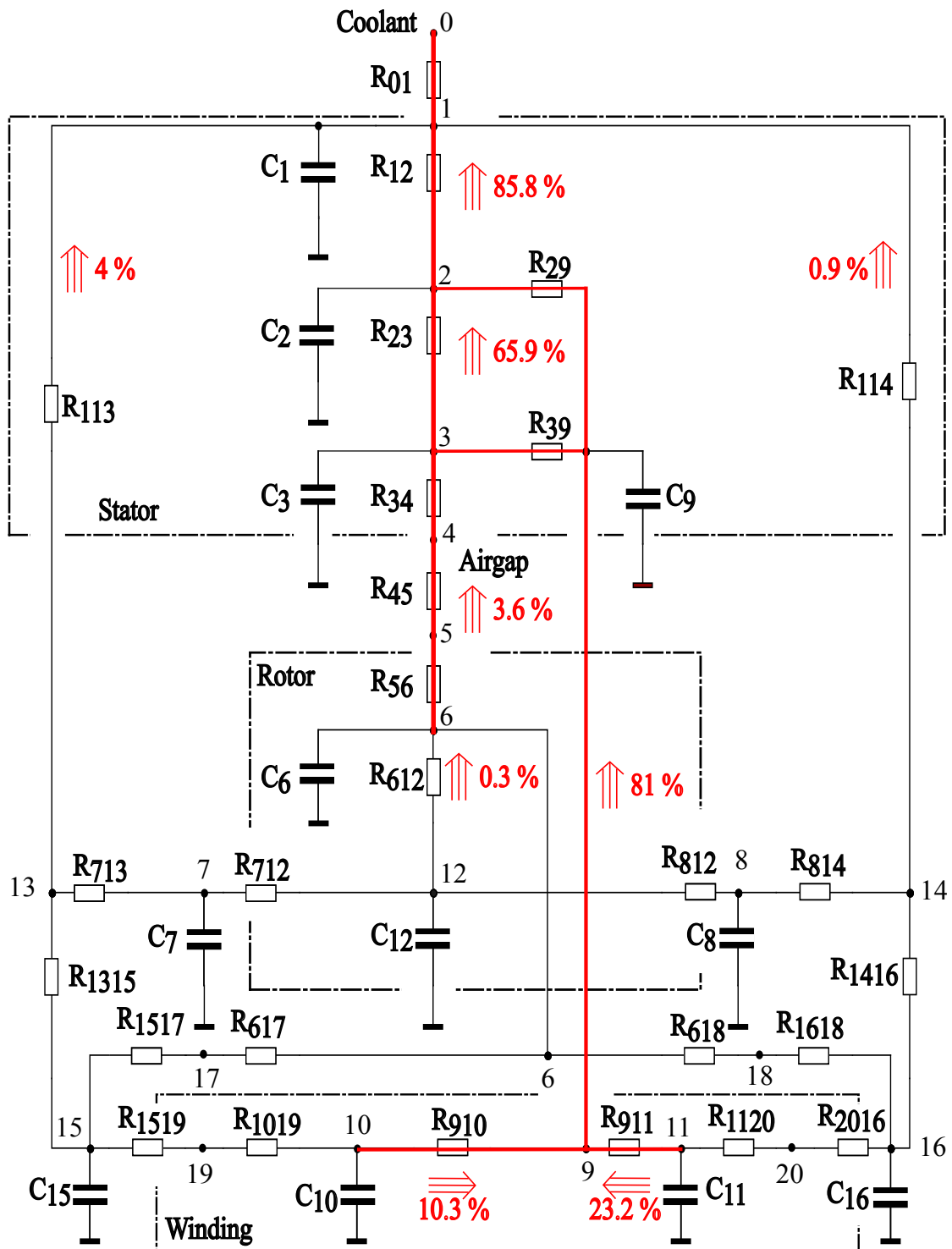


Figure 4.40: LPTN model with most relevant heat flow paths (red lines) and loss distribution.

4.4.2 Real Time Model

Based on the results of the sensitivity analysis, the thermal network was reduced to a 3-node model which represents the three main components: the stator with the thermal capacitance

$$C'_1 = C_1 + C_2 + C_3, \quad (4.4)$$

the winding thermal capacitance

$$C'_2 = C_9 + C_{10} + C_{11}, \quad (4.5)$$

and the rotor thermal capacitance

$$C'_3 = C_6 + C_{12}. \quad (4.6)$$

Fig. 4.41 shows the simplified thermal network with the thermal resistances R'_{01} as coolant to stator thermal resistance, R'_{12} as stator to winding node thermal resistance and R'_{13} as stator to rotor thermal resistance.

The thermal resistances are calculated from the previously identified most relevant thermal paths with

$$R'_{01} = R_{01} + R_{12}, \quad (4.7)$$

$$R'_{12} = R_{23} + \frac{R_{910}}{4} + \frac{R_{29}R_{39}}{R_{29} + R_{39}} \quad (4.8)$$

and

$$R'_{13} = R_{34} + R_{45} + R_{56}. \quad (4.9)$$

The losses injected into the corresponding nodes in the full model are summarized in the corresponding node in the reduced model.

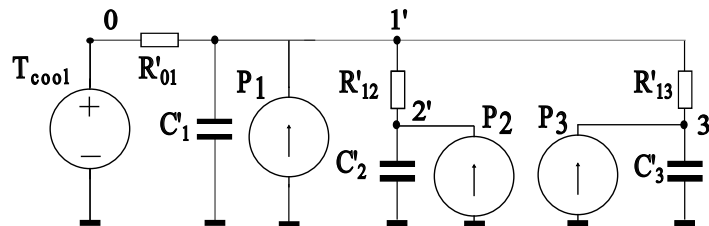


Figure 4.41: Reduced thermal model; nodes: 0' coolant, 1' stator, 2' winding and 3' rotor.

The lubrication oil flow which cools the rotor is directly considered by the subtraction of the cooling power at node 3' (rotor node). The gearbox losses are injected into this rotor, and the stator node (1').

When compared to the detailed model with 21 nodes, the proposed simplified model decreases the computation time by a factor of 12, calculated on a standard office computer with 3.4 GHz CPU frequency and 64 GB RAM. This model is suitable to be computed in a 10 ms task in the inverter software.

4.4.3 Comparison of Real Time Model Performances

The magnet temperature as computed with the simplified real-time capable model is within the ± 5 K range for most operating points. Exemptions are at 4000 and 5000 rpm (Fig. 4.42). Using both, the reduced and the full model, the magnet temperature is slightly overestimated which is attributed to: (i) the simplified modeling of the bearing lubrication (see [6]); (ii) the air gap resistance computation which assumes two concentric cylinders ([97, 128, 161]); (iii) the simplified thermal radiation (increased convection); (iv) and the simplification of the model in the air gap: the air gap inner air is not modeled, therefore the temperature dependency of the air gap resistance is based on the teeth surface and rotor surface temperature (nodes no. 4 and 5).

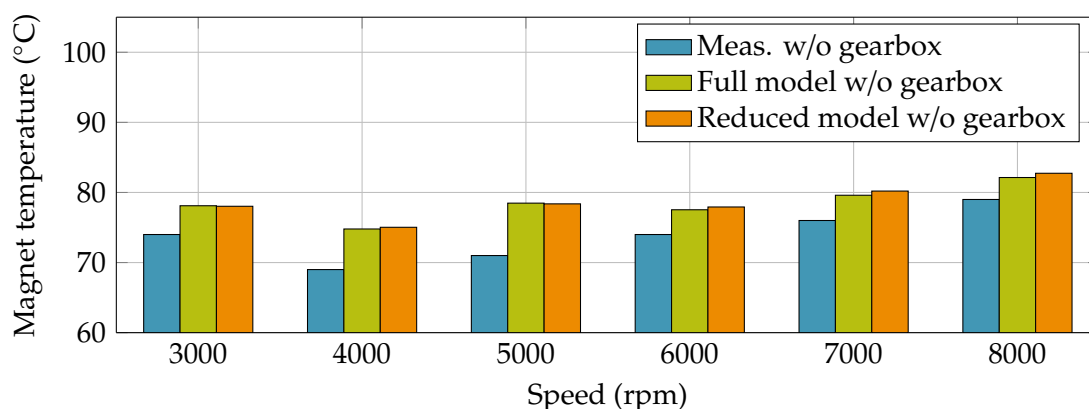


Figure 4.42: Comparison of modeling approaches with measurement results, magnet temperature, steady-state, 20 kW.

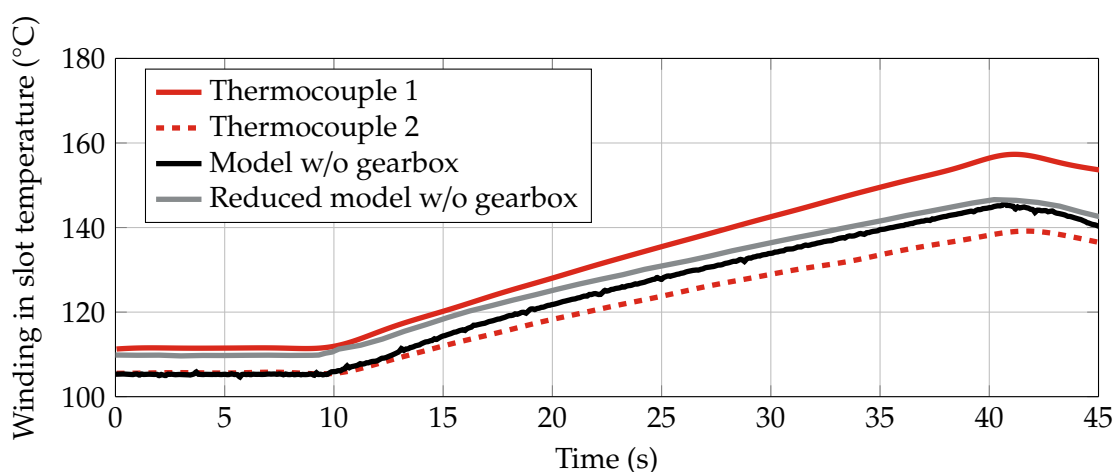


Figure 4.43: Comparison of modeling approaches with measurement results, winding in slot temperature, 250 rpm, 200 Nm torque step for 30 s.

Fig. 4.43 compares both modeling approaches to transient measurement results: the temperatures in the winding nodes are computed within sufficient accuracy. The reduced model has only one node representing the winding temperature, the full model has five nodes (slot, end windings at DE and NDE and end winding surfaces at DE and NDE). As the end winding temperature is usually the hot-spot, the higher temperature computed with the simplified model suffices, as the node represents a mean value of the five nodes in the full model.

4.4.4 Discussion of Real Time Model Inverter Implementation Aspects

The implementation of the model into the control algorithm in the inverter software results in additional challenges:

The model uses the coolant temperature as the ground node. Furthermore, the coolant temperature can change quite fast, e.g., if the thermostat changes the position. The accuracy with which the exact flow rate of the cooling is known may introduce another uncertainty into the model. Node 0 is the ground node of the thermal network; therefore the thermal resistance R_{01} (cooling jacket to coolant) is the most critical resistance. For example, assuming a pump failure, the volumetric flow rate decreases from 6 l/min to 4 l/min, and therefore the relative thermal resistance increases by $\approx 50\%$. With respect to the temperature, however, each kelvin error of the coolant temperature sensor results in an error of the temperatures determined at the nodes in the model.

Using CFD simulations, the sensitivity of the thermal resistance R_{01} (cooling jacket to coolant) to the volumetric flow rate has been computed (Fig. 4.44). As the influence of the volumetric flow rate \dot{V} on the mean convection coefficient h is approximately linear (in the range of interest), the thermal resistance changes with $R_{01} \propto 1/h(\dot{V})$. Therefore, all computed temperatures depend on the accuracy of the temperature sensors used for the known temperature(s): in the present case, the coolant temperature.

Besides changes in the cooling condition, further possible failures which could lead to a temperature drift of the thermal model are changes in the mechanical components (e.g., increased friction due to failures or wear), machine failures (as mentioned in [162]) or winding/insulation lifetime degradation (thermal load peaks). These failures could lead to changes in loss generation or the parameters of the thermal model which are not covered by an LPTN approach. Therefore, using a second, additional temperature sensor, readily available in most applications, to measure the temperature at a new node $4'$ which represents the end winding temperature in a slightly amended simplified thermal model (Fig. 4.45, p. 89) is suggested.

This new thermal network has two defined temperatures: the coolant temperature θ_0 and an end winding temperature $\theta_{4'}$. $R_{24'}$ is the thermal resistance of the path from the sensor to the winding in slot node, as detailed above. As one or two sensors are usually mounted in

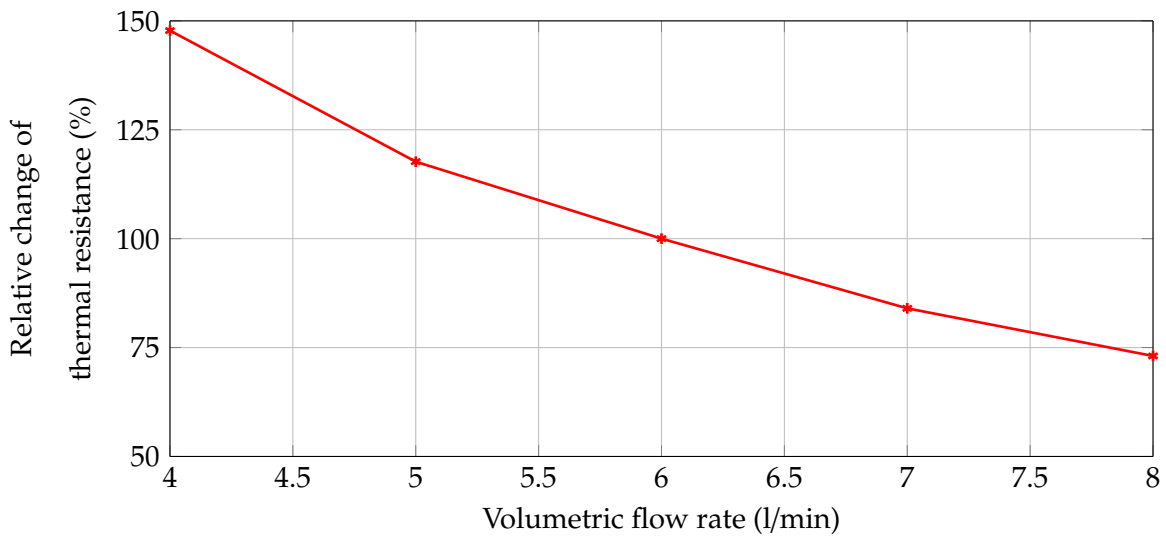


Figure 4.44: eRAD; relative change of thermal resistance R_{01} (cooling jacket to coolant) as function of volumetric flow rate.

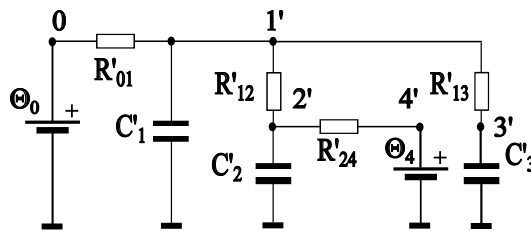


Figure 4.45: eRAD; simplified thermal model with additional sensor.

the winding due to safety reasons, there is no impact on the costs at increased redundancy of the model.

If the analysis (software, electronics) of the coolant sensor has an error of 5 K, the computed rotor (or magnet) temperature is affected by 4 K, if no additional sensor is used. With the second sensor measuring the temperature of the end winding sensor, the magnet temperature is determined with an error of less than 1 K.

In Figs. 4.46 and 4.47 the heat flow (or loss distribution) imposed by the gearbox is compared with the baseline case, using the reduced model to show the impact of the gearbox losses on both the rotor and the end winding temperatures in the FTP-75: 30% of the gearbox losses are injected into the rotor node, 70% into the stator node. For the cycle simulations, the Federal Test Procedure (FTP-75) was preferred over the New European Driving Cycle (NEDC) because of the higher dynamics (see [163]) using a simple quasi-static vehicle model [164] (see Appendix A).

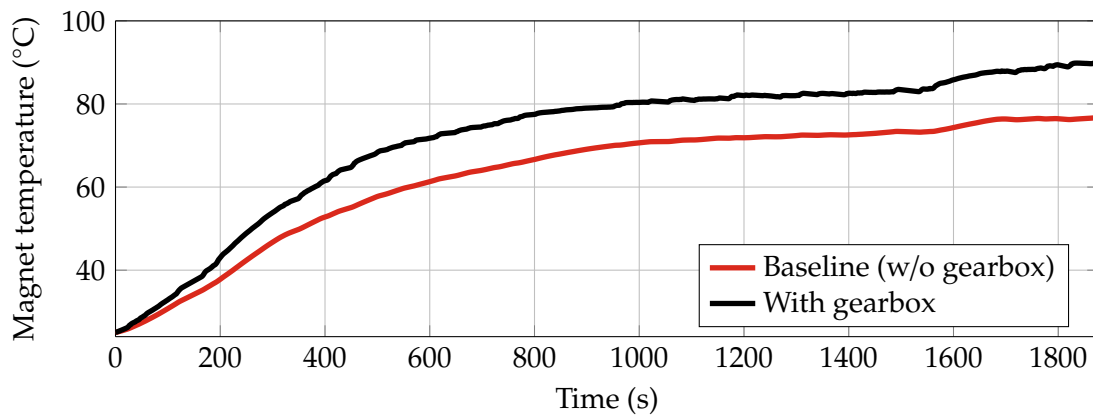


Figure 4.46: eRAD; simulation: magnet temperature in the FTP-75 driving cycle.

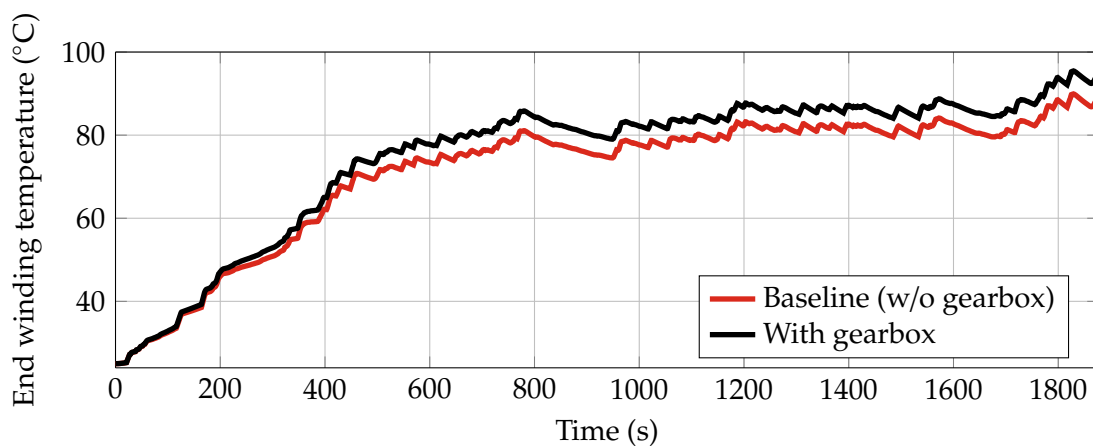


Figure 4.47: eRAD; simulation: end winding temperature in the FTP-75 driving cycle.

4.5 Analysis of Baseline Thermal Packaging Situation

4.5.1 Simulation Approach

In this section the thermal situation of the IPMSM and the driving cycle behavior is reviewed. The gearbox losses and their influence on the machine's thermal behavior are considered. The thermal behavior of the gearbox is not part of the thermal model (Fig. 4.3), but the gearbox losses are injected into the model at the corresponding frame and shaft nodes, with respect to the FEM thermal model simulation results in Section 4.5.5.

As already discussed in this chapter, since the gearbox is thermally connected to the shaft and the housing, the loss distribution within the gearbox is required. The loss generation and distribution within the gearbox is affected by a variety of parameters such as the local speed dependent oil flow distribution [165, 166], the thermal characteristics of the contact zone (teeth), the related contact-generated heat [159], and surface roughness of the gearbox

housing. These parameters are part of the lubrication and gearbox development process and were not explicitly determined for the scope of this work, but are estimated based on the temperature distribution within gearboxes as discussed in [150, 159, 165, 166].

4.5.2 Scenario I - Boost Cycle

Based on the gearbox measurements, an exemplary driving scenario is discussed: starting from a no load operating point at 2380 rpm and a gearbox temperature of 60 °C a boost cycle with 200 Nm is applied for 25 s. Then, the gearbox contributes an additional 3400 W losses which is 60 % of the total machine losses (including bearing and ventilation) in this operating point. For the calculation of the steady-state operating point, the spin losses of the gearbox were considered. During the boost cycle, the additional load-dependent losses were also taken into account. The computed end winding and magnet temperatures are shown in Fig. 4.48.

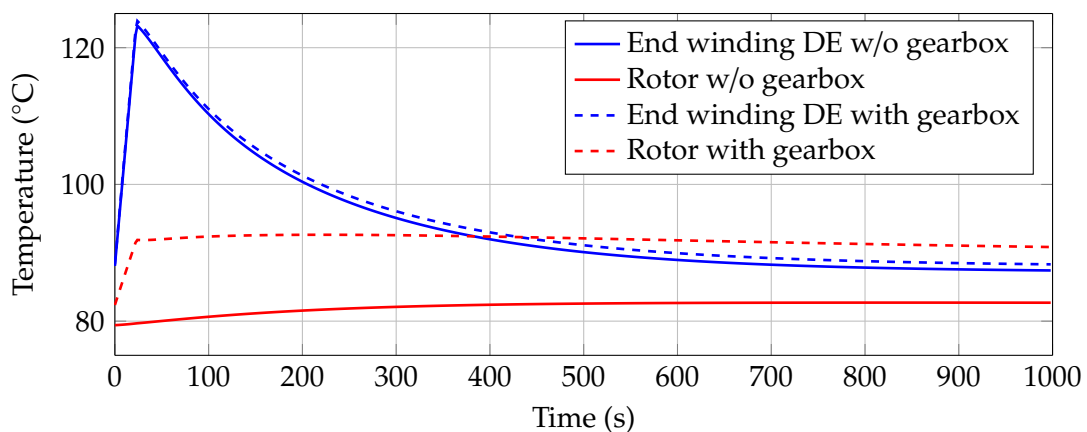


Figure 4.48: eRAD; comparison: influence of gearbox losses for end winding and magnet temperatures for a 25 s boost cycle with 40 % of the gearbox losses injected into shaft.

Under these conditions, the average end winding temperature of both sides reaches a maximum of 124 °C (NDE-DE difference: 1 K) after 25 s. This is only 0.7 K higher than the mean winding temperature without consideration of the gearbox (base-line). Thus, for this specific machine, the additional heat introduced by the gear box losses does not affect the end winding temperature significantly.

The situation is, however, very different for the magnets. The additional heat flow from the rotor due to the gear box increases the temperature of the magnets by 12 K (Fig. 4.48). This may, in turn, severely impede the performance of the motor, as the magnets may provide less magnetic flux, and more phase current might be required for the desired torque to be produced, increasing the losses and thus the heat development further.

4.5.3 Scenario II - FTP-75

To evaluate the gearbox influence on the rotor temperature during a driving cycle, the specified setup was simulated with and without the gearbox using the vehicle model (see Appendix A).

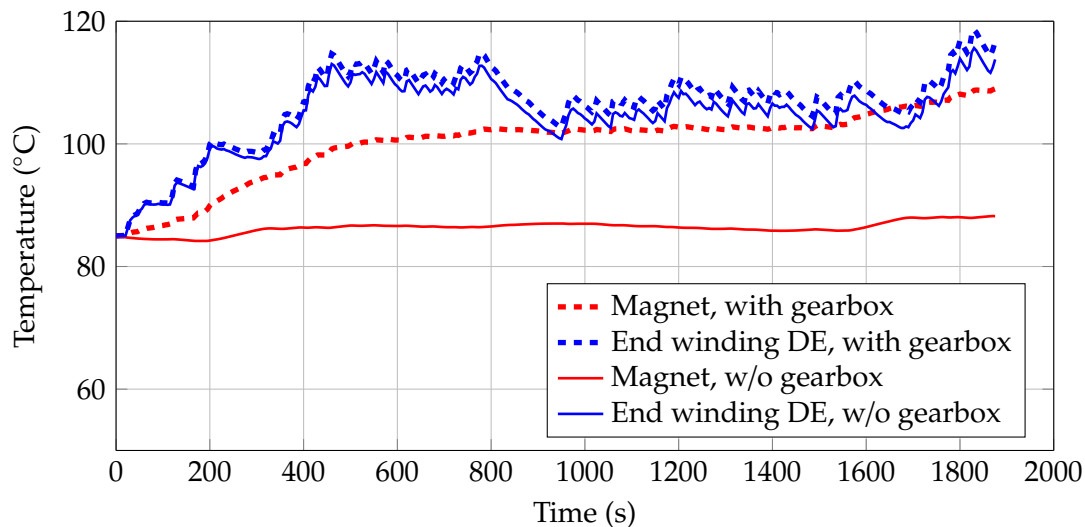


Figure 4.49: eRAD; comparison: magnet and end winding temperatures at DE with 40 % of the gearbox losses injected into shaft and without consideration of gearbox.

Fig. 4.49 indicates the significant influence the gearbox losses may have on the magnet temperature. The magnet temperature after the cycle is 21 K higher if gearbox losses are considered. However, the temperature remains below the critical limits.

4.5.4 Scenario III - Variation of Gearbox Heat Flow

As indicated in the introduction of this section, the distribution of the gearbox losses between the frame and the shaft of the machine may (i) only be known with a certain degree of accuracy and (ii) serve as an additional parameter to consider during the design process of an integrated machine, so as to reduce possible thermal stress on the magnets. Note: since the end winding temperature is only slightly affected by the attached gearbox, this temperature is not analyzed further in this section.

The analysis of the magnet temperatures for different frame-to-shaft heat distribution factors is shown in Fig. 4.50. The gearbox/machine interface is also analyzed using the FEM thermal model in Section 4.5.5.

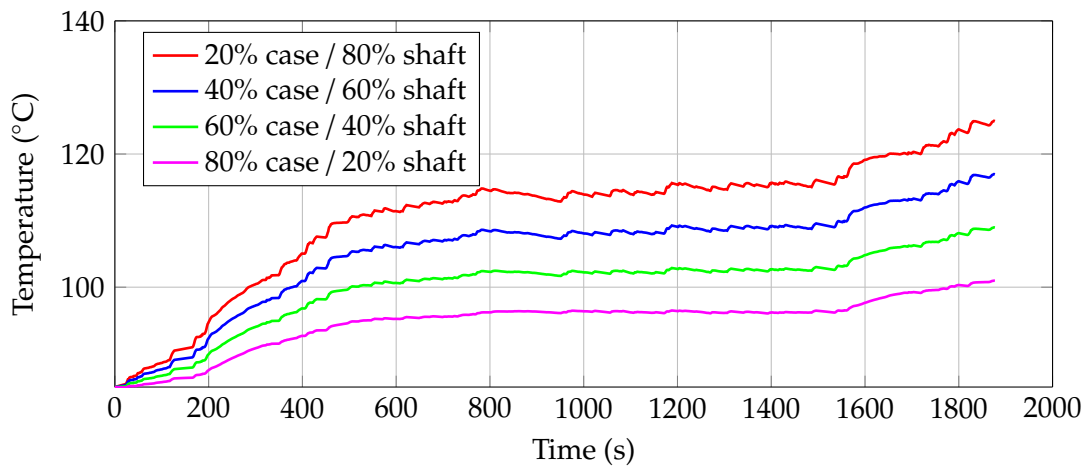


Figure 4.50: Magnet temperature for different loss distribution within the gearbox (ratio frame to shaft).

4.5.5 Numerical Thermal Analysis of the Gearbox-Machine Interface

To prove the assumptions, carried out based on literature and test-rig experience, the FEM thermal model was used to analyze the thermal interface between the attached gearbox and the EM. In the FEM software's post-processor, the heat flux was computed at the interface between the eRAD cooling jacket and the PGS housing.

At 12000 rpm and no-load with deactivated cooling fluid pump, 40% of the losses are injected into the rotor and 60% of the heat goes over the frame/cooling jacket housing into the coolant. If the cooling fluid pump is activated 70% of the losses are flow to the coolant over the housing.

4.6 Design Optimization Study: Alternative Cooling Approach

4.6.1 Review of Possible Approaches and Simulation Study

The research reported in this chapter identified the end windings as thermal bottleneck of the system performance, if the gearbox influence is neglected. The end windings are primarily cooled over the thermal path winding to cooling jacketed. Therefore the cooling fluid is the main heat sink to keep the critical winding temperatures within their limits. One possible approach is to decrease the thermal resistance from the end winding surface to the coolant by building a thermal bridge to the housing using special materials. As with potting materials, the approach of using thermal conductive polymers also tries to decrease the thermal resistance of the winding to the housing and/or stator core.

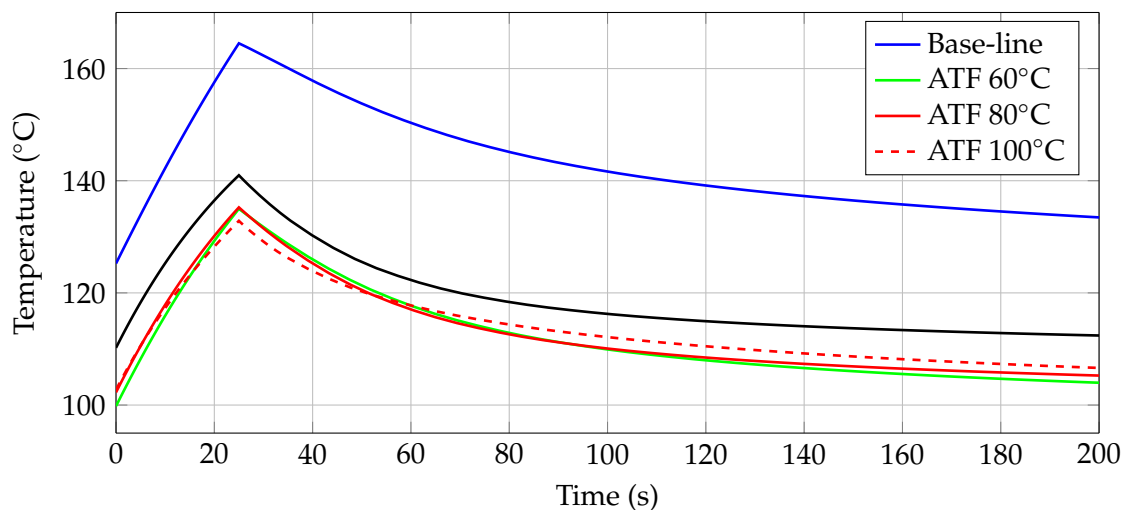


Figure 4.51: Simulated: comparison of end winding temperatures during boost cycle.

Another approach is oil (spray) cooling of the end windings. The heat transfer coefficient between an oil (e.g., automatic transmission fluid, ATF) and the end winding is a nonlinear function of the temperature [167]. In [167] a range of temperatures is presented, they vary between $100 \text{ W/m}^2\text{K}$ at 40°C , to $210 \text{ W/m}^2\text{K}$ at 80°C , up to $300 \text{ W/m}^2\text{K}$ at 100°C oil temperature. Based on these information a fast thermal study was carried out: a 25 s torque step, starting from the nominal operating point at steady-state, is applied. For example, an oil spray temperature (ATF as cooling fluid) of 80°C decreases the maximum temperature of the end winding by 19 K, from 165°C down to 146°C , while that of the winding in the slots decreases only by 6 K, from 147°C down to 138°C . Fig. 4.51 shows this difference between the base-line case (no gearbox, no oil-spray cooling on end winding) and the effect of oil-spray cooling for different ATF temperatures.

The increasing heat transfer coefficient with increasing cooling fluid temperatures may

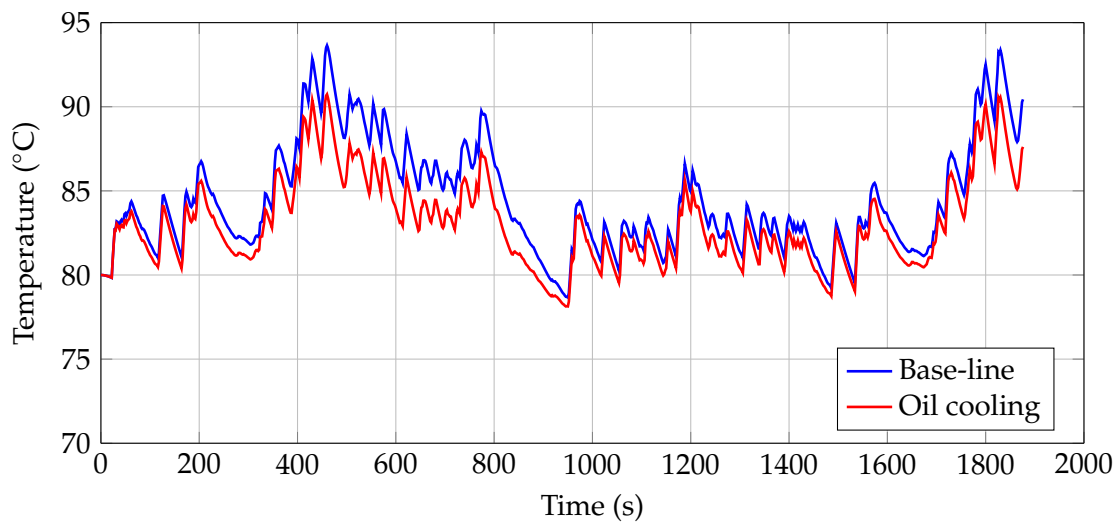


Figure 4.52: Simulated: comparison of end winding DE temperature with and without oil cooling.

suggest that the largest effect would be obtained at high oil temperatures. However, high cooling fluid temperatures heat up the system. Therefore, the largest cooling effort can be obtained for a fluid temperature of 80 °C. This temperature is the best compromise between fluid temperature and heat transfer coefficient.

To conclude the study, the drive performance with ATF cooling at 80 °C was simulated for the FTP-75 driving cycle (Fig. 4.52), the improvement was emphasized. The end winding at the DE has a 3 K lower temperature, the rotor temperature is only 0.3 K lower and therefore not affected by the oil cooling.

4.6.2 Prove of Concept: Oil Cooling of End Windings

Overview

As in the case of the eRAD system a gearbox is attached on the machine's DE, using the lube oil of the gearbox is obvious. Test results were available. The baseline (cooling only using the water jacket) is compared with an oil slinger solution as the simplest approach. More detailed investigations are presented using an external oil pump to generate an oil flow through the shaft and splatter oil on the end windings by holes in the shaft.

Splash Oil Cooling with Oil Slingers

Instead of cooling the stator back iron [168], or the end windings by using an oil pump to generate an automatic transmission fluid (ATF) spray [167], oil slingers for distributing a transmission fluid which cools down the end windings are added.

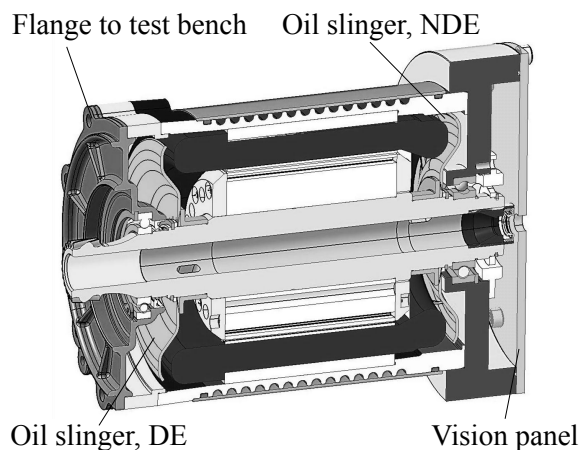


Figure 4.53: eRAD cross section view, with oil slingers.



Figure 4.54: Oil slinger.

To check the possible cooling potential, a prototype EM (Figs. 4.53 and 4.54) with a special oil distribution plate (Fig. 4.55: oil slinger) was available. The oil slingers plunge in an oil sump to generate an oil spray caused by the rotation of the oil slinger. Oil is transported by the rotation of the oil slingers to the end windings which are the thermal hot spots. When the rotor spins, the oil slingers transport oil from the oil sump to the end winding surface to enable a cooling effect to the end windings by the combined material and thermal transport. Furthermore the possible boost time and continuous torque available can be increased.

The prototype is equipped with integrated oil slingers near the end windings at the DE and NDE, a vision panel was used to enable visual review during the tests (Fig. 4.53). Sufficient transport of oil to the end windings is ensured by using fins on the oil slinger surface (Fig. 4.54). The distance of the oil slingers to the end windings is changeable using adjusting shims and plate springs (Fig. 4.53). The test-rig (Fig. 4.56 presents the cross section view) was equipped with oil pipes for control of the oil level.

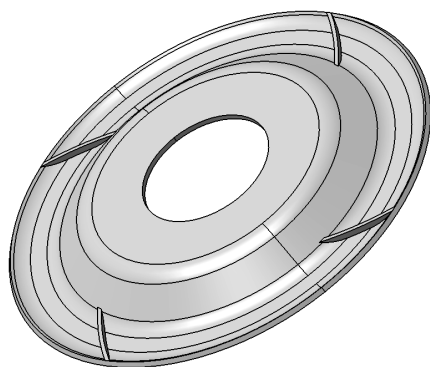


Figure 4.55: eRAD oil slinger design drawing.

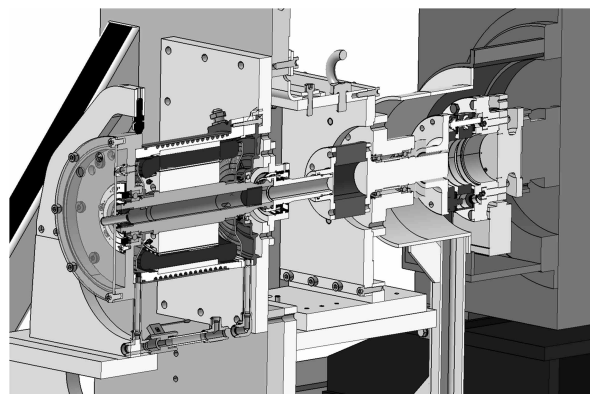


Figure 4.56: Test-rig cross section view.

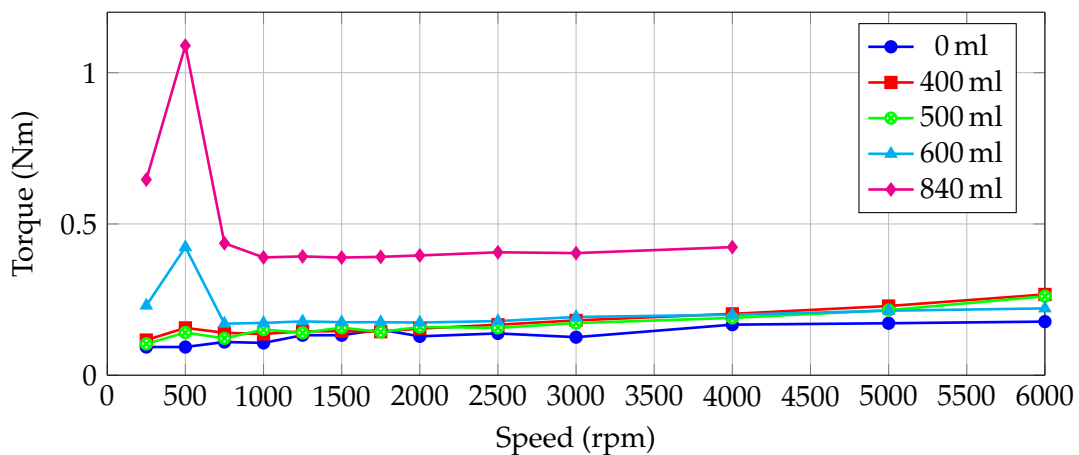


Figure 4.57: Drag torque of oil slingers at different oil levels and shaft speeds.

As the oil movement of the oil slingers causes additional drag torque, measurements have been carried out to show the coherence of the oil level (Castrol BOT 350 M3 75W) and the design of oil slinger fins with the additional drag torque: The rotor was revolved up to 6000 rpm and the drag torque was measured. The mean oil temperature was 25 °C during the drag torque measurements. Figure 4.57 shows representative results up to a maximum oil level of 840 ml. The drag torque has a peak value in the low speed region at approximately 500 rpm, and increases slightly linear with the shaft speed.

Further tests, which are not discussed in detail, showed that the losses significantly increase if another oil or fluid is used. For example, to emphasize a worst case measurement situation for higher oil levels and different fin designs (fin angles and numbers): The additional (measured) speed dependent losses caused by the movement of the fluid can be in the range up to 250 W at 3000 rpm and 750 W at 6000 rpm without oil (air friction). The oil spin losses are in the range of up to 500 W at 2000 rpm to 1870 W at 6000 rpm and within this speed range the losses increase linearly with speed.

The next step was to prove the influence of the alternative cooling approach on the machine's thermal behavior. Maximum torque pulse responses have been applied for both the baseline case and the oil cooled prototype at different speeds. Results for the mean end winding temperature are shown in Figs. 4.58 and 4.59. In the oil cooled case the maximum torque (boost) time is extended by 7 s in the first case (200 rpm, Fig. 4.58). A slightly longer time frame would have been possible, as the temperature limit for the device under test was defined as 165 °C. To avoid destruction of the prototype the temperature limits have been decreased. The figure also illustrates the increased cooling effect during the cool down phase. The peak end winding temperature for that case is 6 K if using the oil slingers. Fig. 4.59 shows the next case, at 1000 rpm and approximately the same boost time. The winding temperature decreased by 26 K at this speed.

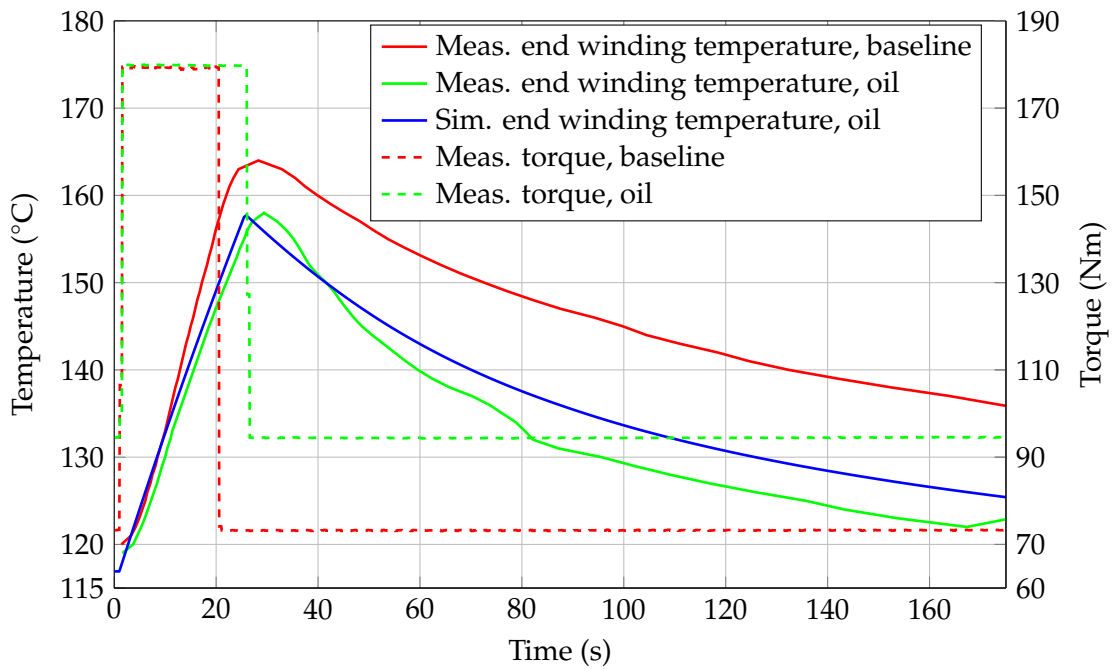


Figure 4.58: Torque pulse step response at 200 rpm using oil slingers.

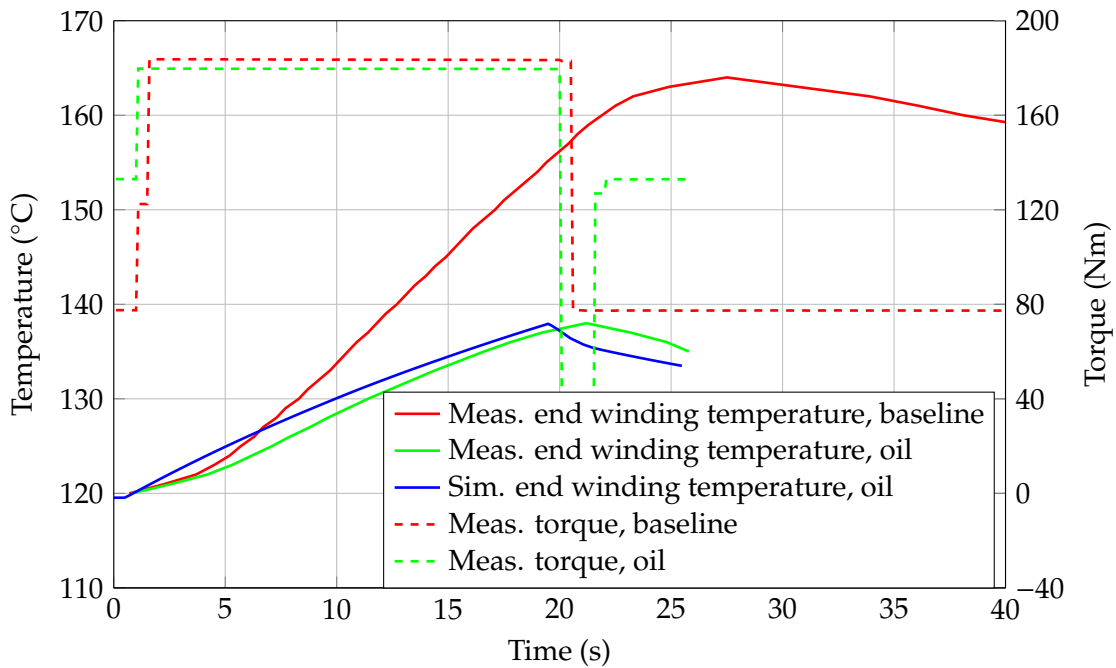


Figure 4.59: Torque pulse step response at 1000 rpm using oil slingers.

Using this measurements, the end winding heat transfer coefficient from the end winding surfaces (nodes 19 and 20 in Fig. 4.3) to the oil was estimated, $180 \text{ W/m}^2\text{K}$ for the 200 rpm run, and $650 \text{ W/m}^2\text{K}$ for the 1000 rpm run.

These measurement and simulation results proved that with this approach the thermal behavior can be increased significantly. The bottleneck of this approach are the spin losses (drag torque) which increase with speed. The goal is to increase the possible boost time and continuous torque (or power) available to the vehicle. As there are always (speed dependent) losses up to a few hundred watts, this solution is not applicable from the system efficiency point of view: e.g., if driving at a freeway with constant speed this solution generates losses which are not defeatable. These additional losses need to be covered by the ICE or the battery. For this reason this solution is not considered in the further research work. The next chapter presents an approach which tries to avoid such additional losses of a few hundred watts.

Oil Cooling using Pump

The approach of this additional cooling method is to generate an oil flow into the hollow shaft of the EM by a pump. The shaft has respectively one opening at the DE and NDE beneath the end windings. Therefore the oil splashes from the shaft opening to the end winding surfaces.

The oil flow can be generated using an external gear pump, which may be integrated into the gearbox or an external pump. Both approaches had been developed in a preceding research project. As with the oil slinger solution, the external gear pump used for the measurements has a speed dependency. Measurement showed that the maximum pump power with 1.4 L/s was reached at 1000 rpm and 30 °C, the drop in pump power was measured at 3000 rpm, then the fluid flow was nearly constant over the whole speed range with 0.6 – 0.7 L/s. To overcome this speed dependency an external pump was used to produce the desired mass flow rates (fluid flow) for the test program. Temperature, speed, torque and the power demand were measured.

Fig. 4.60: As with the oil slingers, the start of each test run was to apply a torque at defined speed to reach a steady-state end winding temperature of 120 °C, then the peak torque of 200 Nm (or power of 50 kW) was applied till the end winding temperature had reached 155 °C. Then, the initial torque value was applied to measure the cool down thermal behavior. This measurement procedure shows both the steady-state and the dynamic behavior for each test run.

As each test run represents the steady-state, the heat up and cool down behaviors, the measurement results are used to identify thermal convection coefficients using the simulation model (Section 4.2, Fig. 4.3).

Figs. 4.60 to 4.62 show the thermal pulse step response used in the measurement run and described above, for different speeds and at different fluid flow rates. An improvement of the machine's performance is demonstrated in the speed range from 200 rpm to 3000 rpm.

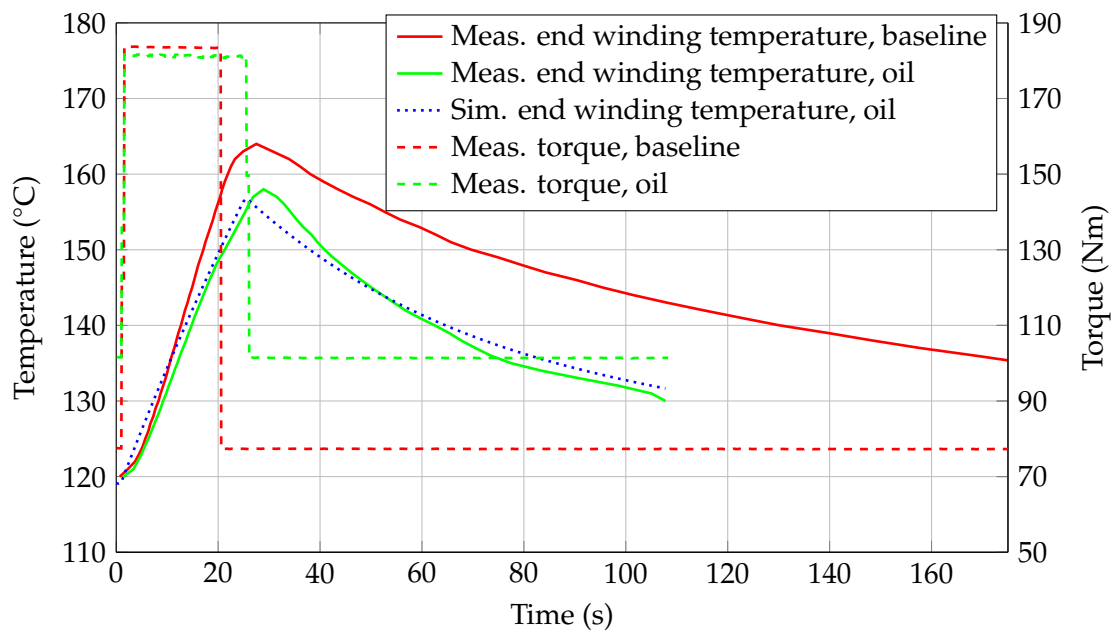


Figure 4.60: Torque pulse step response at 1000 rpm with oil pump at a flow rate of 0.8 L/s .

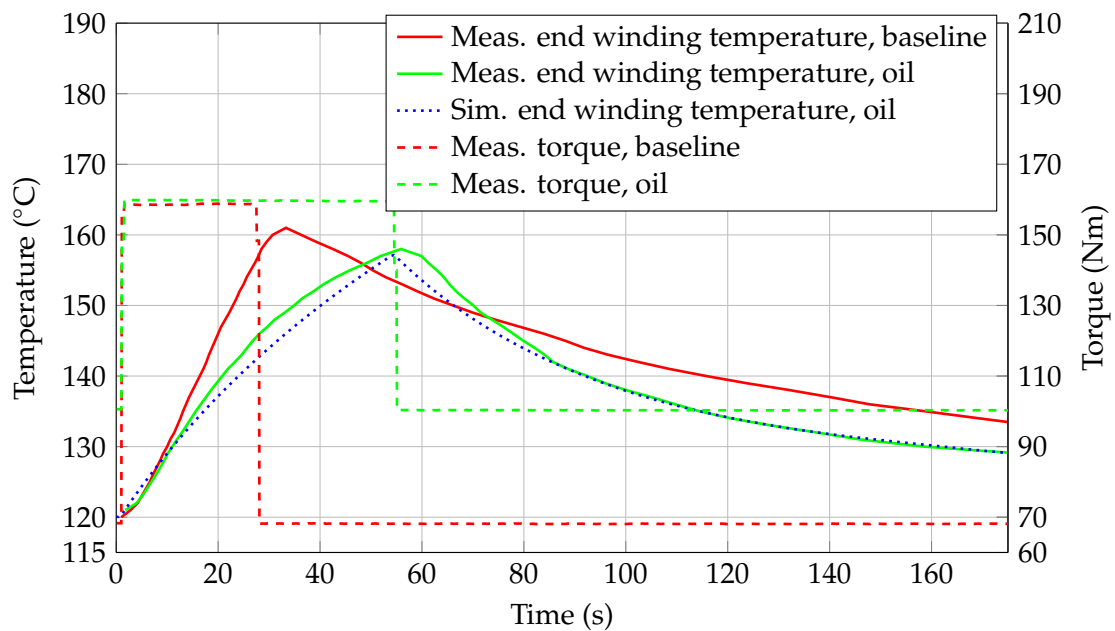


Figure 4.61: Torque pulse step response at 3000 rpm with oil pump at a flow rate of 1.5 L/s .

The measurement runs are used to identify the mean thermal convection coefficient from the end winding surface to the oil with dependency on speed and fluid or mass flow rate (Fig. 4.63). Fig. 4.63: the identification of the mean end winding surface to oil convection coefficients showed that the oil mass flow rate has little influence on the convection coefficient

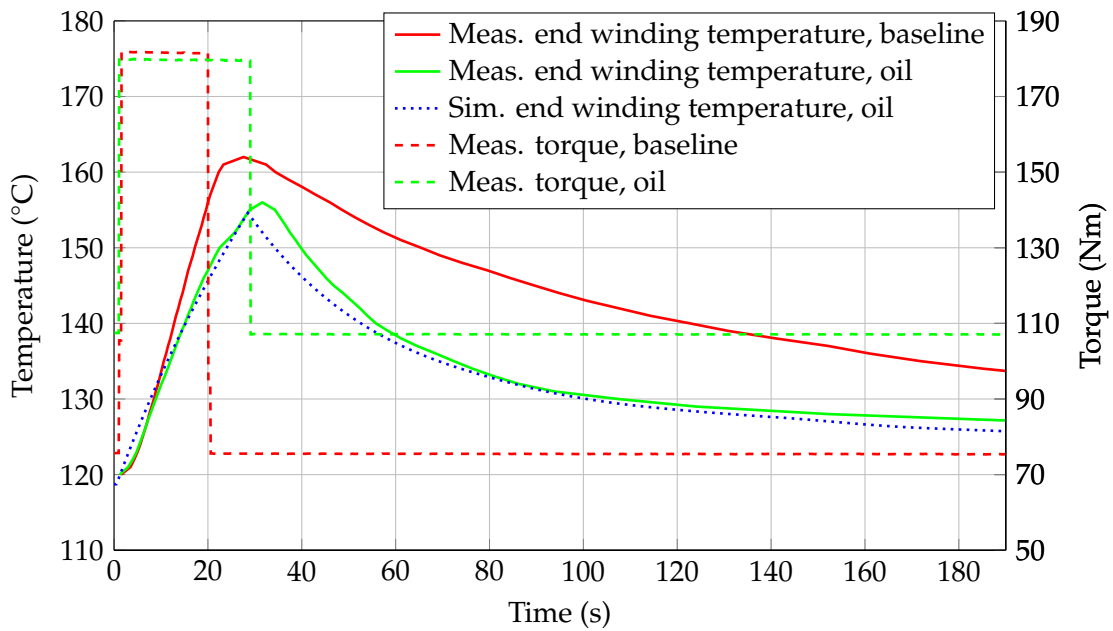


Figure 4.62: Torque pulse step response at 2000 rpm with oil pump at a flow rate of 2.4 L/s .

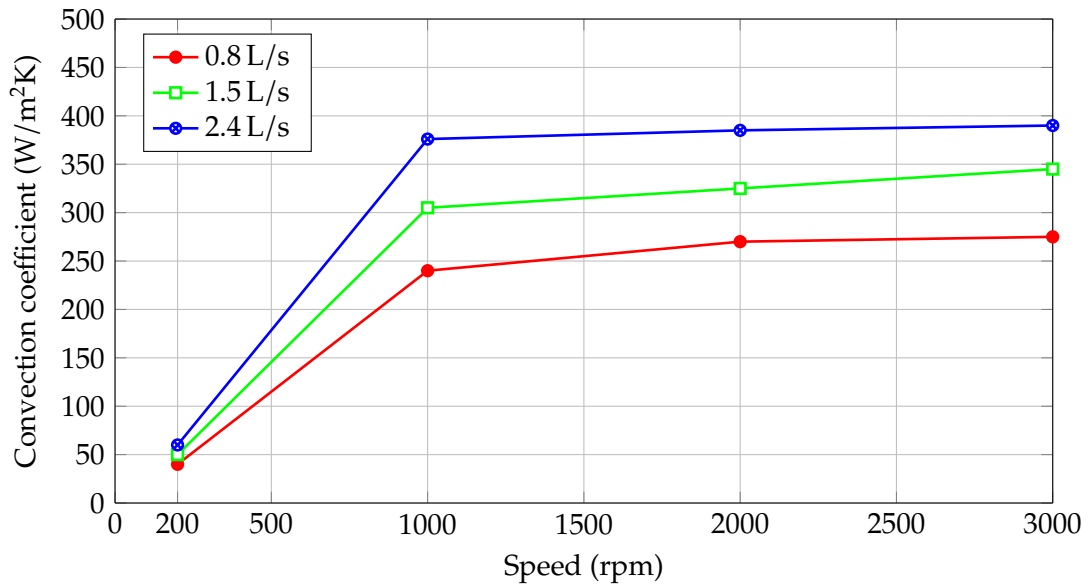


Figure 4.63: Mean convection coefficient from end winding surface to oil at different flow rates and shaft speeds.

and therefore cooling effect at low speeds. The cooling effect increases sharply between 200 rpm and 1000 rpm. At speeds higher than 1000 rpm the speed influence decreases and the mass flow rate dominates the influence on the cooling effect. The total oil amount for generation of those measurement results was 4.5 L. To compute the convection coefficient,

the oil sump temperature, the mass flow rate of the oil and cooling fluid, and end winding temperatures have been measured. The oil sump is cooled using the cooling fluid of the EM. The oil sump temperature (and inlet temperature) was $85^{\circ}\text{C} \pm$ a few K; the outlet temperature was in the range of 100°C (load dependent).

4.6.3 Computation of Convection Coefficients for EM Operation Range

As the measurements available were limited to a few operating points a CFD model was developed to compute the convection coefficients from the end winding (or wetted surface) to the lubricant in Fig. 4.64: ANSYS® CFX®, Release 15.0 was used for the simulations. The CFD model comprises only one end winding, the EM itself is not modeled. The end windings at the DE and NDE slightly differ in terms of the geometrical dimensions, which was neglected in the model.

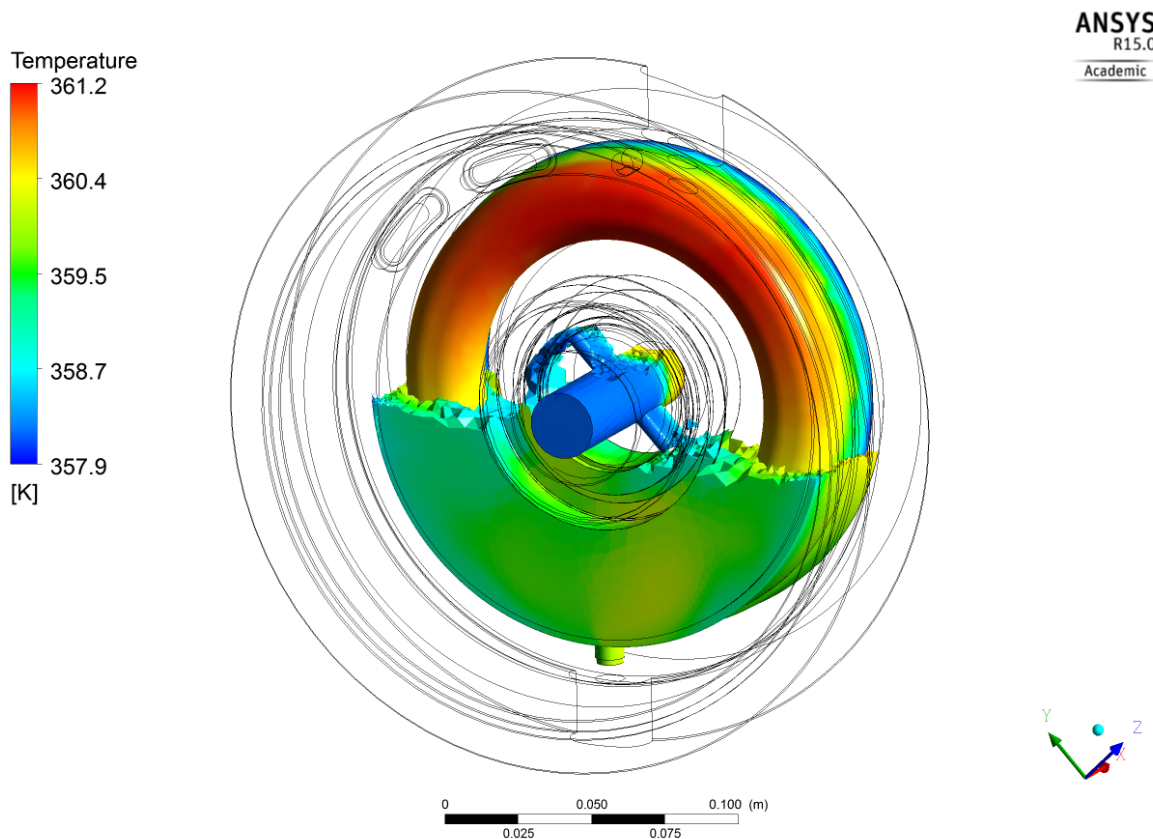


Figure 4.64: eRAD, oil cooling of end windings, CFD simulation results at 200 rpm after 3 s run-in.

The CFD model is used to validate the measurement results in the speed range between 0 and 3000 rpm in Fig. 4.65: the measured coefficients correspond with the computed ones; additionally the cooling effect at 4000 rpm was determined. The results further indicate that

the end winding to fluid convection coefficient does not increase with a further increase in speed. The simulation results proved that the convection coefficient is nearly constant for shaft speeds higher than 1000 rpm, extrapolation of the measured values is possible.

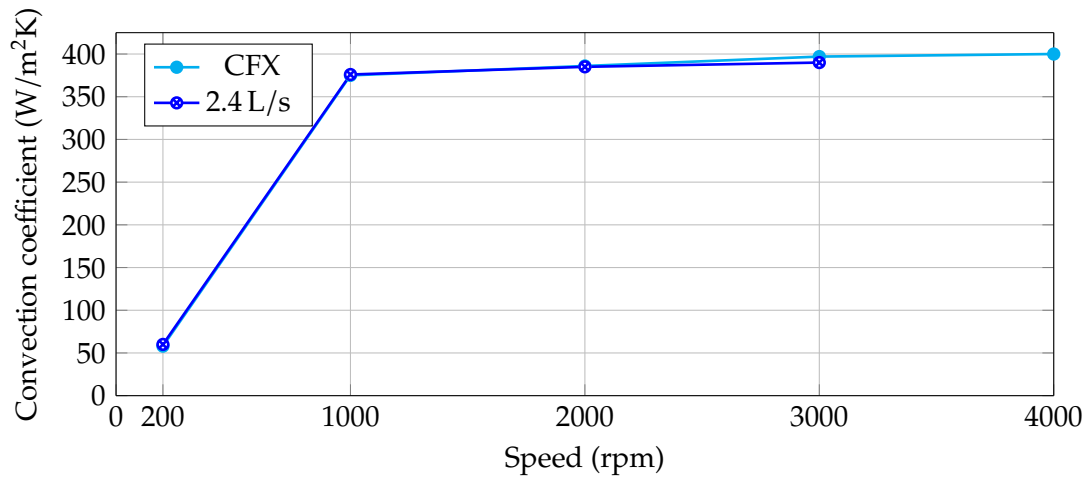


Figure 4.65: eRAD; oil cooling; comparison of CFD computation with measured results; mean convection coefficient from end winding surface to oil at 2.4 L/s flow rate.

The influence of vehicle integration and of an alternative cooling approach on the thermal behavior and modeling of an IPMSM for electric traction application has been studied. To this aim, a complex analytic approach (LPTN) was developed and verified experimentally with test-rig measurements. An additional FEM model was used to allow a more detailed view on the loss distribution between gearbox and EM. Using sensitivity and heat flow analysis to investigate the most critical thermal paths between the winding and the magnets to the coolant, a reduced model was derived by neglecting non-relevant thermal resistances and capacitances. This simplified model allows for online temperature prediction in the inverter software as lower computational capacity is required. Additional heat sources (gearbox) and uncertainties introduced by computed (estimated) or measured signals in the vehicle, influence the accuracy of the model implemented in the inverter software. Especially the influence of the gearbox integration on the magnet and winding temperatures was shown for steady-state and transient (torque step and driving cycle) operating conditions. Considering these uncertainties, a method using an additional temperature sensor to increase the modeling accuracy was introduced. The chapter closed with a design and optimization study using an alternative cooling approach. The study was supported by CFD simulations to derive the convection coefficients necessary to apply in the LPTN.

Chapter 5

Application Study II: Integrated Starter Generator

Using the example of a (crankshaft)-integrated starter generator, with an integrated clutch module and an internal combustion engine attached, a finite element method-based thermal model is introduced. Based on this numerical model, which is verified using measurements, the thermal behavior of the permanent magnet machine is studied. The thermal influence of the vehicle integration on the electrical machine performance is discussed, along with the additional heat sources: internal combustion engine, transmission and dry friction clutch.¹

5.1 System Description

The integrated starter generator (ISG) used as an example case application for the discussions in this chapter, is designed for a hybrid electric vehicle (HEV) and mounted between the internal combustion engine (ICE) and the transmission (TM). The ISG module comes with an integrated clutch to decouple the ICE and allow pure electric propulsion of the HEV, see Fig. 1.5. The electric machine (EM) is designed to: (i) start the ICE, (ii) to support the ICE during acceleration of the vehicle, (iii) to drive the vehicle without ICE support, and (iv) to recover electric energy during braking or deceleration of the vehicle. The energy storage system (ESS) is recharged, if the EM is in generator/recovery mode.

Fig 5.1: The housing of the system has a bell-shaped design to involve a dual-mass flywheel for mechanical damping of the ICE related mechanical oscillations in the drive train. The integrated clutch module is a multi-plate dry friction clutch system (sintered material) with a maximum transmittable torque of 540 Nm. An electromagnetic actuator enables a controlled start of the ICE. For safety reasons, the clutch system is normally open (ICE decoupled). If the clutch is closed, the electromagnetic actuator consumes 25 W continuous electrical power at a voltage range of 6 V to 10 V. The inverter with power electronics is attached to the EM's housing at the bottom. The EM and the inverter are liquid cooled using a 50 % water/glycol

¹Selected results of this chapter have also been published in [43].

mixture. The nominal cooling fluid temperature of the inverter is 75 °C and 85 °C for the EM at a flow rate of 6 L/s.

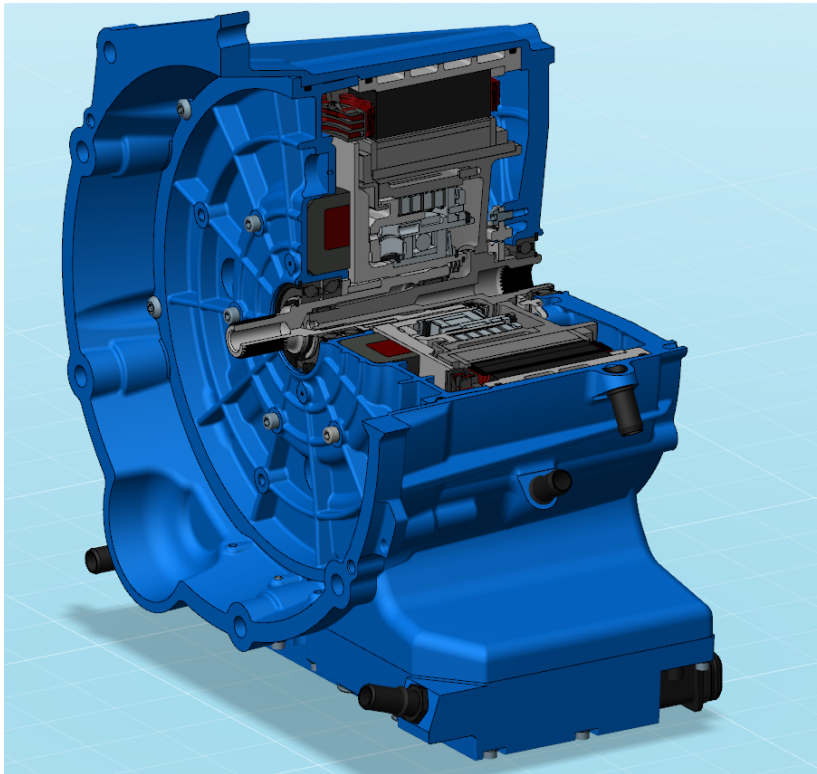


Figure 5.1: ISG 3D illustration.²

Tab. 5.1 details the dimensions of the 80 kW peak interior-mounted permanent-magnet synchronous-machine (IPMSM). Three different skewed rotor types, with 0°, 48° and 72° (electrical) skewing angle, are available. For the 48° skewed rotor prototype, the peak torque is 325 Nm, available from zero up to 2200 rpm (constant torque region) with a maximum speed of 6800 rpm. The DC-link voltage ranges from 270 V to 400 V, depending on the ESS's state-of-charge (SOC).

The real world load spectra of the ISG's EM is defined by various influencing factors during vehicle operation, such as: the torque demand, the HEV operating strategy, and the driver (skills). Because of the complex interaction of EM and ICE, an operating strategy to compute load spectra using a simulation model is required.

For the calculation of the EM torque profile a simple longitudinal quasi-static vehicle model was used (see [164] for the approach). In the case of the ISG an operating strategy was required for the computation of the torque profiles, but was not part of the research work presented.

²Source: Magna Powertrain GmbH & Co KG.

Stator outer diameter	280 mm	Pole pairs	10
Stator steel grade	M270-35A	End winding connection	Delta
Air gap	1 mm	Number of turns	65
Active length	80 mm	Skewed rotor	0°, 48°, 72° electrical
Rotor outer diameter	218 mm	Rotor segments	5
Number of slots	30	Magnets in axial direction	10
Windings	Single tooth	Magnet type	N37UZ ³

Table 5.1: ISG EM data.

5.2 Model

5.2.1 Loss Model

Electric Machine

The winding losses and rotor ventilation (air friction/windage) losses are modeled as presented in Chapter 2. For the computation of the iron losses in different parts of the machine (back iron, teeth and rotor), the (time-domain) approach implemented in ANSYS® Maxwell®, Release 15.0 was used. During the research work also an analytic approach was investigated and implemented, the finite element method (FEM) model was used for cross checking the results, to ensure accuracy.

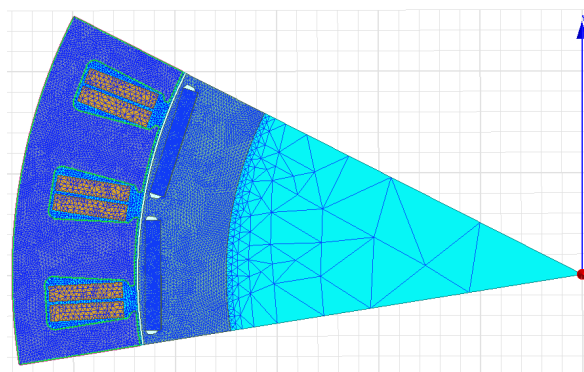


Figure 5.2: ISG, FEM loss computation model, 2D mesh.

The computed iron losses per unit volume and also the magnet losses, are injected in the corresponding volumes of the thermal model. As the magnets of IPMSM are buried in the rotor, and therefore are not directly exposed to the magnetic flux, the 2D computation of the magnets eddy currents was sufficient, and no 3D FEM loss model was used.

³Material data sheet download available on: www.shinetsu.co.jp; accessed on 2015-02-03.

Bearings

Mechanical losses caused by the bearings are computed with semi-analytic/empiric approaches based on databases⁴ for different temperatures and axial load conditions. The axial load of the bearing at the TM end (ball bearing 7006-B-2RSR in Fig. 5.3a) depends on the wear condition of the dry friction clutch: this wear condition changes over the bearing's lifetime; furthermore, this bearing's friction torque (loss power) is related to the axial load (pre-tension). In the example case application, the friction torque of this bearing is in the range of 0.064 Nm (no axial load) up to 0.19 Nm (at 5000 N axial load), both at 7000 rpm. Therefore, in the simulations, a constant axial load of 5000 N (clutch closed) was defined. The temperature, speed and axial load dependency (only for the bearing at the TM end) was implemented using look-up tables in the thermal model.

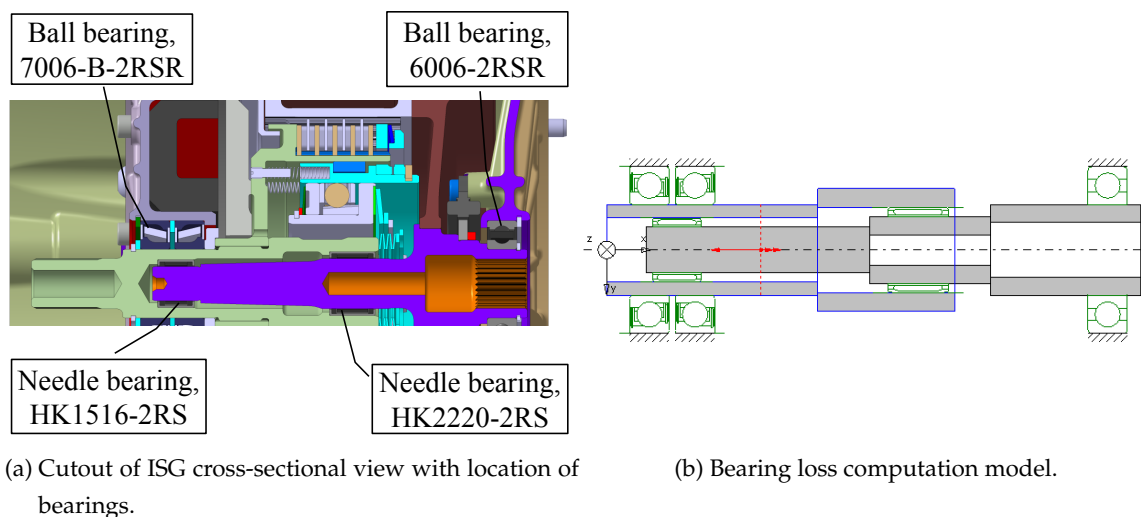


Figure 5.3: ISG, loss computation of the bearings.⁵

Clutch

As the actuator of the dry friction clutch is an electromagnetic system, 25 W ohmic losses of the coil winding are taken into account in the thermal model.

Regarding the frictional losses the situation is more complicated: it is hard to determine a load point which reflects an average thermal operating situation. In dry friction clutches, losses are generated during actuation (opening/closing of the clutch). The thermal energy input caused by friction was computed according to eq. (2.10). Depending on possible differential speeds between EM and ICE which might occur in the vehicle the thermal load may vary in a wide range. Emphasizing a representative situation: If the vehicle is directly

⁴BEARINX, Schaeffler Technologies AG & Co. KG, see www.ina.de for details.

⁵Source: Magna Powertrain GmbH & Co KG.

driven by the EM and more power is required for acceleration, the ICE needs to be started. Then, the clutch is closed (controlled by the clutch control software) to start the ICE. During the start of the ICE the clutch has to transmit torque at the current differential speed between ICE and EM shaft. The expected energy input per actuation therefore varies with the wear of the friction plates, the differential speed and time needed to start the ICE. For the situation described, an expected differential speed of 2200 rpm was defined. Three actuations per minute with 350 W friction losses are taken into account in the model, as a worst case situation.

5.2.2 Numerical Thermal Model

To compute the temperature distribution and the temperature within the machine's components, such as the end winding temperature or the temperature in the center points of the magnets, a numerical model was implemented into the FEM software. The model was reduced to an angle of 36° for symmetry reasons (Figs. 5.4 and 5.5). The geometry was pre-processed with respect to the mesh quality (achieve homogeneously distributed elements), i.e., small parts are simplified or removed, surface geometries have been smoothed, small drill holes have been removed, screws have been removed or combined with the surrounding material. However, some of these simplifications require an adequate replacement with boundary conditions (e.g., a screw is a thermal contact). The bearings are simplified using a geometrical replacement (Fig. 5.4a) and the windings are modeled as one solid body (Fig. 5.4b).

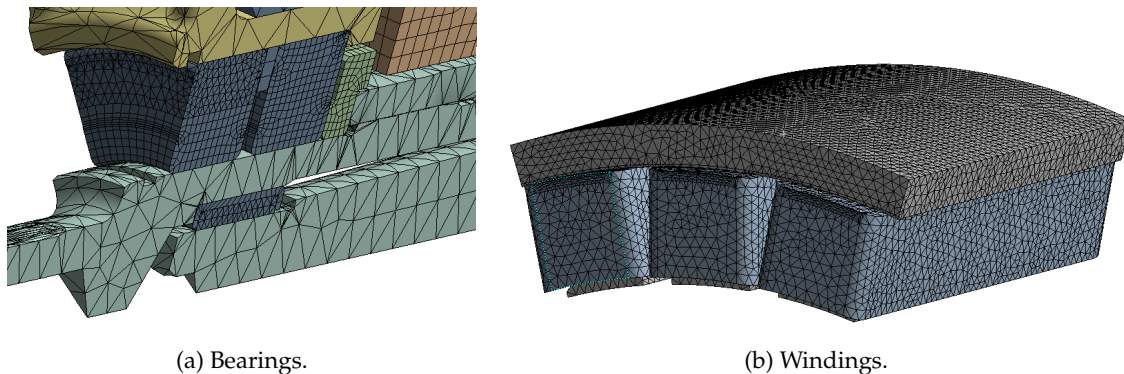
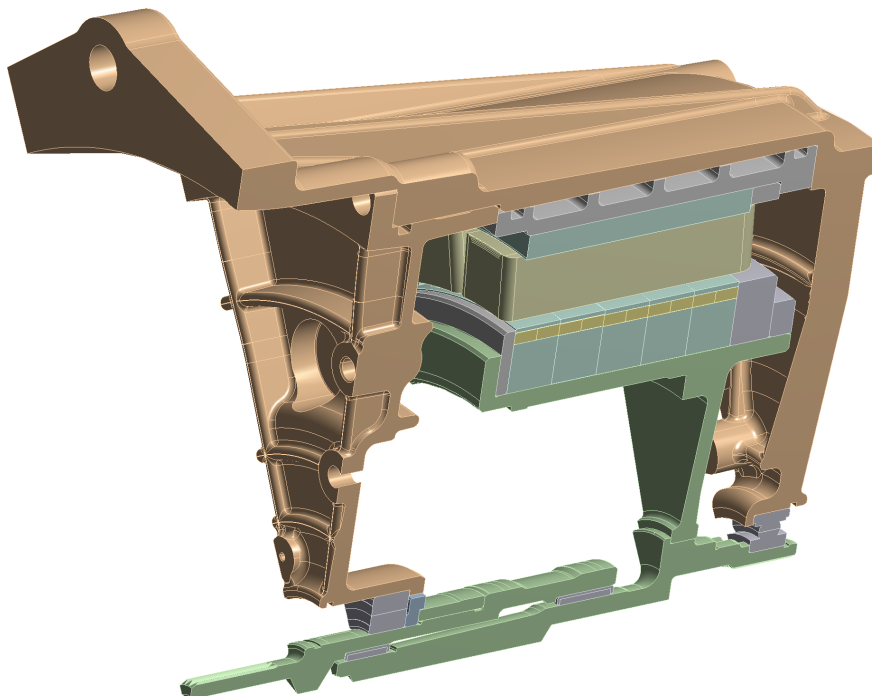


Figure 5.4: ISG, geometrical FEM model simplifications.

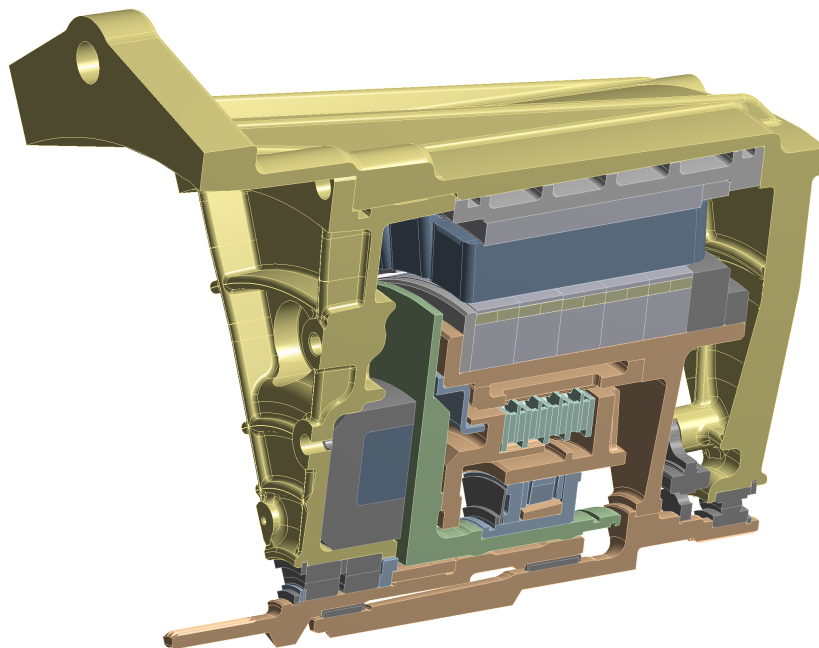
Furthermore, the ISG FEM model was adapted to the test-bench setup of the prototype (Fig. 5.5a) to validate the thermal parameters of the EM's components: the clutch components are removed and temperatures which have been measured on the test-rig (e.g., ambient air), are applied in the model as boundary conditions.

For the system simulation, the EM, the clutch, and the electromagnetic actuator are taken

into consideration (Fig. 5.5b): The inner air was not modeled for the studies presented. As stated before, for the validation of the model the inner air temperature was measured at different locations inside the EM's housing, near the end windings. These measurement results were applied as boundary conditions for the validation simulation. As the inner air, for each operating point measured differs between approx. 75 °C and 85 °C, a mean value of 80 °C was defined for all other simulations.



(a) Thermal model for EM validation, comprising the EM only.



(b) Thermal model for system simulation, including the EM, the clutch and the electric actuator.

Figure 5.5: ISG, FEM thermal models.

5.2.3 Thermal Parameters

Electric Machine

The thermal parameters are defined/computed using a mixed approach: computational fluid dynamics (CFD) simulation results in combination with measurement results and literature (e.g., [97, 101–103, 169]) are used to determine selected heat transfer parameters. Tab. 5.2 shows some of these pre-calculated thermal parameters for the simulation of the ISG application using the approaches introduced in Chapter 3. Thermal conductance and capacitance values, which are not shown in Tab. 5.2, are taken from the corresponding material/product data sheets.

THERMAL RESISTANCE	THERMAL RESISTANCE TYPE	APPROACH FOR PRE-CALCULATION	VALUES
Air gap	Convective	[106, 128]	See Fig 5.6
Inner surfaces to ambient air	Convective	[83, 97, 99, 129]/ eq. (3.29)	≈ 5 to $100 \text{ W/m}^2\text{K}$
Stator core to cooling jacket	Contact	Section 3.5	$3000 \text{ W/m}^2\text{K}$
Cooling jacket to fluid	Convective	CFD Simulation	$2500 \text{ W/m}^2\text{K}$
Cooling jacket to housing	Contact	Section 3.5	300 to $500 \text{ W/m}^2\text{K}$
Winding to stator core	Contact	Material data sheets	$852 \text{ W/m}^2\text{K}$
Bearing HK1516	Contact	[102, 103]	$552 \text{ W/m}^2\text{K}$
Bearing HK2220	Contact	[102, 103]	$552 \text{ W/m}^2\text{K}$
Bearings 7006	Contact	[102, 103]	$468 \text{ W/m}^2\text{K}$
Bearing 6006	Contact	[102, 103]	$768 \text{ W/m}^2\text{K}$
Winding, axial	Conductance	[101]	401 W/mK
Winding, orthogonal	Conductance	[101]	3.3 W/mK

Table 5.2: ISG thermal model parameters.

The winding is defined using orthotropic thermal conductivity parameters: in the axial direction the thermal conductivity of copper is the major one; in the orthogonal direction the insulation material influence is more significant.

The computation of the speed depending convection from the surface of rotating parts to the ambient air inside the machine is a complex task if the air flow inside the machine is considered in detail [99]. Analyzing the approaches of [83, 97, 99, 129], a rotor speed depending forced convection coefficient $h_{\text{conv,surf}}$ (see [99]) was defined based on eq. (3.29), fitted with the measurement results. Although the surface speed varies at each surface inside the housing, the forced convection coefficient of eq. (3.29) is applied to all surfaces in contact with the inner air in the end winding region [97] and the rotor.

The air gap thermal resistance with minor temperature dependency and major speed

dependency, is shown in Fig. 5.6.

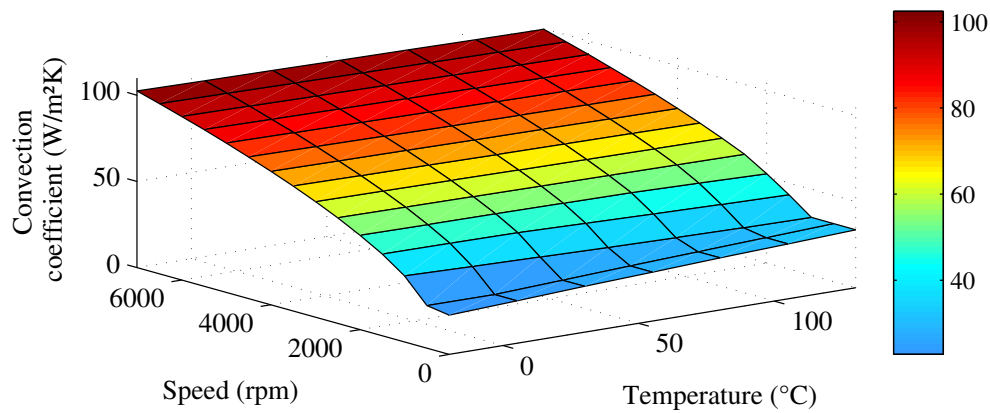


Figure 5.6: ISG air gap thermal convection coefficient.

Clutch

In the case of the clutch (Fig. 5.7), the thermal parameters change during operation, depending on the clutch state: opened or closed. If the clutch is actuated, (pressure dependent) thermal conductance in axial direction between the inner and outer discs and the friction discs occurs. If the clutch is opened, this thermal conductance in axial direction is very low, as in the ideal case the friction discs and inner/outer discs are not in contact with each other. However, for both cases it is hard to determine a realistic value without measurements. Also, the thermal convection coefficients from the disc and clutch drum/carrier surfaces are hard to determine using an analytic approach or literature.

Therefore, all thermal parameters used for the clutch model are totally based on measurement results: The axial thermal conductance values between the discs are assumed as an ideal thermal contact, the contact surfaces between the disc carriers and discs, and the thermal convection coefficients to the ambient air are fitted with clutch test-rig measurement results.

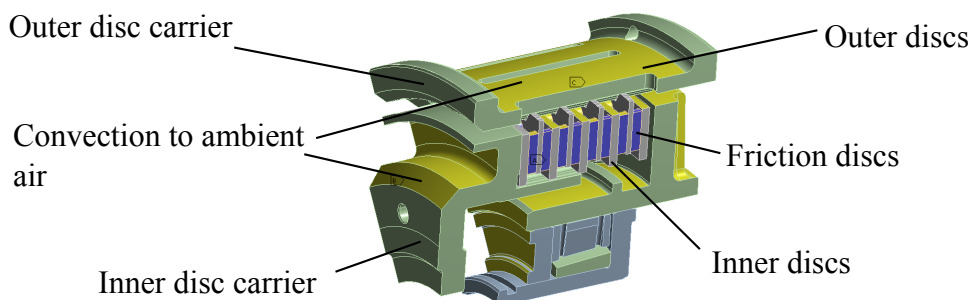


Figure 5.7: ISG clutch model (for validation).

5.3 Model Validation

5.3.1 Losses

The IPMSM losses are computed with an FEM electromagnetic model and compared with measurements in Fig. 5.8. They show sufficient agreement in the low torque and speed region. For example at 500 rpm and 50 Nm the loss difference is only 69 W at a shaft power of 2617 W; the relative loss difference is only 5%.

Fig. 5.9: If the efficiency difference is plotted, the simulation and measurement results show sufficient agreement, too. The deviations are ascribed to the different approaches to compute the current in the inverter software and the maximum torque per ampere (MTPA) computation implemented in the FEM software.

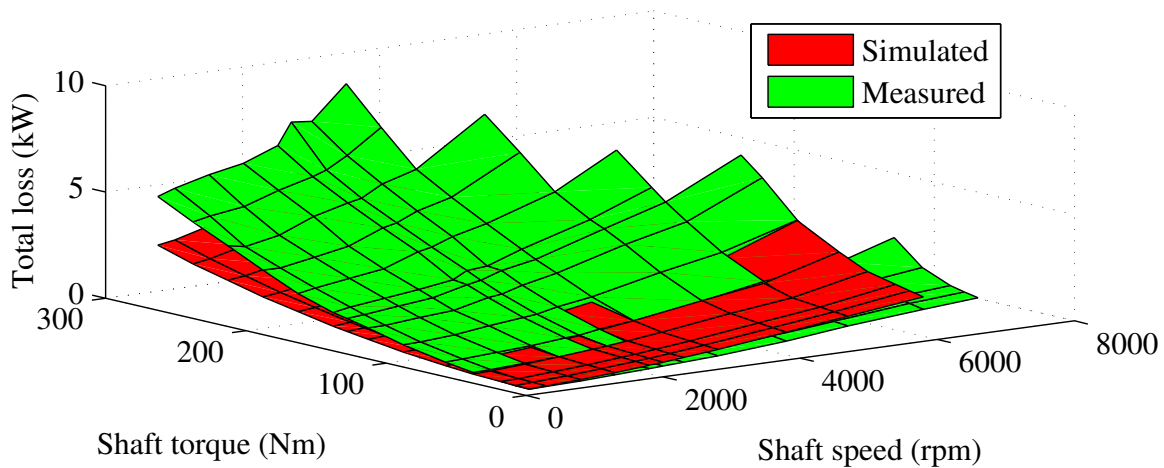


Figure 5.8: ISG, comparison of measured and simulated losses.

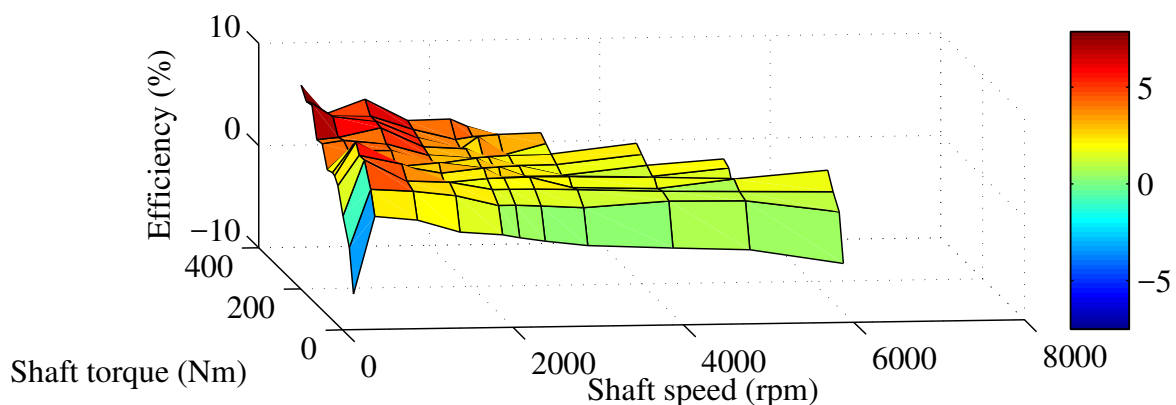


Figure 5.9: ISG, comparison of measured and simulated efficiency.

5.3.2 Numerical Thermal Model Steady-State Validation

Experimental results from thermal measurements are used to validate the thermal resistances, using steady-state operating points at different speeds, torques and coolant temperatures, without the clutch components in Tab. 5.3.

In the simulation model the measured ambient, inner air and coolant temperatures are applied as constant boundary conditions for the steady-state and transient validations. The prototype machine is equipped with thermocouples (TCs) at different locations, i.e., the end winding at the drive end (EW-DE); the end winding at the non-drive end (EW-NDE); the winding in slot (WS); the magnet surfaces in the rotor at the drive end (DE) and the non-drive end (NDE) (R-DE and R-NDE), the housing and the bearings at the DE and NDE; two PT100 thermistors are used as additional reference.

Coolant temp. TC no.	20 % n_{\max} 16 % T_{\max} , 77 °C 105 °C		20 % n_{\max} 13 % T_{\max} , 84 °C 105 °C		20 % n_{\max} 33 % T_{\max} , 71 °C 45 °C		27 % n_{\max} 10 % T_{\max} , 73 °C 103 °C	
	Meas.	Sim.	Meas.	Sim.	Meas.	Sim.	Meas.	Sim.
R-DE 1	90	88	90	93	70	69	77	82
R-DE 2	90	88	90	93	67	69	73	82
R-DE 3	90	88	90	92	69	69	74	82
R-NDE 1	90	89	n/a	n/a	66	69	72	83
R-NDE 2	90	89	n/a	n/a	66	69	72	83
WS 1	118	118	107	112	69	69	105	106
WS 2	n/a	n/a	107	112	71	69	105	106
WS 4	n/a	n/a	107	112	66	69	105	106
WS 5	118	118	107	112	73	69	105	106
WS 6	n/a	n/a	107	112	72	69	105	106
EW-DE 1	n/a	n/a	107	111	n/a	n/a	100	104
EW-DE 3	n/a	n/a	107	111	71	70	104	104
EW-DE 4	n/a	n/a	106	111	69	70	103	104
EW-NDE 1	n/a	n/a	108	112	74	69	106	104
EW-NDE 3	n/a	n/a	108	112	73	69	106	104
EW-NDE 5	118	116	108	112	71	69	105	104
EW-NDE 6	n/a	n/a	108	112	72	69	105	104
Housing	n/a	n/a	97	102	42	46	94	95

Table 5.3: ISG steady-state validation at different shaft torques, speeds and inner air temperatures. All temperatures in °C.

The simulated and measured temperatures of the critical parameters correspond well, with a maximum difference of ± 5 K, which is within the measurement uncertainty of the thermal sensors. A more accurate model would require (transient) coupling with other

simulation approaches (CFD and numerical loss computation) and more detailed measurements, focusing on special modelling issues. Deviations among different sensor locations within the same EM component are caused by the TC mounting/gluing and non-ideal test-rig connections.

5.3.3 Numerical Thermal Model Transient Validation

Machine

To proof the accuracy of the computed material parameters (i.e., volumetric mass density, thermal conductivity, thermal capacitance), transient measurements are mandatory. Furthermore, also the geometrical simplifications, mentioned in Section 5.2, such as removed screws and holes need consideration, as these geometrical model improvements could lead to a change in the thermal mass. Especially the windings are simplified in the FEM models as the modeling of each wire would lead to extremely high computation times.

The computed mean WS temperature is compared with temperatures measured at different positions within the winding in Fig. 5.10: a 8 s peak torque (T_{\max}) step, starting at 10% T_{\max} with 30% n_{\max} shaft speed, was applied. The measured and computed temperatures correspond within acceptable tolerances.

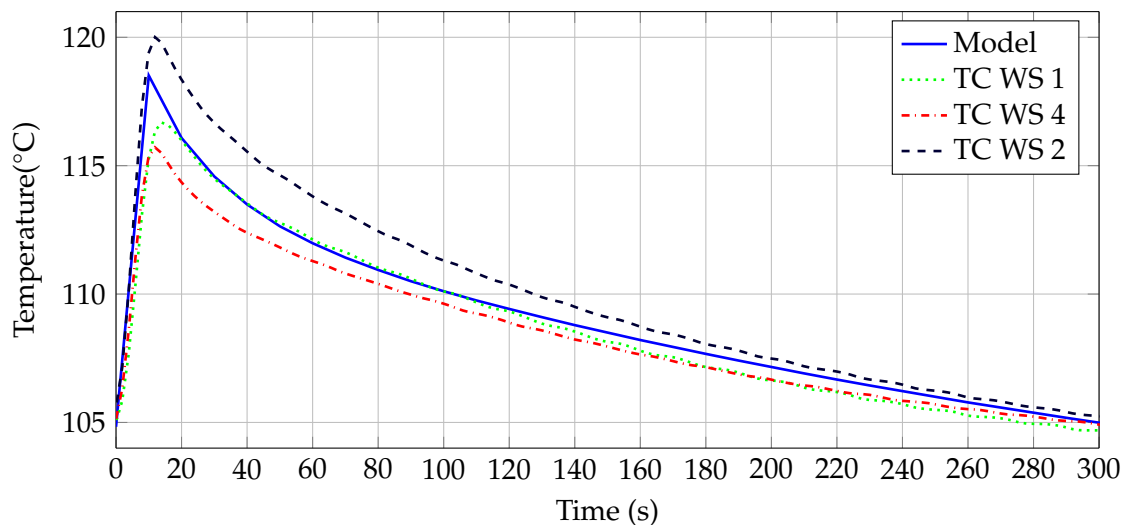
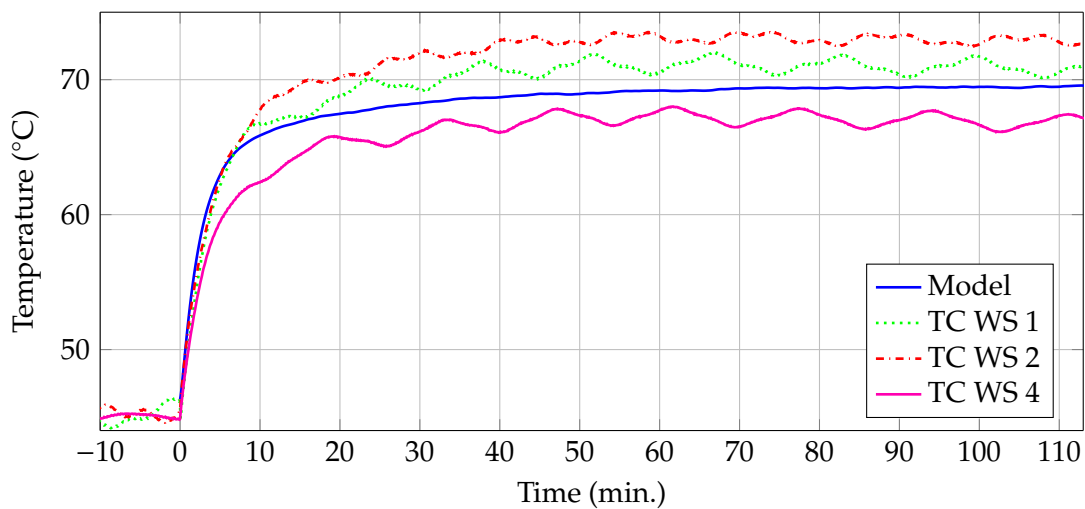
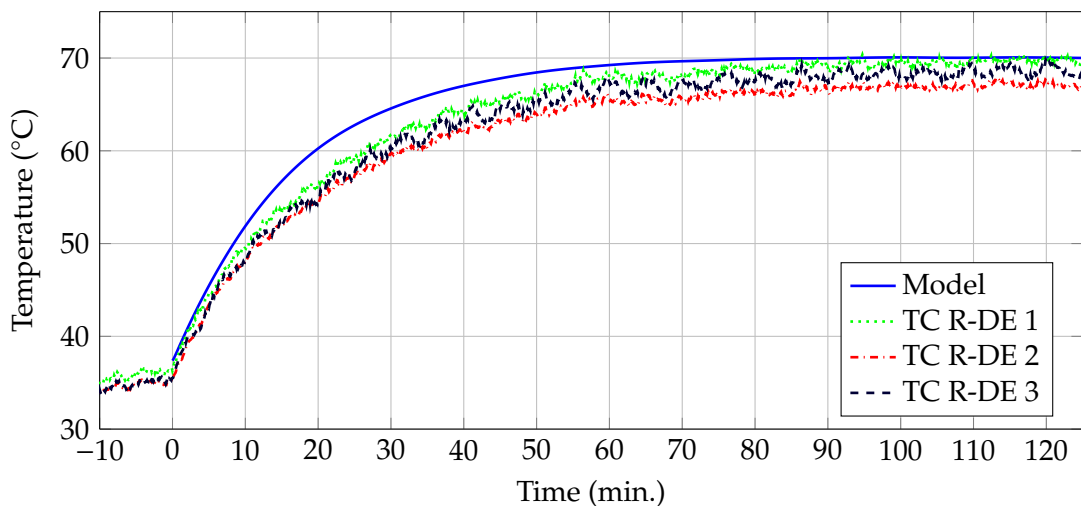


Figure 5.10: Experimental validation of the thermal model: simulated winding-in-slot temperature of a 8 s T_{\max} pulse at 30% n_{\max} compared with temperatures measured with thermocouples (TC), at defined nodes in the winding in the slots (WS).

For further comparison a torque step from 0 to 32% T_{\max} at 20% n_{\max} was applied in Fig. 5.11: the measured and calculated temperatures of the winding in slot and rotor temperatures are presented.



(a) Simulated winding in slot temperatures compared with temperatures measured with thermocouples (TC), at defined nodes in the winding in the slots (WS).



(b) Simulated rotor temperature compared with temperatures measured with thermocouples (TC), at defined nodes in the rotor at the drive end (R-DE).

Figure 5.11: Experimental validation of the thermal model: thermal transient response of torque step from 0 to 32 % T_{\max} at 20 % n_{\max} .

The measured and simulated winding temperatures for the Federal Test Procedure (FTP-72) driving cycle are shown in Fig. 5.12.

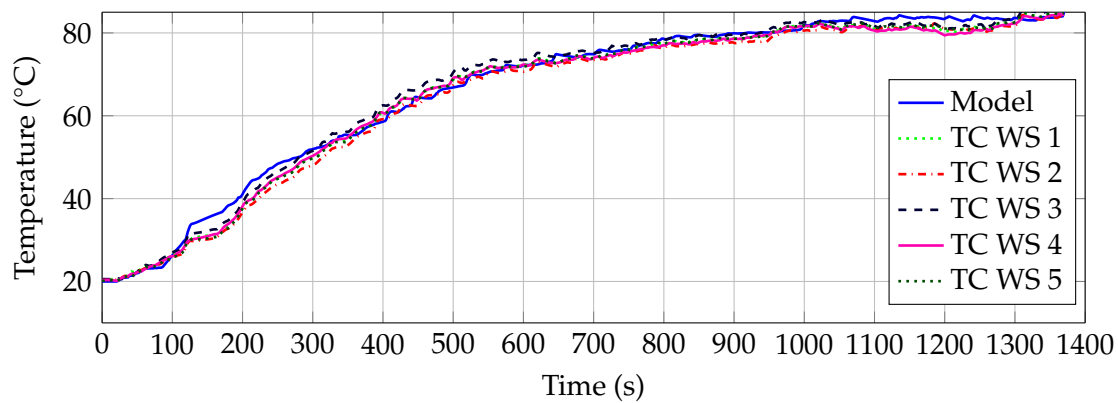


Figure 5.12: Experimental validation of the thermal model: Simulated winding in slot temperature measured with thermocouples (TC), at defined nodes in the slots (WS) during FTP-72 driving cycle.

Friction Clutch

Experimental investigations and verifications were carried out on a clutch test-rig to prove the accuracy of the clutch's thermal model. The cross-sectional view of the clutch test-rig equipped with thermocouples at different locations is shown in Fig. 5.13. The ambient temperature, clutch drum and disc temperature at two locations was measured. Corresponding boundary conditions to reflect the test-rig conditions are applied to the FEM model (Fig. 5.7), for the computation of the validation measurement sequence.

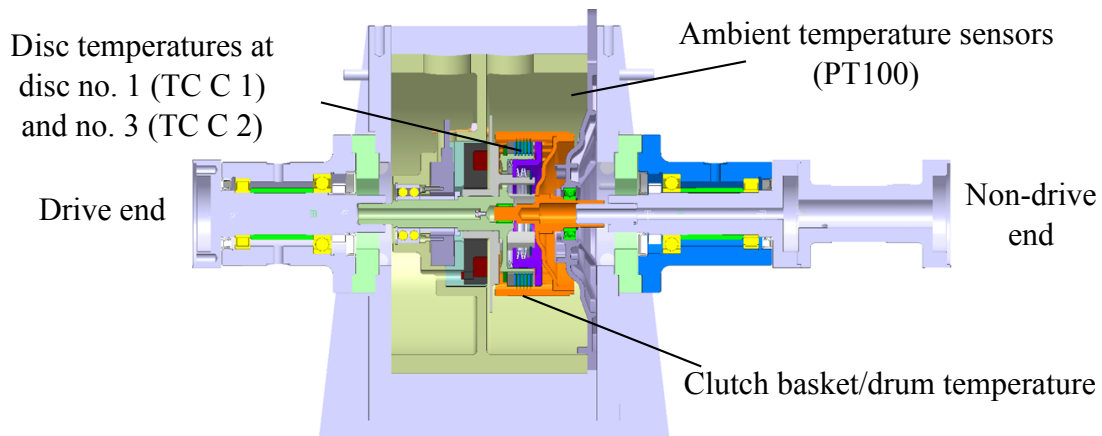


Figure 5.13: Cross-sectional view of ISG clutch test-rig.

To heat up the clutch, a mean heat (loss) power input of 323 W per actuation was applied 30 times using a defined differential speed and torque to be transmitted, with 50 s intermission: Fig. 5.14 shows the computed maximum and minimum temperatures of the discs as well as those measured.

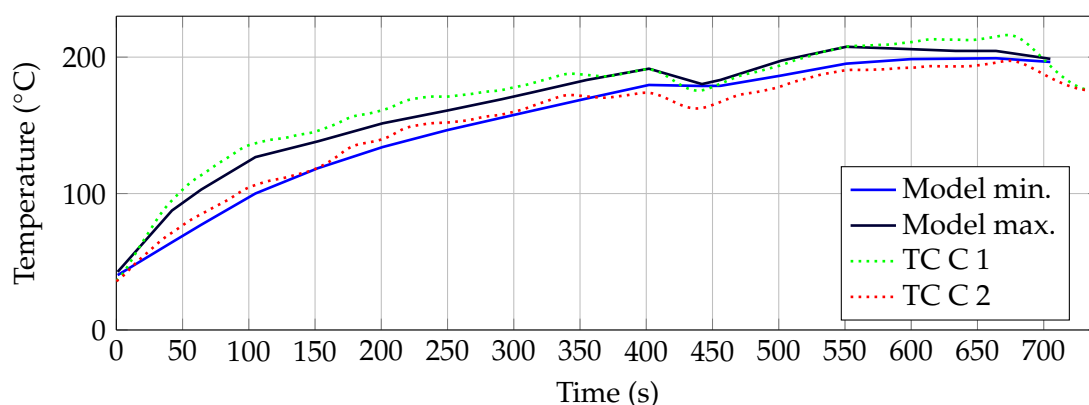


Figure 5.14: Validation of clutch thermal model: Measured and computed disc temperatures during a controlled heating-up sequence.

The thermal responses of the clutch are also within the specified accuracy of the measurement equipment and correspond to the extent required for the purpose of this work: the relative comparison of different integration conditions.

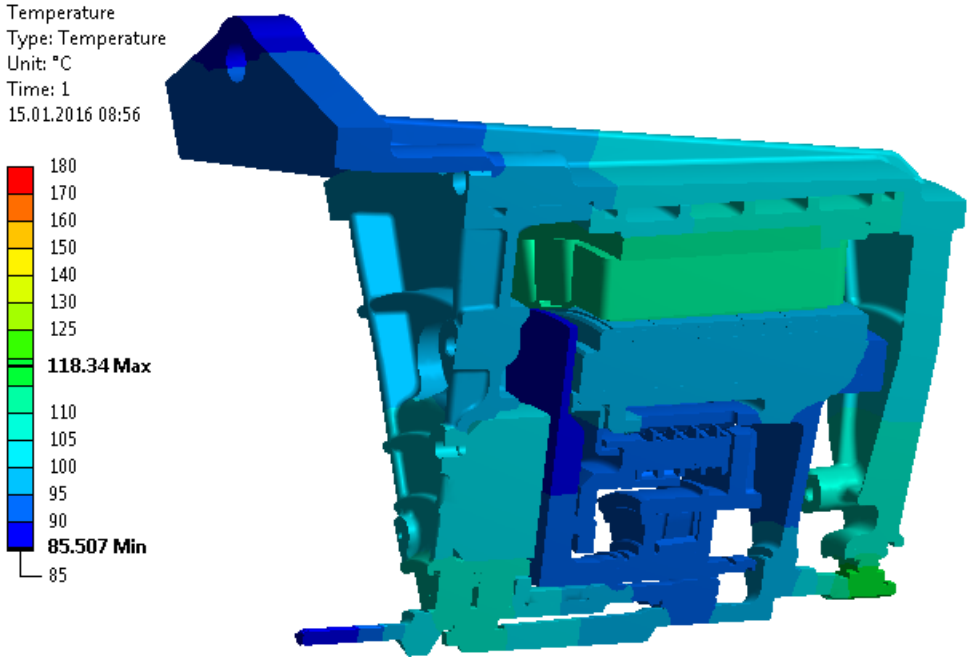
5.4 Dry Friction Clutch and Actuation System Integration

Low Load Operating Point with Constant Clutch Load

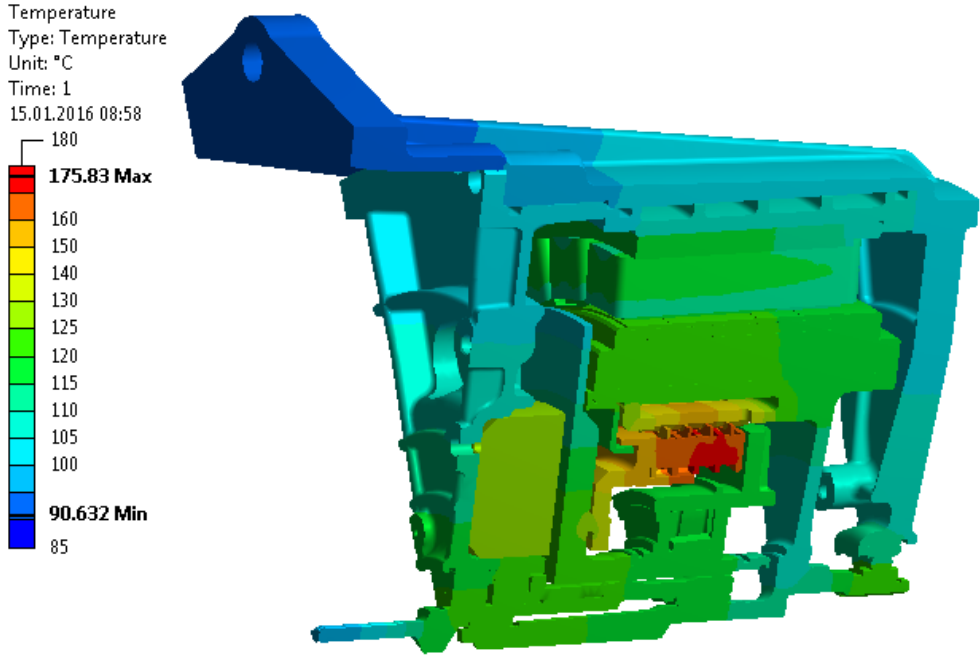
Whenever the ICE and ISG need to be coupled or decoupled, the clutch is actuated. Fig. 5.15b shows the simulation of a worst case actuation (three clutch actuations per minute result in a mean loss of 350 W) for a rather moderate operating point of the ISG of 7.5 kW at 2000 rpm: The influence of the clutch actuation on the different investigated temperatures differs for each of the components: when the ISG is operated at the comparatively low load operating point shown in Fig. 5.15, the computed mean winding temperature increases by 2 K only and the magnet temperature by 25 K.

As the additional losses caused by the dry friction clutch and the actuator are almost the same as the total machine losses in this operating point, which correspond to 36% of the total machine losses in the nominal operating point, the additional heat load on the cooling system is very low. In this case, the possibly maximum occurring heat load of the additional losses is not critical (for the cooling system), as the machine's cooling system is designed to manage total heat loads of more than 10 kW for transient conditions.

Note that the model also further allows investigation of the clutch temperature, which indeed might reach temperatures of more than 200 °C and thus is the hottest element of the system.



(a) Without clutch and actuator losses (low load baseline case).



(b) With clutch and actuator losses.

Figure 5.15: Simulation of clutch influence on machine thermal behavior; 2000 rpm, 7.5 kW, three clutch actuations per minute.

Nominal Operating Point with Variation of Clutch Load

The general findings obtained for the low load case do not change when the ISG is operated at its nominal operating point. In Fig. 5.16 the clutch actuation interval was varied in the nominal operating point: As expected, again, the additional losses introduced into the system by the clutch and the actuator have negligible influence on the winding temperature with a computed increase of 5 K for seven actuations per minute.

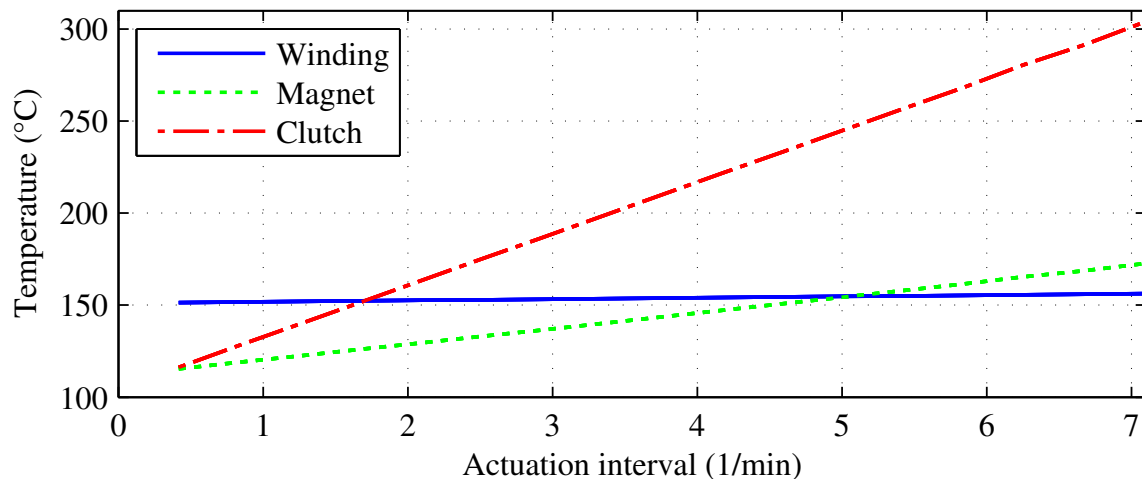


Figure 5.16: Influence of the additional clutch heat load on magnet, winding and clutch temperature at 2380 rpm and 30 kW.

The computed bearing temperatures reach 133 °C for the DE and 155 °C for the NDE bearing. This temperature increase is expected to be problematic for the grease and therefore the lubrication of the bearing: Commonly, standard grease-lubricated bearings have a maximum temperature of approx. 110 °C. Only if special grease-lubricants and bearings are used, temperatures above 150 °C are possible.

A linear increase of the magnet temperature of 6 K per actuation per minute is identified. Therefore, the magnet temperature needs to be monitored in the control software to ensure that the magnets are operated within their absolute maximum ratings.

5.5 Vehicle Integration Study: ICE and Transmission

For ISG applications, a crankshaft temperature of 150 °C and an ambient temperature of 130 °C at both flange sides are worst-case assumptions in the simulations [170].

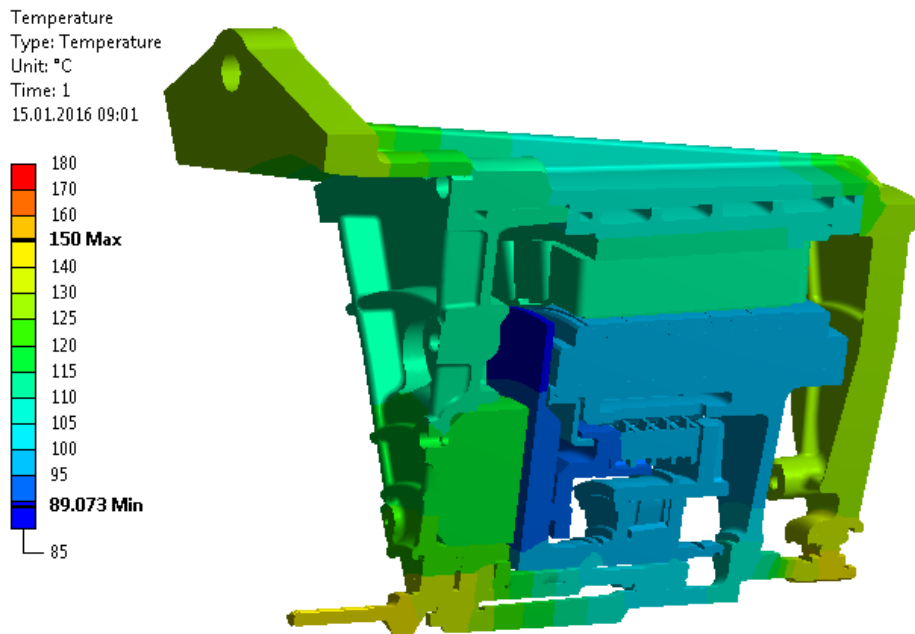


Figure 5.17: Simulation of ICE and TM influence on machine thermal behavior; 2000 rpm, 7.5 kW.

As the vehicle's main clutch also heats up the DE end of the shaft, a DE temperature of 140 °C is defined in the simulation. This, again, is a worst-case assumption: usually, the crankshaft temperature is defined by the oil sump temperature, which has a nominal value of 120 °C. Fig. 5.17 shows the computed temperature distribution with clutch deactivated, for a low load operating point of 30 % n_{\max} , 10 % T_{\max} . The results illustrate the influence of the thermal environment on the machine's temperature: when comparing with the situation without any adjacent heat sources of Fig. 5.15a (low load baseline case), the increase in winding and magnet temperature is below 1 K, the bearing temperature at the DE increases by 23 K and the one at the NDE by 30 K (compared to the baseline case).

In the nominal operating point of the machine (2380 rpm, nominal torque), which can also be referred to as the thermal load point the machine has been designed for, the winding and the magnet temperatures increase by less than 1 K (computed: 0.3 and 0.7 K respectively). However, the bearing temperature at the NDE increases by 14 K, the one at the DE by 16 K, considering absolute temperature values, the NDE bearing with 153 °C might be critical in this case (ICE side).

5.6 Vehicle Integration Study: Steady-State System Simulation

5.6.1 Combined Influence of External Heat Sources

The overall influence of the clutch (three actuations per minute), ICE and TM (for the baseline low load operating point of Fig. 5.15a) is shown in Fig. 5.18. The bearing temperatures are computed to 141 °C, and 145 °C respectively. These temperatures are considered critical, and their reduction would need further consideration in the design process: One possible approach is the use of high temperature grease, which comes with higher costs.

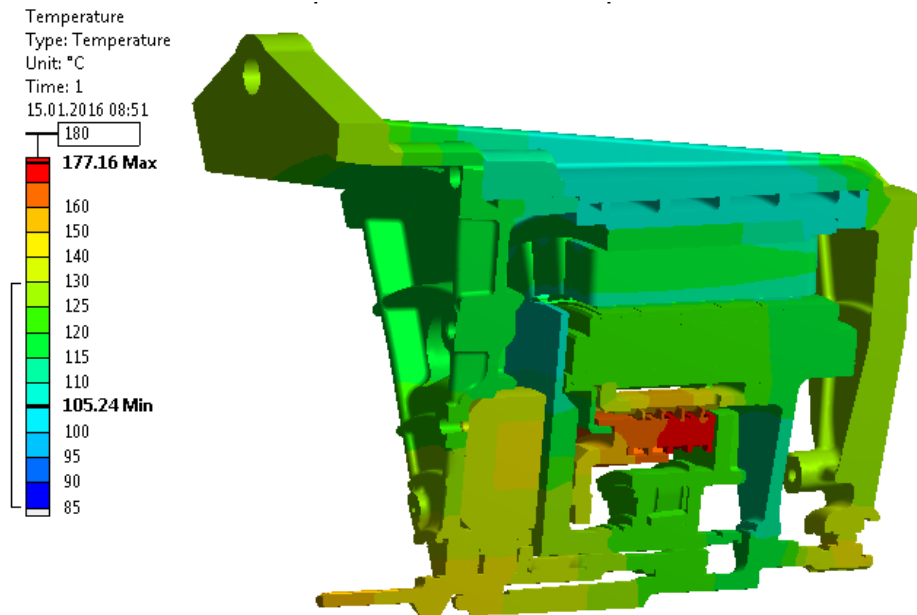


Figure 5.18: Simulation of ICE, TM and clutch influence on machine thermal behavior; 2000 rpm, 7.5 kW.

The same analyses were carried out for machine operation at nominal torque and speed with an inner-air ambient temperature of 105 °C, which is estimated from the test-rig measurements. The computed winding in slot temperature increases by 2 K and the magnet temperature by 25 K.

However, the computed bearing temperature reaches 162 °C at the ICE (crankshaft) side, which is 7 K above the conditions without clutch. This enhances the finding for the low load operating point, that the bearing temperature would need to be reduced in the further design process.

5.6.2 Parameter Correlation Analysis

To investigate the correlation of the additional heat sources (clutch, ICE and TM), a parameter correlation analysis (method of C. Spearman [171]) was carried out, using the numerical simulation model. The sensitivities chart in Fig. 5.19 shows the computed correlations. The Spearman's rank correlation coefficient ρ (also denoted r_s , $-1 \leq \rho \leq 1$) shows the strength of the correlation, where values close to one imply a strong correlation.

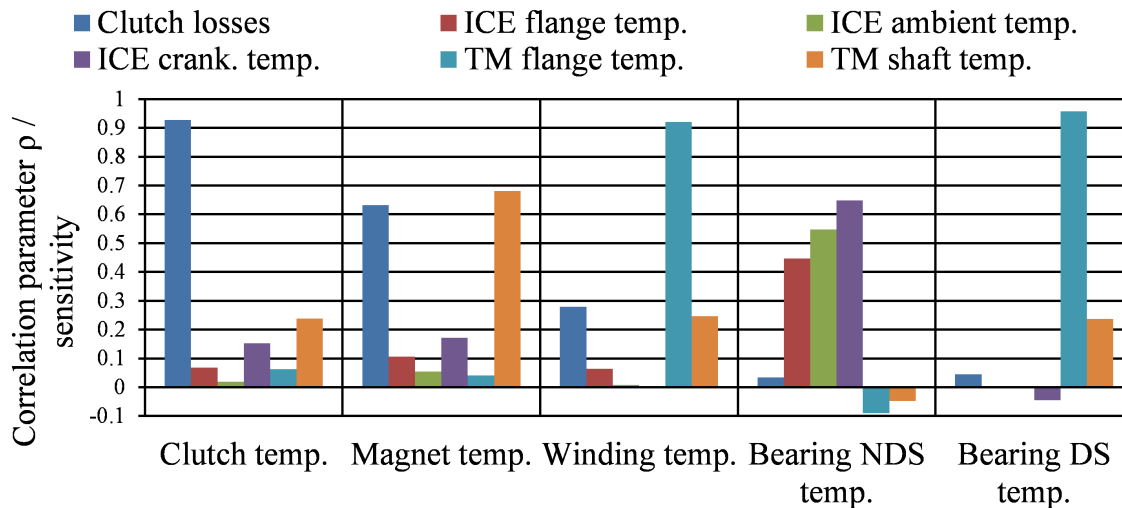


Figure 5.19: Parameter correlation analysis in nominal operating point.

The following most important correlations are identified:

- The clutch temperature correlates strongly with the clutch losses ($\rho = 0.93$).
- The magnet temperature is influenced by the clutch losses ($\rho = 0.63$) and the TM shaft temperature ($\rho = 0.68$).
- The winding temperature is very sensitive to the TM flange temperature ($\rho = 0.92$).
- The bearing at the NDE has a mean correlation to the ICE's boundary conditions ($\rho \approx 0.55$).
- The bearing at the DE is sensitive to the TM flange temperature ($\rho = 0.96$).

The negative correlations are very small, and therefore are neglected in further considerations.

5.7 Real World Simulation: Driving Cycle

To complete the study, the thermal behavior of the EM for the FTP-72 driving cycle was investigated.

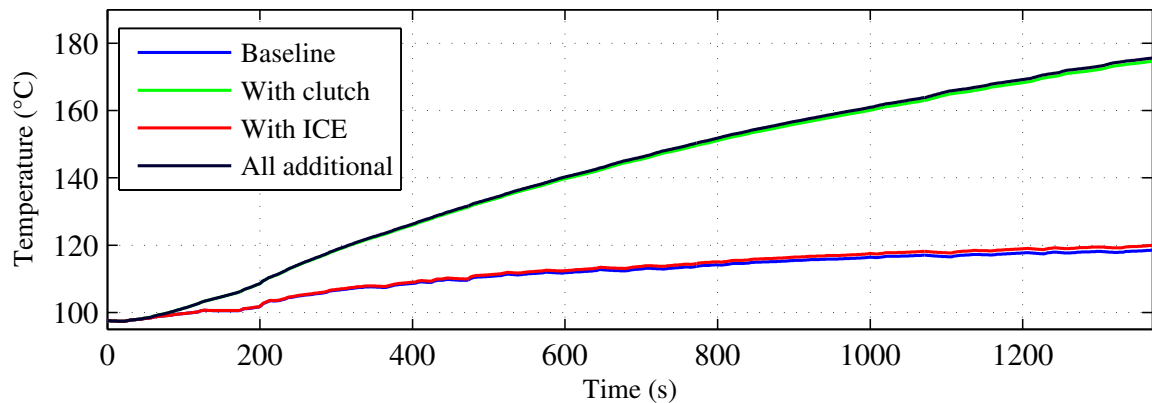


Figure 5.20: FTP-72 driving cycle: computed rotor temperatures, for none, one of the two, or both external heat sources coupled to the ISG.

Exemplarily, Fig. 5.20 shows the computed rotor temperatures, for none, one of the two, or both external heat sources coupled to the ISG. This temperature is commonly considered very critical since it could lead to demagnetization of the magnets.

With both, the clutch (three actuations per minute) and the ICE (shaft temperature) coupled, the computed temperature increases by 78 K over the duration of the cycle. Without these external heat sources, only a 21 K increase is computed.

The influence of vehicle integration on the thermal behavior of an ISG system for a hybrid electric vehicle is studied. To this aim, a numerical thermal model of the EM components was developed and verified experimentally. Using this model, the influences of the integrated dry friction clutch module, including the electromagnetic actuator, and of the ICE on the (thermal) performance of the machine were investigated. Summarizing the results derived in the previous sections:

- a.) *Clutch*: Clutch losses could lead to critical magnet temperatures. The parameter correlation analysis results in a correlation factor of $\rho = 0.63$. Therefore, the magnet temperature and frequency of clutch actuations need to be monitored during vehicle operation. A thermal insulation layer between the rotor stack and its carrier does not provide a suitable solution, as the thermal path for the cooling of the rotor losses would be clipped off.

The winding temperature remains hardly affected by the clutch actuation.

Since the losses introduced into the system by the clutch only influence the rotor temperature to a noteworthy extent, such integration/coupling does not have a significant effect on the stator design parameters (e.g., current loading).

- b.) *ICE/TM*: For the operating points investigated in this work, notwithstanding the clutch, the influence of the ICE and the TM on the three investigated temperatures, winding, magnet, and bearing, was found to be negligible.

The parameter analysis showed a strong correlation ($\rho = 0.92$) between the TM flange and the winding temperature, however this is only critical if clutch losses also occur to an excessive extent.

The magnet temperature is influenced by the TM shaft temperature ($\rho = 0.68$) and the clutch losses ($\rho = 0.63$).

- c.) *FTP-72 driving cycle simulations*: an increase of the rotor temperature by 57 K if all relevant internal (losses occurring within the EM) and external loss sources (ICE/TM, clutch) losses are considered was simulated. A remarkable influence of the clutch losses on the magnet temperature of 6 K per actuation per minute was computed. The bearing at the NDE temperature shows a mean sensitivity ($\rho \approx 0.55$) to the ICE ambient, the ICE flange and the ICE crankshaft temperature. The highest sensitivity has the bearing at the DE temperature to the TM flange temperature ($\rho = 0.96$).

Chapter 6

Application Thermal Performance Comparison

With respect to different cooling approaches, such as air cooling or liquid cooling, published correlations of either power and/or torque density with current loading and magnetic flux density are available in literature. The applicability of these correlations for electric machines used with hybrid electric vehicles and electric vehicles, and their different integration locations (e.g., gearbox, transmission, internal combustion engine) and functionalities, is limited. Using the introduced integrated starter-generator and the electric rear axle drive example case applications, the influences of the rough thermal environment (heat transfer paths) on the air gap shear stress is discussed. Real world driving cycles, heat sinks and sources external to the machine on the thermal design of the machines are regarded, expanding the limitations of the conventional design approach by quantifying the air gap shear stress of the machine. The gearbox influence is studied using the eRAD application. The clutch and internal combustion engine heat load influence is studied using the (crankshaft)-integrated starter generator application.¹

6.1 Approach

As already shown in Chapter 1, tables relating the different performance parameters for various cooling types, and for steady-state operation, are available. Most of these correlations were developed years ago and their application is limited to the case that no additional heat source, heat sink or thermal load is coupled to the electric machine (EM). Here, in the hybrid electric vehicle (HEV) context, examples of such include a gearbox, a transmission (TM), an internal combustion engine (ICE) or any type of actuator that is coupled to the EM.

For example, in the case of the integrated starter generator (ISG) application, the rotor is directly connected to the crankshaft and the crankshaft temperature can reach up to 150 °C with ambient temperatures of 130 °C on both flange sides [170].

To this aim, the thermal load during selected driving cycles for the two example case

¹Results of this chapter have also been published in [45].

applications, the ISG and the electric Rear Axle Drive (eRAD) is investigated. The gearbox influences are studied using the eRAD application. The clutch and ICE (with the TM) heat load influence are studied using the ISG application. Both example case applications consider water-cooled interior-mounted permanent-magnet synchronous-machines (IPMSMs) and enable the vehicle to be driven purely electrically; in the case of the ISG only when the dry friction clutch is opened. For comprehensiveness, the systems are reviewed:

- *eRAD*: The EM of the eRAD application is a 50 kW peak power, 200 Nm peak torque, IPMSM machine with v-shaped buried magnets and distributed winding. An additional gearbox is mounted at the drive end (DE), a disconnect dog clutch allows the EM to be disconnected at higher vehicle speeds (burst speed). The eRAD application is thermally influenced by the gearbox attached (see Chapter 4).
- *ISG*: The ISG machine, with 75 kW peak power and 325 Nm peak torque, is sandwiched between the ICE and the transmission (Fig. 1.5, p. 9); the clutch module with a dry friction clutch is integrated into the rotor. The ISG application is thermally influenced by the transmission and by the ICE over the crankshaft (see Chapter 5). If compared to the eRAD application, whose bearings are direct oil lubricated and therefore also cooled, the bearings of the ISG application may be thermally critical as they are located close to the ICE and transmission and lubricated using a grease.

The eRAD thermal model is calculated using the experimentally validated analytic approach (Section 4.2.2, p. 53) for the investigations presented. For the ISG analysis the experimentally validated finite element method (FEM) thermal model is used (Section 5.2.2, p. 109). Note, that the chosen modeling approach, either analytic (such as lumped parameter) or numerical, does not influence the results worked out in this thesis, as long as the accuracy of the modeling is ensured and the simulation time is not relevant.

EMs have a region with an optimal efficiency, hence working condition, the efficiency is lower outside this region [172]. Here, the influence of such additional heat sources on σ and on A is quantified. σ enables a performance comparison using a single parameter: the air gap shear stress σ was used in [173] as figure of merit and [174] uses this parameter to compare radial and axial flux machines. Referring again to Chapter 1, sizing equations are discussed in [10, 173, 175], a comparative study for the design of EMs for electric vehicle (EV)/HEV applications is presented in [176], a commercial review is given by [172] or [173].

Focusing on the (typically identified as most critical) magnet and end winding temperatures and using mainly the Federal Test Procedure (FTP-75), these influences are quantified by scaling σ . To show the significance of the influences, some parameters such as the recuperation torque and the gearbox loss distribution are varied. The driving cycles are used to further quantify an operation zone of interest which is useful for defining an optimization

strategy of the machine design, which also compares the current sheet loading for both applications.

6.2 Thermal Utilization

6.2.1 eRAD

Overview

Using the presented models and the quasi-static vehicle model (see [164] and [6]) for the eRAD application, the thermal responses of the magnets and end winding at the DE side was analyzed, as these are the hot-spots. The FTP-75 driving cycle was used to investigate the machine's hot-spot temperatures, assuming that deceleration is managed by 100 %, which is a simplification. The influence of the recuperation on the results is emphasized separately. Further common cycles are used to gain more simulation results for the review of the design parameters. The gearbox loss distribution was assumed fixed, based on the FEM computation results in Section 4.5.5, p. 93, but is also varied in Fig. 6.8. Furthermore, the influence of (more realistic) recuperation torques on the thermal response of other driving cycles, e.g., worldwide harmonized light vehicles test procedure (WLTP), and of the gear loss distribution shaft versus frame are investigated. The influence of the recuperation on the results is discussed separately. Further common cycles are used to gain more simulation results for the review of the design parameter σ . In none of the investigated cases did the winding temperature reach its thermal limit: the discussion here focuses on the magnet temperature.

FTP-75 Driving Cycle and Influence of Gearbox on Thermal Response

Fig. 6.1 shows that no critical temperature is reached in the FTP-75 driving cycle. The FTP-75 driving cycle was adapted in the simulation: the transient phase is directly followed by the hot start phase, the 10 min pause before the third phase was omitted. Fig. 6.2 shows the torque and speed operating points which occur during the cycle: all operating points are in the low torque and speed region.

Permanent Magnet Temperature Distribution in FTP-75 driving cycle

The distributions of the machine power and the corresponding magnet temperatures are shown in Fig. 6.3: For 44 % of the operating time, the EM is operated between zero and 25 % of its peak power. For 85 % of the time, it is operated below its nominal power of 20 kW. As can be seen in Fig. 6.3a, with the gearbox attached, the magnets reach 100 to 105 °C for 56 %

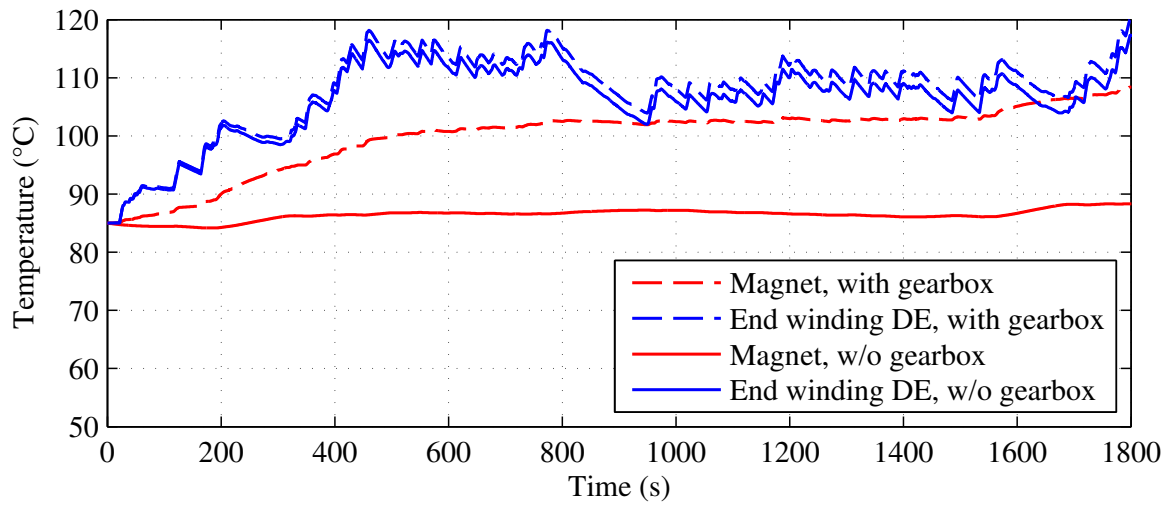


Figure 6.1: eRAD FTP-75 simulation results: comparison of thermal response with and w/o gearbox attached.

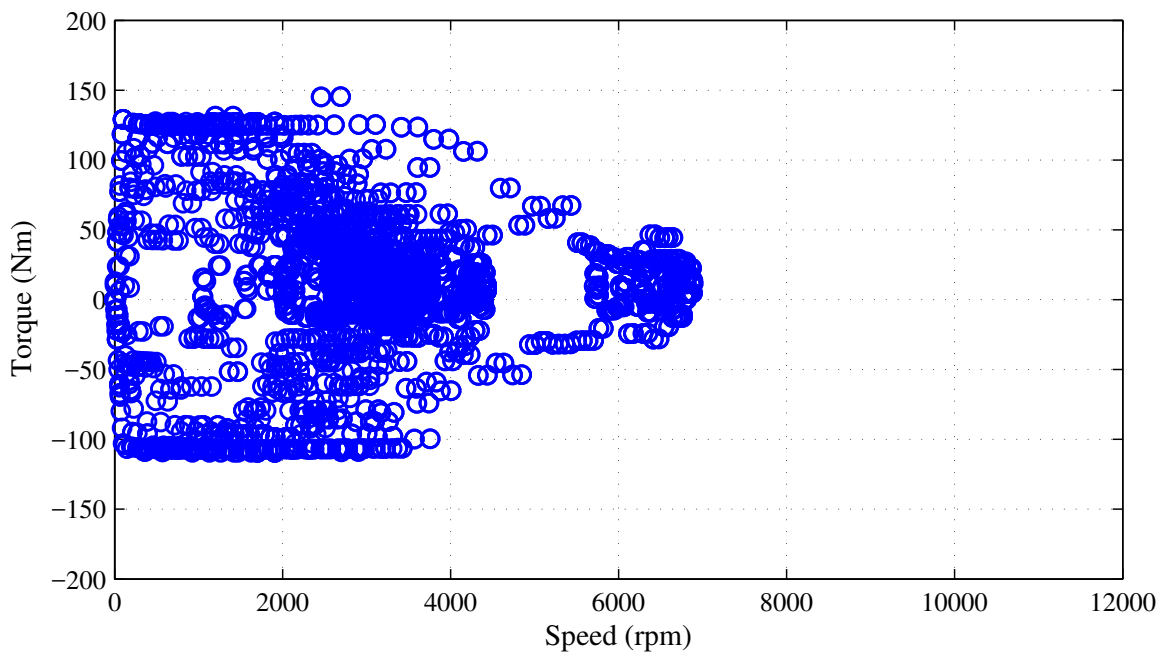
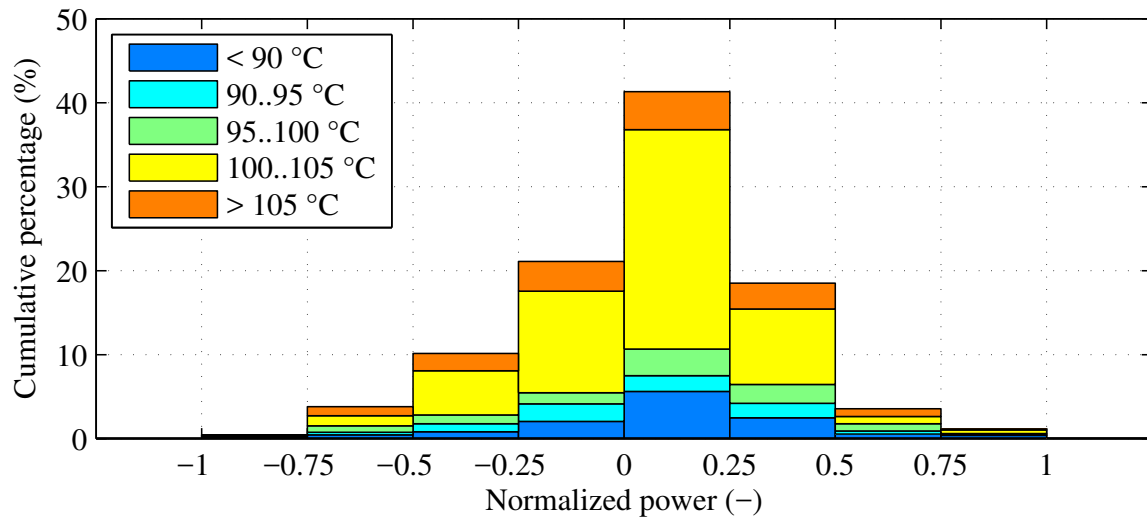


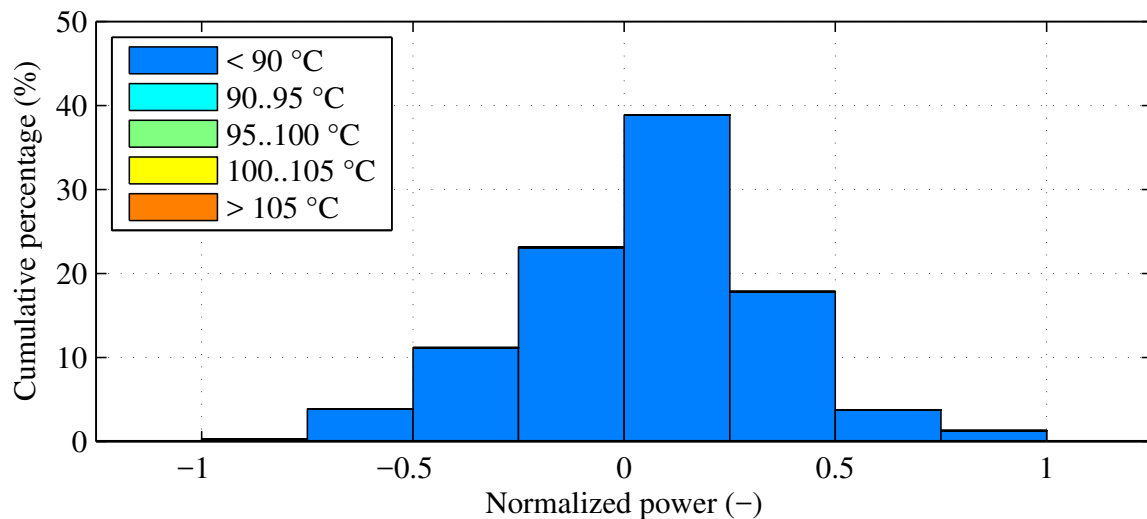
Figure 6.2: eRAD FTP-75 torque speed operating points.

of the time. For 15% of the time, the magnet temperature exceeds 105°C which is 95% of the maximum temperature, as defined by the software and material ratings.

In contrast, if no heat is injected into the EM by the gearbox (Fig. 6.3b), the machine is always operated below 90°C magnet temperature. Thus, the gearbox integration decreases the thermal safety clearance to the maximum magnet temperature, from 20% to 1% of the maximum magnet temperature.



(a) With gearbox attached.



(b) Without gearbox attached.

Figure 6.3: Distribution of eRAD magnet temperature, FTP driving cycle, 40% of gearbox losses are injected into the rotor.

Thermal Loads During Moderate Driving Cycles

Also the thermal loading during moderate driving cycles like the New European Driving Cycle (NEDC) (Fig. 6.4) and the 10-15 mode which is relevant for fuel economy testing in Japan (Fig. 6.5) are used for the studies. These driving cycles with low dynamic are not suitable for thermal (stress) analysis, and not used in practice, as the machine and gearbox load are too low to generate a thermal load according to the real world usage, e.g., 93 % of the time, the machine load is lower than 50 % of the peak power in the NEDC.

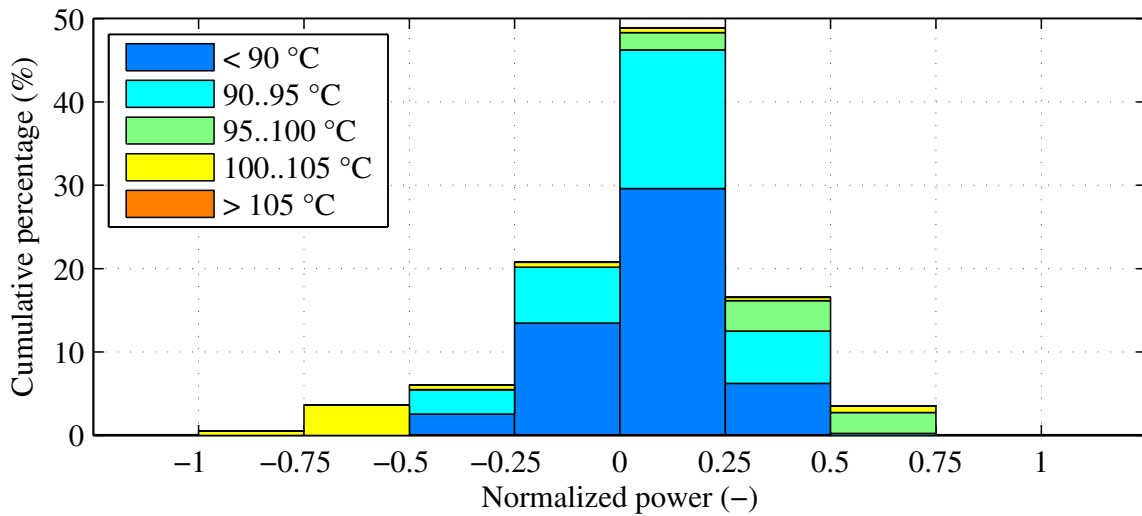


Figure 6.4: Magnet temperature: NEDC, with gearbox attached.

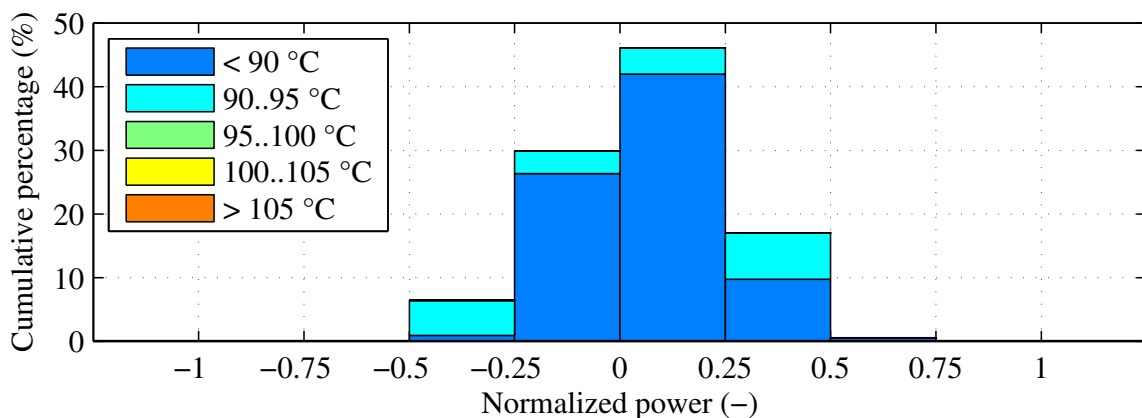
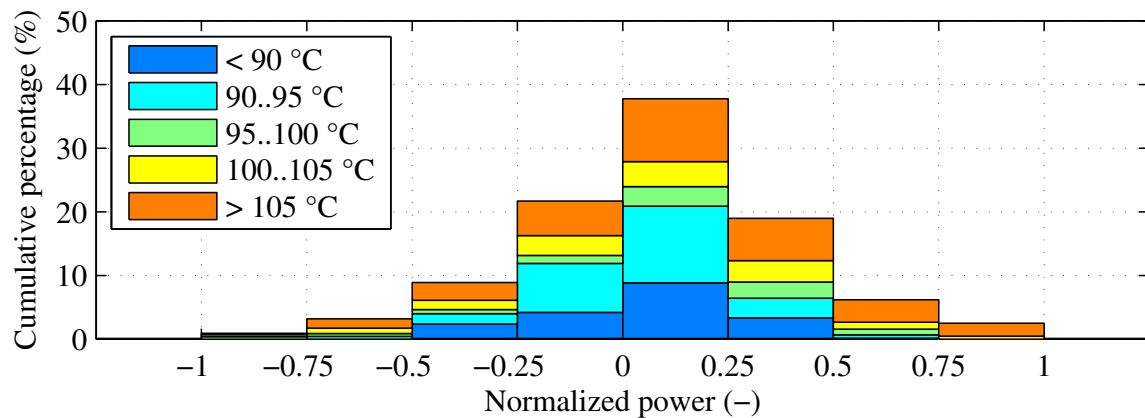


Figure 6.5: Magnet temperature: 10-15 mode (Japan), with gearbox attached.

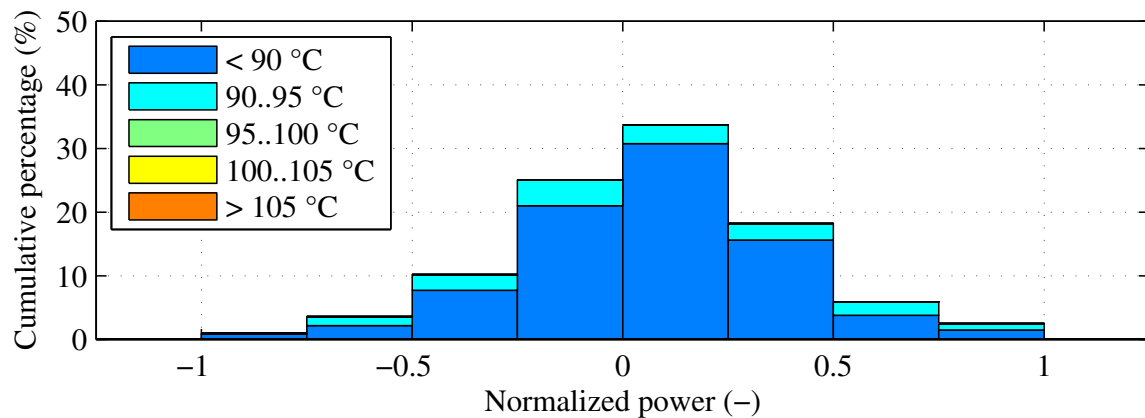
WLTP Driving Cycle

In the EU the WLTP is planned to replace the NEDC for light duty vehicles [177]. The WLTP driving cycle has three classes depending on the ratio of rated power to curb mass (unloaded mass) [178], of which only class three is of relevance for the case studies.

If the gearbox is attached, the magnet temperature exceeds the thermal design point of 105 °C already after 19 minutes. The maximum magnet temperature reached in the cycle is 125 °C which occurs during the extra-high part of the WLTP. The thermal frequency distribution is shown in Fig. 6.6a. If the gearbox is not attached, no critical magnet temperature was reached in the simulations (Fig. 6.6b).



(a) With gearbox attached.



(b) Without gearbox attached.

Figure 6.6: Distribution of eRAD magnet temperature, WLTP driving cycle, 40% of gearbox losses are imposed in rotor.

Influence of Recuperation on Thermal Response

The simplification of 100% recuperation torque, of the EM torque available, will hardly be technically practical, e.g., due to restrictions of the energy storage system (ESS), the influence of the recuperation torque on the magnet temperature was shortly studied: Down to approximately 50% recuperation torque, the duration (residence time) in which the magnet temperature exceeds 105 °C during the cycle does not change significantly. For example, if the recuperation torque is limited to 40% of the EM's maximum torque, the 105 °C residence time decreases to 8.5%. If the recuperation torque is limited to 25%, the magnet temperature only reaches 105 °C at the end of the FTP-75 driving cycle.

6.2.2 ISG

Overview

The ISG is thermally influenced by three external heat sources: (i) the clutch (with temperatures up to 200 °C) which is actuated depending on the HEV's operating strategy and (ii) the ICE with (iii) the TM. The air gap shear stress σ is 25.1 kN/m² (at 2200 rpm) in the nominal operating point, with a maximum torque of 350 Nm. At nominal torque and speed, the winding temperature reaches 170 °C and the magnet temperature 114 °C which is defined as the (thermal) design point.

The worst case situation for both the ICE heat load and clutch is analyzed using the Federal Test Procedure (FTP-72) driving cycle. For the ISG application, the FTP-72 was the relevant one as detailed clutch actuation information from vehicle tests was available.

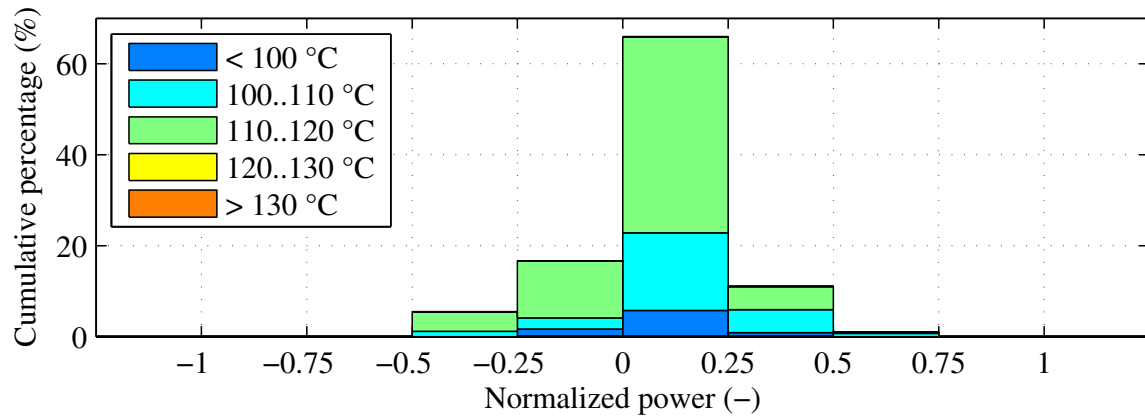
To emphasize the ICE/TM influence on σ , which was identified as negligible, the nominal operating point is regarded for different ICE and TM temperatures at zero clutch load. The influence of the clutch heat load is analyzed separately: the clutch load is varied for the nominal operating point and the FTP-72.

In none of the investigated cases did the winding temperature reach its thermal limit: the discussion focuses on the magnet temperature and bearings.

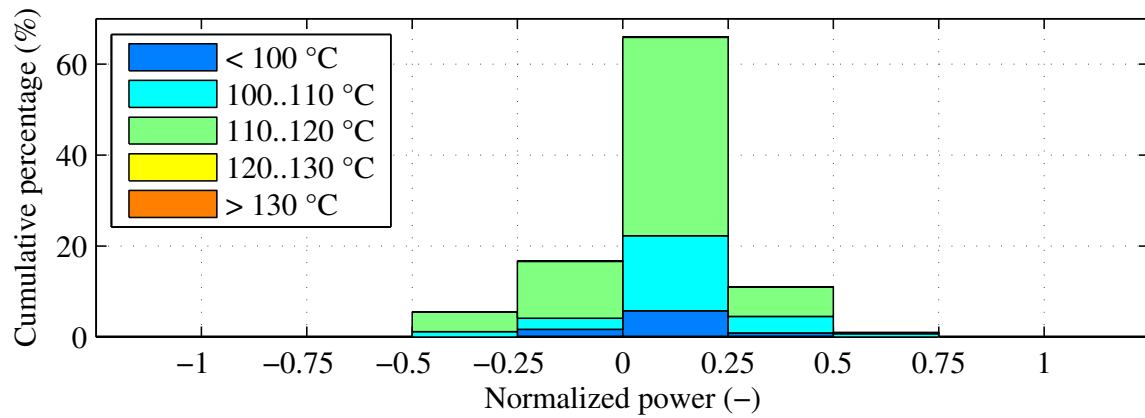
FTP-72 Worst Case Scenario

In Fig. 6.7, the FTP-72 driving cycle simulation results are compared: The baseline (no additional heat loads) is shown in Fig. 6.7a. The ICE and TM temperatures are regarded as boundary conditions in the FEM thermal model in Fig. 6.7b, showing that the ICE and TM influence is negligible. If the ISG is simulated with the ICE's and TM's thermal load, the magnet temperature reaches up to 120 °C.

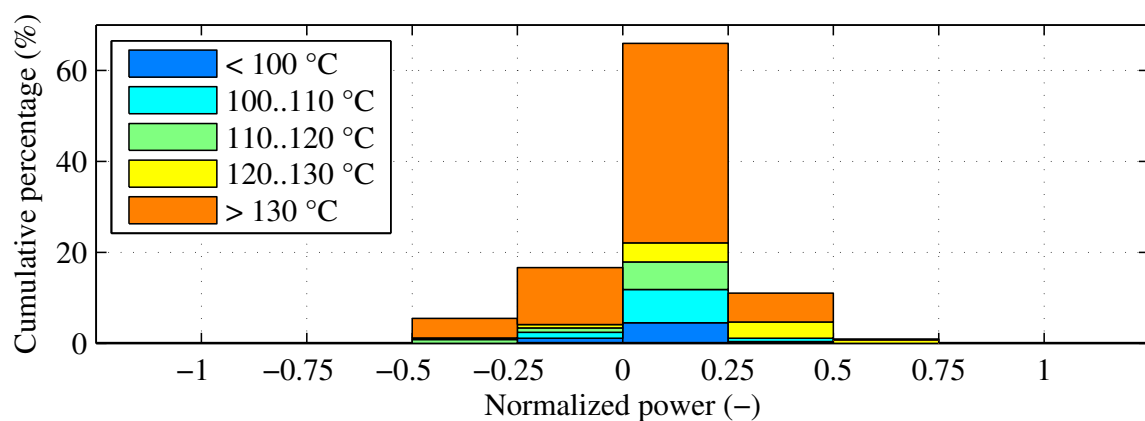
Fig. 6.7c represents one worst case scenario: the magnet temperature reaches 176 °C, which is 4 K below the permissible maximum, if all additional thermal loads (ICE/TM and clutch) are considered in the simulation.



(a) Without additional loads; ideal conditions.



(b) With ICE; vehicle integrated.



(c) With ICE and clutch; vehicle integrated.

Figure 6.7: Distribution of ISG magnet temperature, FTP-72 driving cycle.

6.3 Discussion of the Air Gap Shear Stress

6.3.1 eRAD

The relationship between the air gap shear stress σ (scaling factor) and the gearbox loss distribution between rotor and stator, for the nominal operating point, the FTP-75 and the WLTP is presented in Fig. 6.8. The scaling factors for the driving cycles are calculated based on the magnet temperature safety clearance, which is the temperature difference to the magnet's absolute maximum ratings. In practice, this boundary might be lower, depending on the field weakening current applied to the EM.

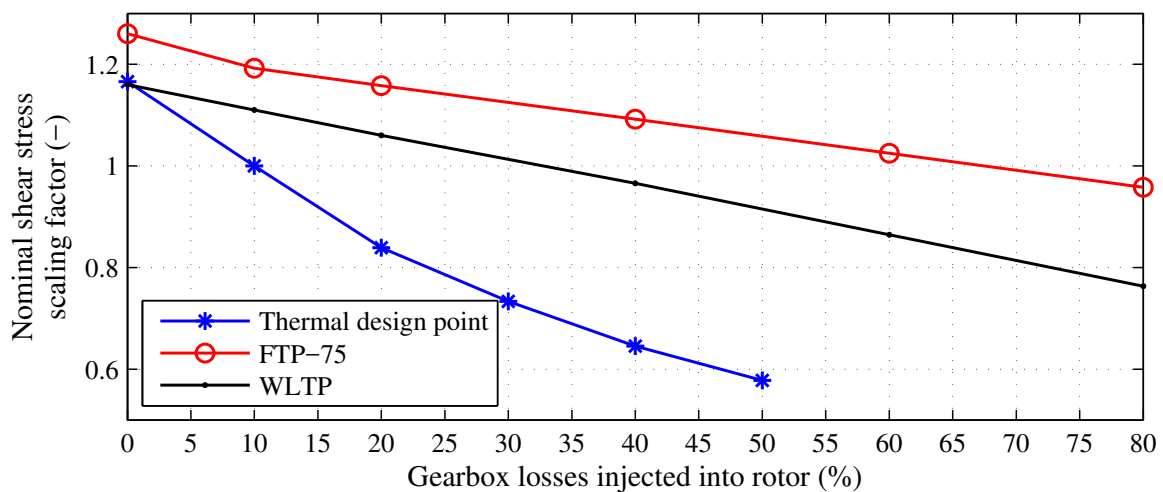


Figure 6.8: Scaling of eRAD air gap shear stress depending on percentage of gearbox heat load injected into rotor. (The remaining losses are injected into the stator.)

The air gap shear stress σ at which the machine can be operated continuously (2380 rpm at 90 Nm) is 30.2 kN/m². Considering the maximum achievable torque, the Toyota/Lexus traction machines have a higher overload capability: this machine might be overloaded by a factor of 2.4, e.g., the Toyota Prius EM by a factor of 4.2 (estimated based on [27] and [28]).

Neglecting the gearbox, an increase of air gap shear stress σ , and therefore machine utilization, of 17% might be possible (see Fig. 6.8). Then the end winding temperature reaches the defined design maximum of 160 °C, when no gearbox is attached. Theoretically, a 27% increase of σ might be possible if the machine is operated at the material (insulation) limit of 180 °C, with the drawback of lifetime degradation (insulation material). Attaching the gearbox to the machine results in 120 °C rotor temperature, the defined maximum, if 10% of the gearbox losses are injected into the rotor. Changing the loss distribution in the simulation, e.g., injecting 40% of the gearbox losses into the rotor, results in a σ reduction by 35%, to stay below its defined maximum.

To discuss the driving cycles, the moderate ones (NEDC and 10-15 mode) are neglected due to the low dynamics, the focus is on the real world driving cycles (FTP-75, FTP-72 and WLTP): The maximum magnet temperature is reached at the end of the FTP-75 driving cycle. No design change is necessary, if 68 % of the gearbox losses are injected into the rotor, For the WLTP, the situation is different, only 32.5 % of the gearbox losses can be injected into the rotor without reworking the machine's design. The results show that the machine, which was already designed for operation with gearbox, might be optimized, if the driving cycles shown here are used for system design.

6.3.2 ISG

ICE Influence on Air Gap Shear Stress

The ICE influence (clutch load zero) is discussed in Fig. 6.9: the ICE temperature is varied from 30 to 250 °C. The influence is remarkable for temperatures higher than 210 °C in the nominal operating point. However, such high temperatures are not relevant in practice. As some of the bearings are located very close to the ISG flange, the optimization potential in Fig. 6.9 is only theoretical, (if the mechanically point of view is neglected).

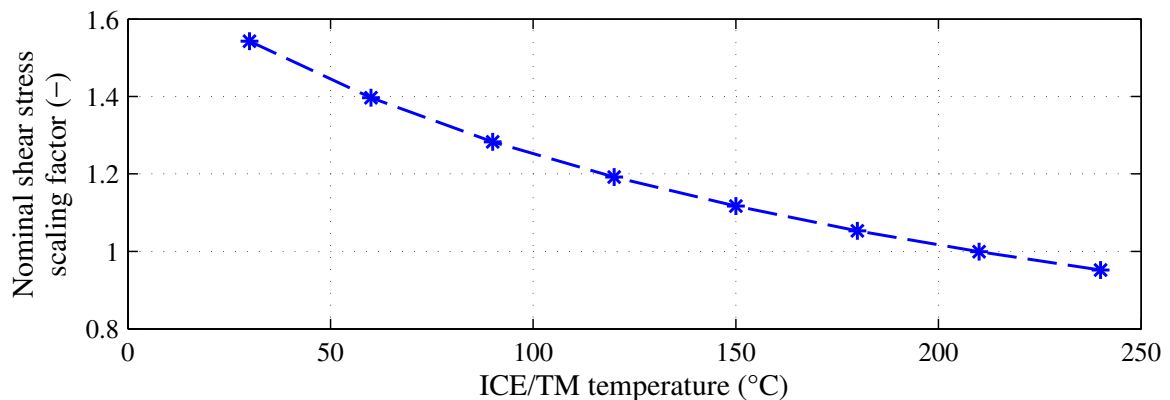


Figure 6.9: Scaling of ISG air gap shear stress air gap shear stress depending on ICE boundary condition temperature; zero clutch load; nominal operating point.

Clutch Load Influence on Air Gap Shear Stress

The clutch load varies depending on the vehicle's operating strategy (start-stop strategy, drive-off purely-electrical) and could also vary during the lifetime, because of the change of the friction plate's tribological parameters. The clutch load ranges from 0 to 2.76 actuations per minute in Fig. 6.10, the ICE and TM heat load was defined as zero in the simulations.

Summarizing the results: a clutch load of higher than 0.3 actuations per minute has a significant impact on the machine's design. As the machine is also restricted to other

requirements, such as maximum bearing temperatures (grease lubrication), the red curve shows the practical (restricted) correlation in Fig. 6.10, e.g., a clutch actuation interval of more than 1.25 times per minute leads to excessively high bearing temperatures.

The clutch actuations per minute shown in Fig. 6.10 for the FTP-72 are the loss energy equivalent injected into the clutch during the cycle; in the simulation model the clutch is actuated depending on the vehicle's operating strategy.

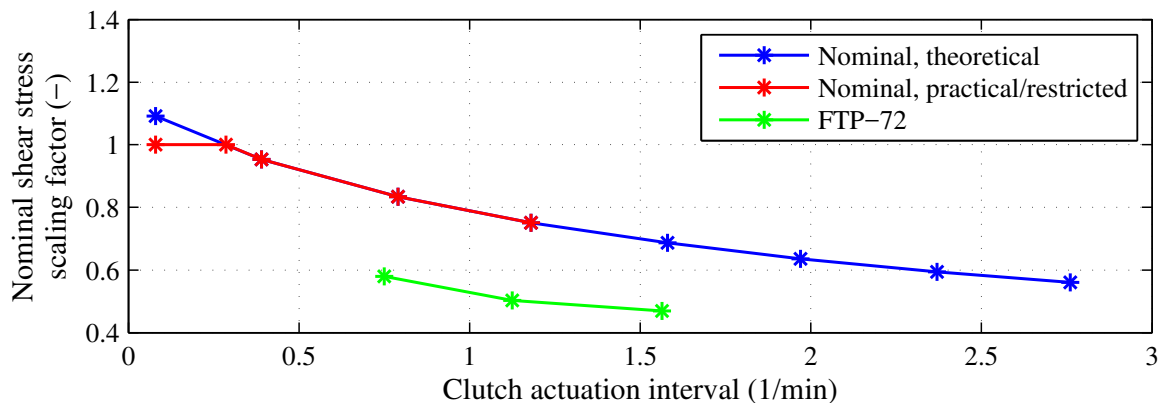


Figure 6.10: Scaling of ISG air gap shear stress air gap shear stress depending on clutch heat load at nominal operating point and FTP-72; ICE not connected.

6.4 Correlation of Mechanical, Thermal and Electric Loading

6.4.1 eRAD

Summarizing the preceding analysis results: the magnet temperature is the critical one if a gearbox is attached. Fig. 6.2 is extended by Fig. 6.11: the data density of the operating points identifies torque-speed zones with high operation frequency; the black colored point indicates the thermal design point, which also defines the nominal air gap shear stress.

Fig. 6.11 shows the discrepancy between the thermal design point and the zone of operation: the machine is mostly operated in a zone (or zones) which differs from the design point. There is a major accumulation of operation points at 3000 ± 300 rpm at ≈ 0 to 50 Nm and two minor ones in the low speed high torque region. This depicts only the electrical/mechanical operation zones of interest. The thermal point of view is shown by Fig. 6.12. Fig. 6.12: it is difficult to define a region where the hot spot temperatures are accumulated, the machine warms up during the driving cycle and passes through many operating points with a minor changing magnet temperature, but the figure shows that the hot spot temperatures are only reached in the high speed region.

If the operating point densities are considered for the definition of air gap shear stress, then

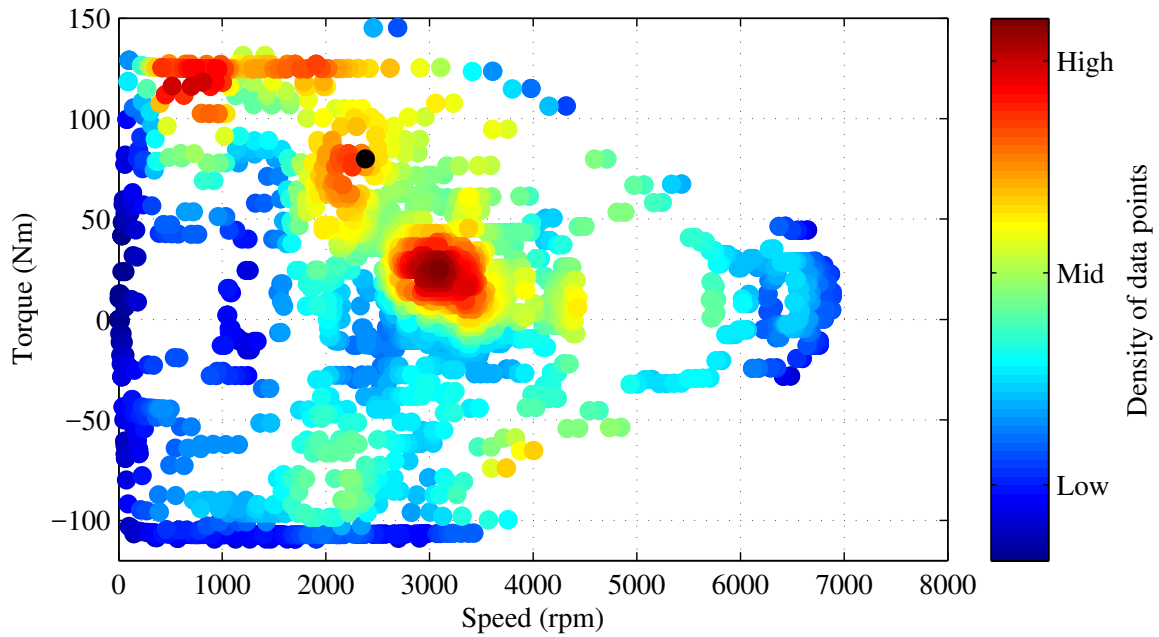


Figure 6.11: eRAD FTP-75 torque speed operating points with density of data points; the black point indicates the nominal operating point.

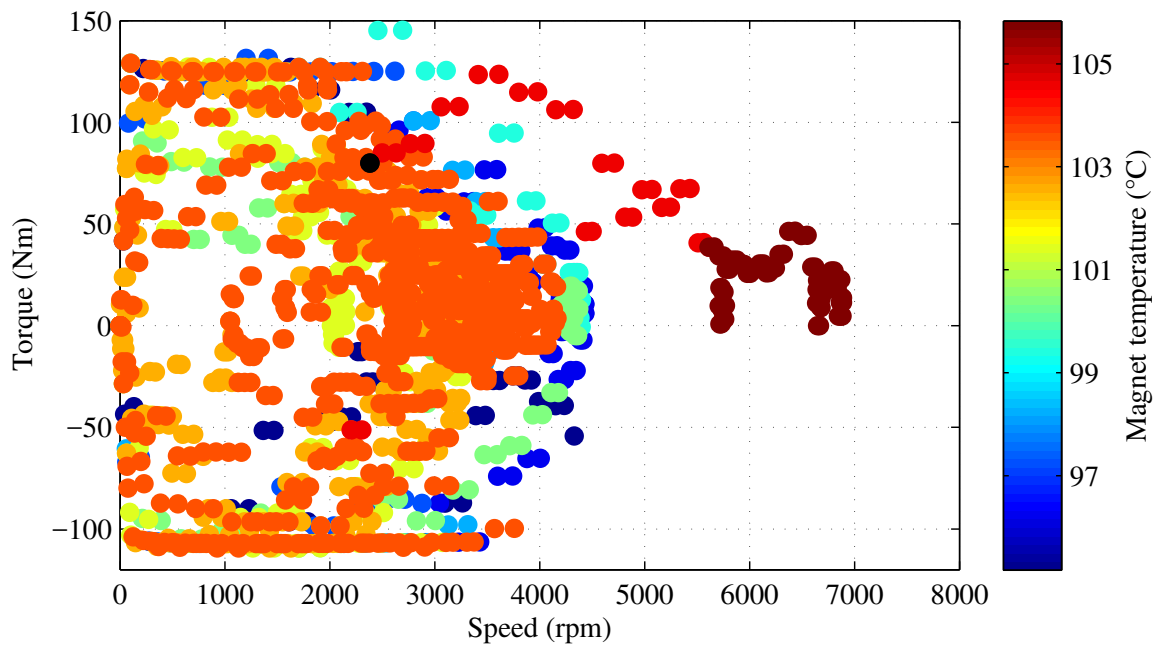


Figure 6.12: eRAD FTP-75 torque speed operating points with magnet temperature; the black point indicates the nominal operating point.

the operating zone nearby 25 Nm and 3100 rpm is from interest. Assuming that the machine has to thermally withstand this operating point, the nominal shear stress is 10 kN/m^2 . Considering the proportionality in eq. (1.3) and if the magnetic load level is not changed, the current density A can be reduced by a factor of 3. Using only these considerations, the machine's cooling system could be simplified to an air cooled one. If the same considerations are made for the density center at 125 Nm and 740 rpm, the situation changes and the current density increases by a factor of 1.6. Therefore, considering only electrical/mechanical operating points, an appropriate definition of σ and A is not possible. Considering the thermal point of view (e.g., in Fig. 6.12) for the magnets shows that the heat load (or temperature) is relevant for every operating point which is reached during a driving cycle.

6.4.2 ISG

Again, as with the eRAD application, the machine design is quantified in Fig. 6.13: the data density of the operating points to identify torque-speed zones with high operation frequency is shown.

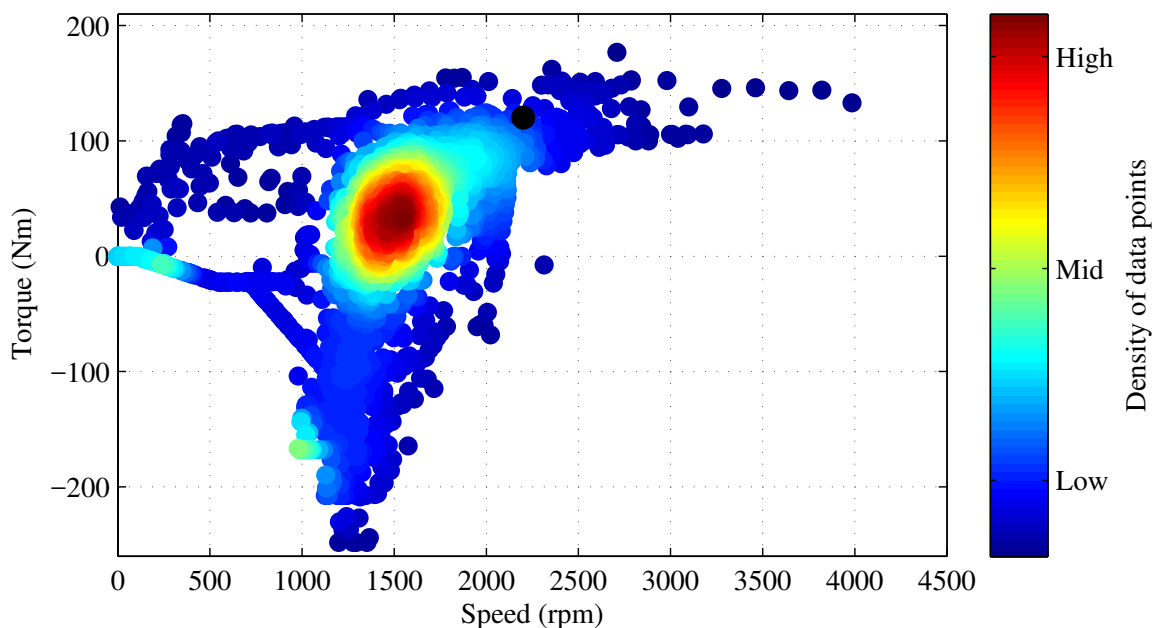


Figure 6.13: ISG FTP-72 torque speed operating points with density of data points; the black point indicates the nominal operating point.

Using eq. (1.3) again, and assuming that the center of the operating point density is the design point, then a reduction of A by 2.64 seems to be achievable.

Considering the thermal load in Fig. 6.13, the discrepancy between the thermal design point and the operation points is shown again: the machine is mostly operated in zones

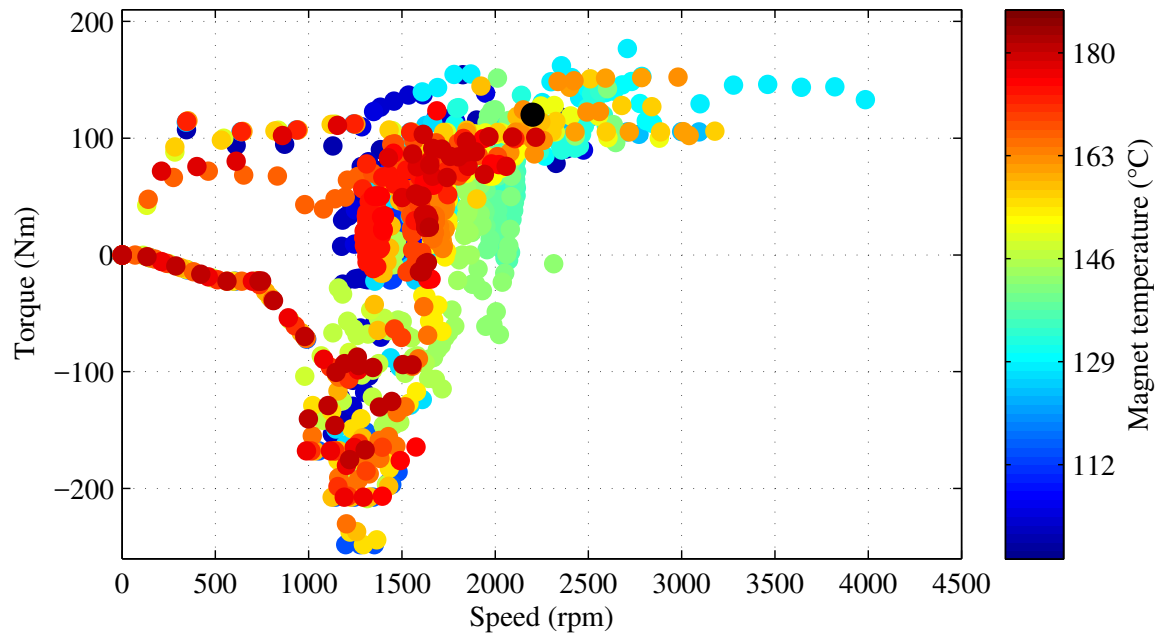


Figure 6.14: ISG FTP-72 torque speed operating points with magnet temperature; the black point indicates the nominal operating point.

which differ from the thermal design point. Furthermore, compared to the eRAD application, there is only one region of interest here. The plot with the temperature shows that thermally critical operating points are reached in a slightly higher torque region as the operation point density plot indicated.

Using the models developed during the research work, the influence of external heat loads on the scaling of the air gap shear stress is investigated for different heat load scenarios and driving cycles with suitable dynamics using the example case applications.

Based on the eRAD analysis, if gearbox losses occur, the design of the EM requires reconsideration. However, this depends on the amount of losses injected into the rotor. The winding temperature was not remarkably influenced in that case, even if 100 % losses are injected into the stator frame. In sum, the results showed that the machine was already optimized for the nominal operating point.

The impact of ICE and clutch losses on the thermal behavior of the ISG application has been also analyzed. The ICE losses have no significant thermal impact for temperatures lower than 210 °C. The clutch losses increase the magnet temperature and are critical for actuation intervals greater than 0.3 per minute. This might be practically relevant (e.g., presuming multiple start/stops during a traffic jam), but can be controlled by the vehicle's operating strategy.

Chapter 7

Conclusion

Aiming to study the thermal effects of electric machine (EM) integration in vehicle environments, the possible influences of, i.e. gearbox, transmission (TM), internal combustion engine (ICE) and actuators (including dry friction clutch) are computed. Different thermal models, i.e., lumped-parameter thermal-network (LPTN) and finite element method (FEM) approaches, had been developed and validated experimentally. The vehicle model follows a quasi-static approach to speed up the simulation and allow for parameter studies.

The research work presented uses two example case studies: an electric Rear Axle Drive (eRAD), with a planetary gear-set (PGS) and disconnect system (DCS) attached, and an integrated starter generator (ISG) attached to the ICE and TM. Both example case studies are liquid cooled interior-mounted permanent-magnet synchronous-machines (IPMSMs) with some tens of kilowatts. For both applications, appropriate loss and thermal models were developed and validated experimentally.

To analyze the influence of vehicle integration on the thermal behavior for the IPMSM of the eRAD traction application, a complex analytic approach (LPTN) had been verified experimentally and was used as the starting point to derive a simplified LPTN. A sensitivity and heat flow analysis was used to investigate the most critical thermal paths between the winding and the magnets to the coolant. The reduced model was derived by neglecting less relevant thermal resistances and capacitances. The derived simplified LPTN allows for online temperature prediction in the inverter software, as lower computational capacity is required. Additional heat sources (gearbox) and uncertainties introduced by estimated/computed or measured signals in the vehicle, influence the accuracy of the model implemented in the inverter software. Especially the influence of the gearbox integration on the magnet and winding temperature was shown for steady-state and transient (torque step and driving cycle) operating conditions. The uncertainties of the readings of the coolant temperature sensor are shortly discussed: an additional temperature sensor at the end winding is introduced and, in many applications, is readily available.

To extend the investigations using the LPTNs, an FEM thermal model was developed to verify the LPTN models on the one hand and to analyze the heat flow between gearbox,

rotor and stator housing, on the other hand.

An alternative cooling approach (oil-spray cooling) was shown to improve thermal behavior of the eRAD machine.

The studies illustrate the role which drive integration plays in thermal studies of electric drives/EMs, notably the consideration of additional heat sinks/sources exterior to the main machine, such as in the case of the eRAD example case application: a gearbox. The temperature of the magnets was 21 K higher with the gearbox attached. Direct end winding cooling allowed for a temperature reduction of 6 K.

The influence of vehicle integration on the thermal behavior of an ISG system for a hybrid electric vehicle (HEV) was also studied. To this aim, as in the case of the eRAD application, a numerical thermal model (FEM) of the electric drive components was developed and verified experimentally. Using this model, the influences of the integrated dry friction clutch module, the electromagnetic actuator and the ICE on the thermal performance of the IPMSM were investigated.

Summary of the results derived in Chapters 5 to 6:

Clutch losses could lead to critical magnet temperatures: the magnet temperature and frequency of clutch actuations requires monitoring during vehicle operation.

The winding temperature is not (low correlation) influenced by the clutch losses. No significant effect on the stator design parameters was identified.

Considering the ICE and TM (vehicle integration): For the operating points investigated in this work, and if the clutch is not considered, the influence of the ICE and the TM was found to be negligible. The TM flange temperature is critical for the winding temperature if (practically not relevant) excessive clutch losses occur. The magnet temperature is influenced by the TM shaft temperature.

The Federal Test Procedure (FTP-72) driving cycle simulations resulted in an increase of the rotor temperature by 57 K if all losses from relevant internal (losses occurring within the EM) and external loss sources (ICE/TM, clutch) are applied as boundary conditions. A remarkable influence of the clutch losses on the magnet temperature was shown.

The influence to the bearings is different (depending on the bearing's location).

The influence of external heat loads on the scaling of the air gap shear stress is investigated for different heat load scenarios and driving cycles using both applications in Chapter 6. Based on the eRAD analysis with gearbox attached, the design of the EM needs to be reconsidered depending on the amount of losses injected into the rotor. The winding temperature was not influenced, even if the gearbox is attached and 100% losses are injected into the stator frame. The machine was already optimized for the nominal operating point.

Regarding the ISG: The ICE losses have no significant thermal impact for temperatures

lower than 210 °C . The ICE analyses indicated a high optimization potential, but taking into account the mechanical restrictions due to the bearings, the situation changes. However, if high temperature grease is used the situation might also change.

The results illustrate the importance of including the additional heat sources and the thermal environment of vehicle-integrated EMs in the design process and the need to consider the operating parameters of selected external heat sources in the control software. Such analyses, as carried out in this research work, may help to determine to which extent the different heat sources must be considered in the design of an EM.

Bibliography

- [1] A. Nollau and D. Gerling, "A new cooling approach for traction motors in hybrid drives," in *Electric Machines & Drives Conference (IEMDC), 2013 IEEE International*, 2013, pp. 456–461.
- [2] C. M. Liao, C. L. Chen, and T. Katcher, "Thermal analysis for design of high performance motors," in *Proc. The Sixth Intersociety Conference on Thermal and Thermomechanical Phenomena in Electronic Systems (ITHERM'98)*, 1998, pp. 424–433.
- [3] I. Adcock, "Winning the power struggle," *Automotive Design, The pan-European magazine of SAE International*, pp. 12–15, April 2012. [Online]. Available: www.sae.org/magazines/pdf/AUTODES0412.pdf
- [4] K. Bennion. (2013, May) Electric motor thermal management. Accessed on 2013-04-17. [Online]. Available: http://www4.eere.energy.gov/vehiclesandfuels/resources/merit-review/sites/default/files/ape030_bennion_2013_o.pdf
- [5] C. Paar, H. Kolbe, and A. Muetze, "Influence of machine integration on the thermal behavior of a PM drive for hybrid electric traction," in *Energy Conversion Congress and Exposition (ECCE), 2014 IEEE*, Sept 2014, pp. 3266–3271.
- [6] C. Paar, A. Muetze, and H. Kolbe, "Influence of machine integration on the thermal behavior of a PM drive for hybrid electric traction," *IEEE Trans. Ind. Appl.*, vol. 51, no. 5, pp. 3914–3922, 2015, available online.
- [7] R. Fischer, *Elektrische Maschinen*. Munich, Germany: Carl Hanser Verlag, 2013.
- [8] J. R. Hendershot and T. Miller, *Design of Brushless Permanent-Magnet Motors*. Magna Physics, 1994.
- [9] J. Willberger, "AC motor design and evaluation for automotive traction applications," Ph.D. dissertation, Graz University of Technology, Graz, December 2011.
- [10] G. Mueller, K. Vogt, and B. Ponick, *Berechnung elektrischer Maschinen*, 6th ed. Weinheim: Wiley-VCH Verlag GmbH & Co. KGaA, 2008.
- [11] A. Binder, *Elektrische Maschinen und Antriebe*. Springer, 2012.

- [12] R. Fischer, *Elektrische Maschinen*. Munich, Germany: Carl Hanser Verlag, 2011.
- [13] M. Ganchev, C. Kral, and T. M. Wolbank, "Compensation of speed dependence in sensorless rotor temperature estimation for permanent-magnet synchronous motor," *IEEE Trans. Ind. Appl.*, vol. 49, no. 6, pp. 2487–2495, Nov 2013.
- [14] G. Rang, J. Lim, K. Nam, H.-B. Ihm, and H.-G. Kim, "A MTPA control scheme for an IPM synchronous motor considering magnet flux variation caused by temperature," in *Applied Power Electronics Conference and Exposition, 2004. APEC '04. Nineteenth Annual IEEE*, vol. 3, 2004, pp. 1617–1621.
- [15] T. Sebastian, "Temperature effects on torque production and efficiency of PM motors using NdFeB magnets," *IEEE Trans. Ind. Appl.*, vol. 31, no. 2, pp. 353–357, Mar 1995.
- [16] A. Wang, H. Li, and C.-T. Liu, "On the material and temperature impacts of interior permanent magnet machine for electric vehicle applications," *IEEE Trans. Magn.*, vol. 44, no. 11, pp. 4329–4332, Nov 2008.
- [17] X. Chen, J. Wang, and A. Griffo, "A high-fidelity and computationally efficient electro-thermally coupled model for interior permanent-magnet machines in electric vehicle traction applications," *IEEE Trans. Transp. Electr.*, vol. 1, no. 4, pp. 336–347, 2015.
- [18] M. V. Marinko Kovacic and I. Gasparac, "Bluetooth wireless communication and 1-wire digital temperature sensors in synchronous machine rotor temperature measurement," in *Power Electronics and Motion Control Conference (EPE/PEMC), 2010 14th International*, Sept 2010, pp. T7–25–T7–28.
- [19] D. Siyambalapitiya, P. McLaren, and P. Acarnley, "A rotor condition monitor for squirrel-cage induction machines," *IEEE Trans. Ind. Appl.*, vol. IA-23, no. 2, pp. 334–340, March 1987.
- [20] S. Stipetic, M. Kovacic, Z. Hanic, and M. Vrazic, "Measurement of excitation winding temperature on synchronous generator in rotation using infrared thermography," *IEEE Trans. Ind. Electron.*, vol. 59, no. 5, pp. 2288–2298, May 2012.
- [21] D. Reigosa, F. Briz, P. Garcia, J. Guerrero, and M. Degner, "Magnet temperature estimation in surface PM machines using high-frequency signal injection," *IEEE Trans. Ind. Appl.*, vol. 46, no. 4, pp. 1468–1475, July 2010.
- [22] Y.-S. Jeong, R. Lorenz, T. Jahns, and S.-K. Sul, "Initial rotor position estimation of an interior permanent-magnet synchronous machine using carrier-frequency injection methods," *IEEE Trans. Ind. Appl.*, vol. 41, no. 1, pp. 38–45, Jan 2005.

- [23] J. Guerrero, M. Leetmaa, F. Briz, A. Zamarron, and R. Lorenz, "Inverter nonlinearity effects in high-frequency signal-injection-based sensorless control methods," *IEEE Trans. Ind. Appl.*, vol. 41, no. 2, pp. 618–626, March 2005.
- [24] M. Ganchev, C. Kral, and T. Wolbank, "Hardware and software implementation of sensorless rotor temperature estimation technique for permanent magnet synchronous motor," in *Electrical Systems for Aircraft, Railway and Ship Propulsion (ESARS), 2012*, 2012, pp. 1–6.
- [25] K. Liu and Z. Q. Zhu, "Online estimation of the rotor flux linkage and voltage-source inverter nonlinearity in permanent magnet synchronous machine drives," *IEEE Trans. Power Electron.*, vol. 29, no. 1, pp. 418–427, 2014.
- [26] W. Schuisky, *Berechnung elektrischer Maschinen*. Springer, 1960.
- [27] M. Olszewski. (2008) Evaluation of the 2007 Toyota Camry synergy drive system. Oak Ridge National Laboratory. Accessed on 2015-04-11. [Online]. Available: <http://www.osti.gov/scitech/servlets/purl/928684>
- [28] ——. (2011) Evaluation of the 2010 Toyota Prius hybrid synergy drive system. Oak Ridge National Laboratory. Accessed on 2015-04-11. [Online]. Available: <http://info.ornl.gov/sites/publications/files/Pub26762.pdf>
- [29] Renault. Renault Twizy modelyear 2016 pricelist (in german). Accessed on 2016-02-06. [Online]. Available: https://www.renault.at/media/-pdf-preisliste-/att00341530/PL_Twizy.pdf
- [30] S. Lukic and A. Emadi, "Effects of drivetrain hybridization on fuel economy and dynamic performance of parallel hybrid electric vehicles," *IEEE Trans. Veh. Technol.*, vol. 53, no. 2, pp. 385–389, March 2004.
- [31] S. Lukic, J. Cao, R. Bansal, F. Rodriguez, and A. Emadi, "Energy storage systems for automotive applications," *IEEE Trans. Ind. Electron.*, vol. 55, no. 6, pp. 2258–2267, June 2008.
- [32] S. Wirasingha and A. Emadi, "Classification and review of control strategies for plug-in hybrid electric vehicles," *IEEE Trans. Veh. Technol.*, vol. 60, no. 1, pp. 111–122, January 2011.
- [33] T. J. E. Miller, *Speed's Electric Motors: An Outline of Some of the Theory in the Speed Software for Electric Machine Design With Problems and Solutions*. Magna Physics, 2004.

- [34] L. Chong, R. Dutta, and M. F. Rahman, "Design and thermal considerations of an interior permanent magnet machine with concentrated windings," in *Electrical Machines and Systems, 2009. ICEMS 2009. International Conference on*, 2009, pp. 1–6.
- [35] H. Sequenz, *Die Wicklungen elektrischer Maschinen - Wechselstrom Ankerwicklungen*. Wien: Springer, 1950, vol. 1.
- [36] A. EL-Refaie and M. Shah, "Comparison of induction machine performance with distributed and fractional-slot concentrated windings," in *Industry Applications Society Annual Meeting, 2008. IAS '08. IEEE*, Oct 2008, pp. 1–8.
- [37] M. Scheidt, "Entwurfskriterien fuer permanent-magneterregte Synchronmaschinen in Zahnspulentechnik unter besonderer Beruecksichtigung der Zusatzverluste," Ph.D. dissertation, Technische Universitaet Kaiserslautern, 2009.
- [38] J. Gstoehl, "Verlustbestimmung eines High Performance Crankshaft Integrated Stater/-Generators [Loss determination of a high performance crankshaft integrated stater/-generator]," Master's thesis, Graz University of Technology, 2015.
- [39] A. Tariq, C. Nino-Baron, and E. Strangas, "Iron and magnet losses and torque calculation of interior permanent magnet synchronous machines using magnetic equivalent circuit," *IEEE Trans. Magn.*, vol. 46, no. 12, pp. 4073–4080, Dec 2010.
- [40] T. Heikkilae, "Permanent magnet synchronous motor for industrial inverter applications - analysis and design," Ph.D. dissertation, Lappeenranta University of Technology, 2002.
- [41] A. Rastogi, "Berechnung von doppeltgespeisten Asynchronmaschinen und permanenterregten Synchronmaschinen als Windgeneratoren und Industrieantriebe," Ph.D. dissertation, Technische Universitaet Darmstadt, 2010.
- [42] ANSYS® Academic Research, Release 15.0, Help System, Maxwell® Online Help, ANSYS Inc.
- [43] C. Paar and A. Muetze, "Influence of dry clutch and ICE transmission integration on the thermal load of a PM based integrated starter-generator," in *Energy Conversion Congress and Exposition (ECCE), 2015 IEEE*, Sept 2015, pp. 106–111.
- [44] —, "Thermal real-time monitoring of a gearbox integrated electric rear axle drive for hybrid electric traction," in *Transportation Electrification Conference and Expo (ITEC), 2015 IEEE*, June 2015, pp. 1–6.

- [45] —, “Discussion of machine placement and integration on the thermal design of HEV IPM machines,” in *Transportation Electrification Conference and Expo (ITEC), 2016 IEEE*, June 2016, pp. 1–6.
- [46] —, “Thermal real-time monitoring of a gearbox integrated IPM machine for hybrid electric traction,” *IEEE Trans. Transp. Electrif.*, vol. PP, no. 99, pp. 1–1, 2016.
- [47] A. Emadi, *Advanced Electric Drive Vehicles*, ser. Energy, Power Electronics, and Machines. Taylor & Francis, 2014.
- [48] J. Gieras, *Permanent Magnet Motor Technology - Design and Applications*. Boca Raton: CRC Press, 2010.
- [49] S. Iwasaki, R. Deodhar, Y. Liu, A. Pride, Z. Zhu, and J. Bremner, “Influence of PWM on the proximity loss in permanent-magnet brushless AC machines,” *IEEE Trans. Ind. Appl.*, vol. 45, no. 4, pp. 1359–1367, July 2009.
- [50] R. Wrobel, A. Mlot, and P. Mellor, “Contribution of end-winding proximity losses to temperature variation in electromagnetic devices,” *IEEE Trans. Ind. Electron.*, vol. 59, no. 2, pp. 848–857, Feb 2012.
- [51] M. Popescu and D. Dorrell, “Skin effect and proximity losses in high speed brushless permanent magnet motors,” in *Energy Conversion Congress and Exposition (ECCE), 2013 IEEE*, Sept 2013, pp. 3520–3527.
- [52] P. Mellor, R. Wrobel, and N. McNeill, “Investigation of proximity losses in a high speed brushless permanent magnet motor,” in *Industry Applications Conference, 2006. 41st IAS Annual Meeting. Conference Record of the 2006 IEEE*, vol. 3, Oct 2006, pp. 1514–1518.
- [53] P. Murgatroyd, “Calculation of proximity losses in multistranded conductor bunches,” *Physical Science, Measurement and Instrumentation, Management and Education, IEE Proceedings A*, vol. 136, no. 3, pp. 115–120, May 1989.
- [54] G. Bertotti, “General properties of power losses in soft ferromagnetic materials,” *IEEE Trans. Magn.*, vol. 24, no. 1, pp. 621–630, Jan 1988.
- [55] S. Steentjes, M. Leßmann, and K. Hameyer, “Advanced iron-loss calculation as a basis for efficiency improvement of electrical machines in automotive application,” in *Electrical Systems for Aircraft, Railway and Ship Propulsion (ESARS), 2012*, Oct 2012, pp. 1–6.
- [56] C. P. Steinmetz, “On the law of hysteresis,” *AIEE Trans.*, vol. IX, no. 1, pp. 1–64, January 1892.

- [57] K. Yamazaki and A. Abe, "Loss investigation of interior permanent-magnet motors considering carrier harmonics and magnet eddy currents," *IEEE Trans. Ind. Appl.*, vol. 45, no. 2, pp. 659–665, March 2009.
- [58] A. Bettayeb, X. Jannot, and J. C. Vannier, "Analytical calculation of rotor magnet eddy-current losses for high speed IPMSM," in *Electrical Machines (ICEM), 2010 XIX International Conference on*, 2010, pp. 1–6.
- [59] L. Chong, R. Dutta, M. F. Rahman, and H. Lovatt, "Experimental verification of core and magnet losses in a concentrated wound IPM machine with v-shaped magnets used in field weakening applications," in *2011 IEEE International Electric Machines Drives Conference (IEMDC)*, May 2011, pp. 977–982.
- [60] A. Wang, Y. Jia, and W. L. Soong, "Comparison of five topologies for an interior permanent-magnet machine for a hybrid electric vehicle," *IEEE Trans. Magn.*, vol. 47, no. 10, pp. 3606–3609, Oct 2011.
- [61] ISO, "ISO/TR 14179-2:2001: Gears - thermal capacity, part 2: Thermal load-carrying capacity," International Organization for Standardization, 2001.
- [62] J. Pyrhonen, T. Jokinen, and V. Hrabovcova, *Design of Rotating Electrical Machines*. Wiley, 2008.
- [63] J. S. Geiger, "Wirkungsgrad und Waermehaushalt von Zahnradgetrieben bei instationaeren Betriebszustaenden [Efficiency and heat regulation of geared transmissions at transient operating conditions]," Ph.D. dissertation, Technische Universitaet Muenchen, 2014.
- [64] J. Durand de Gevigney, C. Changenet, F. Ville, and P. Velex, "Thermal modelling of a back-to-back gearbox test machine: Application to the FZG test rig," *Proceedings of the Institution of Mechanical Engineers, Part J: Journal of Engineering Tribology*, vol. 226, no. 6, pp. 501–515, 2012, accessed on 2016-07-11. [Online]. Available: <http://pij.sagepub.com/content/226/6/501.abstract>
- [65] D.-O. Leimann, *Waermeentstehung und Waermeabfuhr bei Getrieben [Heat Generation and Cooling in Gearboxes]*. Pekrun, Iserlohn, 1982.
- [66] J. Wang, X. Wang, Y. Ma, N. Liu, and Z. Yang, "Analysis of heat transfer in power split device for hybrid electric vehicle using thermal network method," *Adv. Mech. Eng.*, vol. 2014, p. 9, 2014.
- [67] G. Niemann and H. Winter, *Maschinenelemente Band 2: Getriebe allgemein, Zahnradgetriebe - Grundlagen, Stirnradgetriebe [Machine Elements Vol. 2: Transmissions General, Gear Transmissions - Fundamentals, Spur Gears]*. Springer, 2003.

- [68] M. Heizenroether, "Das Stirnraddifferenzial mit Innenverzahnung im Vergleich zum Kegelraddifferenzial inklusive einer Sperrwertanalyse [The spur gear with internal teeth in comparison with bevel gear differential including locking value analysis]," Ph.D. dissertation, TU Muenchen, 2005.
- [69] H. Winter and K. Michealis, "Investigation of the thermal balance of gear drives," in *Proceedings of the Fifth World Congress on the Theory of Machines and Mechanisms 1979*. American Society of Mechanical Engineers, 1979.
- [70] P. Hepermann, "Untersuchungen zur Fresstragfaehigkeit von Gross-, Schraeg- und Hochverzahnungen [Investigations on the scuffing load capacity of large-, helical- and deep-tooth gears]," Ph.D. dissertation, Ruhr-Universitaet Bochum, 2013.
- [71] C. Changenet, X. Oviedo-Marlot, and P. Velex, "Power loss predictions in geared transmissions using thermal networks-applications to a six-speed manual gearbox," *ASME*, vol. 128, pp. 618–625, 2005, accessed on 2016-07-11. [Online]. Available: <http://dx.doi.org/10.1115/1.2181601>
- [72] L. Wu, Z. Zhu, D. Staton, M. Popescu, and D. Hawkins, "Analytical model of eddy current loss in windings of permanent-magnet machines accounting for load," *IEEE Trans. Magn.*, vol. 48, no. 7, pp. 2138–2151, July 2012.
- [73] J. Lammeraner and M. Stafl, *Eddy Currents*. ILIFFE Books Ltd., London and SNTL, Prague, 1964.
- [74] Z. Azar, L. J. Wu, D. Evans, and Z. Q. Zhu, "Influence of rotor configuration on iron and magnet losses of fractional-slot IPM machines," in *Power Electronics, Machines and Drives (PEMD 2010), 5th IET International Conference on*, April 2010, pp. 1–6.
- [75] R. Martins, J. Seabra, A. Brito, C. Seyfert, R. Luther, and A. Igartua, "Friction coefficient in FZG gears lubricated with industrial gear oils: Biodegradable ester vs. mineral oil," *Tribology International*, vol. 39, no. 6, pp. 512 – 521, 2006, accessed on 2016-07-11. [Online]. Available: <http://www.sciencedirect.com/science/article/pii/S0301679X05000988>
- [76] R. Martins, N. Cardoso, H. Bock, A. Igartua, and J. Seabra, "Power loss performance of high pressure nitrided steel gears," *Tribology International*, vol. 42, pp. 1807 – 1815, 2009, special Issue: 35th Leeds-Lyon Symposium. [Online]. Available: <http://www.sciencedirect.com/science/article/pii/S0301679X0900053X>
- [77] H. Winter and K. Michealis, "Untersuchungen zum Waermehaushalt von Getrieben [Investigation of the thermal balance of gear drive]," in *Antriebstechnik 1981*, vol. 20, 1981, pp. 70–74.

- [78] Michaelis, "Die Integraltemperatur zur Beurteilung der Fresstragfaehigkeit von Stirnradgetrieben [The integral temperature for the assessment of the scuffing load capacity of spur gear units]," Ph.D. dissertation, TU Muenchen, 1987.
- [79] G. H. Benedict and B. W. Kelley, "Instantaneous coefficients of gear tooth friction," *A S L E Transactions*, vol. 4, no. 1, pp. 59–70, 1961, accessed on 2016-07-11. [Online]. Available: <http://dx.doi.org/10.1080/05698196108972420>
- [80] J. Durand de Gevigney, F. Ville, C. Changenet, and P. Velex, "Tooth friction losses in internal gears: Analytical formulation and applications to planetary gears," *Proceedings of the Institution of Mechanical Engineers, Part J: Journal of Engineering Tribology*, vol. 227, no. 5, pp. 476–485, 2013.
- [81] E. I. Radzimovsky, "A simplified approach for determining power losses and efficiency of planetary gear drives." *Machine Design*, vol. 9, pp. 101–110, 1956.
- [82] S. Dhar, A. Rawool, S. Ray, and F. Shi, "Lubricant flow and temperature prediction in a planetary gearset," in *SAE Technical Paper*. SAE International, 04 2011. [Online]. Available: <http://dx.doi.org/10.4271/2011-01-1235>
- [83] A. Boglietti, A. Cavagnino, D. Staton, M. Shanel, M. Mueller, and C. Mejuto, "Evolution and modern approaches for thermal analysis of electrical machines," *IEEE Trans. Ind. Electron.*, vol. 56, no. 3, pp. 871–882, March 2009.
- [84] C. Jungreuthmayer, T. Bauml, O. Winter, M. Ganchev, H. Kapeller, A. Haumer, and C. Kral, "A detailed heat and fluid flow analysis of an internal permanent magnet synchronous machine by means of computational fluid dynamics," *IEEE Trans. Ind. Electron.*, vol. 59, no. 12, pp. 4568–4578, 2012.
- [85] J. Dong, Y. Huang, L. Jin, H. Lin, and H. Yang, "Thermal optimization of a high-speed permanent magnet motor," *IEEE Trans. Magn.*, vol. 50, no. 2, pp. 749–752, 2014.
- [86] S. Ramarathnam, A. Mohammed, B. Bilgin, A. Sathyan, H. Dadkhah, and A. Emadi, "A review of structural and thermal analysis of traction motors," *IEEE Trans. Transp. Electr.*, vol. 1, no. 3, pp. 255–265, Oct 2015.
- [87] K. Zhou, J. Pries, and H. Hofmann, "Computationally efficient 3-D finite-element-based dynamic thermal models of electric machines," *IEEE Trans. Transp. Electr.*, vol. 1, no. 2, pp. 138–149, Aug 2015.
- [88] J.-H. Sim, S.-H. Chai, D.-M. Kim, and J.-P. Hong, "Temperature prediction of oil-cooled IPMSM for in-wheel direct-drive through lumped parameter thermal model,"

- in *Electrical Machines and Systems (ICEMS), 2013 International Conference on*, Oct 2013, pp. 134–138.
- [89] G. D. Demetriades, H. Z. D. L. Parra, E. Andersson, and H. Olsson, “A real-time thermal model of a permanent-magnet synchronous motor,” *IEEE Trans. Power Electron.*, vol. 25, no. 2, pp. 463–474, Feb 2010.
- [90] C. Kral, A. Haumer, and S. B. Lee, “A practical thermal model for the estimation of permanent magnet and stator winding temperatures,” *IEEE Trans. Power Electron.*, vol. 29, no. 1, pp. 455–464, Jan 2014.
- [91] A. Boglietti, A. Cavagnino, M. Lazzari, and M. Pastorelli, “A simplified thermal model for variable-speed self-cooled industrial induction motor,” *IEEE Trans. Ind. Appl.*, vol. 39, no. 4, pp. 945–952, July 2003.
- [92] A. Boglietti, A. Cavagnino, and D. Staton, “Determination of critical parameters in electrical machine thermal models,” *IEEE Trans. Ind. Appl.*, vol. 44, no. 4, pp. 1150–1159, July 2008.
- [93] Y. Bertin, E. Videcoq, S. Thieblin, and D. Petit, “Thermal behavior of an electrical motor through a reduced model,” *IEEE Trans. Energy Convers.*, vol. 15, no. 2, pp. 129–134, Jun 2000.
- [94] B.-H. Lee, K.-S. Kim, J.-W. Jung, J.-P. Hong, and Y.-K. Kim, “Temperature estimation of IPMSM using thermal equivalent circuit,” *IEEE Trans. Magn.*, vol. 48, no. 11, pp. 2949–2952, Nov 2012.
- [95] A. Boglietti, A. Cavagnino, D. A. Staton, and M. Popescu, “Impact of different end region cooling arrangements on endwinding heat transfer coefficients in electric motors,” in *Industrial Electronics, 2009. IECON '09. 35th Annual Conference of IEEE, 2009*, pp. 1168–1173.
- [96] P. Zhang, Y. Du, and T. G. Habetler, “A transfer-function-based thermal model reduction study for induction machine thermal overload protective relays,” *IEEE Trans. Ind. Appl.*, vol. 46, no. 5, pp. 1919–1926, Sept. 2010.
- [97] P. H. Mellor, D. Roberts, and D. R. Turner, “Lumped parameter thermal model for electrical machines of TEFC design,” *IEE Proc-B*, vol. 138, no. 5, pp. 205–218, 1991.
- [98] A. Boglietti, A. Cavagnino, and D. Staton, “Determination of critical parameters in electrical machine thermal models,” in *Industry Applications Conference, 2007. 42nd IAS Annual Meeting. Conference Record of the 2007 IEEE*, Sept 2007, pp. 73–80.

- [99] D. Staton, A. Boglietti, and A. Cavagnino, "Solving the more difficult aspects of electric motor thermal analysis in small and medium size industrial induction motors," *IEEE Trans. Energy Convers.*, vol. 20, no. 3, pp. 620–628, Sept 2005.
- [100] D. Howey, P. Childs, and A. Holmes, "Air-gap convection in rotating electrical machines," *IEEE Trans. Ind. Electron.*, vol. 59, no. 3, pp. 1367–1375, March 2012.
- [101] N. Simpson, R. Wrobel, and P. Mellor, "Estimation of equivalent thermal parameters of impregnated electrical windings," *IEEE Trans. Ind. Appl.*, vol. 49, no. 6, pp. 2505–2515, November 2013.
- [102] S. Isert, "Heat transfer through a rotating ball bearing," Master's thesis, Utah State University, 2011.
- [103] Y. R. Takeuchi, M. A. Eb, B. A. Blake, S. M. Demsk, and J. T. Dickef, "Influence of oil lubrication on spacecraft bearing thermal conductance," in *38th Aerospace Mechanisms Symposium*. NASA, 2006, accessed on 2016-06-17. [Online]. Available: <http://www.esmats.eu/amspapers/completelist.php?whichYear=2006>
- [104] N. Bracikowski, M. Hecquet, P. Brochet, and S. V. Shirinskii, "Multiphysics modeling of a permanent magnet synchronous machine by using lumped models," *IEEE Trans. Ind. Electron.*, vol. 59, no. 6, pp. 2426–2437, 2012.
- [105] G. Dajaku, "Electromagnetic and thermal modeling of high utilized PM machines," Ph.D. dissertation, Universitaet der Bundeswehr Muenchen, 2006.
- [106] A. J. Grobler, "Thermal modelling of a high speed permanent magnet synchronous machine," Ph.D. dissertation, North-West University, 2011. [Online]. Available: <http://hdl.handle.net/10394/6528>
- [107] J. P. Holman, *Heat Transfer*, 10th ed. McGraw-Hill, 2010.
- [108] P. Kohnke, *ANSYS Mechanical APDL Theory Reference*, release 15.0 ed., ANSYS, Inc., Southpointe, 275 Technology Drive, Canonsburg, PA 15317, Nov. 2013.
- [109] S. Kugler, "Waermetransport [Heat transfer]," 2008, lecture notes, University of Applied Sciences Wiener Neustadt.
- [110] F. S. Graham and T. J. McDougall, "Quantifying the nonconservative production of conservative temperature, potential temperature, and entropy," *Journal of Physical Oceanography*, vol. 43, no. 5, pp. 838–862, 2013, accessed on 2016-07-11. [Online]. Available: <http://dx.doi.org/10.1175/JPO-D-11-0188.1>

- [111] J. Anderson, *Computational Fluid Dynamics*. Berlin, Heidelberg: Springer Berlin Heidelberg, 2009, ch. Governing Equations of Fluid Dynamics, pp. 15–51. [Online]. Available: http://dx.doi.org/10.1007/978-3-540-85056-4_2
- [112] T. L. Bergman, A. S. Lavine, F. P. Incropera, and D. P. Dewitt, *Fundamentals of Heat and Mass Transfer*, 7th ed. Wiley, 2011.
- [113] B. Pentenrieder, "Finite element solutions of heat conduction problems in complicated 3D geometries using the multigrid method," Master's thesis, Technische Universitaet Muenchen, 2005.
- [114] G. Nikishkov, *Programming Finite Elements in Java*, 1st ed. Springer-Verlag London, 2010.
- [115] J. Tu, G. H. Yeoh, and C. Liu, *Computational fluid dynamics: a practical approach*, 1st ed. Amsterdam [u.a.]: Elsevier, 2008;2007;2010;.
- [116] *ANSYS CFX-Solver Theory Guide*, Release 15.0 ed., ANSYS, Inc., Southpointe, 275 Technology Drive, Canonsburg, PA 15317, Nov. 2013.
- [117] M. Kronbichler. (2010, Feb.) Computational fluid dynamics. Lecture notes. Uppsala University. Accessed on 2016-04-27. [Online]. Available: http://user.it.uu.se/~martinkr/AppliedScientificComputing/CFD_notes.pdf
- [118] P. Wesseling, *Principles of Computational Fluid Dynamics*, 1st ed., ser. Springer Series in Computational Mathematics 29. Springer-Verlag Berlin Heidelberg, 2001.
- [119] *ANSYS® CFX®, Release 15.0, Help System*, ANSYS Inc.
- [120] G. Laccarino. (2004) Solution methods for the incompressible navier-stokes equations. Handout. Stanford University, Center for Turbulence Research. Lecture notes, accessed on 2016-07-11. [Online]. Available: <https://web.stanford.edu/class/me469b/handouts/incompressible.pdf>
- [121] A. Bejan and A. D. Kraus, *Heat Transfer Handbook*. Wiley, 2003.
- [122] V. Gesellschaft and V. Chemieingenieurwesen, *VDI-Wärmeatlas [VDI Heat Atlas]*. Springer, 2013.
- [123] —, *VDI Heat Atlas*. Springer, 2010.
- [124] R. Pechanek and L. Bouzek, "Analyzing of two types water cooling electric motors using computational fluid dynamics," in *Power Electronics and Motion Control Conference (EPE/PEMC), 2012 15th International*, 2012, pp. LS2e.4–1–LS2e.4–5.

- [125] P. Zheng, R. Liu, P. Thelin, E. Nordlund, and C. Sadarangani, "Research on the cooling system of a 4QT prototype machine used for HEV," *IEEE Trans. Energy Convers.*, vol. 23, no. 1, pp. 61–67, 2008.
- [126] A. V. Hütte and W. Boning, *Hütte Taschenbücher der Technik: Elektrische Energietechnik.. Maschinen*. Springer, 1978, no. Bd. 1. [Online]. Available: <http://books.google.at/books?id=vopSngEACAAJ>
- [127] G. Friedrich, S. Vivier, R. Khlissa, K. E. K. Benkara, and B. Assaad, "Determination of rotor-stator heat exchange coefficients in the case of totally enclosed machines: Application to an integrated starter-generator," in *Energy Conversion Congress and Exposition (ECCE), 2013 IEEE*, 2013, pp. 1526–1533.
- [128] G. Taylor, "Distribution of velocity and temperature between concentric rotating cylinders," in *Proceedings of the Royal Society of London*, ser. A, vol. 151, no. 874, 1935, pp. 494–512.
- [129] G. E. Luke, "The cooling of electric machines," *AIEE Trans.*, vol. XLII, pp. 636–652, Jan 1923.
- [130] A. Boglietti, A. Cavagnino, and D. Staton, "Determination of critical parameters in electrical machine thermal models," *IEEE Trans. Ind. Appl.*, vol. 44, no. 4, pp. 1150–1159, July 2008.
- [131] *Handbuch der Gusswerkstoffe [Handbook of casted materials]*, Honsel AG, Fritz-Honsel-Straße 30, 59872 Meschede.
- [132] Metallguss Mertens GmbH. Accessed on 2016-05-06. [Online]. Available: http://www.metallguss-mertens.de/Metallguss_Mertens_Usingen_Infomaterial.pdf
- [133] Voestalpine Steel Division. Isovac 270-35 data sheet. Accessed on 2016-05-07. [Online]. Available: https://www.voestalpine.com/division_stahl/content/download/34052/362582/file/DS%20isovac%C2%A9%20270-35%20A.pdf
- [134] M. Centner, R. Hanitsch, and U. Schafer, "Comparison of high-speed induction motors employing cobalt-iron and silicon electrical steel," in *Electrical Machines, 2008. ICEM 2008. 18th International Conference on*, Sept 2008, pp. 1–6.
- [135] P. Mellor. Advancements in thermal modelling of electrical machines. Accessed on 2016-05-07. [Online]. Available: <http://www.mondragon.edu/en/phs/research/research-teams/electrical-energy/news-folder/electrical-machines/phil-mellors-presentation>

- [136] S. Jacobs. (2008, July) Enhanced fully processed electrical steels for automotive traction applications. Accessed on 2016-05-07. [Online]. Available: http://www.abmbrasil.com.br/cim/download/20080702_sigrid.pdf
- [137] S. Nategh, A. Krings, O. Wallmark, and M. Leksell, "Evaluation of impregnation materials for thermal management of liquid-cooled electric machines," *IEEE Trans. Ind. Electron.*, vol. 61, no. 11, pp. 5956–5965, Nov 2014.
- [138] A. Boglietti, E. Carpanento, M. Cossale, M. Popescu, D. Staton, and S. Vaschetto, "Equivalent thermal conductivity determination of winding insulation system by fast experimental approach," in *Proceedings of the IEEE International Electric Machines and Drives Conference 2015 (IEMDC'15)*, 2015.
- [139] L. Haodong, W. K. Keith, and B. Daniel, "Thermal models and electrical machine performance improvement using encapsulation material," in *Proceedings of the IEEE International Electric Machines and Drives Conference 2015 (IEMDC'15)*, 2015.
- [140] H. Koefler, "Elektrische Maschinen II," Lecture notes, 2009.
- [141] DIN Deutsches Institut fuer Normung e.V., "Pressverbaende - Berechnungsgrundlagen und Gestaltungsregeln," DIN Deutsches Institut fuer Normung e.V., 02 2001.
- [142] T. Knopik, "Steigerung des Wirkungsgrades und der Ausnutzung von Norm-Asynchronmotoren mit Kurzschlusskaefig," Ph.D. dissertation, Technischen Univer-sitaet Darmstadt, 2012.
- [143] G. Kylander, "Thermal modelling of small cage induction motors," Ph.D. dissertation, School of Electrical and Computer Engineering, 1995.
- [144] ISO, "ISO151312 - rolling bearings - thermal speed rating - calculation of coefficients," International Organization for Standardization, 2001.
- [145] M. Popescu, D. Staton, A. Boglietti, A. Cavagnino, D. Hawkins, and J. Goss, "Modern heat extraction systems for electrical machines - a review," in *Electrical Machines Design, Control and Diagnosis (WEMDCD), 2015 IEEE Workshop on*, March 2015, pp. 289–296.
- [146] O. Maloberti, A. Gimeno, A. Ospina, G. Friedrich, K. E. K. Benkara, and L. Charbonnier, "Thermal modeling of a claw-pole electrical generator: Steady-state computation and identification of free and forced convection coefficients," *IEEE Trans. Ind. Appl.*, vol. 50, no. 1, pp. 279–287, Jan 2014.
- [147] D. A. Staton and E. So, "Determination of optimal thermal parameters for brushless permanent magnet motor design," in *Industry Applications Conference, 1998. Thirty-Third IAS Annual Meeting. The 1998 IEEE*, vol. 1, Oct 1998, pp. 41–49 vol.1.

- [148] A. Boglietti, A. Cavagnino, M. Parvis, and A. Vallan, "Evaluation of radiation thermal resistances in industrial motors," *IEEE Trans. Ind. Appl.*, vol. 42, no. 3, pp. 688–693, May 2006.
- [149] A. Boglietti, A. Cavagnino, and D. Staton, "TEFC induction motors thermal models: a parameter sensitivity analysis," *IEEE Trans. Ind. Appl.*, vol. 41, no. 3, pp. 756–763, May 2005.
- [150] M. Yazdani, M. C. Soteriou, F. Sun, and Z. Chaudhry, "Prediction of the thermo-fluids of gearbox systems," *Int. J. Heat Mass Transfer*, vol. 81, no. 0, pp. 337–346, 2015. [Online]. Available: <http://www.sciencedirect.com/science/article/pii/S0017931014009235>
- [151] R. K. D. Nirvesh S. Mehta, Nilesh J. Parekh, "Improve the thermal efficiency of gearbox using different type of gear oils," *International Journal of Engineering and Advanced Technology*, vol. 2, 2013.
- [152] S. Nategh, "Thermal analysis and management of high-performance electrical machines," Ph.D. dissertation, KTH School of Electrical Engineering, 2013.
- [153] G. Funck, "Waermeabfuehrung - Waermeabfuehrung bei Getrieben unter quasistationaeren Betriebsbedingungen," Ph.D. dissertation, TU Muenchen, 1985.
- [154] Z. Gao, R. S. Colby, T. G. Habetler, and R. G. Harley, "A model reduction perspective on thermal models for induction machine overload relays," *IEEE Trans. Ind. Electron.*, vol. 55, no. 10, pp. 3525–3534, Oct. 2008.
- [155] T. Huber, W. Peters, and J. Bocker, "A low-order thermal model for monitoring critical temperatures in permanent magnet synchronous motors," in *Power Electronics, Machines and Drives (PEMD 2014), 7th IET International Conference on*, 2014, pp. 1–6.
- [156] L. Qi, G. Zhang, and Y. Liu, "Modeling and simulation of the thermal network in a space gear-bearing system," in *Information and Automation (ICIA), 2010 IEEE International Conference on*, June 2010, pp. 201–205.
- [157] K. Watanabe, M. Tani, T. Yamamuro, and M. Kubo, "Development of integrated powertrain simulation for hybrid electric vehicles considering total energy management," in *SAE Technical Paper*. SAE International, 04 2012, accessed on 2016-07-11. [Online]. Available: <http://dx.doi.org/10.4271/2012-01-1012>
- [158] T. Kiss, J. Lustbader, and D. Leighton, "Modeling of an electric vehicle thermal management system in Matlab/Simulink," in *SAE Technical Paper*. SAE International, 04 2015, accessed on 2016-07-11. [Online]. Available: <http://dx.doi.org/10.4271/2015-01-1708>

- [159] M. Yazdani and M. C. Soteriou, "A novel approach for modeling the multiscale thermo-fluids of geared systems," *Int. J. Heat Mass Transfer*, vol. 72, no. 0, pp. 517–530, 2014, accessed on 2016-07-11. [Online]. Available: <http://www.sciencedirect.com/science/article/pii/S0017931014000635>
- [160] K. Bennion and J. Cousineau, "Sensitivity analysis of traction drive motor cooling," in *Transportation Electrification Conference and Expo (ITEC), 2012 IEEE*, 2012, pp. 1–6.
- [161] M. Fénot, Y. Bertin, E. Dorignac, and G. Lalizel, "A review of heat transfer between concentric rotating cylinders with or without axial flow," *International Journal of Thermal Sciences*, vol. 50, no. 7, pp. 1138–1155, 2011, accessed on 2016-07-11. [Online]. Available: <http://www.sciencedirect.com/science/article/pii/S1290072911000548>
- [162] M. Botha, "Electrical machine failures, causes and cures," in *Electrical Machines and Drives, 1997 Eighth International Conference on (Conf. Publ. No. 444)*, Sep 1997, pp. 114–117.
- [163] M. Jafari, A. Gauchia, K. Zhang, and L. Gauchia, "Simulation and analysis of the effect of real-world driving styles in an EV battery performance and ageing," *IEEE Trans. Transp. Electrif.*, vol. 1, no. 4, pp. 391–401, 2015.
- [164] L. Guzzella and A. Amstutz. (2005) The QSS toolbox manual. Accessed on 2014-06-07. [Online]. Available: <http://www.idsc.ethz.ch/Downloads/DownloadFiles/qss>
- [165] F. V. G. Leprince, C. Changenet and P. Vexel, "Investigations on oil flow rates projected on the casing walls by splashed lubricated gears," *Adv. in Tribology*, 2012.
- [166] L. Manin and D. Play, "Thermal behavior of power gearing transmission, numerical prediction, and influence of design parameters," *J. of Tribology*, vol. 121, pp. 693–702, October 1999.
- [167] M. Kamiya, Y. Kawase, T. Kosaka, and N. Matsui, "Temperature distribution analysis of permanent magnet in interior permanent magnet synchronous motor considering PWM carrier harmonics," in *Proc. International Conference on Electrical Machines and Systems (ICEMS)*, 2007, pp. 2023–2027.
- [168] Z. Huang, S. Nategh, M. Alakula, V. Lassila, and J. Yuan, "Direct oil cooling of traction motors in hybrid drives," in *Proc. IEEE International Electric Vehicle Conference (IEVC'12)*, 2012, pp. 1–8.
- [169] J. Guosheng, D. Liyong, and K. Ken, *Advanced Thermal Management Materials*. New York Heidelberg Dordrecht London: Springer, 2013, vol. VIII.

- [170] H. Schaefer, *Integrierter Starter-Generator (ISG)*. Renningen: Expertverlag, 2001, vol. 3, no. Fachbuchreihe / Haus der Technik.
- [171] C. Spearman, "The proof and measurement of association between two things," *American Journal of Psychology*, vol. 15, no. 1, pp. 72–101, Jan. 1904, accessed on 2016-06-17. [Online]. Available: <http://www.jstor.org/stable/1412159>
- [172] J. de Santiago, H. Bernhoff, B. Ekergård, S. Eriksson, S. Ferhatovic, R. Waters, and M. Leijon, "Electrical motor drivelines in commercial all-electric vehicles: A review," *IEEE Trans. Veh. Technol.*, vol. 61, no. 2, pp. 475–484, Feb 2012.
- [173] G. D. Olavarria, A. Reinap, and M. Alaküla, "Cost estimation of electric traction machine and gearbox for a hybrid vehicle application," in *Electric Drives Production Conference (EDPC), 2014 4th International*, Sept 2014, pp. 1–5.
- [174] D. J. Patterson, G. Heins, M. Turner, B. J. Kennedy, M. D. Smith, and R. Rohoza, "An overview of the compactness of a range of axial flux PM machines," in *2015 IEEE International Electric Machines Drives Conference (IEMDC)*, May 2015, pp. 96–101.
- [175] V. B. Honsinger, "Sizing equations for electrical machinery," *IEEE Trans. Energy Convers.*, vol. EC-2, no. 1, pp. 116–121, March 1987.
- [176] M. Zeraoulia, M. E. H. Benbouzid, and D. Diallo, "Electric motor drive selection issues for HEV propulsion systems: A comparative study," *IEEE Trans. Veh. Technol.*, vol. 55, no. 6, pp. 1756–1764, Nov 2006.
- [177] K. Steininger and R. Gardner. Transposition of WLTP into European Union and UN regulations, informal document no. GRPE-70-13. Accessed on 2016-03-29. [Online]. Available: <https://www.unece.org/fileadmin/DAM/trans/doc/2015/wp29grpe/GRPE-70-13.pdf>
- [178] UNECE. Working party on pollution and energy (GRPE). Accessed on 2014-06-07. [Online]. Available: http://www.unece.org/trans/main/wp29/wp29wgs/wp29grpe/wltp_dhc11.html
- [179] EPA. Federal test procedure revisions. Accessed on 2014-06-07. [Online]. Available: <http://www.epa.gov/otaq/sftp.htm#cycles>

List of Publications

The work presented in this thesis has resulted in the following journal and conference publications. These papers are subjected to copyright by the particular conference organizer, mainly by the IEEE. Some journal publications are extended versions of a conference publication (J1/C3, J2/C4).

Journal Publications

- J1** C. Paar, and A. Muetze, "Thermal Real-Time Monitoring of a Gearbox Integrated IPM Machine for Hybrid Electric Traction", *IEEE Trans. Transp. Electrification*, vol. PP, no. 99, 2016.
- J2** C. Paar, A. Muetze, and H. Kolbe, "Influence of Machine Integration on the Thermal Behavior of a PM Drive for Hybrid Electric Traction," *IEEE Trans. Ind. Appl.*, vol. 51, no. 5, pp. 3914-3922, Sept.-Oct. 2015.

Conference Publications

- C1** C. Paar, and A. Muetze, "Discussion of Machine Placement and Integration on the Thermal Design of HEV IPM Machines," *Transportation Electrification Conference and Expo (ITEC), 2016 IEEE*, June 2016, pp. 1-6.
- C2** C. Paar, and A. Muetze, "Influence of Dry Clutch and ICE Transmission Integration on the Thermal Load of a PM Based Integrated Starter-Generator," *Energy Conversion Congress and Exposition (ECCE), 2015 IEEE*, Sept. 2015, pp. 106-111.
- C3** C. Paar, and A. Muetze, "Thermal Real-Time Monitoring of a Gearbox Integrated Electric Rear Axle Drive for Hybrid Electric Traction," *Transportation Electrification Conference and Expo (ITEC), 2015 IEEE*, June 2015, pp. 1-6.
- C4** C. Paar, H. Kolbe, and A. Muetze, "Influence of Machine Integration on the Thermal Behavior of a PM Drive for Hybrid Electric Traction," *Energy Conversion Congress and Exposition (ECCE), 2014 IEEE*, Sept. 2014, pp. 3266-3271.

List of Figures

1.1	Design process of electric drives/EMs for automotive applications.	2
1.2	Traditional design points of electric drives/EMs.	3
1.3	eRAD placement in drive train.	9
1.4	eRAD CAD view.	9
1.5	ISG placement in the drive train.	9
1.6	ISG exploded view.	9
1.7	eRAD distributed winding.	10
1.8	ISG concentrated winding.	10
1.9	ISG stator design.	11
3.1	LPTN modeling example, solid block.	31
3.2	eRAD, FEM model, windings.	42
3.3	Stator core to frame coefficient [97].	43
3.4	Radiation between two surface areas [109].	46
4.1	Cross-sectional view of the eRAD.	51
4.2	eRAD, FEM loss model.	52
4.3	LPTN with capacitances and heat sources.	55
4.4	eRAD, schematic representation of cross-sectional view with relevant dimensions for computation of R_{12} and R_{23} , and nodes nos. 0-3.	56
4.5	eRAD machine model; FEM model screenshots.	57
4.6	eRAD, FEM machine model details at non-drive end (NDE).	58
4.7	eRAD, planetary gear-set and disconnect system, geometry of FEM model.	59
4.8	Meshed eRAD PGS FEM model.	60
4.9	eRAD, computational fluid dynamics (CFD) simulation results; computation of cooling jacket to coolant heat transfer coefficient.	62
4.10	eRAD, air gap thermal conductance.	63
4.11	eRAD, factor for adapting the cooling effect of the bearing lubricant flow in the LPTN.	63
4.12	eRAD, test-rig with thermal insulation box and lubrication tubes.	66
4.13	Measured EM spin losses as a function of speed and temperature.	66

4.14	Measured gearbox losses for different oil sump temperatures at zero torque.	67
4.15	eRAD, EM, DCS and PGS spin losses (zero torque) strip-down measurement results at 50 °C oil sump temperature.	68
4.16	eRAD EM LPTN model; steady-state; comparison of measured and computed end winding drive end (DE) (node no. 11) temperatures at 20 kW.	69
4.17	eRAD EM LPTN model; steady-state; comparison of measured and computed end winding NDE (node no. 10) temperatures at 20 kW.	69
4.18	eRAD EM LPTN model; steady-state; comparison of measured and computed winding in slot (node no. 9) temperatures at 20 kW.	70
4.19	eRAD EM LPTN model; steady-state; comparison of measured and computed rotor (node no. 6) temperatures at 20 kW.	70
4.20	eRAD EM LPTN model; thermal transient; winding in slot (node no. 9) temperature, 30 s peak torque step response at 250 rpm.	71
4.21	eRAD EM LPTN model; thermal transient; end winding DE (node no. 11) side, 30 s peak torque step response at 2380 rpm.	71
4.22	eRAD EM LPTN model; long term transient validation of full model.	72
4.23	eRAD EM numerical thermal model; steady-state validation; computed vs. measured magnet temperatures, between NDE and center position, at 20 kW shaft power for different shaft speeds.	73
4.24	eRAD EM numerical thermal model; steady-state validation; computed vs. measured winding in slot temperatures at stator stack centre, at 20 kW shaft power for different shaft speeds.	74
4.25	eRAD EM FEM model; thermal transient; winding in slot temperature, 30 s peak torque step response at 250 rpm.	75
4.26	eRAD EM FEM model; thermal transient; end winding DE locations, 30 s peak torque step response at 250 rpm.	75
4.27	eRAD EM FEM model; thermal transient; winding in slot temperature, 30 s peak torque step response at 2380 rpm.	76
4.28	eRAD EM FEM model; thermal transient; end winding DE locations, 30 s peak torque step response at 2380 rpm.	76
4.29	eRAD EM numerical thermal model; transient validation, run in at 2380 rpm, 83 Nm; FEM temperature plot.	77
4.30	eRAD PGS FEM model; transient; comparison of measured and computed oil sump temperature at 12000 rpm and w/o cooling.	77
4.31	eRAD numerical thermal model; gearbox transient validation; temperature at 12000 rpm after 2500 s.	78
4.32	eRAD numerical thermal model; gearbox transient validation; temperature at 12000 rpm after 4500 s.	78

4.33 IPMSM cross section view, with location of gearbox loss injection and location of some LPTN nodes.	80
4.34 End winding sensitivity analysis without gearbox.	81
4.35 End winding temperature sensitivity analysis with gearbox.	82
4.36 Magnet/rotor temperature sensitivity analysis without gearbox.	82
4.37 Magnet temperature sensitivity analysis with gearbox.	83
4.38 Sensitivity analysis: influence of relative change of stator to housing interface gap thermal resistance (R_{12}) on the magnet temperature.	84
4.39 Sensitivity analysis: influence of relative change of air gap thermal resistance (R_{45}) on the magnet temperature.	84
4.40 LPTN model with most relevant heat flow paths (red lines) and loss distribution.	85
4.41 Reduced thermal model; nodes: 0' coolant, 1' stator, 2' winding and 3' rotor.	86
4.42 Comparison of modeling approaches with measurement results, magnet temperature, steady-state, 20 kW.	87
4.43 Comparison of modeling approaches with measurement results, winding in slot temperature, 250 rpm, 200 Nm torque step for 30 s.	87
4.44 eRAD; relative change of thermal resistance R_{01} (cooling jacket to coolant) as function of volumetric flow rate.	89
4.45 eRAD; simplified thermal model with additional sensor.	89
4.46 eRAD; simulation: magnet temperature in the FTP-75 driving cycle.	90
4.47 eRAD; simulation: end winding temperature in the FTP-75 driving cycle.	90
4.48 eRAD; comparison: influence of gearbox losses for end winding and magnet temperatures for a 25 s boost cycle with 40 % of the gearbox losses injected into shaft.	91
4.49 eRAD; comparison: magnet and end winding temperatures at DE with 40 % of the gearbox losses injected into shaft and without consideration of gearbox.	92
4.50 Magnet temperature for different loss distribution within the gearbox (ratio frame to shaft).	93
4.51 Simulated: comparison of end winding temperatures during boost cycle.	94
4.52 Simulated: comparison of end winding DE temperature with and without oil cooling.	95
4.53 eRAD cross section view, with oil slingers.	96
4.54 Oil slinger.	96
4.55 eRAD oil slinger design drawing.	96
4.56 Test-rig cross section view.	96
4.57 Drag torque of oil slingers at different oil levels and shaft speeds.	97
4.58 Torque pulse step response at 200 rpm using oil slingers.	98
4.59 Torque pulse step response at 1000 rpm using oil slingers.	98

4.60	Torque pulse step response at 1000 rpm with oil pump at a flow rate of 0.8 L/s .	100
4.61	Torque pulse step response at 3000 rpm with oil pump at a flow rate of 1.5 L/s .	100
4.62	Torque pulse step response at 2000 rpm with oil pump at a flow rate of 2.4 L/s .	101
4.63	Mean convection coefficient from end winding surface to oil at different flow rates and shaft speeds.	101
4.64	eRAD, oil cooling of end windings, CFD simulation results at 200 rpm after 3 s run-in.	102
4.65	eRAD; oil cooling; comparison of CFD computation with measured results; mean convection coefficient from end winding surface to oil at 2.4 L/s flow rate.	103
5.1	ISG 3D illustration.	106
5.2	ISG, FEM loss computation model, 2D mesh.	107
5.3	ISG, loss computation of the bearings.	108
5.4	ISG, geometrical FEM model simplifications.	109
5.5	ISG, FEM thermal models.	111
5.6	ISG air gap thermal convection coefficient.	113
5.7	ISG clutch model (for validation).	113
5.8	ISG, comparison of measured and simulated losses.	114
5.9	ISG, comparison of measured and simulated efficiency.	114
5.10	Experimental validation of the thermal model: simulated winding-in-slot temperature of a 8 s T_{max} pulse at 30 % n_{max} compared with temperatures measured with thermocouples (TC), at defined nodes in the winding in the slots (WS).	116
5.11	Experimental validation of the thermal model: thermal transient response of torque step from 0 to 32 % T_{max} at 20 % n_{max}	117
5.12	Experimental validation of the thermal model: Simulated winding in slot temperature measured with thermocouples (TC), at defined nodes in the slots (WS) during FTP-72 driving cycle.	118
5.13	Cross-sectional view of ISG clutch test-rig.	118
5.14	Validation of clutch thermal model: Measured and computed disc temperatures during a controlled heating-up sequence.	119
5.15	Simulation of clutch influence on machine thermal behavior; 2000 rpm, 7.5 kW, three clutch actuations per minute.	120
5.16	Influence of the additional clutch heat load on magnet, winding and clutch temperature at 2380 rpm and 30 kW.	121
5.17	Simulation of ICE and TM influence on machine thermal behavior; 2000 rpm, 7.5 kW.	122

5.18	Simulation of ICE, TM and clutch influence on machine thermal behavior; 2000 rpm, 7.5 kW.	123
5.19	Parameter correlation analysis in nominal operating point.	124
5.20	FTP-72 driving cycle: computed rotor temperatures, for none, one of the two, or both external heat sources coupled to the ISG.	125
6.1	eRAD FTP-75 simulation results: comparison of thermal response with and w/o gearbox attached.	130
6.2	eRAD FTP-75 torque speed operating points.	130
6.3	Distribution of eRAD magnet temperature, FTP driving cycle, 40% of gearbox losses are injected into the rotor.	131
6.4	Magnet temperature: NEDC, with gearbox attached.	132
6.5	Magnet temperature: 10-15 mode (Japan), with gearbox attached.	132
6.6	Distribution of eRAD magnet temperature, WLTP driving cycle, 40% of gearbox losses are imposed in rotor.	133
6.7	Distribution of ISG magnet temperature, FTP-72 driving cycle.	135
6.8	Scaling of eRAD air gap shear stress depending on percentage of gearbox heat load injected into rotor.	136
6.9	Scaling of ISG air gap shear stress air gap shear stress depending on ICE boundary condition temperature; zero clutch load; nominal operating point.	137
6.10	Scaling of ISG air gap shear stress air gap shear stress depending on clutch heat load at nominal operating point and FTP-72; ICE not connected.	138
6.11	eRAD FTP-75 torque speed operating points with density of data points; the black point indicates the nominal operating point.	139
6.12	eRAD FTP-75 torque speed operating points with magnet temperature; the black point indicates the nominal operating point.	139
6.13	ISG FTP-72 torque speed operating points with density of data points; the black point indicates the nominal operating point.	140
6.14	ISG FTP-72 torque speed operating points with magnet temperature; the black point indicates the nominal operating point.	141
A.1	FTP-75 speed profile.	183
B.1	eRAD EM numerical thermal model, steady-state validation: computed vs. measured magnet DE temperatures at 20 kW shaft power for different shaft speeds.	185
B.2	eRAD EM numerical thermal model, steady-state validation: computed vs. measured magnet NDE temperatures at 20 kW shaft power for different shaft speeds.	186

- B.3 eRAD EM numerical thermal model, steady-state validation: computed vs. measured end winding DE temperatures at 20 kW shaft power for different shaft speeds. 186
- B.4 eRAD EM numerical thermal model, steady-state validation: computed vs. measured end winding NDE temperatures at 20 kW shaft power for different shaft speeds. 187

- C.1 eRAD EM FEM model; thermal transient; end winding NDE, 30 s peak torque step response at 250 rpm. 189
- C.2 eRAD EM FEM model; thermal transient; end winding NDE, 30 s peak torque step response at 2380 rpm. 190
- C.3 eRAD EM FEM model; thermal transient; winding in slot temperature, 30 s peak torque step response at 1000 rpm. 190
- C.4 eRAD EM FEM model; thermal transient; end winding DE locations, 30 s peak torque step response at 1000 rpm. 191
- C.5 eRAD EM FEM model; thermal transient; end winding NDE, 30 s peak torque step response at 1000 rpm. 191

- D.1 eRAD, LPTN, Simulink model structure. 194
- D.2 eRAD, Simulink loss model. 195

List of Tables

1.1	Typical and realized shear stress values of EMs.	7
3.1	Computed examples of fluid to housing heat transfer coefficients for different material and fluid parameter combinations.	38
4.1	eRAD, IPMSM characteristics.	50
4.2	Core losses computed for selected operating points, comparison of FEM calculation methods.	52
4.3	Comparison of total losses: data obtained from FEM, loss model and measurement results.	65
4.4	eRAD EM LPTN model; steady-state; comparison of measured and computed temperatures at different operating points.	68
4.5	eRAD EM numerical thermal model; steady-state validation; computed and measured temperature differences; 20 kW shaft power, different speeds.	73
5.1	ISG EM data.	107
5.2	ISG thermal model parameters.	112
5.3	ISG steady-state validation.	115
D.1	eRAD thermal resistances: parameters with computation approach and sources.	196

Acronyms

AC alternating current. 18

CAD computer-aided design. 9, 35

CFD computational fluid dynamics. 14, 29, 30, 35–37, 39, 49, 58, 59, 61, 62, 102–104, 112, 116, 165, 168

DC direct current. 17, 18, 44

DCS disconnect system. 10, 50, 53, 58, 59, 67, 68, 77, 78, 143, 165, 166

DE drive end. 14, 43, 49, 50, 53, 54, 58, 64, 67–71, 73, 75, 76, 81–83, 88, 92, 95, 96, 99, 102, 115, 121, 122, 128, 129, 166, 167, 197, 198

EHD elastohydrodynamic. 24

eHub electric wheel-hub. 7

EM electric machine. V, VI, XI, XII, 1–5, 7–10, 12, 14, 25, 27, 29–31, 38–41, 43–46, 50, 53, 58, 59, 61, 65–77, 79, 80, 93, 96, 99, 102, 104–111, 116, 125–130, 133, 136, 142–145, 165, 166, 169–171, 183–187, 189–191

EMF electromotive force. 10

EOL end of line. 61

eRAD electric rear axle drive. V–VII, XI, XII, 4, 9, 10, 12, 14, 20, 21, 25, 27, 42, 43, 45, 49–53, 57–62, 68–78, 80, 93, 95, 96, 128, 129, 140–144, 165–167, 169–171, 184–187, 189–191

ESS energy storage system. 105, 106, 133

EV electric vehicle. 1, 128

EWDE end winding at the drive end. 73, 115

EWNDE end winding at the non-drive end. 72, 73, 115

- FEM** finite element method. 1–3, 12–14, 20, 21, 27, 29–31, 33, 35, 37, 42–44, 51, 52, 57–63, 65, 72–78, 80, 90, 92, 93, 104, 107, 109, 111, 114, 116, 118, 128, 129, 134, 143, 144, 165, 166, 168, 170, 171, 189–191
- FTP-72** Federal Test Procedure 72. 117, 125, 134, 135, 137, 138, 140, 141, 144, 169
- FTP-75** Federal Test Procedure 75. 89, 95, 128, 129, 133, 136, 137, 183
- HEV** hybrid electric vehicle. V, VI, XI, XII, 1, 8, 9, 21, 49, 79, 105, 106, 127, 128, 144
- HV** high-voltage. 50
- ICE** internal combustion engine. V, VI, XI, XII, 4, 8–10, 14, 49, 99, 105, 106, 108, 109, 119, 122, 127, 128, 134, 135, 137, 138, 142–145, 169
- IM** induction machine. 1, 7, 44, 53
- IPMSM** interior-mounted permanent-magnet synchronous-machine. VI, 1, 8, 21, 49, 50, 53, 65, 70, 74, 77, 79, 80, 90, 104, 106, 107, 114, 128, 143, 144, 167, 171
- ISG** (crankshaft)-integrated starter generator. V, VI, VIII, XI, XII, 4, 9–12, 14, 21, 22, 45, 105–109, 111–115, 118, 119, 121, 122, 127, 128, 134, 135, 137, 142–144, 165, 168, 169, 171, 184
- LPTN** lumped-parameter thermal-network. V, 3, 14, 27, 29–32, 46, 49, 51, 53–55, 61–65, 68–72, 74, 79, 80, 88, 104, 143, 165–167, 170, 171, 194
- LV** low-voltage. 50
- MMF** magnetomotive force. 5, 10
- MTPA** maximum torque per ampere. 12, 114
- NDE** non-drive end. 43, 50, 53, 54, 58, 64, 67–69, 72, 73, 81–83, 88, 96, 99, 102, 115, 121, 165, 166, 197, 198
- NdFeB** neodymium, iron and boron. 20, 49
- NEDC** New European Driving Cycle. 89, 131, 132, 137
- PGS** planetary gear-set. 50, 53, 58–60, 67, 68, 77, 78, 93, 143, 165, 166
- PM** permanent magnet. 20
- PMSM** permanent-magnet synchronous-machine. 6, 12

PWM pulse-width modulation. 7, 18, 20

RANS Reynolds-averaged Navier-Stokes. 36

SOC state-of-charge. 106

SUV sport utility vehicle. 9

TC thermocouple. 70, 72, 74, 115, 116, 118

TE totally-enclosed. 7

TEFC totally-enclosed fan-cooled. 45, 46, 81

TM transmission. VI, 4, 9, 10, 14, 105, 108, 122–124, 126–128, 134, 137, 143, 144, 168, 169

VFD variable frequency drive. 3

WLTP worldwide harmonized light vehicles test procedure. 129, 132, 136, 137

WS winding in slot. 115, 116

Symbols

Matrices

C	Ws/K	thermal capacitance vector/matrix
K	W/K	thermal (element) conductivity matrix
k	W/mK	thermal conductivity matrix
n		normal vector
P	W	vector of loss injections
τ	N/m ²	(shear) stress tensor

Scalars

α		pole coverage ratio: relative pole area, ratio of mean to maximum flux density in pole area
α	1/K	linear temperature coefficient (of resistivity)
β_b	rad	base circle helix angle
δ	m	skin depth
δ	m	air gap
ε		profile overlap
ε		emissivity
ζ_w		press fit length ratio
η		efficiency
η	Ns/m ²	dynamic viscosity
μ_f		friction coefficient
$\mu_{f,m}$		mean friction coefficient
$\mu_{f,r}$		rolling friction coefficient
ν	m ² /s	kinematic viscosity
ξ		relative conductor height
ρ	kg/m ³	density
ρ	m	radius of curvature
ρ	Ωm	electrical resistivity
ρ_{ref}	Ωm	electrical resistivity at reference temperature
ρ		Spearman's correlation factor
σ	N/m ²	air gap shear stress

Symbols

σ_n	N/m ²	nominal air gap shear stress
$\hat{\sigma}$	N/m ²	peak air gap shear stress
σ	W/m ² K ⁴	Stefan-Boltzmann constant
σ	S/m	electrical conductivity
τ_{sp}	m	slot pitch
τ	s	time constant or time difference
τ_p	m	pole pitch
ϕ	rad	phase angle
ψ_{PM}	Wb	permanent magnet flux
ω	rad/s	angular velocity
A	m ²	area
A_c	m ²	coolant (fluid) to jacket area
A	A/m	effective electric loading
\hat{A}_1	A/m	fundamental wave electric loading peak value
B	T	effective flux density
\hat{B}_1	T	fundamental wave peak flux density
\hat{B}	T	peak flux density
B_{ref}	T	reference flux density: reference value for consideration of nonlinear flux density dependency of core losses
C_{sp}		splash oil factor
C	Ws/m	utilization factor: electromagnetic utilization (factor of Esson)
C_1		tooth width factor
C_2		immersion depth factor
C_{air}		air friction coefficient
C_m		dimensionless torque
C	J/K	thermal capacity
c	J/kgK	specific heat
c_w		drag coefficient
d	m	diameter
$d_{j,c,b}$	m	cooling channel bottom diameter
d_δ	m	air gap diameter
D_h	m	hydraulic diameter
$d_{r,o}$	m	rotor outer diameter
$d_{s,i}$	m	stator inner diameter
$d_{s,o}$	m	stator outer diameter
$d_{s,sl,b}$	m	stator slot (bottom) diameter

E	J	energy
E_{clutch}	J	clutch heat generation energy
E_{O}	N/m ²	E-modulus (Young's modulus)
E_{rad}	W/m ²	rate of energy emission by radiation
F	N	force
f	Hz	frequency
F_r		Fraude number: dimensionless number, ratio of flow inertia to gravity (or an external field)
f_{ref}	Hz	reference frequency: reference value, nonlinear frequency dependency of core losses
F_r	N	rotor force
F		transfer factor
F_v	N	vehicle driving resistance/force
g	m/s ²	force of gravity
g		integer number
G_{th}	K/W	thermal conductance
H	A/m	magnetic field strength
h	m	height
HF		hybridization factor
h_{sl}	m	slot height
h_t	m	tooth height
$h_{\text{th},j,s}$	W/m ² K	contact heat transfer coefficient from jacket to stator stack
$h_{\text{th,conv}}$	W/m ² K	convective heat transfer coefficient
h_{th}	W/m ² K	thermal heat transfer coefficient
$h_{\text{th},c,j}$	W/m ² K	convective heat transfer coefficient
$h_{\text{th},r,a}$	W/m ² K	convective heat transfer coefficient from rotating surfaces to air
h_{tot}	m ² /s ²	specific total enthalpy
H_v		gear loss factor
I_{RMS}	A	RMS current
I	A	effective current
i		index number
I_{ph}	A	phase current
J	A/m ²	current density
j		index number
K		press fit calculation factor
k	W/mK	thermal conductivity

Symbols

k_1	Ws/m ³ K	factor for computation of rotating surfaces to air convection coefficient
k_2	W/m ² K	factor for computation of rotating surfaces to air convection coefficient
k_{air}	W/mK	thermal conductivity of air
k_a	W/mK	equivalent thermal conductivity of the insulation
k_{wr}	W/mK	thermal conductivity of the winding replacement material
k_{Fe}	W/mK	thermal conductivity of the core material
$k_{\text{f,sl}}$		slot fill factor
k_j	W/mK	thermal conductivity of the cooling jacket/frame
k_{cu}		correction factor
k_p		processing factor: factor for core losses
k_{rot}		factor for consideration of rotational masses (inertia)
$k_{\text{w},1}$		winding factor
l	m	length
l_a	m	active length: length multiplied with iron fill factor
l_c	m	conductor length
L_d	H	d -axis inductance: inductance, direct-axis direction
L_q	H	q -axis inductance: inductance, quadrature-axis direction
m	kg	mass
m_{ph}		number of phases
m_{sl}		number of conductors per slot
$m_{\text{v},c}$	kg	vehicle curb weight
$m_{\text{v},l}$	kg	vehicle load weight
m_v	kg	vehicle mass/weight
n		integer number
N_{ph}		number of turns per phase
N_{sl}		number of slots
Nu		Nusselt number: dimensionless quantity for description of convective heat flow between a solid surface and a fluid
P	W	power
\hat{P}	W	peak power
p	N/m ²	pressure
p_{core}	W/kg	specific losses: core losses per gravimetric unit

$P_{in,mech}$	W	mechanical input power
P_{air}	W	air friction losses
P_{bear}	W	bearing losses
P_{cu}	W	copper losses
$P_{cu,AC}$	W	AC copper losses
$P_{cu,add}$	W	additional copper losses
$P_{cu,DC}$	W	DC copper losses
$P_{cu,e}$	W	proximity eddy-current losses
P_{fe}	W	core losses
P_{gbx}	W	(total) gearbox losses
$P_{gbx,bear}$	W	gearbox bearing losses
$P_{gbx,oc}$	W	oil churning gearbox losses
$P_{gbx,seal}$	W	gearbox sealing losses
$P_{gbx,tf}$	W	gearbox tooth friction losses
$P_{gbx,tg}$	W	gearbox total gear mesh losses
P_{mag}	W	magnet losses
Pr		Prandtl number: dimensionless quantity for description of relation between viscous diffusion and thermal diffusion rates
Q	J	energy transfer rate
q	W	heat transfer rate
q		number of slots per pole per phase
R	Ω	electrical resistance
r	m	radius
$r_{bear,i}$	m	bearing inner radius
Re		Reynolds number: dimensionless quantity for description of fluid flow patterns
R_{th}	W/K	thermal resistance
R_{01}	W/K	coolant to stator jacket thermal resistance
R_{12}	W/K	stator jacket (surface) to yoke thermal resistance
R_{23}	W/K	yoke to teeth thermal resistance
S_E	kg/ms ³	energy source
T	Nm	torque
\hat{T}	Nm	peak torque
Ta		Taylor number: dimensionless quantity for description of fluid flow properties
T	K	temperature
T_{ref}	K	reference temperature

Symbols

t	s	time
T_{\max}	Nm	maximum torque
T_r	Nm	rotor torque
V	m^3	volume
v	m/s	velocity or speed
w	m	width
w_c	m	coil width
w_{sl}	m	slot width
w_t	m	tooth width
x	m	x-direction
x	m	distance or length
X_R		factor of roughness
y	m	y-direction
y	m	distance or length
y		coil span (number of slots)
z	m	z-direction
z		teeth number
z	m	distance or length
J	A/m^2	current density vector

Vectors

G	K/W	thermal conductivity matrix
g	m/s^2	gravity or acceleration vector
Q	W	heat flow vector
q	W/m^2	heat flux vector
S_M	$\text{kg}/\text{m}^2\text{s}^2$	momentum source (vector)
T	K	temperature vector
v	m/s	velocity vector
x	m	position vector

Appendix A

Vehicle Model

For the cycle simulations a simplified vehicle model was used for evaluation of the thermal behavior using the following driving cycles: Relevant driving cycles for governmental emission homologation of vehicles are the New European Driving Cycle (NEDC) for the EU and the Federal Test Procedure (FTP-75) for the United States. The fuel and emission regulations depend on national legislation [178, 179]. Furthermore, in the future (as proposed by the EU-parliament) the Worldwide Harmonized Light Vehicles Test Procedure (WLTP) may be relevant [178]. FTP-75 (Fig. A.1) was mainly considered in the case studies, because

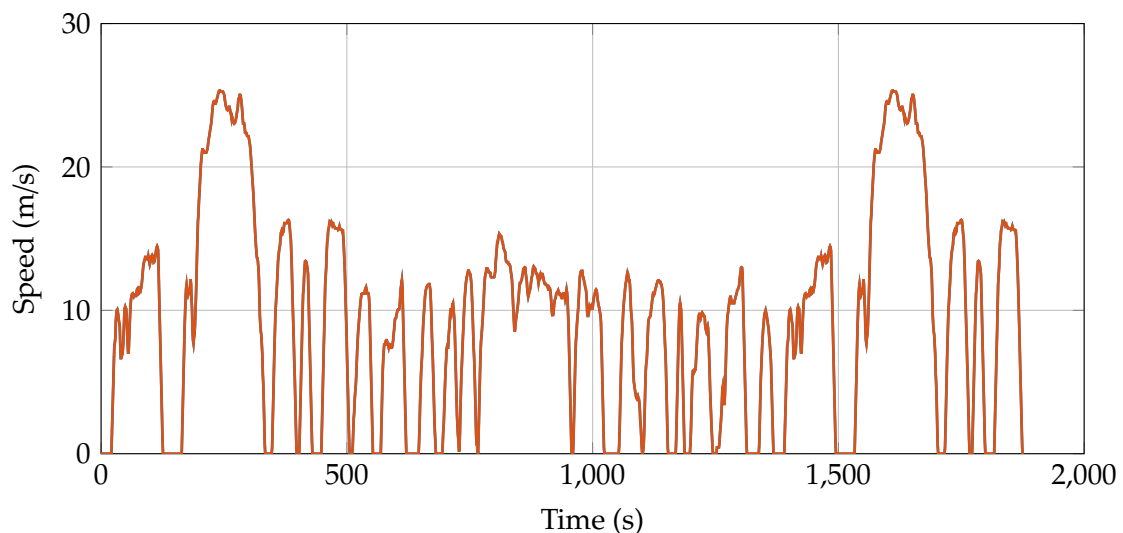


Figure A.1: FTP-75 speed profile.

it requires higher torque dynamics to fulfill the speed target over time, when compared to the NEDC.

For the calculation of the electric machine (EM) torque profiles a simple longitudinal vehicle model using a quasi-static approach was used [164]. The quasi-static vehicle model calculates the torque profile for the EM from a given speed profile without considering dynamic effects in the vehicle drive train. Hybrid vehicle control strategies were not consid-

ered.

Electric Rear Axle Drive (eRAD) application: The mid-size car defined for the simulations has a curb weight of $m_{v,c} = 2058$ kg. A load (driver) weight of $m_{v,l} = 75$ kg was assumed for the simulations to calculate the total driving force

$$F_v = mv_g\mu_{f,r} + \frac{Av^2\rho c_w}{2} + (m_{v,c}k_{rot} + m_{v,l})v, \quad (A.1)$$

with vehicle speed v , (air) density ρ , total vehicle weight $m_v = m_{v,c} + m_{v,l}$ and force of gravity $g = 9.81$ m/s². The rolling friction constant, which depends on the road surface to wheel contact, was assumed with $\mu_{f,r} = 0.008$. The vehicle cross sectional area is $A = 2.28$ m² with a drag coefficient of $c_w = 0.29$. The factor k_{rot} is a simplification to consider the rotational masses (inertia) of the drive train as a percentage share of the curb weight, and was estimated with 5% of the curb weight ($k_{rot} = 1.05$). The total driving force is used to calculate the required shaft torque of the EM via the tire radius. The front/rear torque distribution of the vehicle is defined with 40% : 60% in the simulations.

Integrated starter generator (ISG) application: For the ISG application a complex vehicle model (implemented in MATLAB/Simulink) was used. The model allowed simulation of the clutch operating strategy. The output of the simulation results have been used without further discussion in the research work.

Appendix B

eRAD Numerical Thermal Model Steady-State Validation

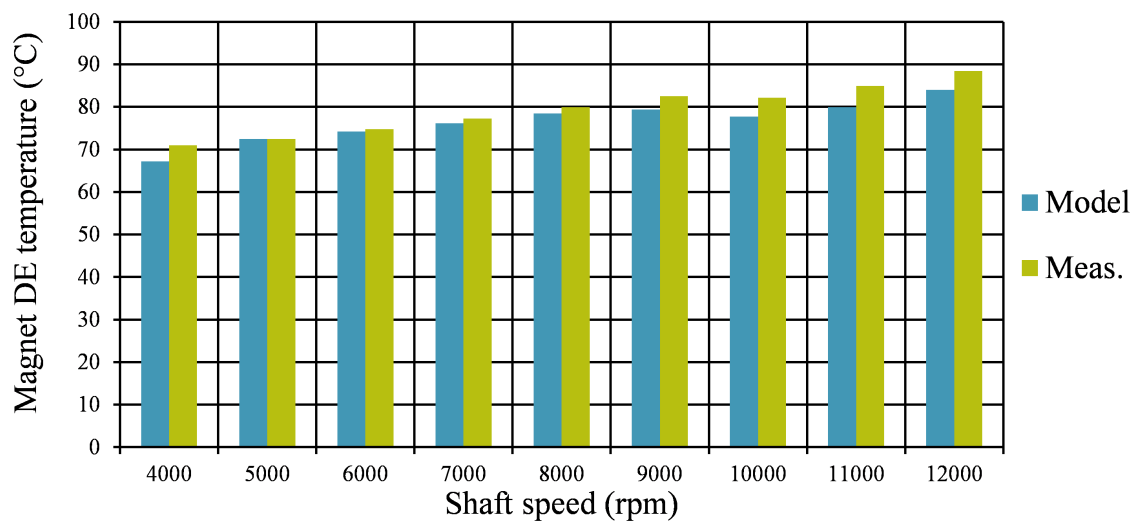


Figure B.1: eRAD EM numerical thermal model, steady-state validation: computed vs. measured magnet DE temperatures at 20 kW shaft power for different shaft speeds.

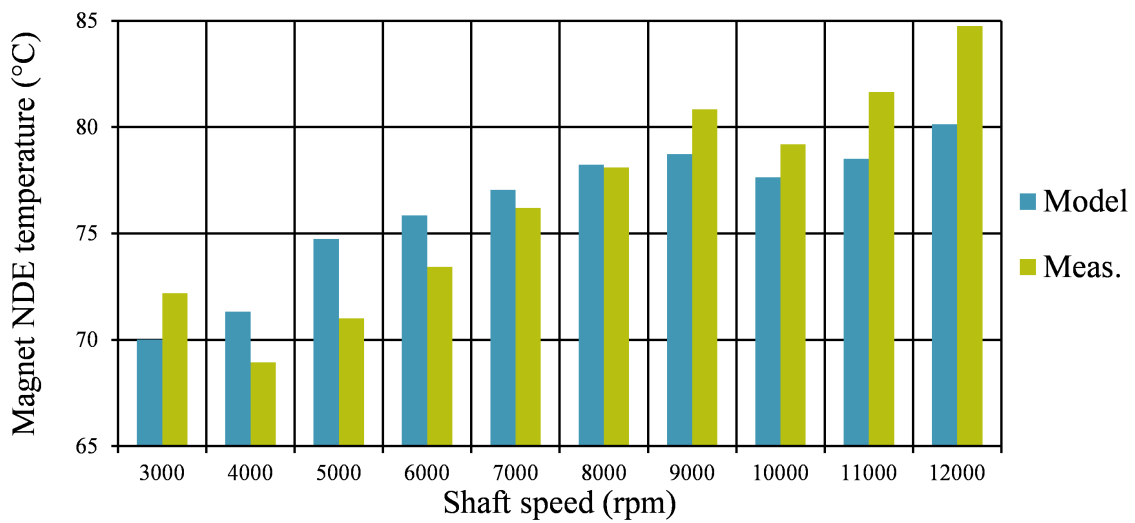


Figure B.2: eRAD EM numerical thermal model, steady-state validation: computed vs. measured magnet NDE temperatures at 20 kW shaft power for different shaft speeds.

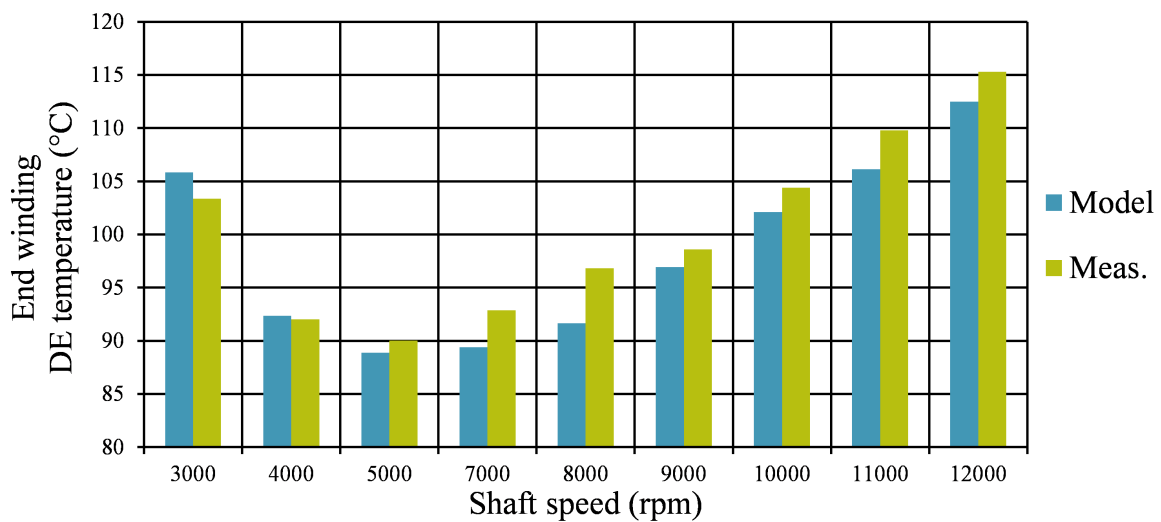


Figure B.3: eRAD EM numerical thermal model, steady-state validation: computed vs. measured end winding DE temperatures at 20 kW shaft power for different shaft speeds.

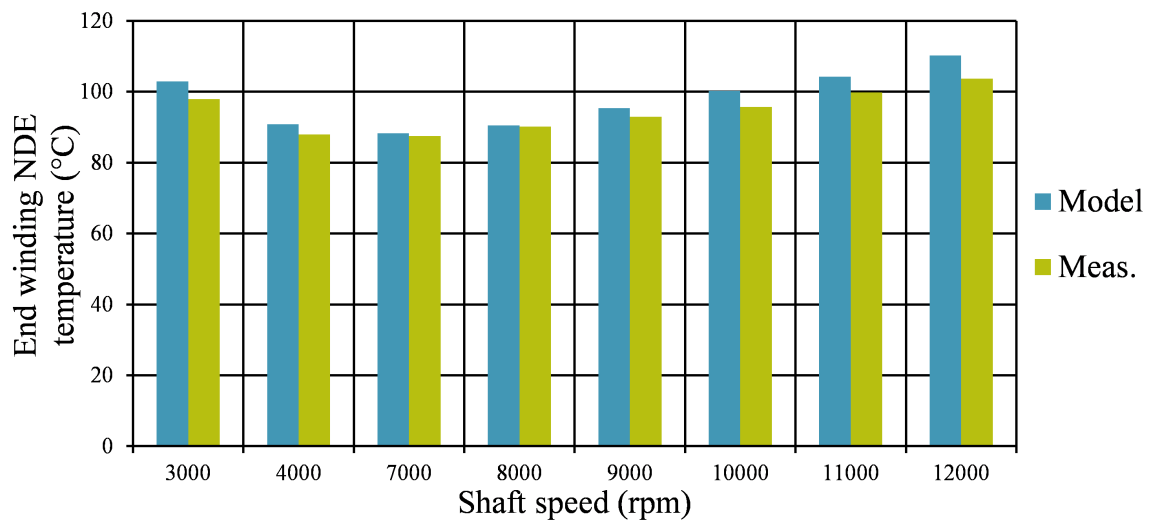


Figure B.4: eRAD EM numerical thermal model, steady-state validation: computed vs. measured end winding NDE temperatures at 20 kW shaft power for different shaft speeds.

Appendix C

eRAD Numerical Thermal Model Transient Validation

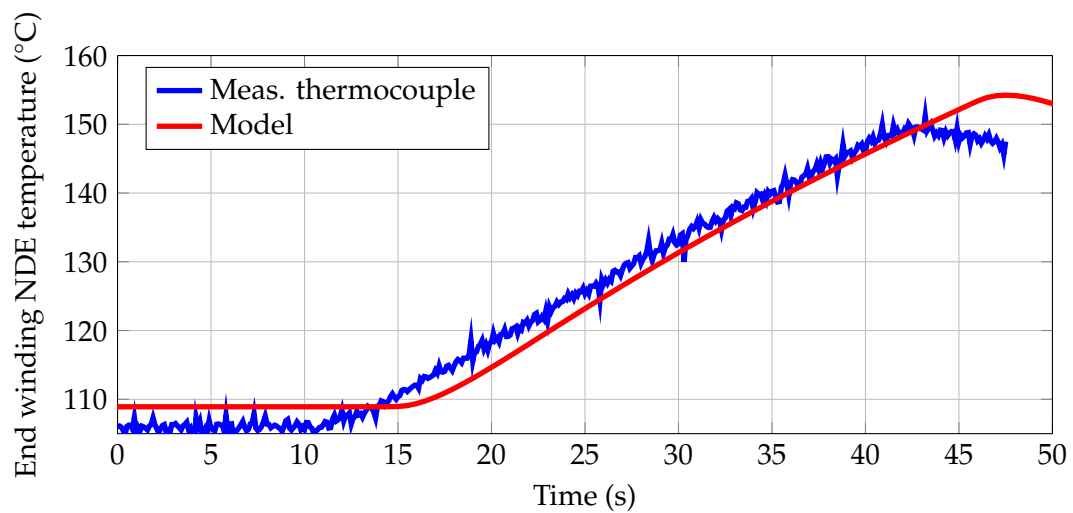


Figure C.1: eRAD EM finite element method (FEM) model; thermal transient; end winding NDE, 30 s peak torque step response at 250 rpm.

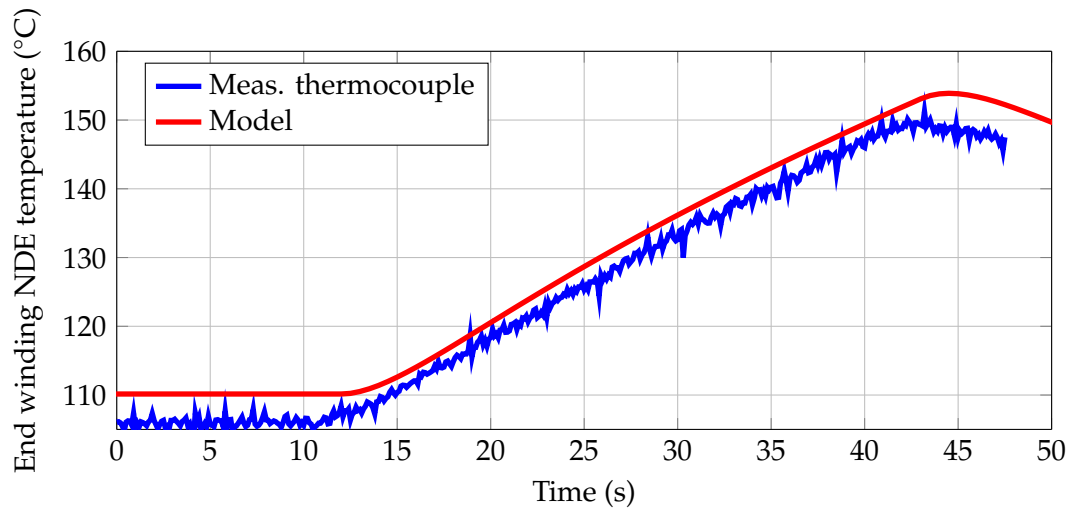


Figure C.2: eRAD EM FEM model; thermal transient; end winding NDE, 30 s peak torque step response at 2380 rpm.

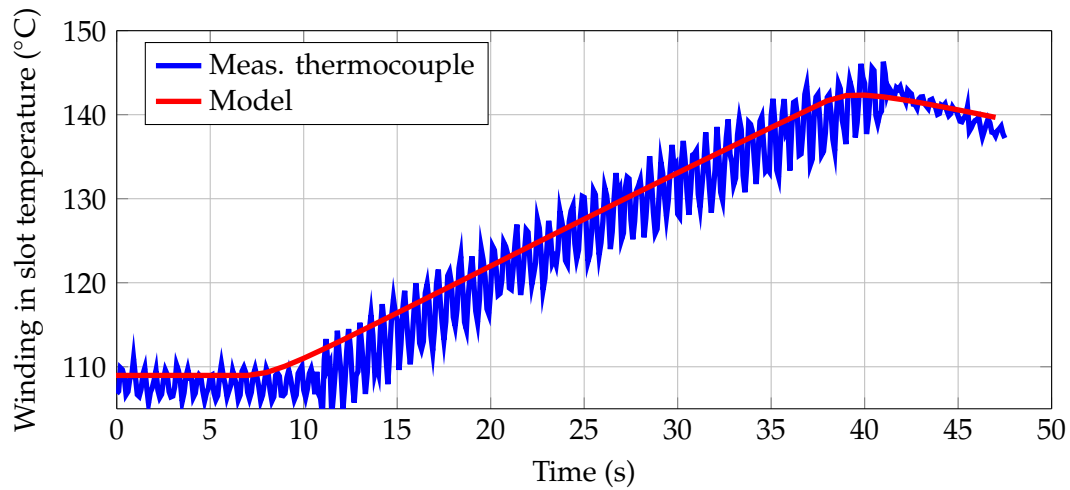


Figure C.3: eRAD EM FEM model; thermal transient; winding in slot temperature, 30 s peak torque step response at 1000 rpm.

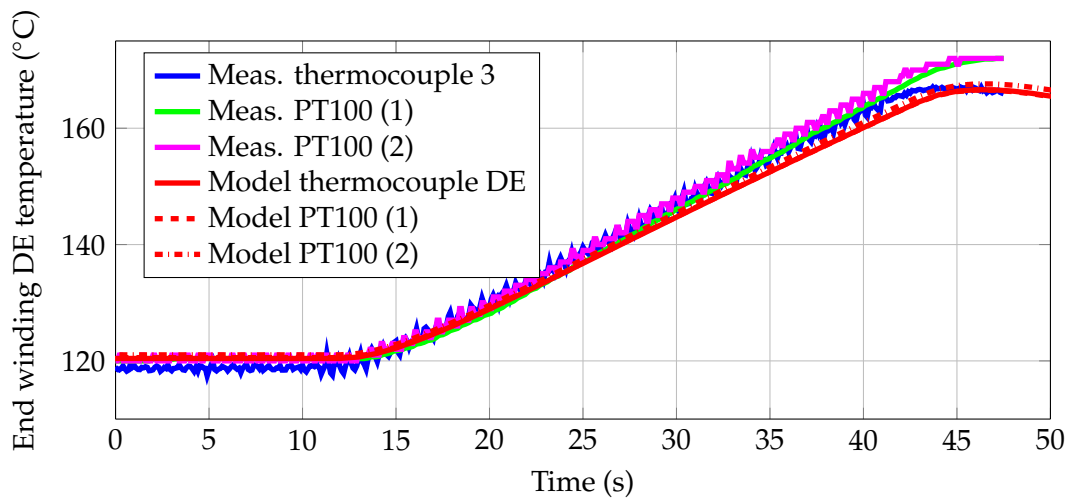


Figure C.4: eRAD EM FEM model; thermal transient; end winding DE locations, 30 s peak torque step response at 1000 rpm.

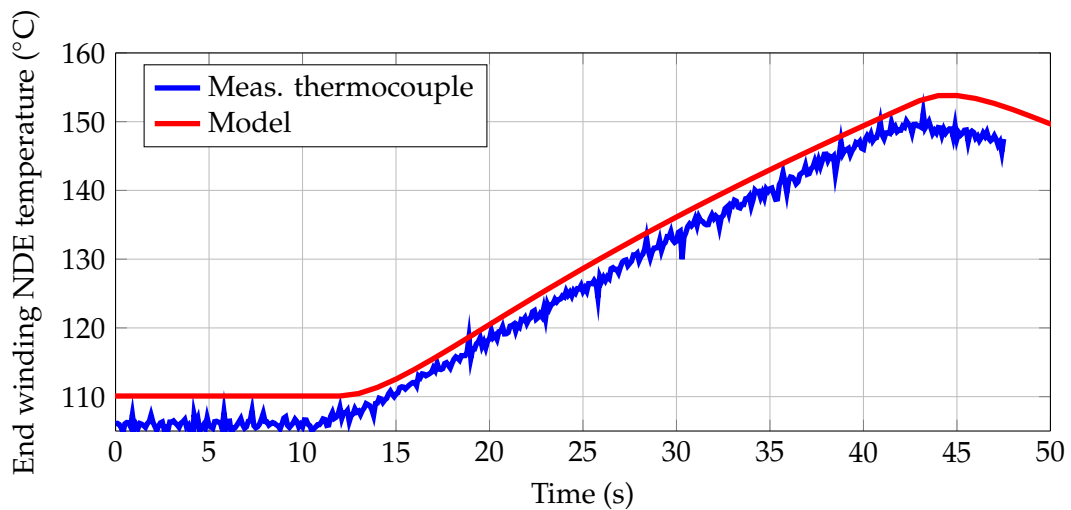


Figure C.5: eRAD EM FEM model; thermal transient; end winding NDE, 30 s peak torque step response at 1000 rpm.

Appendix D

eRAD Lumped Parameter Thermal Model Implementation

D.1 MATLAB/Simulink Implementation

D.1.1 Model Structure Overview

Fig. D.1 illustrates the model structure in MATLAB/Simulink.

The MATLAB/Simulink workspace variables are organized in the main structures: (i) OP, this structure contains all variables which define the operating points and inputs into the model; (ii) MDL is the parameter structure; (iii) VAL the validation structure; (iv) SLK are signals and parameters; (v) TMP are temporary variables which are assigned in another scripts or m-files. However, all these structures have following sub-structure variables

- `.v` contains the value specifying the parameter, this variable could be a scalar, vector or a matrix array.
- `.x` specifies sampling values for parameters specified in `.v`. This variable is defined as vector.
- `.y` specifies sampling values for parameters specified in `.v`, if `.v` is an 2D-array.
- `.z` specifies sampling values for parameters specified in `.v`, if `.v` is an 3D-array.
- `.xComment`, `.yComment`, `.zComment`, `.vComment` or `.Comment` are contain an optional description to understand the variable structure.
- `.vUnit`, `.xUnit`, `.yUnit`, `.zUnit` are an optional unit definition.

Example, number of stator slots (scalar):

```
MDL.numSlotS.Comment = 'Number of stator slots';
```

```
MDL.numSlotS.vUnit = '-';
```

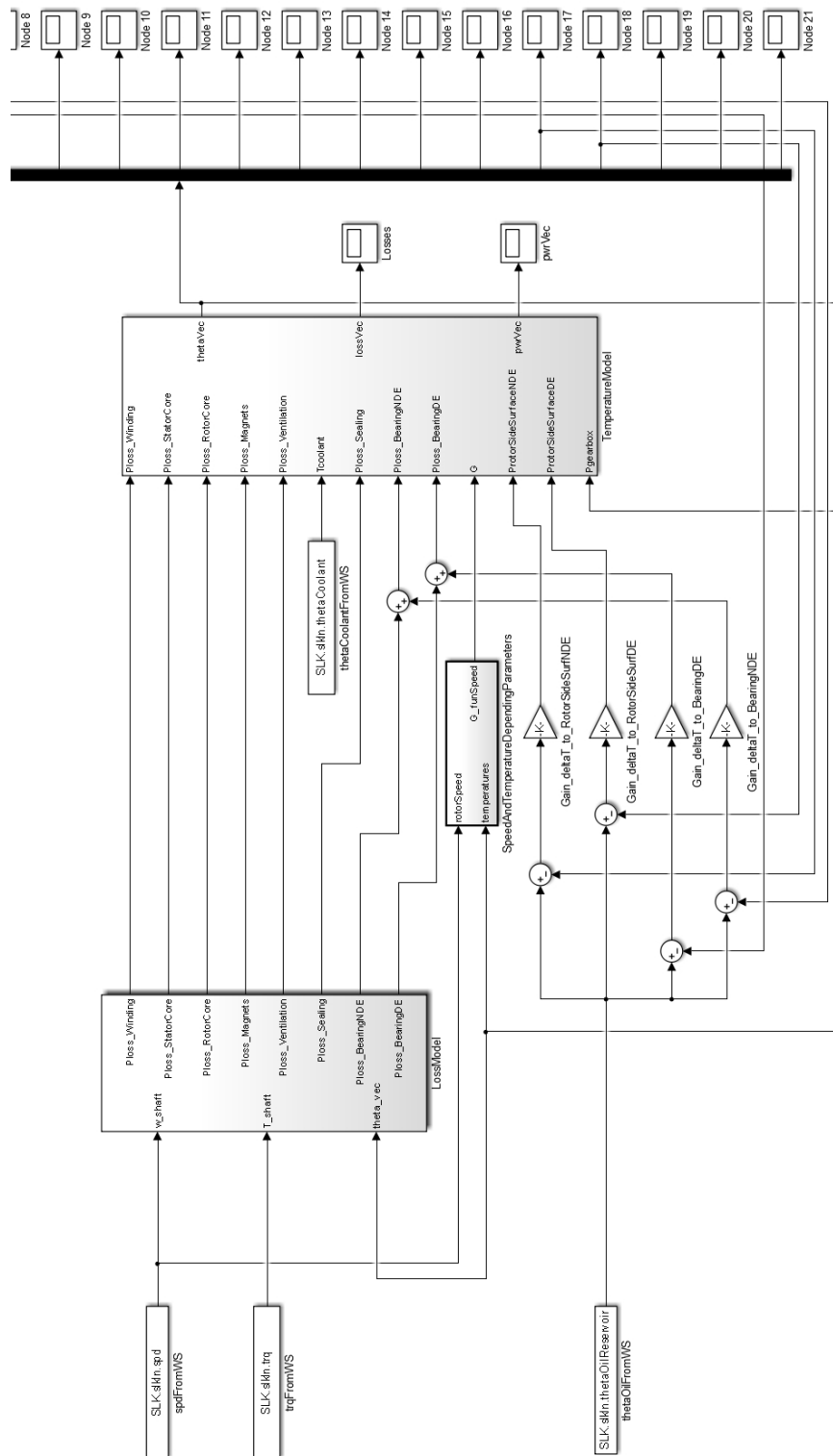


Figure D.1: eRAD, lumped-parameter thermal-network (LPTN), Simulink model structure.

MDL.numSlotS.v = 45;

Input signals speed, torque, oil reservoir temperature and coolant temperature are defined in the structure 'SLK.slkIn'. Output signals are the node temperatures of the lumped parameter model and consolidated in the structure 'slkOut'.

D.1.2 Loss Model

The loss information is implemented using look-up-tables (in MATLAB/Simulink). The shaft speed and torque signals are an input in the subsystem. The winding temperature in the slots is taken as reference for the temperature dependency of the copper (winding) losses.

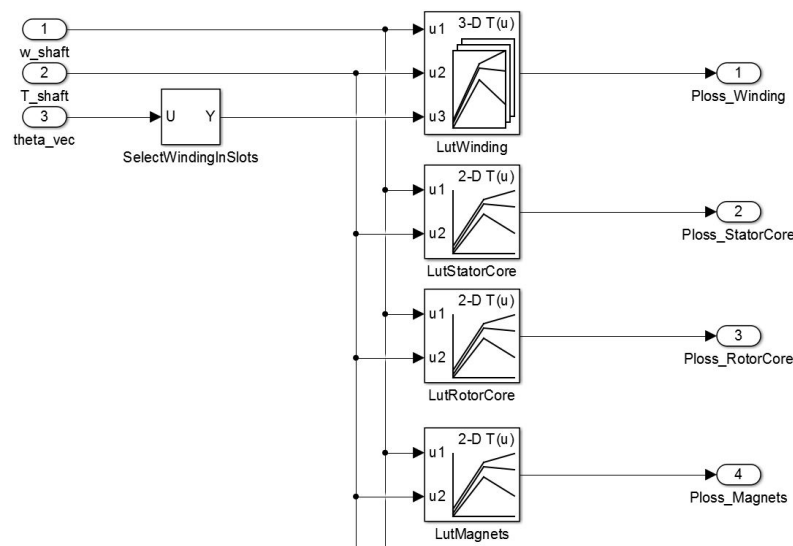


Figure D.2: eRAD, Simulink loss model.

D.2 Thermal Model Parameters

Table D.1: eRAD thermal resistances: parameters with computation approach and sources.

Therm. Res.	Thermal Path	Parameter	Comment
R_{01}	Cooling jacket to coolant	Convection coefficient to coolant: $\approx 2000 \text{ W/m}^2\text{K}$; changes with fluid flow speed	Source: CFD
R_{12}	Cooling jacket to stator stack	Jacket/stack thermal resistance: $400 - 1200 \text{ W/m}^2\text{K}$, and iron thermal conductance: $28 \text{ W/m}^2\text{K}$	Conductive path from cooling jacket towards contact resistance between jacket and stator stack and yoke resistance
R_{23}	Yoke to teeth	Thermal conductance of iron stack in radial direction 28 W/mK	Half of overall yoke resistance and half of resistance of all teeth connected in parallel
R_{34}	Yoke to teeth surface	See R_{23}	Half of teeth resistance
R_{45}	Teeth surface to rotor surface	Airgap	Approach of Taylor
R_{56}	Rotor surface to rotor node	Magnet thermal cond. $8 \text{ W/m}^2\text{K}$, iron to magnet $860 \text{ W/m}^2\text{K}$, iron therm. cond. 28 W/mK	Mapping of v-shaped geometry
R_{612}	Rotor to shaft	Shaft/rotor stack contact resistance: $860 \text{ W/m}^2\text{K}$	Conductive path from rotor node (mapped rotor model) to shaft towards contact resistance
R_{29}	Yoke to winding		See R_{39}
R_{39}	Teeth to winding		Thermal resistances between stator stack and winding towards slot insulation, impregnation and wire insulation; approach of Simpson: replacement thermal resistance

R_{113}	Frame non-drive end (NDE) to cooling jacket	Frame thermal conductance 154 W/mK	Conductive thermal path from frame (equivalent axial/radial section) to cooling jacket node
R_{114}	Frame drive end (DE) to cooling jacket	Frame thermal conductance 154 W/mK	
R_{712}	Shaft surface to bearing NDE	Half of bearing resistance: 0.045 W/K	Conductive thermal path from shaft midpoint to midpoint of bearing, source: [103]
R_{812}	Shaft surface to bearing DE	Half of bearing resistance: 0.045 W/K.	Conductive thermal path from shaft midpoint to midpoint of bearing, source: [103]
R_{814}	Bearing DE to frame DE	Half of bearing resistance: 0.045 W/K and thermal conductance	Conductive thermal path from bearing midpoint to frame midpoint, source: [103]
R_{713}	Bearing DE to frame DE	Half of bearing resistance: 0.045 W/K	Conductive thermal path from bearing midpoint to frame midpoint, source: [103]
R_{1315}	Frame NDE to air volume NDE	Assumption: 30 W/m ² K	Convection from frame surface to air volume in end winding region, source: [97]
R_{1517}	Rotor side surface to air volume NDE	Assumption: 100 W/m ² K	Convection from frame surface to air volume in end winding region, source: [97]
R_{617}	Rotor to side surface rotor NDE	Magnet thermal conductance: 8 W/mK	Thermal conduction from rotor midpoint to side surface
R_{618}	Rotor to side surface rotor DE	Magnet thermal conductance: 8 W/mK	Thermal conduction from rotor midpoint to side surface
R_{1618}	Rotor to air volume DE	Assumption: 100 W/m ² K	Convection from rotor surface to air volume in end winding region, see [97]

R_{1416}	Frame DE to air volume DE	Assumption: $30 \text{ W/m}^2\text{K}$	Convection from frame surface to air volume in end winding region, see [97]
R_{1519}	Air volume NDE to winding area surface NDE	Assumption: $30 \text{ W/m}^2\text{K}$	Convection from end winding surface to air volume, see [97]
R_{1019}	End winding surface NDE to end winding midpoint NDE	Calculation of winding replacement material	Approach of Simpson [101]
R_{910}	Winding in slot to end winding midpoint NDE	Thermal conduction of copper: 401 W/mK	Thermal conduction
R_{911}	Winding node in slot to end winding midpoint DE	Thermal conduction of copper: 401 W/mK	Thermal conduction
R_{R1120}	End winding surface DE to end winding midpoint DE	Calculation of winding replacement material	Approach of Simpson [101]
R_{1620}	Air volume DE to winding area surface DE	$\approx 30 \text{ W/m}^2\text{K}$	Convection from end winding surface to air volume, see [97]